ARCHITECTURAL AND HVAC APPLICATIONS OF IMPINGING JET VENTILATION USING FULL SCALE AND CFD SIMULATION

by

Jatuwat Varodompun

A dissertation submitted in partial fulfillment
of the requirements for the degree of
Doctor of Philosophy
(Architecture)
in The University of Michigan
2008

Doctoral Committee:

Associate Professor Mojtaba Navvab, Chair
Associate Professor Klaus-Peter Beier
Associate Professor Aline J. Cotel
Assistant Professor Fernando L. Lara
Senior Engineer Venkat S. Manian

DEDICATION

To my family

ACKNOWLEDGMENTS

I would like to thanks my advisor, Mojtaba Navvab, who has supported me from the beginning of my studies. As an advisor and colleague, he provided support, opportunities, valuable suggestions and freedom-all which were necessary for my academic journey. As a friend and mentor, he offered understanding, opinions, trust, complements and forgiveness.

TABLE OF CONTENTS

LIST OF TABLES

Table

LIST OF FIGURES

Figure

LIST OF APPENDICES

NOMENCLATURE

ACH	Air Change per Hour
A	Supply (nozzle) area
$A_{PD>10}$	Area of selected plane where draft discomfort exceeds 10%
$A_{t>3C}$	Area where temperature of 1-0.1 m exceeding 3°C
A_{room}	Room area
$\overline{C}$	Average Concentration at a given location
C_0	Initial Concentration
$C_{1000ppmv}$	Concentration (CO_2) at 1000 ppmv
C_a	Room (CO_2) air concentration level
C_{cfd}	Concentration (CO_2) generated by CFD simulation
C_e	Concentration at an exhaust/ return
$C_i(t)$	Concentration at a given time
C_s	Concentration at a supply
F	Force
I_{cl}	Clo-value
L	Length scale
M	Metabolic rate
M_p	Total CO_2 emission rate
PD	Local Thermal Comfort Percentage of Dissatisfied
PMV	Predicted Mean Vote
PPD	Predicted Percent of Satisfied
P_a	Vapor pressure
Q	Ventilation rate
RH	Relative Humidity
Re	Reynold Number
Ri	Richardson Number
THP	Total Heat Production of number of occupants x total heat generating by human body
$T_{2.7-0.1}$	Average air temperature of CFD nodes at 0.1, 1.1, 1.8, and 2.7m height
$T_{1.8-0.1}$	Average air temperature of CFD nodes at 0.1, 1.1, and 1.8m height
$T_{a,l}$	Local air temperature
T_e	Air temperature at an exhaust/ return
T_r	Mean Radiant Temperature
T_s	Supply air temperature
U	Velocity
$U_{1/2}$	Half of max. velocity along jet profile
U_m	Max. velocity along jet profile
U_{mo}	Max. velocity along jet profile of 3D jet
U_o	Supply maximum velocity
VEF, ε	Ventilation Effectiveness
VEF_c, E_z, ε_c	Concentration Ventilation Effectiveness
VEF_t, ε_t	Thermal Ventilation Effectiveness
V	Room volume
V_{bz}	Calculated fresh air rate for occupants according to ASHRAE 62 standard called breathing zone outdoor air
V_{oz}	Actual fresh air intake rate or zone outdoor air
W	Work rate
W_p	Humidity load
a	Velocity profile power factor
b_y	Distance along y-axis of 3D jet
b_z	Distance along z-axis of 3D jet
d	Nozzle diameter

f	Pipe friction coefficient
h	Nozzle height from the floor or nozzle width
h_c	Heat transfer coefficient
η	Normalize supply area to the room area
θ	Normalized temperature
θ_o	Normalized temperature at a nozzle
f_{cl}	Clothing area factor
g	Gravity acceleration
k	Constant for thermal ventilation rate calculation
μ	Dynamic viscosity
q	Cooling/Heating load
q_{rad}	Radiative Cooling/Heating load
r	Distance along nozzle radius
r_{max}	Nozzle radius
ρ	Density
t	Time
τ_i	Local Mean Age
τ_r	Inversed room air change
v	Air velocity
$\bar{v}_{a,l}$	Local mean air velocity
v_c	Supplied CO_2 specific volume
v_s	Supplied air specific volume
w_a	Room humidity level
w_s	Supply humidity level
x	Distance along x-axis
x_{max}	Rectangular nozzle width
y	Distance along y-axis
y_{max}	Rectangular nozzle length
$y_{1/2}$	Distance along y-axis of jet half velocity
z	Distance along z-axis

ABSTRACT

To enhance thermal comfort and Indoor Air Quality (IAQ) by using least amount of energy is a challenge for building ventilation system. One answer to this challenge is "ventilation strategies" which are characterized by the placement of the terminal configurations and the control schemes such as supply temperature and velocity. Mixing (MJV), displacement (DV), and newly introduced impinging jet (IJV) system, are the available options for a common ventilated room. Past studies show that IJV performs impressively yet this system is still lacking of studies in many aspects. For the practitioners to use this system, impinging jet characteristics, terminal configurations, operation method such as Variable-Air-Volume (VAV) and Constant-Air-Volume (CAV), and space volume, are four objectives that must be answered with the first priority. In the process of completing these objectives, this dissertation has maximized the use of Computational Fluid Dynamics (CFD) by not only for visualizing the flow but also for developing a new ventilation index called CFD ventilation performances. This index is unique for CFD and impossible to be obtained from full scale experiment. Recommended by the standards such as ASHRAE RP-1133, full scale experiment was rather used for validating the CFD results such as predictive models of an impinging jet. After implementing this newly developed index, well-known indices such as ventilation effectiveness and PMV-PPD (Predicted-Mean-Vote and Predicted-Percentage-of-Dissatisfaction) with related ventilation theories, parameters to make IJV provided the better IAQ and consumed less energy are the results. With high ventilation effectiveness at least 1.1, IJV still can be supplied with normal velocity and typical cool temperature which is not possible for DV, while disadvantages are stratification discomfort and draft near supply terminals. Given the confirmed promising results of a case study classroom, there are many architectural applications possible for implementing IJV. Laboratories, passenger terminals, operating, tunnels, atrium, etc, are all good candidates that come with different settings and requirements. The configurations of IJV in these applications combining with many unknown impacts from furniture lay-out, people movement, transient simulation, etc, raises the demands of not only IJV future studies but also improving the advanced research tools such as CFD.

CHAPTER 1
INTRODUCTION TO HVAC VENTILATION STRATEGIES

Ventilation is a mandatory tool for enhancing occupants' well-being. Acceptable thermal comfort and Indoor Air Quality (IAQ) are also an essential part of it. Ventilation affects room temperature, relative humidity (RH), Mean Radiant Temperature (MRT), and velocity; all of which are critical thermal comfort factors [1]. Unlike the latter variables though, clothing, and activities of occupants are also additional factors which cannot be controlled by ventilation. In order to quantify thermal comfort with all of these variables, a complex numerical process must be undertaken. The result of this numerical process is a thermal comfort indicator called by many practitioners, a 'Predicted Mean Vote' and a 'Predicted Percentage of Dissatisfaction' (PMV-PPD). In contrast to thermal comfort variables which can be sensed by human perception, IAQ variables are usually undetectable. Numerous indoor air pollutants, including organic and inorganic gases, infectious microorganisms, biological agents, and nonbiological particles and fibers can severely damage short and long-term human health [2]. In the worst case, the symptoms can develop into Sick Building Syndrome (SBS) which may reduce productivity and may even cause death [3]. To overcome this problem, many ventilation techniques such as source removal, air filtration, air tightness, ventilation air exchange, ventilation strategies, HVAC system design, and others are available to mitigate the consequences of various pollutant species [2, 3]. One example is that of airborne infectious agents which can be effectively controlled by using engineering techniques such as filtration, ventilation air exchange, disinfection procedures and pressure control [2].

To assure acceptable thermal comfort and IAQ, the operation of a ventilation system sometimes uses energy. The rate of energy consumption depends on the means of ventilation whether it be natural or mechanical. Natural ventilation tends to be preferable since it requires no energy. Thus, many practitioners consider it as a part of sustainable design. The promotion of natural ventilation in buildings is still controversial because it is

highly dependent on outdoor conditions. Control cannot therefore be precise. Room temperature, humidity, and wind velocity can fluctuate with outdoor climatic variation. In addition, when outdoor climate is poor, occupants may be impacted by pollutants, odors, particles, and noise.

To avoid these effects, mechanical ventilation may be necessary. Mechanical ventilation can control room temperature and IAQ more precisely by heating, cooling, humidifying, dehumidifying, filtering, and distributing the conditioned air throughout the building [4]. With all these capabilities, the mechanical ventilation is mainly referred to as the Heating, Ventilating, and Air Conditioning (HVAC) system. The filtration system which minimizes particles before distributing outdoor air to the occupied space is unique to the HVAC system and is not available in natural ventilation. When air is distributed through ductwork, the windows can be sealed from outdoor dust and noise. This allows the room acoustics and IAQ to be controlled and even improved.

These unique capabilities come with the major drawback of energy consumption for operating the HVAC system. The 2006 annual energy review reveals that within the total annual energy usage of the United States, about 55% is used by industrial and commercial sectors. Out of this 55%, 18% is used by HVAC systems [5]. Many HVAC technologies have been developed for reducing energy usage. One of them, called the economizer, takes in outdoor air when outdoor conditions are appropriate (13-18^{o}C or 55-65^{o}F). When such a device is operated, it can effectively reduce energy consumed by the heating and cooling system. Nowadays, for human comfort and because of a global energy shortage and global warming issues, the development of more energy efficient HVAC technologies which provide better thermal comfort and cleaner indoor air are major challenges for both researchers and practitioners around the world.

In order to have both acceptable thermal comfort and IAQ with less energy use, research on ventilation and other techniques has been conducted by many organizations around the world. The oldest and most referenced organization is the American Society of Heating, Refrigerating, and Air Conditioning Engineers (ASHRAE). The most important role of ASHRAE is not just to study ventilation, but also to provide the guidelines and standards for proper ventilation uses. ASHRAE Standard 55 is used where thermal comfort in any

given space is concerned [6], while ASHRAE Standard 62 is used for assuring acceptable IAQ [7]. For energy conservation, ASHRAE standard 90 covers not only the ventilation system, but also the building envelope, lighting system, appliance load, etc. All the above mentioned standards include the design methods, variables, and thresholds for guaranteeing Indoor Environment Quality (IEQ). Not only have many states and countries adopted these standards as a code for building ventilation design, but also those in the sustainability movement. One example is The Leadership in Energy and Environmental Design (LEED) which already implemented these standards in their scoring criteria [8]. In order to meet these state and international standards, this dissertation uses not only the previously mentioned three standards, but also other important standards such as ISO 7730 and ASHRAE RP-1133. Similar to the ASHRAE Standard 55, ISO 7730 discusses the thermal comfort, but it also provides additional details such as thermal comfort class [9]. Unlike the previously mentioned standards, ASHRAE RP-1133 is used mainly for simulation validation and verification and particularly for Computational Fluid Dynamics (CFD) [10].

Past studies show that ventilation strategy might be one of the solutions to improve thermal comfort, IAQ, and energy HVAC conservation [1, 11]. Ventilation strategy includes the placement of supplies/returns and their temperature, velocity, humidity, and pollutant concentration. In this dissertation, the ventilation strategy called Impinging Jet Ventilation (IJV) and other available strategies were investigated and compared. Here in the first chapter, each available ventilation strategy is introduced first and then it is followed by a brief description. Thereafter, the objectives and methods are systematically presented which led to the outcomes. The contribution made by each is presented at the end of this chapter.

INTRODUCTION TO VENTILATION STRATEGIES

Organizations and practitioners have grouped ventilation strategies by their characteristics and applications [1, 12]. **ASHRAE Handbook of Fundamentals 2005** has suggested four ventilation strategies: Mixing System, Displacement Ventilation, Unidirectional Airflow Ventilation (ceiling to floor and wall-wall), Under Floor Air Distribution and Task/Ambient Conditioning [1]. In the book, **Ventilation of Buildings**

by Awbi which is referenced by many practitioners, ventilation strategies have been categorized differently [13]. Instead of four ventilation strategies, Awbi suggested five ventilation strategies: Mixing Jet Ventilation (MJV), Local Exhaust Ventilation (LEV), Piston Ventilation, Displacement Ventilation (DV), and Impinging Jet Ventilation (IJV) [13]. The conceptual diagrams of these strategies are shown in **Figure 1**. In these diagrams, blue and red arrows similarly indicate the supply air stream and the return/exhaust air stream, respectively. Different ventilation strategies make the patterns of these streamlines vary and likewise as to their performances. To understand how each ventilation strategy performs and is operated, the five descriptions of ventilation strategies proposed by Awbi can be found as follows:

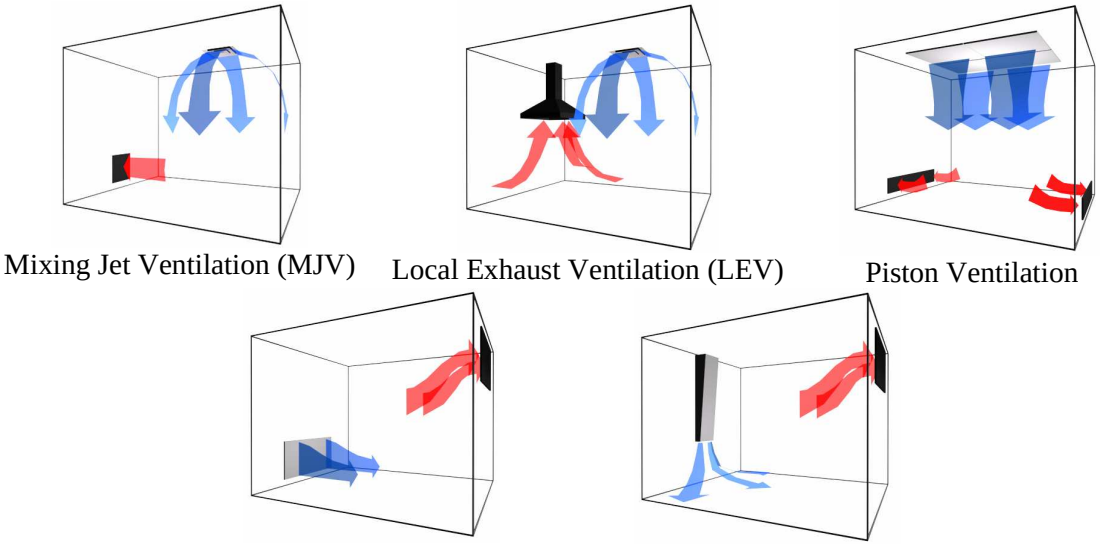

Figure 1 Conceptual diagrams of five ventilation strategies

Mixing Jet Ventilation (MJV), called the Mixing System by ASHRAE 2005, has been the most common choice for most practitioners since the HVAC was first introduced. MJV fully utilizes turbulent flow by supplying high momentum jet into the space. Thus, the temperature and concentration are usually assumed to be homogeneous or well-mixed, while stratification is eliminated. In a well-mixed room, heating and cooling is fast and effective, but, at the same time, the IAQ is sometimes questionable. Past studies suggest that the ventilation effectiveness[1] of other strategies where stratification is utilized were higher [7]. When MJV is applied, another concern

[1] See Equation 7 and Equation 8 in Chapter 2

is that noise might come from the vibrating diffusers. To avoid this advantage, strong supply and return velocity must be matched with the diffusers and grills recommended by manufacturers in order to satisfy the room acoustic criteria.

Local Exhaust Ventilation (LEV) was invented to compensate for the weakness of MJV by capturing the pollutants right above the sources and not allowing the pollutants to be mixed freely. LEV does not rely on the supply but rather uses the capturing device; that is, an exhaust vent. This exhaust vent is operated effectively when placed right above and close to the pollutant sources. Because of this configuration, LEV is commonly used in industrial applications where the location of pollutant sources must be known and specific. In other applications, LEV might be inappropriate because the source locations are not fixed and the exhaust vent might not be visibly appealing for many designers.

Piston Ventilation, called **Unidirectional Airflow Ventilation** by ASHRAE fundamentals 2005, supplies clean air from the ceiling or wall with extremely low velocity and avoids the mixing process. To obtain the same flow rate, the supply terminal size must be large in order to push the pollutants in one direction-either from ceiling to floor or from wall to wall. Overall the IAQ is better than with MJV if monitoring adjacent to or right below or next to the supply [14]. As mentioned in the ASHRAE fundamental 2005, this system replaces MJV in the applications like clean rooms and operating rooms because it has higher ventilation [15]. Similar to the MJV, a weakness of Piston Ventilation is that no advantage is obtained from stratification.

Displacement Ventilation (DV), categorized as the **Underfloor System** by ASHRAE fundamentals 2005, was first introduced in the late 1970's. The principle of this system is to supply low momentum air (slightly cooler than room temperature) from the bottom of the room (either wall or floor) and vent the warm and polluted air out near ceiling. Sometimes the supply terminals are integrated with the furniture to provide **Task and Ambient Ventilation** which allows the user to adjust the heating and cooling personally. The unique feature of DV is the utilization of stratification that comes from avoiding direct mixing of the supplied and room air. As a result, the IAQ, as compared to MJV, is improved because ventilation effectiveness goes higher

than one, particularly under cooling scenarios [7]. An additional benefit of low supply velocity comes from the ease of acoustic control. Low and warm supply velocity though make heating less efficient [12]. Nowadays, DV is being investigated as an engineering technique to minimize the presence of Environmental Tobacco Smoke. Yet there is not solid evidence that DV can remedy ETS problems [16]. Past studies also showed high levels of pollutants in both mixing and displacement ventilated rooms [17]. For every ventilation strategy, ETS has the most complex pollutant distribution patterns because of the countless number of pollutants from ETS sources and the occupants' smoking behavior and movement [18].

Impinging Jet Ventilation (IJV), introduced in the late 1990's, is claimed to have advantages from both MJV and DV [19]. In theory, the supply terminal of IJV faces towards the floor at the appropriate height and the return is placed near the ceiling like the DV. When activated, the high momentum jet hits the floor drastically decreasing its velocity. See **Figure 2**. The undisturbed room air allows stratification to effectively occur. Like DV, this characteristic increases ventilation effectiveness and promotes better IAQ [13]. An advantage over DV system can be found when using IJV under heating scenarios where low supply velocity is not suitable. Mid to high supply velocity as used with IJV can prevent warm air from rising too quickly. Rather the warm air is mixed with the room air as happens with the mixing system. Because of these advantages, an IJV system called Air Queen® is being manufactured by Fresh AB Company and has already been installed in many buildings in Sweden [20].

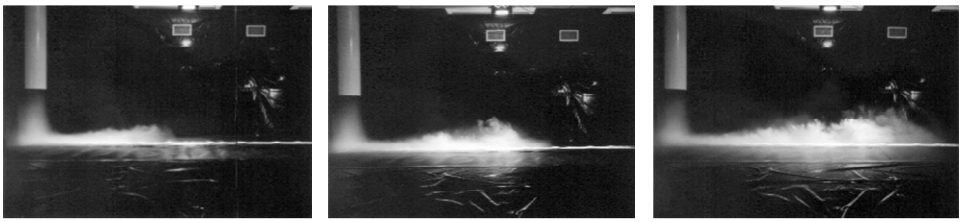

Figure 2 Gas tracer test of IJV system [21]

VENTILATION STRATEGY CHARACTERISTICS

After introducing available ventilation strategies, the characteristics of each ventilation strategy based on results from past studies are discussed here. Previously, three factors

were mentioned which determine how effective ventilation strategies are. These three factors, IAQ, thermal comfort, and energy consumption, will now be explored.

For IAQ, the concentration profile along the room height as shown **Figure 3** can represent the performance of each ventilation strategy. The IAQ performance can be judged by the pollutant concentration level in the breathing zone[2]. Supplying from the ceiling, MJV might have a high pollutant concentration level in the breathing zone leading to a poor IAQ. By placing the capturing device above the pollutant sources, LEV can significantly remedy the excessive pollution. In this system, high concentration can only be found if monitoring near the exhaust. Another method to solve poor IAQ of MJV is to push the air in one direction and avoid the direct mixing of the fresh air and the contaminated air. With this technique, Piston Ventilation, high concentrations increase towards the return or exhaust. To further improve IAQ, ventilation strategies must utilize stratification as in systems like DV and IJV. In stratification, fresh air enters on floor level and warm and polluted air is exhausted at the ceiling. This results in measurably much lower pollutant concentrations in the breathing zone. Improvements in IAQ using DV, IJV, or other strategies are thus realized. More studies and actual implementations of these systems by researchers and practitioners worldwide can be expected to increase.

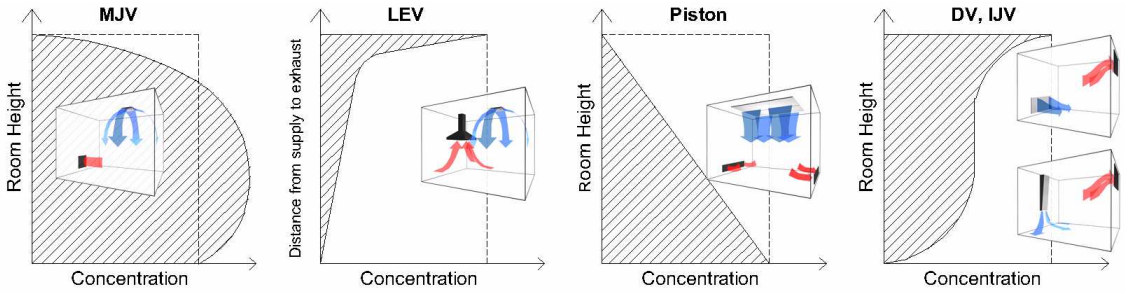

Figure 3 Conceptual concentration profiles along the room height generated by different ventilation systems [13]

Besides IAQ, a thermal comfort comparison between MJV, DV, and IJV made by Awbi, et al., [21] shows that local temperature, velocity and air distribution are different. DV and IJV have lower air temperature near the floor and both have high velocity near the supplies. See **Table 1**. In 2003, they further investigated just the DV and IJV in classroom applications (see **Figure 5** and **Figure 6**) and found that the PMV-PPD of both

[2] ASHRAE 62-2004 defines breathing zone as the region within an occupied space between planes 3 and 72 in. (75 and 1800 mm) above the floor and more than 2 ft (600 mm) from the walls or fixed air conditioning equipment.

systems is on average equal. A range of 5-25% along the room height and the higher PPD near the floor was found in IJV system as plotted in **Figure 8**. Similar to the concentration profile, the air temperature of both strategies gradually increases from floor to ceiling level about 3^{o}C or 5.4^{o}F (See **Figure 7**). Humidity control relies on the HVAC coil temperature which must be less than or equal to 13^{o}C (55^{o}F) to effectively dehumidify excessive moisture. In DV where a warm supply temperature of 18^{o}C or 65^{o}F is recommended [1], the humidity control might be problematic if the same coil temperature is assumed. To overcome this problem, devices such as Reheat Coil and Power Induction Unit (PIU) which allow dry heat to be added to the cool supply air, are options. Overall, ventilation strategies can impact thermal comfort. In order to avoid the thermal discomfort, knowledge or guidelines for proper implementation of any ventilation strategy must be available to practitioners.

Supply type	Temperature		Velocity		Air distribution		Noise
	Summer	Winter	Summer	Winter	Summer	Winter	
MJV	Uniform	Uniform with lower flow rate	High in some occupied zones	As the summer case	Acceptable	Acceptable	Some noise
DV	Somewhat lower near floor and supply terminal	Like summer but lower temperature difference vertically	Somewhat high near supply but very low over the floor	As the summer case	Acceptable everywhere	Not so good close to window	Silent
IJV	Somewhat lower near floor and supply terminal	As summer but lower temperature difference vertically	Somewhat high near supply terminal but very low over the floor	As the summer case	good	Not so good close to window	Silent

Table 1 Summary of ventilation strategies comparison [22]

As a cost for achieving thermal comfort and IAQ, ventilation through the HVAC demands energy. In the HVAC system, energy is used by both to distribute the conditioned air by fan and by controlling the supply temperature of the HVAC refrigerant or water loop. Flow rate reduction of any ventilation strategy can decrease the fan energy demand. This reduction is possible if designers size the fan properly. Otherwise, any given HVAC system must have a special device called a Variable Flow Drive (VFD) which can adjust the flow rate and consume only the energy which is needed. Unlike fan energy, the relationship between supply temperature and energy consumption is not as straightforward. In the most optimized scenarios, given thermal zones served by the same Air Handling Unit (AHU) require the same supply temperature for proper dehumidification which is typically 13^{o}C or 55^{o}F. Theoretically speaking, this supply air

does not require additional treatments such as reheating, cooling, or mixing and, thus, no extra energy is needed. However, some ventilation strategies such as DV have a specific supply temperature range which is around 18°C or 65°F. When placing or renovating some particular zone served by an existing AHU where the supply temperature is 13°C or 55°F to DV, either Reheat Coil (See **Figure 4**) or a Power Induction Unit, which is a box with a small fan for mixing room and supply air, is needed to increase the supply temperature. These processes require extra energy and additional HVAC costs. Based on these characteristics, the ventilation strategies that minimize flow rate while supplied with typically cool air temperature significantly increase energy conservation.

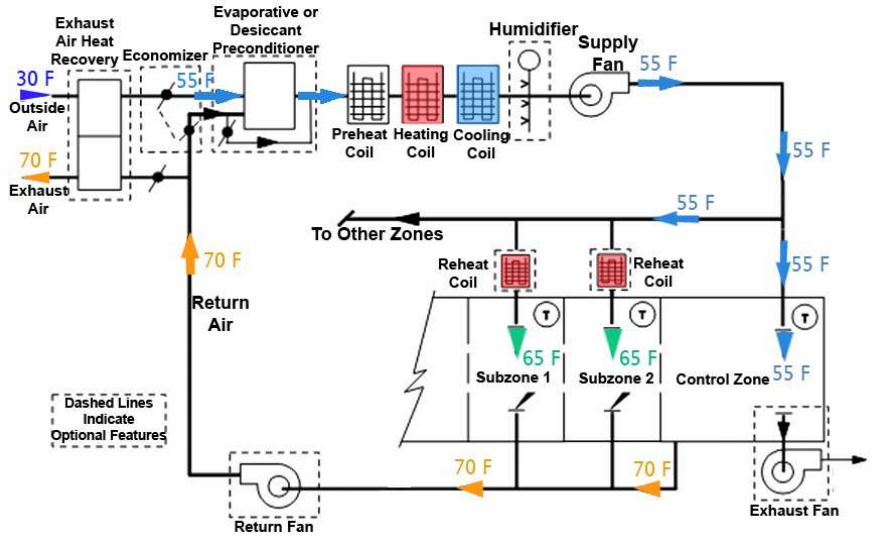

Figure 4 Supply temperature control with single AHU system

Instead of directly reducing the flow rate or maintaining the suitable supply temperature, there is another way to reduce the HVAC energy demand. Reducing the fresh air intake can substantially reduce the energy used by HVAC. However, fresh air intake must be adequate for occupants for the achievement of an acceptable IAQ as suggested by the ASHRAE Standard 62 [7]. The reduction of fresh air can be made if the room IAQ is guaranteed to be within the threshold suggested by this standard. The use of proper ventilation strategy allows this to be possible. Efficient ventilation strategy tends to demand less fresh air, while unfavorable ventilation strategy tends to need more. The benefit of fresh air reduction depends on the outdoor climate because it only reduces the energy demand when the outdoor condition is inappropriate for free cooling or heating. A more detailed discussion of this topic can be found in Chapter 2.

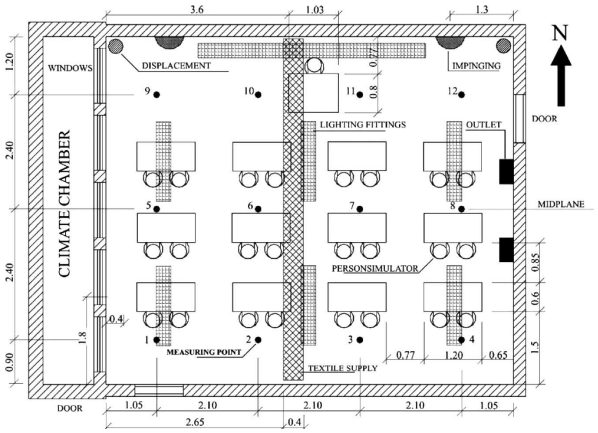

Figure 5 Layout of mock-up classroom for ventilation test (left)[3] [21]
Figure 6 Image of mock-up classroom (right) [21]

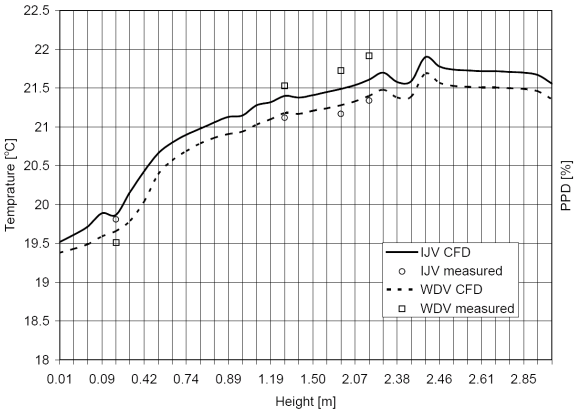

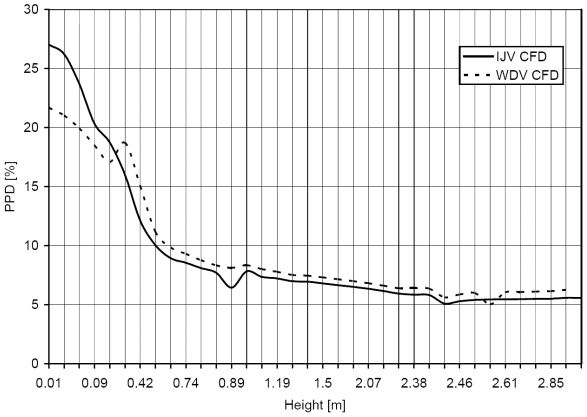

Figure 7 Temperature gradient along the room height of IJV and DV (left) [21]
Figure 8 PPD along the room height of IJV and DV (right) [21]

RESEARCH STRATEGIES

To study ventilation strategies and their impacts, understanding of available research strategies or tools is essential. Out of all the possible tools, a full-scale experiment and a Computational Fluid Dynamics (CFD) simulation have been selected to be used in this dissertation. A full-scale experiment is familiar to most practitioners, but the numbers of sensors are limited and airflow visualization is not possible. CFD provides an almost limitless number of sensors so that allow airflow to be visualized. **Figure 9** is an example of CFD capability in visualizing airflow using the technique called isosurface. Isosurface is the hypothetical surface constructed by connecting the same air temperature. To plot the isosurface requires large numbers of data points which, in a full-scale experiment, they are usually inadequate in number.

[3] Special thanks to Prof. Karimipanah and Prof. Awbi for these images and results

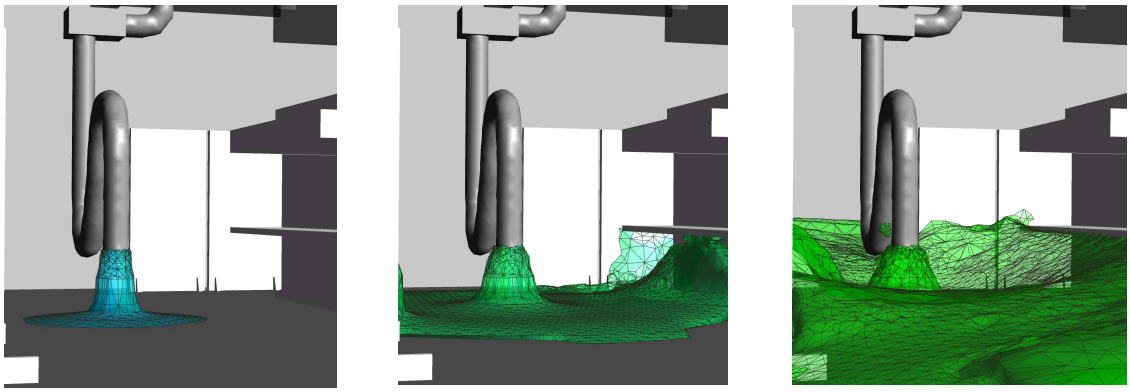

Figure 9 Isosurfaces generated by CFD simulation

A major disadvantage of CFD is that its validity is questioned by many practitioners. The previous study conducted by the author is one attempt to validate CFD simulation and the results show that the appropriate CFD setting can give valid results. The normalized temperature profile[4] generated by CFD corresponds to the concentration profile captured from Laser Induced Fluorescence (LIF) [23]. See **Figure 10**. This study concluded that accurate CFD results come from correct CFD input parameters which stem from either full-scale or scale experiments. LIF technique has been commonly used in research related to both fluid mechanics and architectural airflow. Cotel, et al., used PIV and LIF to study the effect of jet impinging on stratified interfaces [24], while Brecht demonstrated the use of LIF in architectural airflow in a trajectory air jet in a livestock building [25].

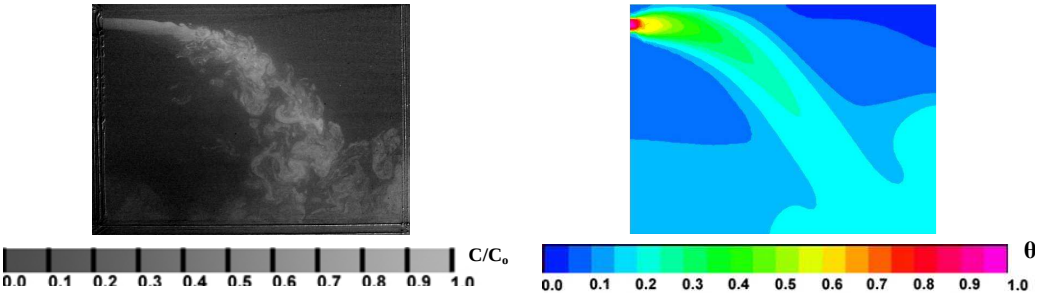

Figure 10 Comparison of LIF and CFD results

Besides the validity issue, another limitation of CFD is the great time required for computing the results. Large numbers of grids and transient state simulation consumes a huge amount of computational power and time. Some flow problems might not be possible to be solved by using CFD because they might take more than a 100 years with

[4] Calculated by **Equation 32**

the current super computer capability [26]. When facing these types of problems, the full-scale or scale experiment is the best alternative. In building ventilation, monitoring the flow by using full-scale techniques such as sensors, gas tracers, etc. has been common among practitioners for decades. In this case, the validity and computational limit are not the concern. One example of applying a full-scale monitoring technique is seen at the main terminal of the Kansai International Airport in Japan [27]. In this study, flow sensors were placed around the main terminal to monitor the building in real time.

CFD, scale, and full-scale experiment are not the only available techniques to study airflow. The Schlieren technique, which allows users to visualize full-scale air flow caused by the thermal properties of air, is a good example of such an alternative. The detailed mechanism of this technique can be found in the book, **Schlieren & Shadowgraph Techniques** by Settles [28]. In contrast to gas tracing, the Schlieren technique is capable of revealing the plume from heat sources, including those of human beings. **Figure 11** shows that the thermal plume from a human body is successfully formed in a displacement ventilated room (left), while the plume does not exist in a mixing ventilated room (right) [29, 30]. This result demonstrates not only the use of the Schlieren and Shadowgraph techniques but also confirms the success of utilizing stratification of DV over MJV.

Figure 11 Airflow patterns captured by Schlieren and Shadowgraph techniques [29, 30]

A full detailed discussion of all research strategies used in this dissertation can be found in **Chapter 2**; while the validity of CFD simulation for IJV can be found in **Chapter 3**.

RESEARCH OBJECTIVES

As discussed earlier, past studies demonstrated many advantages and potential of the IJV system, but there are still many variables in need of investigation in order to maximize

the performances and avoid the disadvantages of this system. Ahead of many variables, impinging jet characteristics, terminal configuration, the Variable Air Volume (VAV), and Constant Air Volume (CAV) operations of HVACS systems, and space volumes are the first priority of study in this dissertation. In addition to these variables, there are multiple variables such as the pollutant type and location, floor characteristics, actual real-time performances, etc, which have yet to be investigated. Undeniably, they are important and are deserving of future study. The variables chosen for this dissertation are directly related to architectural and HVAC applications which the practitioners need to know prior to apply IJV. Based on these variables, four objectives have been formulated and their variables and sequences are shown in **Figure 12**. Brief descriptions of each objective are following.

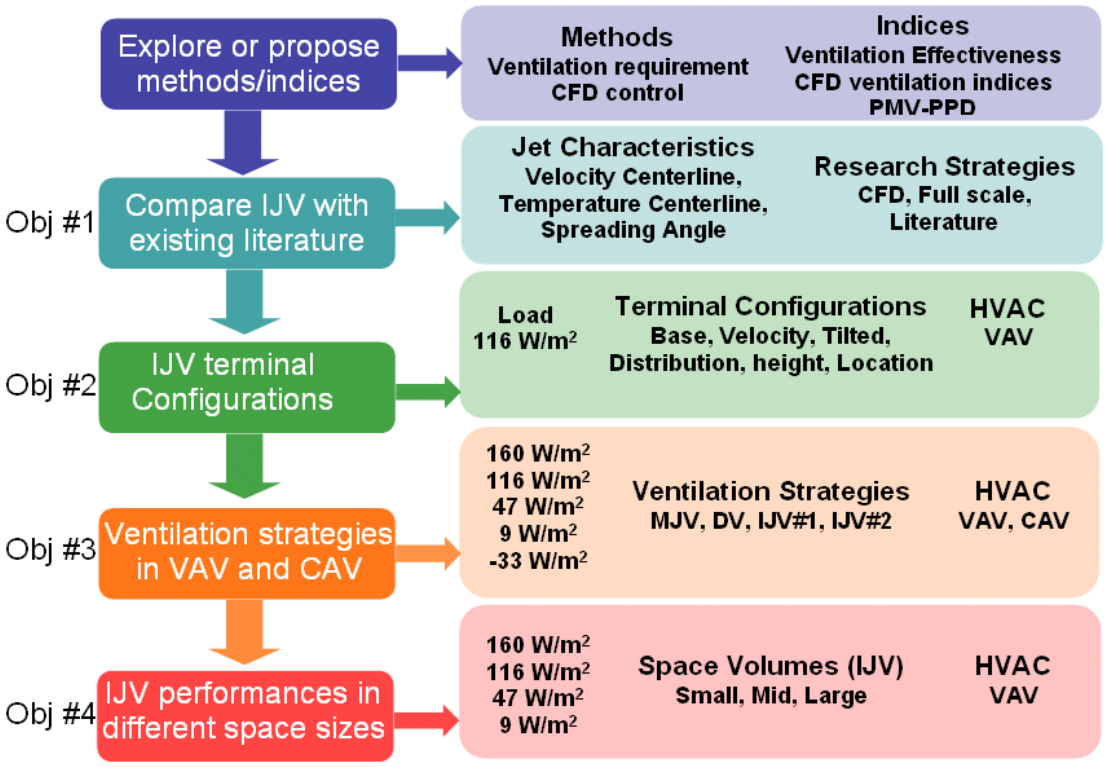

Figure 12 Diagram of dissertation objectives

In the first objective, impinging jet behavior is to be investigated using both full-scale and CFD simulations. Temperature and velocity are monitored at different locations and distances in order to formulate the predictive models. Not only is the CFD validated by the full-scale data, but it also shows that practitioners can use predictive models to predict

the jet behavior when CFD or full-scale is not available. For further discussion see **Chapter 3**.

The second objective is to investigate the terminal configurations of the IJV system. Nozzle velocity profiles, heights, locations, velocity, tilted angles, air distribution patterns, are all variables to be studied by using 14 parametric cases. For comparing each option, ventilation indices include ventilation effectiveness, PMV-PPD, and a new indicator called CFD ventilation performances. See details in **Chapter 4**.

In the third objective, HVAC operations with both VAV and CAV are to be tested against three ventilation strategies, MJV, DV, and IJV. Using validated CFD parameters obtained from **Chapter 3**, these ventilation strategies are to be studied based mainly on CFD where some unique scenarios like intense solar radiation occur. Ranging from very high cooling and heating load, parametric CFD simulations of 64 cases are tested against many ventilation indices. The results show the advantages and disadvantages of each ventilation system under specific scenarios. See the details in **Chapter 5** and **Chapter 6**.

Finally, the fourth objective aims to investigate the impact of space volumes. Similar to the previous objective, important ventilation indices are used to evaluate IJV systems in three different space volumes-small, medium, and large. Along with these variables and the additional four cooling load scenarios where the VAV system is applied, at least 24 CFD parametric cases are required. The results are presented in **Chapter 7**.

OUTCOMES AND CONTRIBUTIONS

Upon completion of these four objectives, one outcome of this dissertation is the establishment of **appropriate parameters of IJV for architectural and HVAC applications**. These parameters include appropriate supply temperature, velocity, and operated cooling load in order to maximize energy conservation, thermal comfort, and IAQ. A detailed discussion can be found in **Chapter 8** where these parameters are applied to the actual case study classroom. These results have been published by the author in a peer-reviewed article in "The Journal of Greenbuilding" [31] and have been presented at two majors conferences, the EPIC 2006 [32] and the IAQVEC 2007 [33, 34]. By contributing to a multi-disciplinary approach in the field of building ventilation, these IJV parameters may be used by architects, engineers, and designers who may have an

important role in designing many architectural applications such as classrooms, laboratories, atrium, commercial spaces, museums, etc. One successful example of an IJV system can be seen in a casino as shown in **Figure 13**. When stratification occurs, a pollutant from the human respiratory system, CO_2, successfully floats up toward the ceiling and clean air is maintained in the breathing zone.

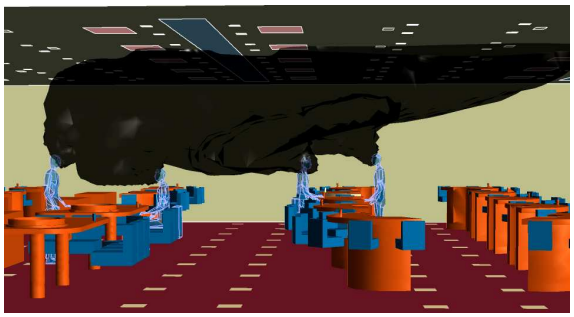

Figure 13 the successful IJV system in casino hall

Unlike the previous case, if the ventilation system is not designed or operated appropriately, there are many consequences. A computer room, Angell Hall at the University of Michigan, is an example of a mixing ventilated room which shows these negative effects. Monitored results shown in **Figure 14** reveal air temperature and velocity along the room height. Excessive draft[5] exceeding the 10% threshold was found at the mentoring location. Not only can a mixing ventilated room be drafty as a result, but also an impinging ventilated room that was not properly designed can exhibit the same consequences.

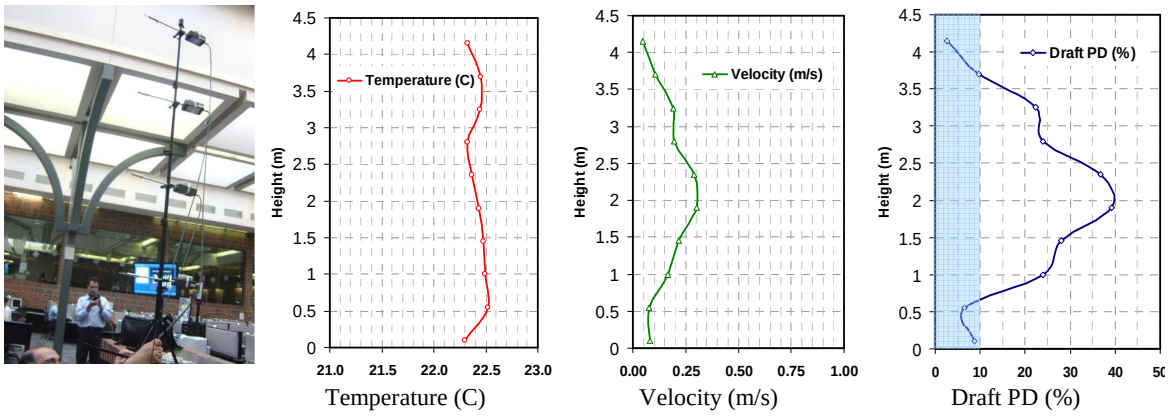

Figure 14 Measured flow data at Angel Hall, University of Michigan

Generated by CFD simulation, **Figure 15** shows a draft profile of an IJV system at head height of the large space size. When the supply velocity is too strong, IJV can also create

[5] See calculation in Chapter 2.

drafty conditions as indicated by the magenta-highlighted area where draft PD exceeds 10%. Further discussion can be found in **Chapters 3-5**. With this draft, air velocity throughout the room is intensively strong. Under these circumstances, stratification, as shown in **Figure 13**, occurs with great difficulty, and thus the IAQ might be not as high as expected. This result shows how ventilation indices in this case, draft and IAQ, are linked to another.

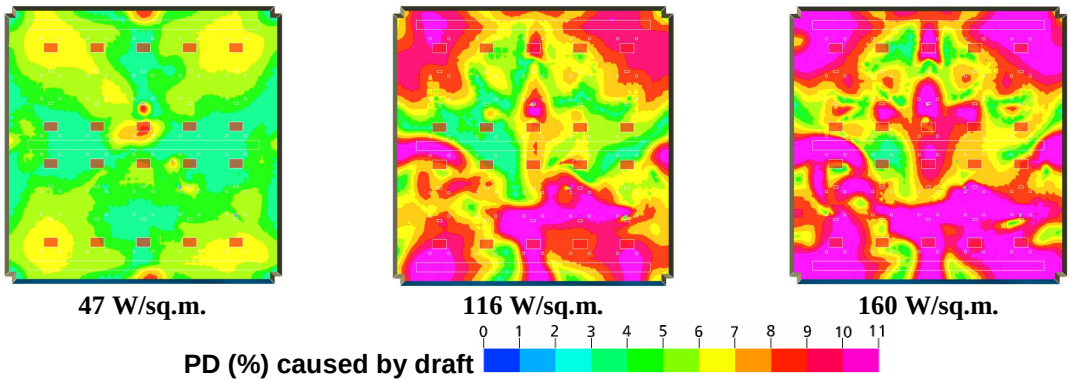

Figure 15 Color coded CFD data of draft PD plotted at 1.8m height

Further studies of the IJV system are necessary and may provide solutions to some of the most difficult problems in ventilation design, namely Environmental Tobacco Smoke [16]. ASHRAE suggests that the outright banning of smoking from the space is the only way to prevent second-hand smoke and even standard engineering ventilation techniques are not accepted as an effective solution [16]. The results from this dissertation show that the IJV potentially improves IAQ more effectively than the conventional dilution system. Many ventilation techniques, such as ventilation rate, isolation, zoning, and pressurization can enhance the IJV performances. These potentials should be investigated and the outcomes might be used to resolve or minimize ETS or other hazardous pollutants in the future. ETS is an example of an extremely hazardous space, but the IJV might also find a place in any space where improving the IAQ in general is important. Currently, such spaces with IJV systems are rare in USA, but there are examples of various applications which use the IJV in Europe, particularly in Sweden. At the very least, this dissertation is a first attempt to promote the use of this system in the USA with the hope that this dissertation will initiate studies and research about this system in the future.

CHAPTER 2
RESEARCH STRATEGIES AND VENTILATION RELATED THEORIES

Related theories and research strategies are important in order for readers to understand this dissertation. In the first half of this chapter, the topic to be discussed is a detailed description of the research strategies used. In the second half, not only were related theories from past studies summarized and introduced, but also new theories and indices.

RESEARCH STRATEGIES

As mentioned in this first chapter, full-scale experiment and CFD simulation are the two main research strategies used mainly in this dissertation. The research tool most commonly applied by HVAC practitioners is the former, the full-scale experiment. In a full-scale experiment, many types of sensors, such as Constant Temperature Anemometer (CTA), thermocouples, CO_2 Sensors, and others, are placed in the space to sample the environmental parameters [35]. Since the measurements take place on-site and in real-time, the collected data are widely considered to be acceptably valid. On the negative side, a full-scale experiment can be very costly if mock-up units or sensors must be built and purchased. Because of these extra costs, the number of sensors as well as the number of data points is limited. One sample of the budget issue can be found in the study at the Kansai International Airport. In this study, the objective is to monitor the air temperature of the terminal atrium to improve the HVAC control strategies [27]. To fulfill this objective, the researchers have to wait until the building is finished before conducting the full-scale experiment on-site. If the researchers had proposed to study the building prior to its completion, a mock-up would have been needed and thus, it would have been too costly. These weaknesses can be resolved using CFD simulation because it does not require an actual space. Only a high performance computer is needed to perform CFD simulation from the beginning to the end and, thus, time and costs can be minimized. The CFD simulation process starts from a typical 3D model and then it must be transformed to a CFD model by the process of meshing which will create an adequate number of

nodes and elements for the further simulation process. After inputting and solving the flow problem by computer, each node/element in the CFD model consists of flow parameters such as temperature, velocity, humidity level, density, etc... Then, these data can be plotted in various formats such as color contour format which allows the flow to be easily visualized. Once practitioners intuitively visualize the flow, it might help them to have better understanding or ultimately reach the solutions of their airflow problems.

Currently, HVAC practices and studies increasingly rely on CFD. Because it has been used by many practitioners, CFD simulation method has been accepted as a significant ventilation tool and added in ASHRAE fundamentals 2005, Chapter 34 [1]. Despite many advantages of CFD discussed previously, limitations and the validity of CFD is still frequently questioned by many practitioners. Turbulent flow behavior and the smallest eddies are obstacles that CFD still can not overcome and accurately predict. The behavior of full turbulent spectrum is not completely understood and is still under investigation. For instance, the Navier-Stokes equations embedded in a CFD algorithm can be simplified by using turbulent viscosity (μ_t) such as in the k-ε model [13, 36]. Using this assumption, CFD might predict results that differ from the actual flow because the turbulent mixing differs from mixing relying on pure diffusivity where viscosity plays an important role. Not only is this assumption imperfect in CFD, but it also has limitations on its spatial resolution. CFD requires large clusters of nodes and elements to be able to predict accurate airflow behavior. In theory, to predict the behavior of the smallest eddies, the total CFD nodes/elements must be at least equal to the Reynold number[6] to the power of three (Re^3) [26]. As a function of length, scale and velocity, the Re of a large object with a very high velocity may be very high and thus the number of CFD nodes estimated by Re^3 may also be extremely large. With an extremely large set of CFD nodes, even the current state-of-the-art computer can still not handle this complexity with an economic computational time. This forces the users to optimize or reduce the size of CFD model, but the consequence of this reduction makes CFD limited to the small scale of turbulent flow.

[6] See calculation in Equation 28

To compensate for some of these weaknesses, the CFD standard, ASHRAE RP-1133, requires a full-scale experiment to be performed for validating the CFD results. In order for this dissertation to comply with this standard, a HVAC-IEQ laboratory was specially built for the supporting activities which needed a full-scale experiment. A set of instruments such as an Indoor Flow measurement System (IFS) and infrared (IR) thermography were employed to record the monitored airflow variables. In the following sections, these techniques and equipment will be described in detail.

Indoor flow measurement system

Among many tools for a full-scale experiment that are available in the market, the tool to be used in this dissertation must comply with specific criteria which enable both temperature and velocity of the unknown directional flow to be measured. Among many candidates, the Indoor Flow System-200 (IFS-200) by Dantecdynamics satisfies these criteria the best. The diagram of how this system functions and the actual setup are shown in **Figure 16**. Hardware and software are the two key components of this system. Four omni-transducers, a CTA module, a connector box, a noise shield cable, a Data Acquisition Card (DAQ), and computer are the hardware that are required for operating IFS-200 software [37]. The monitoring process begins with signals from a probe (omni-transducers) which link to a CTA module. Then, the CTA module converts the electrical signal, prepares the data, and reduces noise before sending the filtered signals to a connector box. The data from a connector box, which can support up to 16 CTA modules, is processed and sent to the DAQ. After that, depending on the speed and sampling rate, the DAQ sends the data to the attached computer. IFS-200 software installed in that computer interprets and translates the data into a readable format.

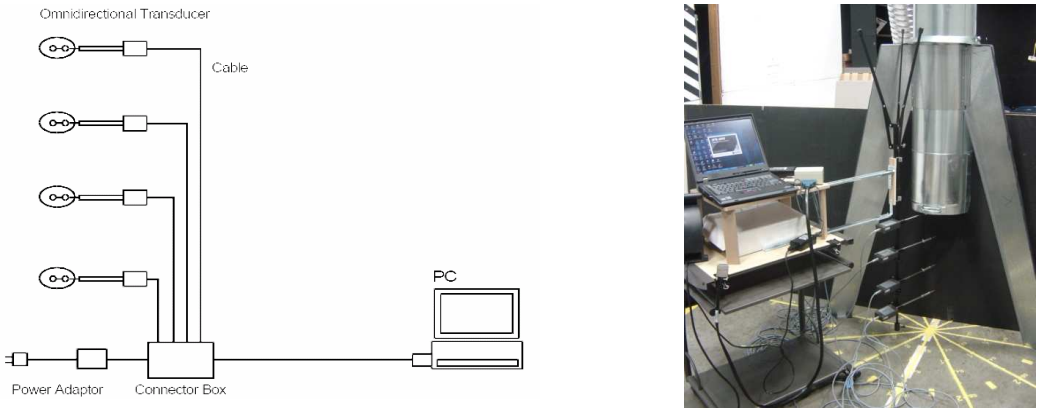

Figure 16 Diagram of IFS-200 system and the actual setup [38]

IFS-200 and other indoor monitoring systems function quite similarly, except that IFS-200 is more convenient. The testing procedure is designed to minimize errors that occur when actual monitoring takes place. Unfortunately, no matter how superior the system is; two types of error are unavoidable. One error is caused by sensor limitation, but which can be minimized by using high-quality and accurate sensors. Accepted by many standards such as ASHRAE and ISO, omni-transducers are used in this study having a temperature error of 0.5^{o}C and a velocity error of 0.03 m/s, and are thus adequate enough for indoor flow measurement. Another type of error is experimental error which stems from the experimental procedures themselves, like the placement of sensors and their orientation and the unsteadiness of lab instruments, etc... To minimize this error, three repeated measurements are taken under the same conditions with each measurement lasting 20 seconds. After testing, **Table 2** shows that the experimental error of velocity measurement is large compared to other errors. The experimental error of temperature is small relative to sensor error, while the experimental error of velocity is almost half that of sensor error.

Variables	Sensor error	Average exp. error	Max exp. error	Min exp. error
Temperature (C)	0.5 ^{o}C	0.020 ^{o}C	0.035 ^{o}C	0.001 ^{o}C
Velocity (m/s)	0.03 (0-6m/s)	0.015 m/s	0.043 m/s	0.003 m/s

Table 2 Monitoring system error summary

To avoid these errors, understanding of both hardware and software of full-scale monitoring systems is also helpful. In the following section, only the detailed descriptions of operating and calibrating the software are presented. For the readers who wish to know more about IFS-200, full detailed descriptions of each hardware component are provided in APPENDIX A.

IFS-200 Software

Created by Dantecdynamics, IFS-200 software was designed to specifically measure indoor airflow [38]. The screen-captured images of this software are shown in **Figure 17**. **Figure 17** (mid) shows the real-time gauge of temperature and velocity which are converted from the electrical voltage using 5^{th} order polynomial coefficients as shown in **Figure 17** (right). These coefficients can be used to adjust the temperature and velocity ranges that should match the ranges of the experiment. **Table 3** shows the coefficients for plugging in the polynomial function as presented in **Equation 1**. Based on the

requirements of this dissertation, these coefficients were set to allow the temperature range from 0-45°C and velocity up to 0-6 m/s with errors presented in **Table 2**. Once these coefficients are set, users can adjust the recording period, number of recording cycles, and pausing period (for the next recording cycle). For instance, users can obtain data of 30 second (recording period) or hourly (pausing period) intervals for 24 hours (recording cycles). In this software, the special feature for calculating local thermal comfort indicators such as draft and turbulent intensity is also available.

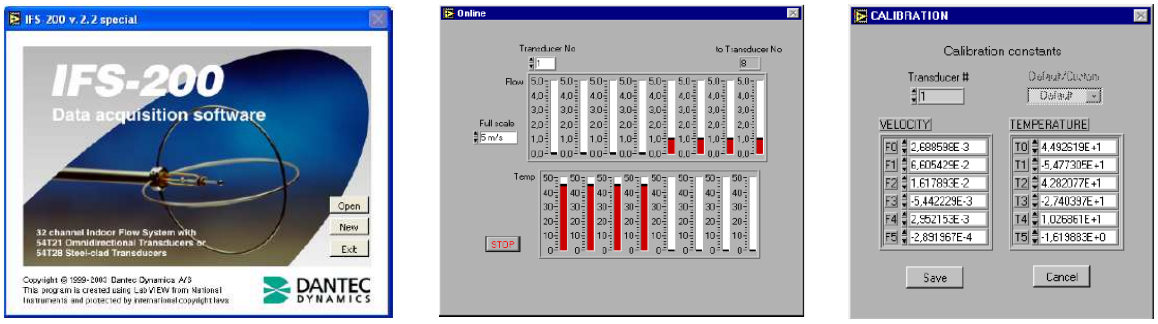

Figure 17 IFS-200 software cover (left), real-time gauge (mid), calibration page (right)

$$U = C_0 + C_1E^1 + C_2E^2 + C_3E^3 + C_4E^4 + C_5E^5 \qquad \text{Equation 1}$$

Where U = Velocity (m/s)
C = Coefficient
E = Electrical voltage

Coefficients	Velocity (0-6 m/s)	Temperature (0-45C)
C_o	+2.688598E-3	+4.492619E+1
C_1	+1.785040E-1	-5.477305E+1
C_2	+1.181528E-1	+4.282077E+1
C_3	-1.074034E-1	-2.740397E+1
C_4	+1.574443E-1	+1.026861E+1
C_5	-4.168007E-2	-1.619883E+0

Table 3 Polynomial coefficients of both velocity and temperature for IFS-200 software

HVAC-IEQ laboratory

IFS-200 is the stand-alone system intended for use under the controlled conditions of the HVAC-IEQ laboratory. This laboratory was specially constructed for supporting these ventilation strategy studies with support from **Architectural Engineering and Construction (AEC)** and **Utilities & Plant Engineering (UPE)** at the University of Michigan. The term, Indoor Environment Quality (IEQ), refers to areas relating to human well-being such as thermal comfort and IAQ which may be impacted by changing HVAC

scenarios. In order to test different HVAC scenarios, the HVAC equipment in this laboratory is designed as shown in the HVAC system diagram of **Figure 17**.

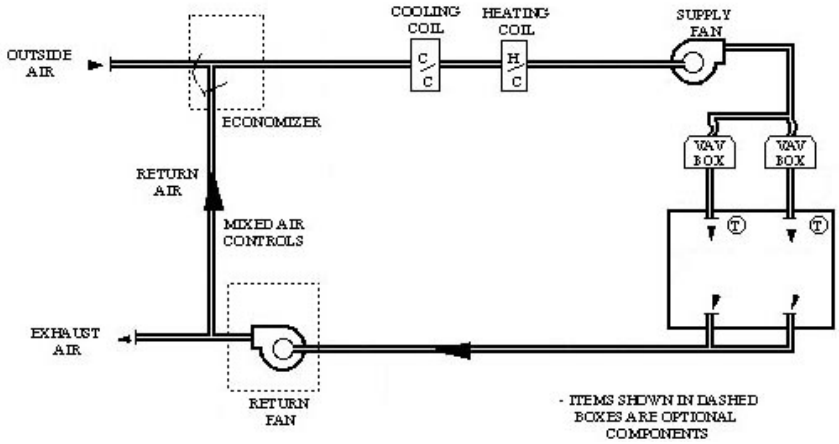

Figure 18 Diagram of HVAC system in HVAC-IEQ laboratory

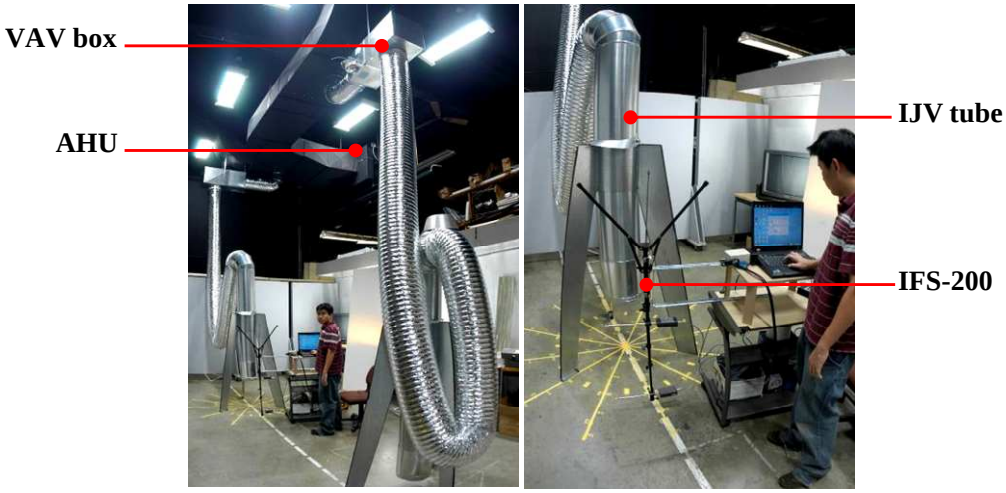

Figure 19 HVAC-IEQ Laboratory

This HVAC system consists of one Air Handling Unit (AHU) with a maximum supply flow rate of 9,600 ft^3 per minute (cfm) which can be reduced by adjusting the Variable Flow Drive (VFD) [39]. To deliver the controlled supply temperature, a fan driven by the VFD blows the air through the cooling and heating coil which is supplied by water from chillers and boilers. Then, supplied air flows through the main duct and then is split into two supply terminals. Each terminal is connected to the Variable Air Volume (VAV) boxes (see **Figure 19**) which allows users to control the flow rate independently. The control of VAV boxes is available for both manual and automatic modes. Automatic control allows each VAV to reduce or increase the flow rate according to the temperature sensed by its thermostat. While manual control allows users to override the thermostat

operation and directly assign the flow rate for each VAV box. After the air is supplied, mixed, and reaches the balanced temperature, the mixed room air is then returned directly to the AHU, where a series of dampers controls the ratio of room air to the fresh air intake. Then, again, the air is blown through the fan, where the process begins and continues to run as long as the system is activated. In the following section, the detailed mechanisms and capabilities of the HVAC-IEQ laboratory are discussed, including the cooling load, supply temperature, flow rate and BAS controls.

Cooling load control

The HVAC system operates by balancing heat and maintaining the controlled temperature. To balance the heat, a device that generates a heating or cooling load is required. Purposely selected for this task, a baseboard heater generates heat from the coil which is supplied with steam or hot water. The emitted heat is controlled by a valve that, in turn, adjusts the flow rate of the steam and of the hot water, so that users can freely adjust the amount of cooling load. To have the flexibility of cooling load control, this control mechanism must be independent of the main HVAC system.

Supply temperature control

One of many important features of the HVAC-IEQ laboratory is the supply temperature control. There the supply temperature can be controlled by different techniques depending on climatic variations. Four modes of supply temperature control are available and commonly used by the HVAC system as shown in **Figure 20** [40]. When the outdoor air temperature is less than 13^{o}C (55^{o}F), the system utilizes both heating coils and fresh air intake to alter the supply temperature. Operation with mode 1 can be used when the outdoor air is very cold by almost completely closing the damper so that there is only minimal fresh air intake. When warmer supply air is needed, the system will increase the flow rate of steam in the heating coil. With this operation mode, the Michigan winter where the outside air temperature is typically below freezing (0^{o}C or 32^{o}F) presents a major problem. Cold outside air can be drawn into the system too quickly, causing the coils and other instruments to freeze. To protect the HVAC components, the AHU fan is programmed to shut down and the fresh air damper is closed automatically. If the space demands cooling, and the outdoor air is already cool, but not below freezing, the system can be operated under mode 2. Here the heating valve is shut down, and the damper can

be adjusted for the fresh air intake according to the cooling demand. This operation mode is very desirable because the cooling costs nothing.

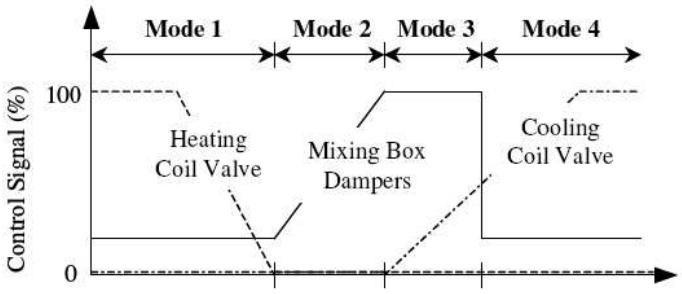

Figure 20 Typical operating modes of an AHU [40].

When the outdoor air temperature rises above 13^{o}C (55^{o}F), the cold water from chiller is needed as a cooling source. Mode 3 will be used if the outdoor air temperature is less than the room temperature. Within this range, the fresh air damper is fully open, and when more cooling is needed, more chilled water will be drawn through the valve into the cooling coil to match the supply temperature (usually 13^{o}C (55^{o}F)) as needed. The system will be switched to mode 4 if the outdoor air is warmer than the room temperature. In this mode, the fresh air damper will be moved to the minimum position, and only allow the amount of fresh air required for the minimum ventilation which satisfies IAQ criteria. The cooling source is coming solely from chilled water. If the cooling demand increases, the cooling coil valve will be opened wider for a higher flow rate of chilled water.

Flow rate control

Flow rate control is also as important as the temperature control, and it can be controlled in two steps. The primary step is to control it directly by VFD, while the secondary step is to control the flow rate from the VAV box. In theory, VFD can alter the flow rate from 0-9,600 cfm. But due to the static pressure, controlling by means of this device might be difficult for the low flow rate range. Static pressure is usually caused by friction from ductworks and HVAC components, and it must be overcome by the air pressure generated by a fan [41]. When the system is operated solely with VFD, flow rate coming out of both terminals is equal. In this case, users have no means to adjust the flow rate independently. This limitation can be overcome be using VAV boxes which allowing occupants to use their damper to control the flow rate effectively and individually. To

obtain the desired flow rate, it is important for the users to synchronize supply air pressure from the VFD and the damper position of VAV boxes.

BAS control

Both supply temperature, flow rate, and other parameters of the HVAC-IEQ laboratory are controlled by a Building Automation System (BAS) using software called Insight by Siemens [42]. This software is capable of controlling the HVAC system through control points and sensors not only for the HVAC-IEQ laboratory, but also for the entire The University of Michigan campus. The applications of this software are not just for this study, but they can be used for the actual building control and maintenance. Once the HVAC-IEQ is connected to the BAS system, it can be controlled through the internet where users remotely control HVAC parameters such as supply temperature, supply velocity, room temperature, set point, etc... This flexibility and the software features allow users to create control schemes which match their need. One example of a customized control scheme created by the author for controlling the IJV system is shown in **Figure 21**.

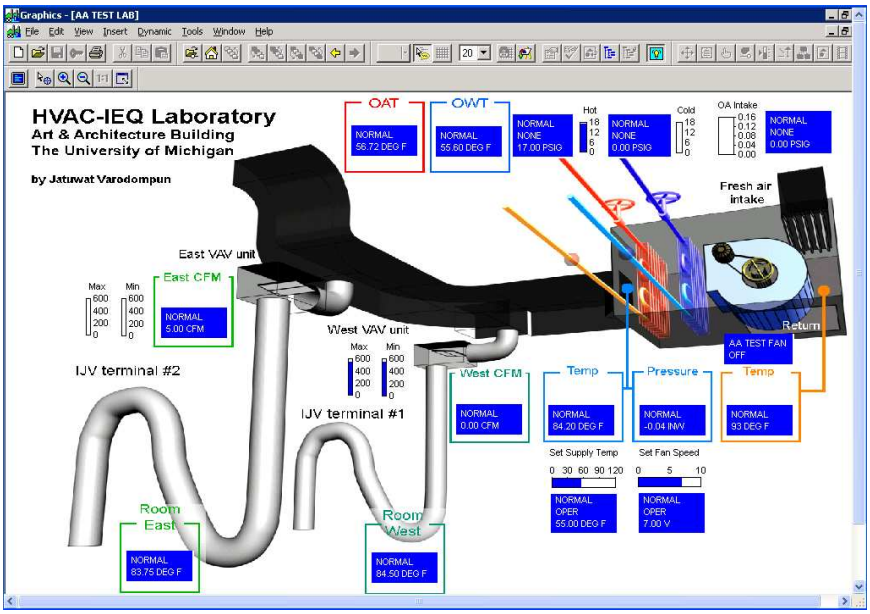

Figure 21 Control scheme of IJV system in HVAC-IEQ laboratory using INSIGHT, BAS software, by SIEMENS

Infrared Thermography Techniques

A major weakness of full-scale experiments is flow visualization. In order to compensate for this weakness, advanced visualization techniques are possible alternatives. The

Particle Imaginary Velocemetry (PIV) and Laser Induced Fluorescence (LIF) are some examples commonly used to visualize flow in fluid mechanics studies [23, 43, 44]. The LIF is also used for the study of building ventilation. One example is the ventilation of the livestock building by Van Brecht, et al.. and Ozcan, et al.., who applied the LIF technique to study the trajectory of an air jet supplying from the ventilation system [25, 45]. However, due to their cost and complexity, the use of these visualization techniques is still limited to building ventilation practices.

Compared to the previously mentioned techniques, thermal infrared thermography is even costlier, but much simpler. This technique has been successfully used in military and crime surveillance for many years and is beginning to be popular in building sciences studies. This technique is helpful increasing building energy conservation because it detects leakage in a building due to poor design and construction. Since the camera 'sees' infrared, the infrared radiation from an object is correlated to its surface temperature. This is then very useful for studying heat transfer in ventilated spaces. Especially customized for building research, FLIR ThermaCAM E45 is the infrared camera used in this dissertation (as shown in **Figure 22**) [46]. This model has a detectable temperature range of -20^{o}C to 200^{o}C and thermal sensitivity of 0.1^{o}C at 25^{o}C. This range and sensitivity capture the heat transfer at a resolution of 160x120 pixels which can then be saved in universal formats such as JPEG. This image format can be viewed by any typical software. But when using the specialized software, ThermaCAM quick view, users can adjust the temperature range and process with some simple statistical analysis of a captured image [47]. After the processing by this software, an image of the impinging jet temperature profile as shown in **Figure 23** is a good example of the result that this camera can produce.

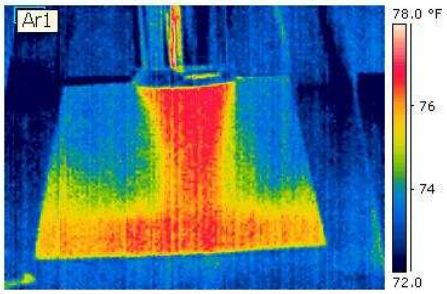

Figure 22 FLIR ThermaCAM E45 (left)
Figure 23 Impinging jet temperature using thermal infrared thermography (right)

Computational Fluid Dynamics (CFD)

Differing from the full-scale techniques described previously, CFD simulation is another method to study architectural airflow. For this application, many types of software including FLUENT, FLOWVENT, ANSYS CFX, etc..., are available. Based on the Navier-stokes equation, the calculation platforms of these software are likely similar, but unique features and user interfaces make each particular software unique. Distinguished by its excellent data visualization feature, ANSYS CFX can also handle any complex geometry such as irregular shape objects. Users can simulate a complex architectural space and then see the flow cross-section, display temperature isosurface, animate the air stream, and export the filtered data easily. These features allow for a more advanced understanding of building airflow for both architects and engineers. Thermal analysis using a temperature profile is a good example of how CFD data can be visualized and provides information for the design decision-making process. An example of this analysis is the natural ventilation of a solar chimney at the Michigan Solar House (MiSO) as shown in **Figure 24** by Navvab and Varodompun [48]. Besides thermal analysis, CFD simulation is also used in other applications, such as wind load studies and pedestrian comfort. **Figure 25** shows an example of the air pressure profile on the building skins of buildings in Las Vegas generated by CFD simulation [49].

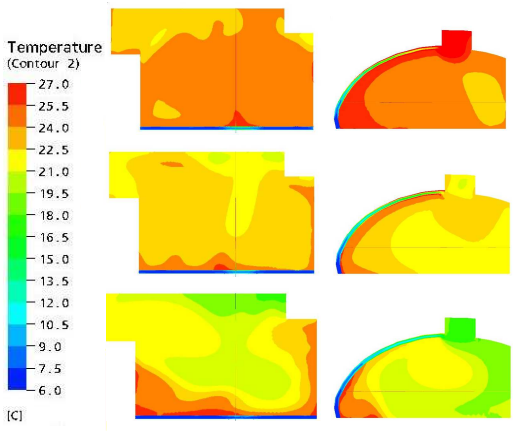

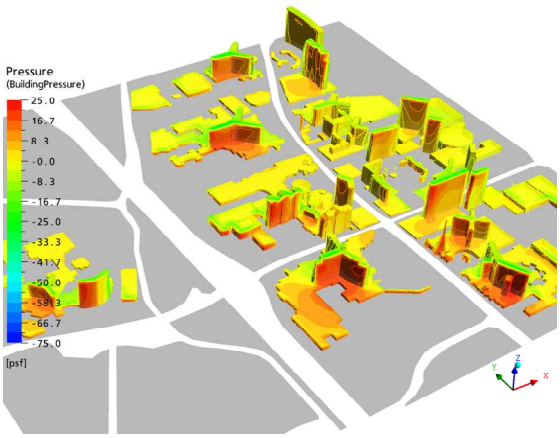

Figure 24 Temperature profiles of Michigan Solar House (left) [48]
Figure 25 Effect of wind pressure on buildings in Las Vegas (Stripes) (right) [49]

CFD capabilities described previously require users' expertise. The CFD simulation process and parameters are important basics which will be discussed as following.

<u>CFD simulation process</u>

To perform CFD simulation, single CFD software is not alone adequate. A series of other software utilities must also be applied. **Figure 26** shows a list of selected software including AutoCAD, 3DsMAX, ANSYS ICEM, and ANSYS CFX, which are used to perform 2D drawing, 3D modeling, meshing, and CFD simulating, respectively. The process first begins with creating the 3D representation of studied space using AutoCAD and 3DsMAX [50, 51]. The result, a 3D model, is then transferred to ANSYS ICEM where a raw 3D geometry is meshed [52]. **Figure 27** is an example of a meshed geometry or CFD model containing a large number of CFD nodes important for the CFD computation process. Then, the CFD model is transferred to ANSYS CFX, a CFD-based program, which has three sub-software utilities consisting of ANSYS CFX Pre, Solver, and Post [36]. Once the CFD model is in CFX Pre, it will allow users to set up both necessary airflow components including boundary conditions such as INLET, OUTLET, WALL, OPENING, etc.., and scenario conditions such as initial condition, airflow speed, and solver models. The specified CFD model can then be transferred and solved by CFX Solver where the CFD result file is produced. At the end of the CFD simulation process, the results of the CFD simulation can be transferred to CFX Post, allowing users to visualize the data, export the data, and create the animation. In brief, this summarizes the procedure for CFD simulation. More detailed information is found in the ANSYS CFX users' manual [36, 52].

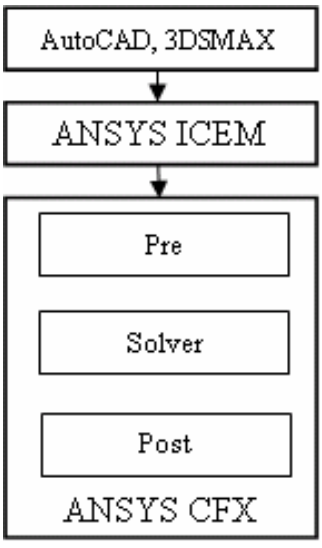

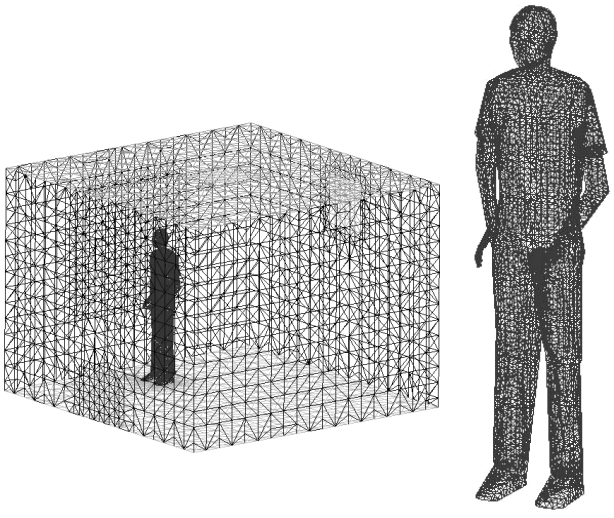

Figure 26 CFD simulation pipeline (left)
Figure 27 Example of CFD model in different resolutions (right)

CFD simulation parameters

In the CFD simulation process, many CFD parameters are involved. These parameters, the CFD code, computational method, time integral scheme, turbulent model, and scheme for the advection term, are sensitive and imperative for CFD accuracy. With increasing CFD usage, the accuracy of CFD analysis is the concern of many organizations. In Europe, the International Energy Agency [53] produced a report called, "Energy Conservation within Buildings and Communities Systems Programme". Annex 20 of this report discusses the CFD model and accuracy. Airflow patterns within a building were evaluated to compare 20 CFD simulations with actual measurement using the tested cell [53, 54]. The tested cell is a simple room with a complex supply diffuser which enabled the research team to independently model or set the complex supply diffuser in various desired ways. Upon comparing the results, the experimental data and the CFD results varied widely among the research groups. As a result, Annex 20 concludes that CFD must be carefully set up for each specific application of five technical parameters: the turbulent model, the modeling of the characteristic supply jet, boundary conditions, grid size and number, and the numerical procedure. In the USA, a CFD simulation guideline is also proposed by ASHRAE in ASHRAE RP-1133. Chen, et al.. who wrote this standard, also makes the same recommendation where CFD parameters must be systematically reported [10]. The author of this dissertation has also used these parameters to validate the IJV using full-scale experiment data in a previous publication [31], as well as in the present publication.

In **Table 4**, the recommended format of Yoshei, et al.. [55], shows the CFD parameters used in this dissertation. The first parameter is the CFD code which can be any software available on the market. Then, the second parameter is a computational method which can be either steady state or transient state. A time integral scheme, which is the number of iterations in the CFD solving process, is the third parameter. Generally, 40 to 100 iterations is enough for converging the steady state simulation [36]. The fourth parameter is the turbulent model. Turbulent models are the main calculation platform in CFD simulation [56, 57]. Turbulent models including k-ε, Renormalized Group k-ε (RNG k-ε), k-Ω, Large Eddy Simulation (LES), Direct Numerical Simulation (DNS), etc.., are different in numerical method, time consumption, result resolutions, and suitable applications. Details of each turbulent model are described in **Indoor Air Engineering**

[11] by Zhang. More details of the numerical process for each model are presented in the user manual of each CFD software including ANSYS CFX [36]. Lastly, the fifth parameter is the scheme for the advection term which is a method of computational resolutions available for high resolution and upwind schemes. High resolution may provide more accurate results, but it is time-consuming. On the other hand, upwind loses some accuracy to the reduction in computational time.

CFD code	ANSYS CFX 5.7-10.0
Computational method and time integral scheme	Unstructured grid (Tetra + prism layer)
	Steady state (60 iterations)
Turbulent model	RNG k-ε or k-Ω
Scheme for advection term	Upwind

Table 4 CFD parameters used in this dissertation

VENTILATION RELATED THEORIES

Research strategies must be utilized based on practical theories. In ventilation studies, the body of knowledge is immense and impossible to be presented all in this section. After reviewing past studies, only five related theories have been selected to be discussed here: the ventilation requirement, ventilation criteria, ventilation control using CFD simulation, and flow dimensionless parameters.

Ventilation Requirement

The first step in using both full-scale and CFD for a simulated ventilated room is to study the concept of the ventilation requirement. The ventilation requirement is the minimum flow rate required to maintain an acceptable threshold of thermal comfort and IAQ in a room. Depending on the desired thermal comfort and IAQ, the ventilation requirement is then used to calculate the necessary room temperature, humidity level, and CO_2 level. Once the ventilation requirement has been determined, the flow rate of supply air must be equal to the highest requirement [11, 49]. The concept of ventilation requirement is based on the assumption that the supply air parameters, supply temperature, humidity, velocity, and pollutant concentration, are usually better than those of the room where the heat, water vapor, and heat sources are located. In reality, the ventilation rate of the maintained temperature, water vapor, and CO_2 is not exactly equal, but usually the control of room temperature is given top priority. People feel comfortable only in a narrow range of air

temperature, but a greater range of humidity and CO_2 can be tolerated. An example of determining the minimum flow rate from the supply air temperature can be seen in **Figure 28**. Each dotted line represents the ventilation requirements of temperature, humidity level, and carbon dioxide. The solid line represents the minimum ventilation rate needed to be supplied. When cool air temperature is supplied, the flow rate to maintain appropriate room temperature can be extremely low. If supplying with the flow rate, the room level of CO_2 might exceed the threshold. To reduce CO_2 to within the threshold limit, the CO_2 level must be used to calculate and then picked as a minimum ventilation rate (see red circle) instead of using temperature. When this situation happens, thermal comfort in the room is unsatisfactory because the cool air is forced to continuously supply as long as CO_2[7] remains high. The situation can be reversed when the supply temperature is warm. The flow rate must be increased to meet the thermal demand first (see red circle). At this point, the flow rate is automatically higher than the demand from both water vapor and CO_2. This situation might make temperature, humidity and CO_2 level met the expected criteria, but the energy necessary for ventilation in this high thermal demand state can be excessive. The ideal circumstance is when all demands are equal (green circle) and when all can be ventilated with the lowest ventilation rate. The following sections show how each variable controls the ventilation requirement numerically.

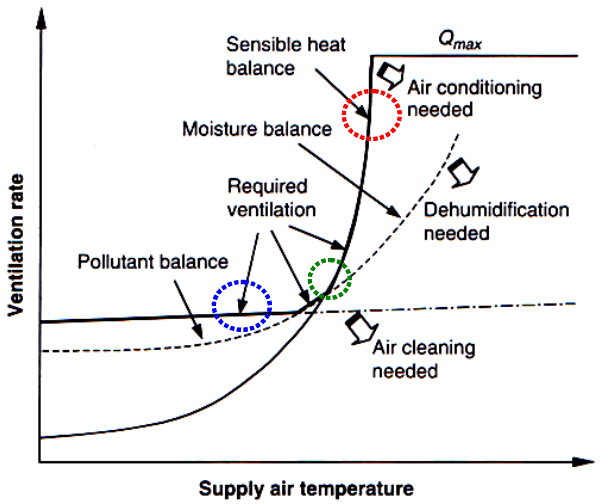

Figure 28 Minimum requirement of three ventilation criteria [11]

Thermal ventilation requirement

[7]This problem typically occurs when applying the VAV system.

The room air temperature (T_a) is the most used variable for controlling the ventilation rate or flow rate (Q) based on **Equation 2**. In this equation, other variables that change room temperature include supply air temperature (T_s) and the cooling or heating load[8] (q), which is the amount of heat in the space. This equation represents how the HVAC is being controlled using these variables. Constant Air Volume (CAV) and Variable Air Volume (VAV) are the available methods of control. CAV is operated by changing the supply temperature, but maintaining the constant flow rate; while VAV is operated by changing the flow rate, but maintaining the constant supply temperature. More detailed discussion of these control strategies can be found in Chapter 5 and 6, ASHRAE Fundamental 2005 or other related literatures [1, 4, 41, 58].

$$Q = \frac{q}{k(T_a - T_s)} \qquad \text{Equation 2}$$

Where
- Q = flow rate (CFM, m^3/sec)
- q = total cooling load (Btu/h, W)
- T_a = room temperature (F, C)
- T_s = supplied temperature (F, C)
- k = 1.08 in IP system[9], 1,227 in SI system

Humidity ventilation requirement

Like the thermal one, humidity control is based on the same principle as shown in **Equation 3**. The room humidity level (w_a) depends on supply humidity level (w_s), flow rate (Q), and total vapor load (W_p) which is mostly generated by humans and by infiltration [11]. Once the humidity level is computed, it is usually converted to the format of Relative Humidity (RH) using the psychrometric chart [59].

$$Q = \frac{W_p v_s}{(w_a - w_s)} \qquad \text{Equation 3}$$

Where
- Q = flow rate (CFH, m^3/s)
- W_p = total vapor emission rate (lbs/h, kg/s)
- w_a = room air humidity level ($kg_{vapor}/kg_{dry\ air}$)
- w_s = supplied air humidity level ($kg_{vapor}/kg_{dry\ air}$)
- v_o = supplied air specific volume (cu.ft/lbs, m^3/kg)

Pollution ventilation requirement

[8] Details on the load calculations are found in many HVAC handbooks such as **ASHRAE Fundamentals**
[9] Calculation can be found in **ASHRAE Handbook of Fundamentals 2005**

Once the temperature and humidity level is satisfied, the last factor to be met is the IAQ, which concerns various types of pollutants from many sources. To study all pollutant spices might be impossible. The most common pollutant and the one most strictly to be controlled is CO_2. Since it is not filterable, it must be reduced by allowing more fresh air into the room. The minimum ventilation rate to reduce indoor CO_2 from ASHRAE 2004-62 depends on the activities and density of the occupants [13] and can be calculated by using **Equation 4**. The room level of CO_2 (C_a) is calculated from the CO_2 concentration of supply air (C_s), flow rate (Q), and the total CO_2 (M_p), according to the number of occupants and their activities (THP). See **Equation 5.** In addition to this equation, an alternative method of calculation of CO_2 production is possible using **Figure 29**. For instance, a seated occupant (1 MET) generates CO_2 at 0.25 liters/min. [15]. By replacing CO_2 with a different pollutant, **Equation 4** can still be applied to calculate an adequate ventilation rate for that type of pollutant.

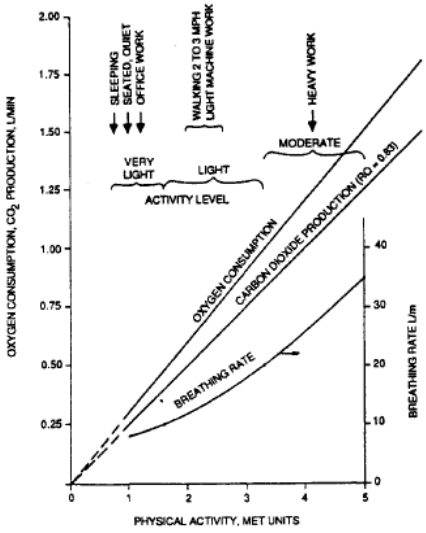

Figure 29 O_2 demand and CO_2 production of different occupants' activities [15]

In some cases, the CO_2 concentration can be described in PPM-V units, i.e., parts per million of CO_2 volume in air volume. When this unit is applied, **Equation 5** is then used to calculate the ventilation rate [11] and the result will be the same as in **Equation 4**.

$$Q = \frac{M_p}{(C_a - C_s)} \qquad \text{Equation 4}$$

$$Q = \frac{M_p v_c}{(C_{a-ppmv} - C_{s-ppmv})} \times 10^6 \qquad \text{Equation 5}$$

$$M_p v_c = \frac{THP}{24600} \qquad \text{Equation 6}$$

Where
- Q = flow rate (CFH, m^3/s)
- M_p = total CO_2 emission rate (lbs/h, kg/s)
- C_a = room air CO_2 level (lbs/cu.ft, kg/m^3)
- C_s = supplied air CO_2 level (lbs/cu.ft, kg/m^3)
- $C_{a\text{-}ppmv}$ = room air CO_2 PPMV (m^3CO_2/m^3air)
- $C_{s\text{-}ppmv}$ = supplied air CO_2 PPMV (m^3CO_2/m^3air)
- v_c = supplied CO_2 specific volume (cu.ft/lbs, m^3/kg)
- THP = Total Heat Production (W) of number of occupants x total heat generating by human body

Ventilation Criteria

After the room ventilation system is controlled using the ventilation requirement, the conditions within the room must be in compliance with several of the ventilation criteria. The following sections will discuss both the familiar criteria, such as Ventilation Effectiveness (VEF, ε) and Predicted Mean Vote and Predicted Percent of Satisfied (PMV-PPD), and the newly introduced criteria of CFD Ventilation Performances.

Ventilation Effectiveness (VEF, ε)

The ventilation effectiveness index is commonly used by ventilation practitioners to compared how the ventilation systems or air distribution systems perform in given rooms [1, 13, 60]. High ventilation effectiveness directly benefits the room IAQ and has been adopted as a scoring category in the sustainability campaign of LEED [8]. Ventilation effectiveness is considered from two aspects [60]. The first aspect is room heat transfer to which **Thermal Ventilation Effectiveness/thermal VEF (ε_t)** is applied. Calculated by using air temperature at the supply (T_s), exhaust[10] (T_e), and the room average or the breathing zone average ($\overline{T}$), as shown in **Equation 7,** ε_t is then equal to one if T_e and $\overline{T}$ are equal. High ε_t is desirable and is achieved by maintaining T_e higher than $\overline{T}$. Using the same principle, **Concentration Ventilation Effectiveness/ Concentration VEF (ε_c)** is the second aspect directly related to IAQ. ε_c is calculated by using the pollution concentration measured at the exhaust[11] (C_e), concentration at the supply terminal (C_s), and the average concentration at a given space ($\overline{C}$) shown in **Equation 8**. Similar to ε_t, ε_c also decreases or increases by the relationship between the concentration at the exhaust and the room average or the breathing zone average.

[10] The room is completely mixed. If not, the total room average temperature is used.
[11] The room is completely mixed. If not, the total room average pollutant concentration is used.

$$\varepsilon_t = \frac{T_e - T_s}{\overline{T} - T_s} \quad \text{Equation 7}$$

$$\varepsilon_c = \frac{C_e - C_s}{\overline{C} - C_s} \quad \text{Equation 8}$$

Another way to compute ε_c is to use the local mean age of air. A short local mean age indicates that the air is efficiently ventilated at a given point. A long local mean age shows a poorly ventilated area such as a stagnant point where the pollutants are generally high. Local mean age is not only obtained from a full-scale experiment using the gas tracer technique, but also from a CFD simulation. Based on the gas tracer technique, ASHRAE-129 is the standard for determining the local mean age of air and ε_c which are functions of the pollutant (tracer gas) concentration ($C_i(t)$) over time (t) divided by the initial concentration (C_0) [61]. See **Equation 11**. τ_r or inversed room air change (ACH in 1/h) represents the average mean age of air in the room and is calculated from the ventilation rate (Q in m^3/h) and the room volume (V in m^3) as written in **Equation 10**. The ratio of inversed room air change (τ_r) to the local mean age (τ_i) give ε_c as a result (See **Equation 9**). Further detail regarding local mean age and ε_c is found in ventilation handbooks and related publications by Awbi, et al.. [13, 62, 63].

$$\varepsilon = \frac{\tau_r}{\tau_i} \quad \text{Equation 9}$$

$$\tau_r = \frac{1}{ACH} = \frac{Q}{V} \quad \text{Equation 10}$$

$$\tau_i = \frac{1}{C_0}\int_o^\infty C_i(t)dt \quad \text{Equation 11}$$

Air Distribution Configuration	ε_c (E_z)
Ceiling supply of cool air	1.0
Ceiling supply of warm air and floor return	1.0
Ceiling supply of warm air 15°F (8°C) or more above space temperature and ceiling return.	0.8
Ceiling supply of warm air less than 15°F (8°C) above space temperature and ceiling return provided that the 150 fpm (0.8 m/s) supply air jet reaches to within 4.5 ft (1.4 m) of floor level. **Note**: For lower velocity supply air, E_z = 0.8.	1.0
Floor supply of cool air and ceiling return provided that the 150 fpm (0.8 m/s) supply jet reaches 4.5 ft (1.4 m) or more above the floor. **Note**: Most underfloor air distribution systems comply with this proviso.	1.0
Floor supply of cool air and ceiling return, provided low velocity displacement ventilation achieves unidirectional flow and thermal stratification	1.2
Floor supply of warm air and floor return	1.0
Floor supply of warm air and ceiling return	0.7
Makeup supply drawn in on the opposite side of the room from the exhaust and/or return	0.8
Makeup supply drawn in near to the exhaust and/or return location	0.5

Table 5 Ventilation Effectiveness suggested by ASHRAE 62-2004 [7]

ε_c of each ventilation strategy was determined by ASHRAE 62-2004 See **Table 5**. Generally, any strategy operating with a cooling mode has high ε_c, and any strategy operating with a heating mode has low ε_c [64]. DV has the highest VEF in cooling mode with a ε_c of 1.2, while the MJV generally has a ε_c of 1. When both systems switch to heating, the ε_c is reduced to 0.8 and 0.7, respectively [7]. It should be noted that an ε_c of IJV does not yet exist, but is thereby proposed in this dissertation.

$$V_{oz} = \frac{V_{bz}}{\varepsilon_c}$$ Equation 12

The application of ε_c can be found in **Equation 12**. Outdoor air in the breathing zone, (V_{bz}), the minimum ventilation rate recommended by ASHRAE 62-2004 in Table 6-1 is divided by ε_c to determine the zone outdoor airflow (V_{oz}). Zone outdoor airflow is an actual flow rate that is induced into the HVAC system.

Since ε_c affects the fresh air intake rate, it indicates the relationship between ventilation effectiveness and the energy consumption of the HVAC system. This relationship is described by the HVAC air-side diagram in **Figure 30**. When ε_c increases, the fresh outdoor air intake (V_{oz}) decreases, and so does the demand on the operation of the HVAC system, especially when the outdoor air is not thermally suitable. An example of fresh air intake for AHU with a single duct VAV system under different ventilation strategies was demonstrated by Stanke [65]. He commented that rooms maintaining the cooling mode will tend to get higher ε_c than rooms with heating mode as a majority. In contrast to ε_c, ε_t directly relates to overall flow rate or the minimum ventilation requirement (Q) of a ventilated room as written in **Equation 13**. If ε_t increases, the actual overall flow rate (Q) decreases, and thus the fan size and energy for the HVAC is decreased. Otherwise, if the flow rate remains constant, high ε_t can reduce the temperature difference (T_a-T_s). For the HVAC design, this means that either supply temperature can be warmer; otherwise the room temperature is cooler.

$$Q = \frac{q}{k(T_a - T_s)\varepsilon_t}$$ Equation 13

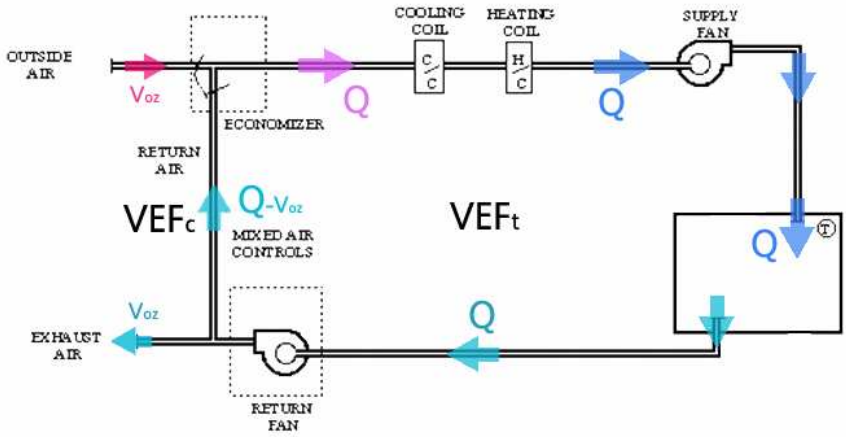

Figure 30 Relationship of overall flow rate and fresh air intake in HVAC system

The energy conservation of a high ε_t is still controversial. The advantage of the reduction of overall flow rate is valid, but once the flow rate is lower, the return air is also warmer. Once the warm air returns to the AHU, it increases the cooling coil load. More cooling energy is consumed at the plant (chiller) so that more or colder chilled water is produced. But this may, in turn, cause the designed cooling system to be undersized. The energy conservation at the fan, but wastage at the cooling coil may be balanced out and may result in the same overall energy usage [1]. The controversial impact of high or low ε_t is not dealt within this dissertation, but rather the impact of energy conservation is discussed using ε_c.

CFD Ventilation Performances

A negative impact comes about when using only ventilation effectiveness since the local thermal discomfort, the interaction between the occupants at a given location and the thermal environment,[12] is disregarded [9]. Local thermal discomfort, as defined by ASHRAE 55, includes temperature stratification, draft, radiant asymmetry, and floor temperature [6]. Since the two former indicators are directly impacted by the use of ventilation strategies, only those two are referenced in this dissertation. Stratification discomfort can happen in a DV and an IJV ventilated room where stratification is usually utilized for enhancing the IAQ. When the temperature is too stratified, stratification discomfort occurs and increases the Percentage of Dissatisfied (PD). A PD of 10% is to be expected when the temperature difference from the height of 1.1 to 0.1m differs more

[12] This is an environment concerned with thermal comfort factors- temperature, relative humidity, mean radiant temperature, wind velocity, clothing and activities.

than 3°C or 5.4°F [1, 13]. Draft occurs when high velocity air blows on certain human body parts, such as the ear and neck. In cool temperatures, a person tends to be more sensitive to drafts and this sensitivity can be justified by the PD calculated by **Equation 14**. Using this equation, an air temperature of 23.5°C and an air velocity of 0.15 m/s on an occupant's ear or neck leads to a PD of 10% [1, 13].

$$PD = (34 - t_{a,l})(\bar{v}_{a,l} - 0.05)^{0.62}(0.37\bar{v}_{a,l}Tu + 3.14) \qquad \text{Equation 14}$$

Where
- PD = Discomfort caused by draft (%)
- $T_{a,l}$ = local air temperature, in degrees Celsius, 20 °C to 26 °C
- $\bar{v}_{a,l}$ = local mean air velocity (m/s), if <0.05, use 0.05 m/s
- Tu = local turbulence intensity, in percent, 10 % to 60 % (if unknown, 40 % may be used)

Determining locations for monitoring the local thermal comfort is difficult. ASHRAE 55 suggests that the monitoring location be in the occupied area, but that the temperature and velocity be largely varied within that area. In order to resolve this limitation, new indicators called **CFD ventilation performances** are introduced here. CFD simulation determines both draft and stratification discomfort and is then mapped and plotted on any given plane. Once mapped, the area where the given threshold is exceeded can be quantified and then normalized by room area. The outcomes are both normalized, so that draft and stratification discomfort then become dimensionless. Normalized stratification discomfort is calculated by the ratio between room area and temperature differences exceeding 3°C (from 1.1m to 0.1m) to the total room area. See **Equation 15**. Based on this concept, normalized draft area is then calculated by the ratio between room area where the dissatisfaction (PD) caused by draft (calculated by **Equation 14**) exceeds 10% as shown in **Equation 16**.

This same concept is applied to actual pollutant levels not given by using ventilation effectiveness as an indicator. The actual pollutant level is needed to prevent critical conditions which may affect the occupants' health. In **Equation 17**, normalized CO_2, which is the ratio between the average CO_2 at nose level to the standard CO_2 at 1000 ppmv, is proposed as an indicator for CFD ventilation performances [13]. 1000 ppmv of CO_2 is the highest threshold recommended by ASHRAE for any occupied space. Increasing the fresh air intake rate is usually the best strategy to avoid exceeding the 1000 ppmv level [66, 67].

Equation 15	Equation 16	Equation 17
Stratification discomfort	Draft	Normalized CO_2
$\frac{A_{t>3C}}{A_{room}}$	$\frac{A_{PD>10}}{A_{room}}$	$\frac{C_{cfd}}{C_{1000\,ppmv}}$
$A_{t>3c}$ = area of selected plane where temperature of 1-0.1 m exceeding 3°C A_{room}= room area	$A_{PD>10}$= area of selected plane where draft discomfort exceeds 10% A_{room}= room area	C_{cfd}= CO_2 concentration of selected plane $C_{1000ppmv}$= CO_2 at 1000ppmv

Table 6 Summary of CFD ventilation performances equations

In order to use CFD ventilation performances, CFD simulations which provide dense grid resolution are necessary. As discussed before, a full-scale experiment is usually limited by the sensors' availability thus making indicators, such as stratification discomfort and draft, almost impossible to quantify. **Table 6** shows the calculation of three variables, including stratification discomfort, draft, and CO_2. Relative Humidity (RH) is a missing indicator which is excluded here, but it was included in the PMV-PPD calculation discussed in the following section.

Predicted Mean Vote (PMV) and Predicted Percent of Satisfied (PPD)

Local thermal discomfort may be fine for analyzing dissatisfaction in a thermal environment with specific variables, but it is not a useful indicator for identifying the overall thermal comfort of any given space. Thermal comfort occurs when the heat produced by humans and that of the environment is balanced [1, 68]. The heat balance of a human body in a given time of exposure and climatic condition is affected by temperature, humidity, radiation, wind speed, frequency of persistence, clothing, activity and body position [69]. Generally, the preferred air temperature ranges from 20.5-23.3°C (69-74°F) for winter and 23-28.8°C (73.5-84°F) for summer[13]; while the preferred RH in a conditioned space is 50%. However, a RH ranging from 20%-75% also satisfies the thermal comfort criteria [6, 9]. To prevent draft, the mean air velocity should not exceed 0.1-0.18 m/s (0.35-0.6 fps)[14] [1]. With the many criteria to consider, thermal comfort is difficult to determine. To solve this problem, a single indicator, Predicted Mean Vote or PMV, is proposed. Based on radiant energy balance between the human body and the

[13] At RH 50%
[14] At PPD of 10% and range of mean air temperature of 20-26°C

environment, PMV is used to describe comfort range statistically [1]. PMV is composed of both personal and environmental factors which are usually based on the SI system. The former includes metabolic rate (M), work (W), and clothing (f_{cl}). The latter consists of room temperature (T_a), radiation (T_r), humidity (P_a), and wind velocity (h_c). Metabolism (M) depends on foods and breathing rates which thus determine the typical occupant's metabolic rate per skin surface area found in **Table 7**. Due to the inefficiency of the human body, work (W) is usually only generated at 20% of a given metabolic rate. A clothing area factor (f_{cl}) is calculated from the Clo-value (I_{cl}) shown in **Table 8**. If the Clo-value is more than 0.5, **Equation 18** is used, and for the others **Equation 19** is used. Besides the air temperature, mean radiation temperature (T_r) is obtained by a globe thermometer in a full-scale measurement or it is calculated by **Equation 20** if using a CFD simulation. Vapor pressure can be obtained from the psychrometric chart or by using **Equation 21**, if the humidity level (w_p) is given. Air velocity reduces air film resistance and increases evaporation rate and accelerates heat loss from the body by reducing the convective heat transfer coefficient (h_c). The highest h_c is picked by either **Equation 22** or **Equation 23**. Once these variables are determined, a PMV calculation is presented in **Equation 24**. The effect of clothing (t_{cl}) is presented in **Equation 25** [13]. In this dissertation, the metabolic rate and clothing of occupants were fixed at M (for seating) of 58 W/m^2 and (I_{cl} for light working) of 0.7.

Activities	Metabolic rate (W/ m^2)
Reclining	46
Seated, relaxed	58
Standing activity (shopping)	93
Medium activities (garage work)	165

Table 7 Metabolic rate of typical activities

Clothing ensemble	I_{cl} (clo)
Node	0
Short	0.1
Light work ensemble	0.7
Typical Indoor winter cloth	1
Heavy Business suit	1.5

Table 8 Clo-value of typical clothing

Equation 18 (top) Equation 19 (bottom)	Equation 20	Equation 21	Equation 22 (top) Equation 23 (bottom)
$f_{cl} = 1.05 + 0.1 I_{cl}$ $f_{cl} = 1.00 + 0.1 I_{cl}$	$q_{rad} = 5.6705 \times 10^{-8} T_r^4$	$w_p = 0.62 \times 10^{-5} P_a$	$h_c = 2.38(T_{cl} - T_a)^{0.25}$ $h_c = 12.1\sqrt{v}$
I_{cl}= Clo-value (Clo) f_{cl}= clothing area factor	q_{rad}= radiation energy (W/m^2) T_r = mean radiation temperature (K)	w_p=humidity level (kg/kg) P_a= water vapor pressure (Pascal)	h_c= heat transfer coefficient (W/m^{2}K) T_{cl}=clothing temperature (C) T_a=air temperature (C) v=air velocity (m/s)

Table 9 Equations for PMV parameters

$$PMV = (0.303e^{-0.036M} + 0.028)\{(M-W) - 3.05\times10^{-3}[5733 - 6.99(M-W) - P_a] - 0.42[(M-W) - 58.15] - 1.7\times10^{-5}M(5867 - P_a) - 0.0014M(34 - T_a) - 3.96\times10^{-8} f_{cl}[(T_{cl}+273)^4 - T_r^4] - f_{cl}h_c(T_{cl} - T_a)$$

Equation 24

$$t_{cl} = 35.7 - 0.028(M-W) - 0.155I_{cl}\{(M-W) - 3.05\times10^{-3}\times[5733 - 6.99(M-W) - P_a] - 0.42[(M-W) - 58.15] - 1.7\times10^{-5}M(5867 - P_a) - 0.0014M(34 - T_a)$$

Equation 25

$$PPD = 100 - 95\exp\{-0.03353(PMV)^4 + 0.2179(PMV)^2\}$$

Equation 26

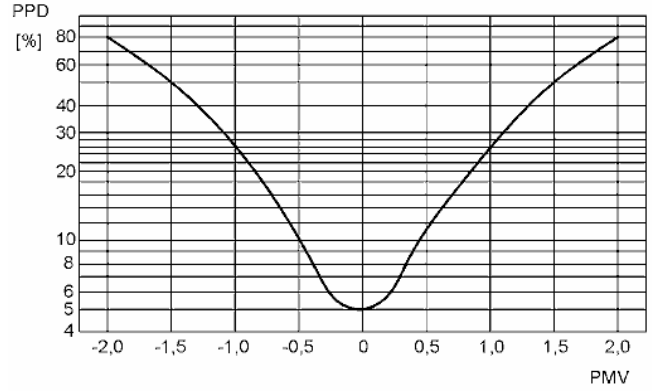

Figure 31 PMV-PPD curve

Equation 18 through **Equation 26** are referenced from ASHRAE 55 and ISO 7730 for the PMV and PPD calculations [6, 9]. Typically, PMV ranges from +3 to -3 or from hot to cold {-3(cold), -2(cool),-1(slightly cool), 0 (neutral), +1(slightly warm), +2(warm), and +3(hot)}. A PMV of 0 is the most desirable [9, 70]. A PPD can be calculated directly from the PMV and from the values ranging from 0-100% of thermal dissatisfaction. The relationship between the PPD and the PMV is shown in **Figure 31** and calculated by **Equation 26**. At a PMV=0, PPD equals 5%. To calculate both the PMV and the PPD, complications and inconveniences are avoided by using available tools such as PSYCHTOOL where users examine various comfort factors that interactively impact PMV-PPD [71].

Category	Overall Thermal Comfort		Local Discomfort			
	PPD	PMV	DR%	PD% caused by		
				Stratification discomfort	Warm or cool floor	Radiant asymmetry
A	<6	-0.2 < PMV < + 0.2	<10	<3 (2C)	<10	<5
B	<10	-0.5 < PMV < + 0.5	<20	<5 (3C)	<10	<5
C	<15	-0.7 < PMV < + 0.7	<30	<10 (4C)	<15	<10

Table 10 ISO 7730-2005 thermal comfort categorization spaces[9]

In ISO-7730, appendix A shows the thermal comfort categorization as presented in **Table 10**. The space categories, A-C, are ranked according to expected upper and lower PMV,

PPD, and PD. The PD includes stratification discomfort, floor temperature, and radiant asymmetry [9]. As with local thermal discomfort, the best monitoring location to measure PMV-PPV is difficult to determine. The same concept of using CFD nodes to compute the CFD ventilation performances is also applied here in order to obtain the average PMV-PPD at a given height.

Ventilation control using CFD simulation

Ventilation control using CFD simulation differs from the control in an actual building. The control relates directly to the simulation types available in CFD which include **steady state** or **transient state** [36]. The transient state is time and memory-consuming, but the actual HVAC functions (thermostat and fans activation) can be simulated. On the contrary, the steady state takes less time and memory, but the actual HVAC functions are not applicable. Since this research deals with many parametric studies, time is a major constraint. Steady state CFD simulation is thus chosen.

A limitation of steady state is that room conditions, such as temperature, depend on cooling load and HVAC capacity. The room temperature can not be directly controlled. Instead, the thermal energy balance automatically determines the room temperature, which is affected by loads, supply temperature and supply flow rate as described by **Equation 2**. In this equation, it is assumed that the air is completely mixed and thus the room air temperature is homogeneous. In reality, stratification of air temperature renders this equation immaterial.

In most spaces, only the breathing zone (or 0-1.8 m height) is assumed to be utilized [13]. Compared to the area close to the ceiling (higher than 1.8m), thermal comfort and the occupant's satisfaction within this breathing zone must be carefully controlled. In traditional mixing systems (MJV), the air temperature is quite homogeneous and therefore cooling or heating energy is wasted in conditioning the whole space. To solve this limitation, DV and IJV are the solution since these methods condition mainly the breathing zone. The advantage is also described by thermal ventilation effectiveness, ε_t, calculated with **Equation 7**. High ε_t means the breathing zone temperature is closer to the supply temperature than to the average room temperature. ε_t is not only useful for comparing the thermal performances of different ventilation strategies, but also for

applying CFD ventilation controls. Using a single CFD simulation case, the overall space temperature is fixed at about 23.5°C using **Equation 2**. If the breathing zone temperature comes out lower than the overall space temperature, ε_t will be higher than one. This ε_t is used then to adjust the actual flow rate rather than to set the average temperature of the breathing zone closer to the control temperature (set point temperature). See **Equation 13**. Once this method is applied, it should be noted that the average room temperature may be higher than that of the control temperature. This process of determining ε_t (using Equation 27) and flow rate can be found in **Figure 32** where two series of grids are applied. The 0.50x0.50 m grids of 0.1, 1.1 and 1.8m are averaged in order to represent the breathing zone temperature ($T_{1.8\text{-}0.1}$), while a grid of 2.7m is added to calculate the overall space temperature ($T_{2.7\text{-}0.1}$).

$$\varepsilon_t = \frac{T_{2.7-0.1} - T_s}{T_{1.8-0.1} - T_s} \qquad \text{Equation 27}$$

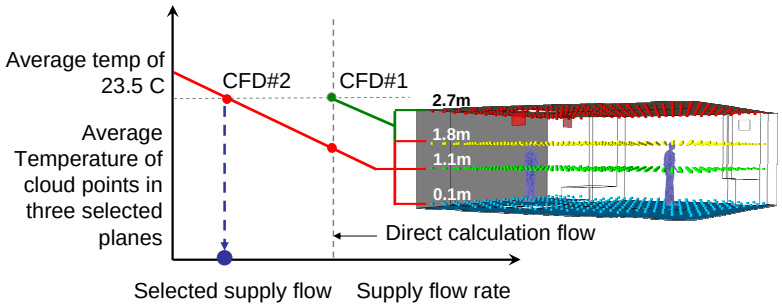

Figure 32 The CFD temperature control method

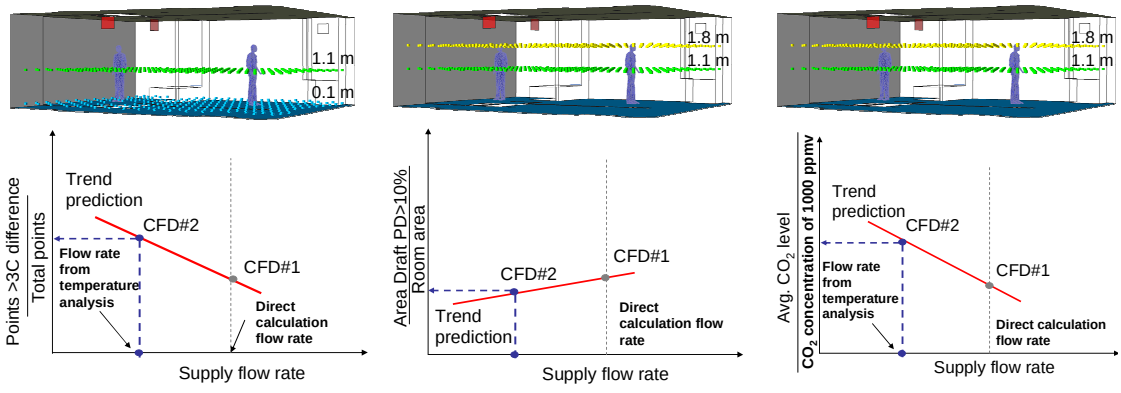

Figure 33 Stratification discomfort, draft, and pollutant concentration (CO_2) predicted by CFD simulations.

The outcome is an actual flow rate for a second CFD simulation (CFD#2). If CFD#1 shows a room temperature of 23.5°C or 74°F, CFD#2 will also show a breathing zone

temperature close to 23.5°C or 74°F, the control temperature. Obtained from the CFD#2, both PMV-PPD and CFD ventilation performances as well as the stratification discomfort, draft, and normalized CO_2 are accurately determined in the same way as the temperature control. See **Figure 33**.

Table 11 concludes the CFD grid planes that are used to calculate ventilation indexes. Since ε_t relates to the heat transfer of the human body, grid planes from ankle to head are selected. Associated with human respiration ε_c, the grid planes at the nose level sitting and standing are averaged. CO_2 and draft are categorized separately for both sitting and standing. Defined by ASHRAE 55, stratification discomfort can be calculated by grid planes at 0.1 and 1.1m [6]. In contrast to the other indexes, the calculation of PMV-PPD is based on heat transfer from the core of the body and on the environment [1]; therefore, only the grid plane at the body core level, 1.1m, is used.

	Standing	Sitting
ε_t	0.1-1.8m	
ε_c	0.6-1.8m	
CO_2 and draft	1.8 m	1.1 m
Stratification discomfort	0.1-1.1m	
PMV-PPD	1.1m	

Table 11 CFD grid planes selection

Flow Dimensionless Parameters

The last section of this chapter is dedicated to a discussion of flow dimensionless numbers which are significant for flow characterization, particularly in fluid dynamics. Among the many dimensionless numbers available, two important dimensionless numbers, including the Reynold Number (Re) and the Richardson Number (Ri), are discussed.

Reynold Number (Re)

Calculated by fluid density (ρ), velocity (u), length scale (L), and fluid viscosity (μ) as shown in **Equation 28**, Re is the ratio of inertia force and viscous force and is used to determine the flow turbulence. If the ratio between inertia force and viscous force is low, fluid viscosity dominates and the flow is laminar. If the ratio between inertia and viscous force is high enough, the flow tends to be turbulent. The flow is then also independent of fluid viscosity. The transition range between laminar and turbulent depends on applications and many factors such as surface roughness, heat transfer, vibration, noise,

etc.. In pipe flow, flow with Re less than 3,000 is laminar, but the flow becomes turbulent if the Re is more than 3,000 [1].

$$\mathrm{Re} = \frac{\rho U L}{\mu} = \frac{F_{inertia}}{F_{viscous}} \qquad \text{Equation 28}$$

Richardson Number (Ri)

When a fluid density difference is present, Ri becomes an important parameter. Typically the density of fluid [35] changes, when the temperature varies. In a ventilated room, mixing between different air temperatures is common; thus, Ri is quite a significant parameter. Calculated by using **Equation 29,** Ri has the same variables as Re, including ρ, u, L. The additional variables from Re are gravity acceleration (g) and density difference of fluid ($\Delta\rho$).

$$Ri = \frac{\Delta\rho g L}{\rho U^2} = \frac{F_{bouyancy}}{F_{inertia}} \qquad \text{Equation 29}$$

As the ratio between buoyancy force and inertial force, Ri is used to quantify the mixing rate in addition to Re. In general, when Ri is low, the entrainment and mixing of the fluid layer occurs easily. When Ri is high, the mixing and entrainment of the fluid layer hardly occurs. The entrainment of fluids when Ri is equal or less than one is most effective because inertia force highly dominates buoyancy force.

In this study, the Re and Ri are set up based on terminal characteristics. **Table 12** includes the variables used for calculating both numbers. Supply velocity is used as a reference velocity (U_o). Air dynamic viscosity (μ) and air density (ρ) are based on supply temperature. The air density difference is calculated from room air temperature and supply temperature. The length scale (L) is calculated by the nozzle diameter (d) or, in some cases, the inversed square of nozzle supply area (A).

$\mathrm{Re} = \frac{\rho U_o L}{\mu}$			$Ri = \frac{\Delta\rho g L}{\rho U_o^2}$		
	Re parameters	Units		Ri parameters	Units
ρ	Air density of supply temperature	kg/m^3	ρ	Air density of supply temperature	kg/m^3
U_o	Peak supply velocity	m/s	U_o	Peak supply velocity	m/s
L	Inverse square of supply area (√A)	m	L	Inverse square of supply area (√A)	m
μ	Supply air dynamic viscosity	kg/m*s	$\Delta\rho$	The difference of air density of control temperature and supply temperature	kg/m^3

Table 12 Defined Re and Ri used in this study

CHAPTER 3
IMPINGING JET CHARACTERISTICS

In architectural applications, an impinging jet is categorized by the location of a nozzle where radial, wall, and corner impinging jets are possible options. These available options are shown in a diagram shown in **Figure 34**. Locating the nozzle at the center of the room, radial impinging jet or a radial wall jet has previously been investigated by Poreh, et al.. in 1967 who studied the characteristics of an impinging jet in an isothermal environment [72, 73]. Karimipanah and Awbi are the first researchers who have extensively investigated another type of impinging jet called a wall impinging jet [21, 22]. They used full-scale experiment and CFD to study both jet characteristics and their performances within a ventilated classroom [21]. Unlike radial and wall jets, a corner impinging jet has not yet been investigated; and so, it will be investigated here in this dissertation first time. In this chapter, the first objective is to quantify the characteristics of the impinging jet. An additional objective is to discover parameters for obtaining validated CFD results which will then be applied in further CFD simulations in the following chapters. This chapter begins with a discussion of general impinging jet behavior and then proceeds to the experimental and simulation results of three different options for an impinging jet.

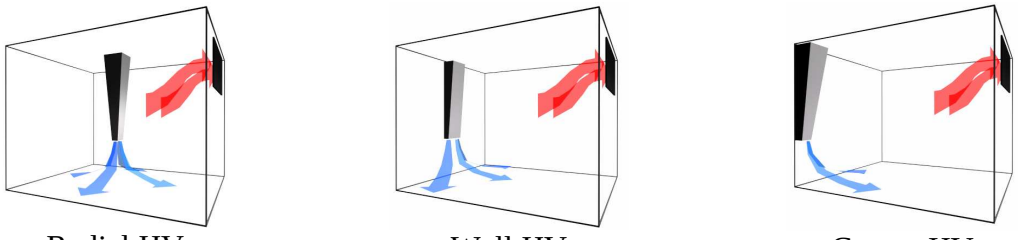

Radial IJV Wall IJV Corner IJV

Figure 34 Diagram of three options for an IJV system

IMPINGING JET BEHAVIOR

For a better understanding of the impinging jet behavior that is to be discussed in this section, readers should have a basic knowledge of jet and plume which is to be found in

Appendix B. Unlike a typical free jet, the placement of the supplies and returns make an impinging jet unique because the supply terminals must face the floor with 0.3-1m height and the returns must be located near the ceiling. This setting allows impinging jet structures to develop as a **free jet region**, an **impinging region**, and a **wall jet region**. Initially, the jet behaves as a free jet which is called the **free jet region**. Then, the impinging surface (floor) starts to impact the jet at 75% of the distance from the jet nozzle. The velocity at the centerline quickly reduces to zero when the jet hits the floor. The point where the velocity decreases to zero and the pressure is strongest is called the **stagnation point** and occurs in the **impinging region**. After that, the remaining momentum distributes along the impinging surface where a jet boundary layer is formed and there sharply decreases its velocity. In this region, the jet behaves as a typical wall jet and this is why it has been called the **wall jet region** [21]. See **Figure 35**. Since a boundary layer is formed only near the floor surface, the ambient room air is not disturbed by the jet velocity. Normally, this disturbance occurs when using an overhead mixing system or a MJV.

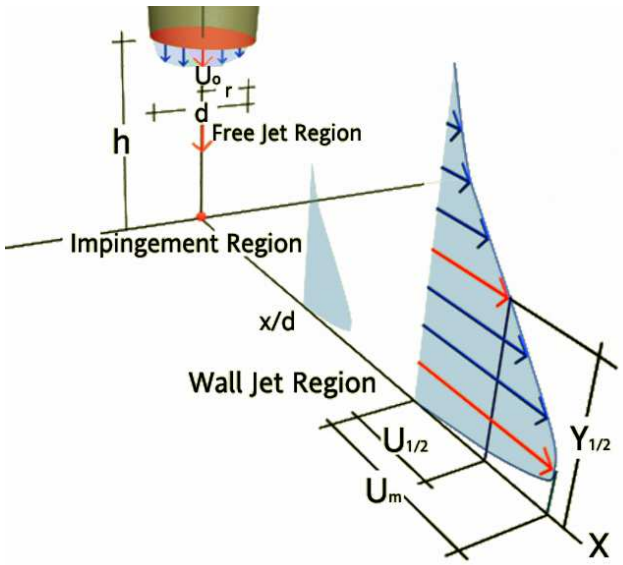

Figure 35 Three jet regions and the definitions of impinging jet characteristics

Among these three regions, the wall jet region is the most important and the chief concern. If it is not properly designed, its velocity can disturb the occupants who may feel thermal discomfort. The typical characteristics of a wall jet are usually described with two parameters: maximum velocity of the centerline jet (U_m) and the spread angle of the jet. The maximum velocity typically decays along the normalized nozzle distance

(x/√A or x/d), and the decay rate is slow or fast depending on the jet structure regions[15]. While the velocity dissipates, the jet spreads wider. This spreading characteristic of the jet is normally measured by using the height of half the maximum velocity ($y_{1/2}$ at $U_{1/2}$); so that the larger the value, the wider the jet spread [74].

THE COMPARISON OF RADIAL IMPINGING JET WITH PAST STUDY

Comparing past impinging jet study with this study shows remarkable developments in the present application of radial impinging jets. In the 1970s, Poreh and Tsuei investigated the radial impinging jet or radial wall, not for architectural application, but rather for fluid mechanics studies. Their results show jet characteristics such as velocity profile, turbulent intensity, jet structure, etc.. [72] This jet characteristic will then be compared with CFD results coming from a different setting. After going through many trials, two variables, turbulent models and nozzle velocity profiles, appear to show the greatest influence on jet characteristics.

CFD turbulent model for Impinging Jet Study

Many turbulent models, such as k-ε, RNG k-ε, k-Ω, Reynolds Stress etc.., are available in CFD software, and yet, among these models, the best model for impinging jet simulation is still unconvincing. Awbi, et al.. suggested that either k-ε or RNG k-ε are both correct enough for HVAC study. Using the same calculation platform as k-ε, the RNG k-ε model consumes 15% more computational power than typical k-ε, but the results are more accurate, especially for impinging jet study [13]. Different results are reported by Knowles who suggests that the k-ε actually tends to over-predict U_m along the nozzle distances [75]. The ANSYS CFX manual also discusses the applications of each model. The k-ε and RNG k-ε limitations in aerospace applications are also mentioned. Both models poorly predict the flow behavior at the complex boundary layers and wakes behind airplane wings. This concern is forcing scientists to develop a better turbulent model that compensates for the weaknesses of the k-ε and of the RNG k-ε model. k-Ω is the answer for such an application. It is also a suitable candidate for impinging jet studies where a complex flow boundary layer occurs in the transitional region, as well as in most problems in aerospace applications. To discover and prove which model is the best for

[15] including potential core, characteristic decay, axisymmetric decay, and terminal region

impinging jet studies, the same setting as Poreh's experiment was simulated by using both RNG k-ε and k-Ω. Settings and results are discussed in the following segment.

Full-scale and CFD simulation setting

The experimental setup of Poreh, et al. was conducted on a flat aluminum plate with a radius of 1.75m (69 inches). A two-inch diameter impinging tube was located 0.6m (2ft) above the center of the aluminum plate which supplied an isothermal air jet at room temperature towards it at a velocity of 103m/s (340ft/s). The velocity profiles of the jet distributing along the floor are reported at the different normalized distances. The same setting is repeated by CFD simulation using two turbulent models, RNG k-ε and k-Ω as shown in **Figure 36**. The high nozzle velocity of the full-scale experiment may lead to instability in the CFD simulation. Thus, the Reynolds number (Re) is reduced from $1.96x10^5$ to $1.96x10^4$ for this application by decreasing the supply velocity to 10.3m/s (34f/s). Additional CFD parameters are shown in **Table 4**.

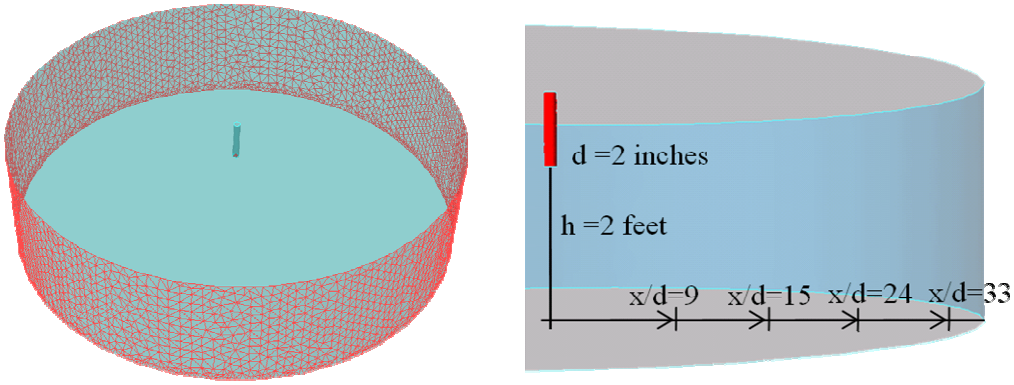

Figure 36 CFD model of impinging jet for comparison with Poreh, et al.

Comparison of full-scale and CFD results

After plotting and observing the normalized velocity profile (U/U_o) from the CFD simulation, varying outcomes result from the different turbulent models. In **Figure 37**, k-Ω produces velocity profiles which dissipate faster and spread wider than the RNG k-ε. The velocity profiles of both turbulent models are compared to the measured data from Poreh, et al. in **Figure 38**. Since the jet velocity profiles of k-Ω fit Poreh's data better, the k-Ω model appears to have a higher accuracy than the RNG k-ε. This finding may improve the accuracy of IJV simulations which are based on the RNG k-ε model previously recommended by Awbi, et al. [13]. Like other turbulent models, k-Ω also has

limitations. The k-Ω model being investigated in this study does still not completely fit the velocity curves of Poreh, et al. because the limitation of k-Ω is in predicting the transition from laminar to turbulent flow near a floor surface [36]. The prediction of the k-Ω model is much improved if velocity is measured far from the nozzle; in this case x/d>33. This reduction of error makes the k-Ω model suitable for ventilation studies because most task areas where velocity and temperature are often monitored are usually located far from the supply terminals. Another way to reduce this error is to implement the nozzle treatment which is discussed in the following section.

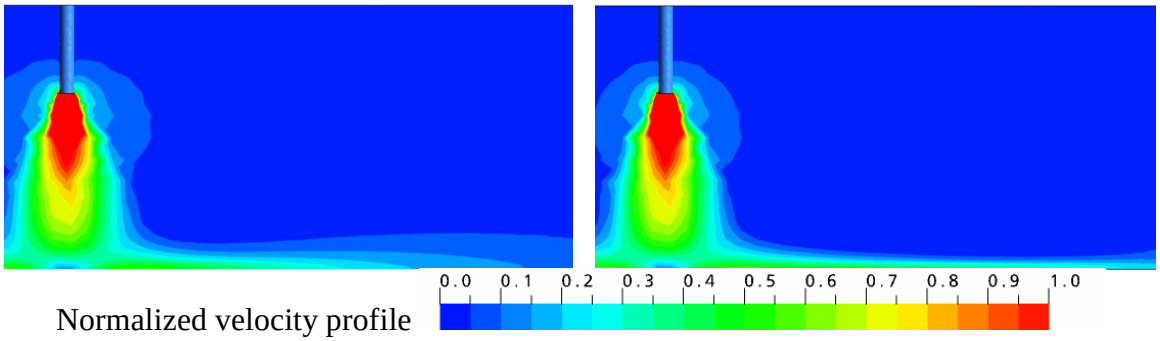

Figure 37 Impinging jet velocity profiles of k-Ω (left) and RNG k-ε (right) model

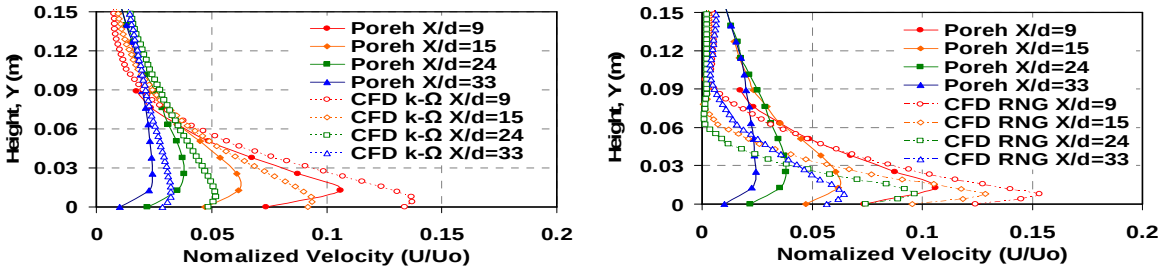

Figure 38 Plots of impinging jet velocity of k-Ω (left) and RNG k-ε (right) model

RADIAL IMPINGING JETS IN ARCHITECTURAL SETTING

The previous study is conducted on a small scale setting where the results differ from the larger scale setting such as in an architectural space. To solve this problem and advance further, both isothermal and buoyant impinging jet (cooling) are set up not only in the HVAC laboratory, but are also modeled in a CFD simulation as shown in **Figure 39** through **Figure 41**. As in the previous test, the results not only demonstrate the behavior of a radial impinging jet, but also prove the validity of CFD simulation. The velocity and temperature profiles of a radial impinging jet (see **Figure 40**) are measured at given nozzle distances in both actual and CFD models in the HVAC laboratory as shown in **Figure 43**. After testing the quality of the CFD model, this laboratory requires 1.5

millions grids to reach grid independency [10, 56]. Then, the k-Ω model showing the greatest accuracy in the previous section is applied. An additional variable which results in more accurate CFD outcomes for both isothermal and non-isothermal conditions is the nozzle velocity profile. A detailed discussion regarding this outcome follows.

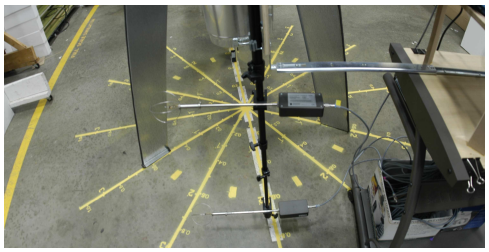

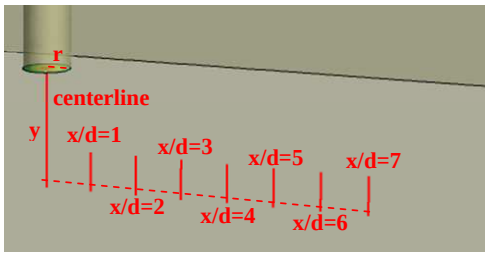

Figure 39 Impinging jet measurement in full-scale HVAC laboratory (left)
Figure 40 Diagram of impinging jet measurement at different nozzle distances (right)

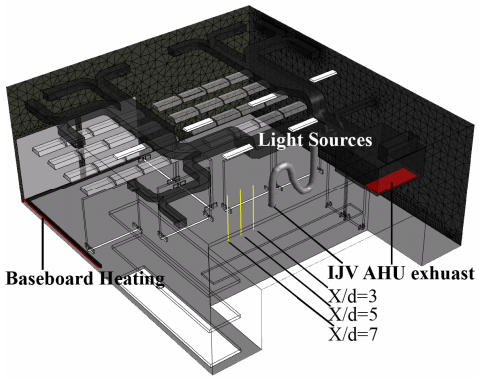

Figure 41 CFD model of full-scale laboratory (left)

Nozzle velocity profiles

With a k-Ω model, the previous study indicates some errors in the velocity profile prediction. Based on past studies of pipe flow [1], nozzle velocity profiles may be the key variable to attain higher CFD accuracy. Two approaches to model velocity profiles are taken; one is the **uniform velocity profile** and the other is the **boundary layer velocity profile** which takes tube friction into account. See **Figure 42** and **Figure 43**.

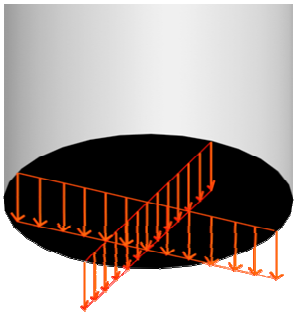

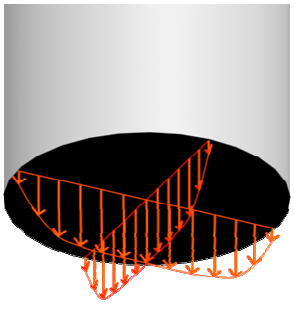

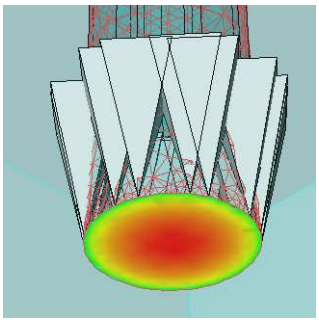

Figure 42 Uniform velocity profile of IJV nozzle (left)
Figure 43 Boundary layer profile of IJV nozzle (mid)
Figure 44 Color plot of boundary layer velocity profile of IJV nozzle (right)

Velocity causes either laminar or turbulent flow in a pipe [1]. Laminar flow occurs (Re<2,000) when velocity in the pipe is low and this increases the slope of the velocity profile. When pipe velocity increases, flow becomes turbulent (Re>4,000) thus making the velocity profile uniform across the section of a pipe. See **Figure 45**. The boundary layer velocity profile is created from **Equation 30** which is commonly used in pipe flow studies. r_{max} is the nozzle diameter; while r is the radius at any given point in a nozzle section. U_o is the maximum velocity at the nozzle center and U is the supply velocity at a given r.

$$U = U_o (1 - \frac{r}{r_{\max}})^{\alpha} \qquad \text{Equation 30}$$

$$a = \sqrt{f} \qquad \text{Equation 31}$$

Equation 31 calculates power factor, α, by using the pipe fiction coefficient (f) which depends on Reynold numbers (Re), pipe index roughness (k), and pipe diameter (D). The relationship can be found in a Moody diagram, as shown in **Figure 46**. The estimated Re is 67,000, while k is 0.6 for a smooth metal surface. At a diameter of 0.3m (300 mm), the relative roughness (k/D) equals to 0.002. Using **Equation 31**, the friction coefficient is 0.28 which gives α=0.167. The results of this equation are shown in **Figure 44** as a color plot on a nozzle where the red color indicates high velocity and the green color indicates low velocity.

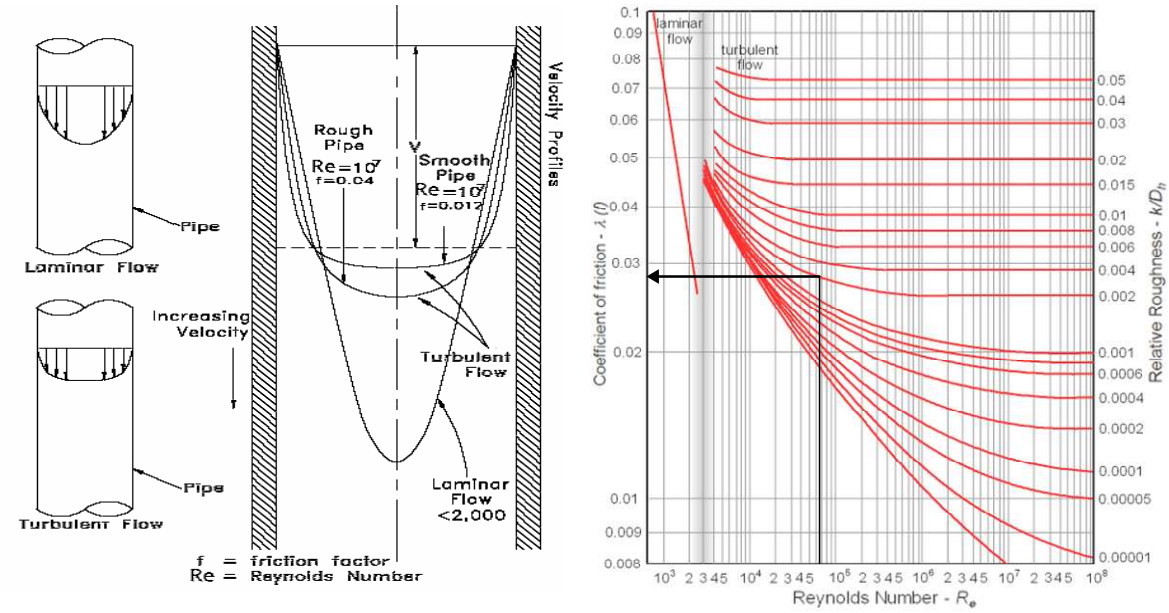

Figure 45 Laminar and turbulent pipe flow (left) [1]
Figure 46 Moody diagram, the friction coefficient of pipe flow (right)

Comparison of CFD and full-scale data of isothermal radial impinging jet

In isothermal testing, a round nozzle diameter of 0.3m (1ft) is fixed at 0.75m (2.5ft) above the floor. A nozzle is placed on a specially built tripod and air is supplied at a velocity of 2.65m/s (8.75f/s) and at the room temperature of 21^{o}C (70^{o}F). The flow characteristics are captured by omni-transducers placed at the various normalized distances. Under steady state condition, each data set is monitored for 20 seconds long, averaged and then compared with the CFD data. In **Figure 47**, the CFD results of both nozzle treatments are plotted. The nozzle with a uniform velocity profile produces a wider jet velocity distribution, especially near the nozzle. After reaching the floor, the velocity of a nozzle with a uniform velocity profile sustains longer and dissipates slower than that of a nozzle with a boundary layer profile.

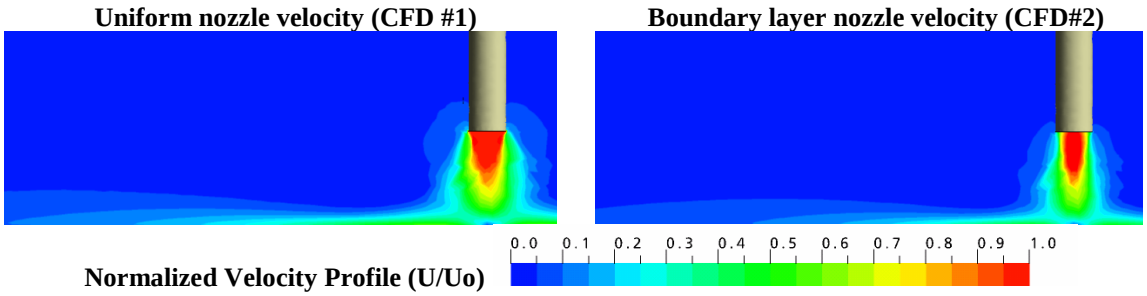

Figure 47 Velocity profiles comparison of different impinging nozzle treatment.

The velocity profiles of different nozzle distances (x/d) are plotted and compared with the results from a full-scale experiment in **Figure 48** where CFD#1 represents a nozzle with a uniform velocity profile and CFD#2 represents a nozzle with a boundary layer profile. Overall, the latter, a nozzle with a boundary layer profile, performs better. When x/d is greater than 5, the CFD results of a nozzle with a boundary layer profile almost match the data measured from the full-scale experiment, while a nozzle with a uniform velocity profile overestimates the normalized velocity at all nozzle distances.

Two common problems which both nozzle treatments fail to predict are the height of jet peak velocity (U_m) in a transitional region where a free jet transforms to a wall jet. In this transitional region (x/d=1), the velocity profile curves predicted by CFD are poor fit for the curves projected from the experimental data. The U_m of full-scale elevates from 0.75 inches at x/d=1 to 2 inches at x/d=7, but both CFD simulations always maintain the height of U_m at 0.5 inches.

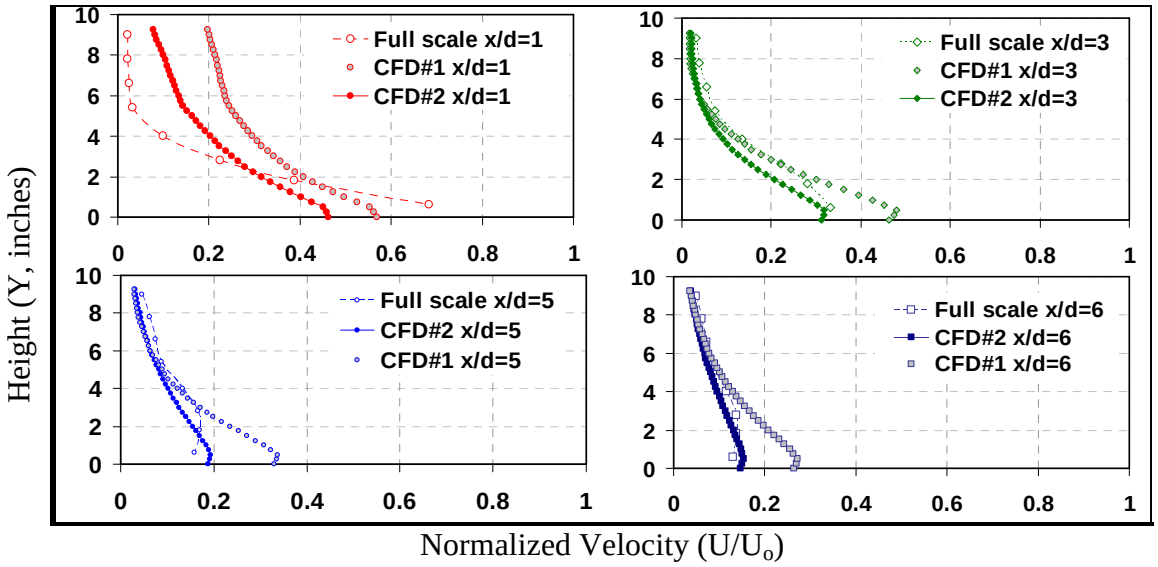

Figure 48 Normalized velocity profiles of CFD and full-scale experiment with different nozzle treatments

When the free jet hits the floor at the stagnation point, the velocity is quickly reduced to zero. This is a unique characteristic of an impinging jet which is noteworthy [72, 73]. **Figure 49** shows the plot of the full-scale data against two CFD simulations. All cases tend to show the same agreement. CFD#1 (uniform velocity profile) conforms closely to the full-scale experiment, while the velocity of CFD#2 (boundary layer profile) dissipates faster than the full-scale.

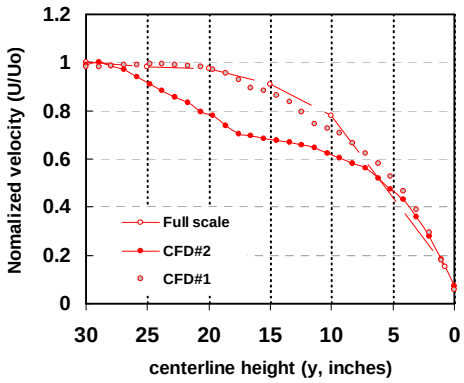

Figure 49 The centerline velocity of CFD with different nozzle treatments and full-scale experiment

Comparison of CFD and full-scale data of buoyant radial impinging jet

Although the previous section demonstrates that the CFD simulation with the appropriate setting can replicate the full-scale experiment with reasonable accuracy, the heat transfer is neglected. Temperature prediction is necessary for thermal comfort analysis, and it must thus be validated. The experiment is conducted in the HVAC-IEQ laboratory operated under the cooling mode by overriding the thermostat function. Located at 0.75m

(2.5ft) height, a nozzle supplied air at a temperature of 13°C (55°F) at 3.15m/s (10.4f/s). The heat gain stems from six fluorescent fixtures and a baseboard heating system. To monitor the HVAC system in the laboratory, temperature sensors are placed in the locations indicated in the HVAC diagram on **Figure 50** (left). Using different color-coding, the time/history data is plotted in **Figure 50**. During the testing period, the outdoor air temperature (red dotted line) rises up to 13°C (25°F), while the supply temperature (dark blue line) holds steady at 13°C (55°F), since it is set. After the room temperature (green line) is constant at 23.7°C (74°F)[16], the measurement is taken within the time period highlighted in orange. In addition to the temperature sensor, an infrared thermography technique is also used to record the surface temperature during the testing period. The surface temperature of the fluorescent fixtures reaches 60°C (140°F) and the surface of the baseboard heater reaches 30°C (86°F) as shown in **Figure 51**. These temperatures are then used for CFD specifications. Based on these experimental data, the HVAC-IEQ laboratory is modeled and then simulated by using CFD. The following section includes a discussion of the results from the full-scale and CFD simulations. These results include the velocity of the isothermal and the buoyant impinging jet, the normalized temperature, and the temperature and velocity at given room heights.

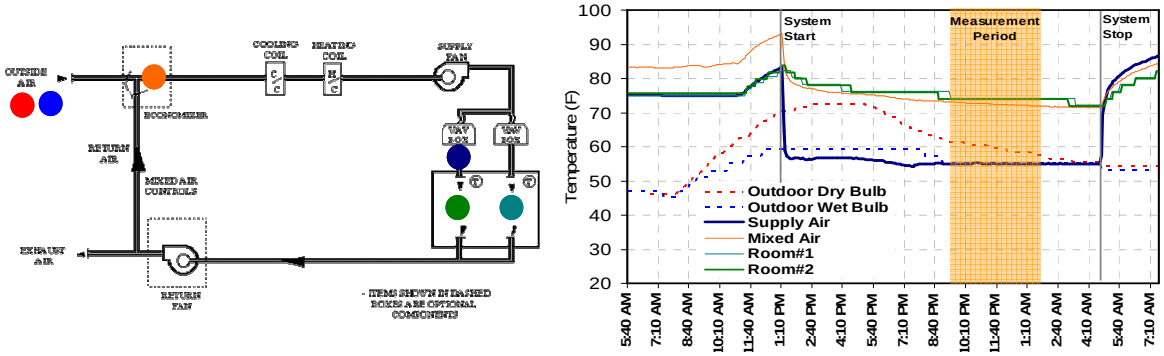

Figure 50 Temperature profiles of HVAC laboratory on the cooling test day

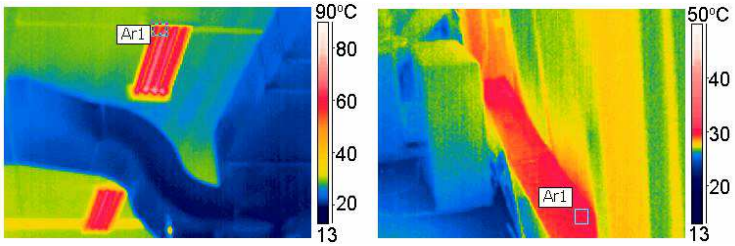

Figure 51 Surface temperature of heat sources, fixture (left) and baseboard heaters (right) taken by infrared camera

[16] This measurement took place at x/d=9 from an IJV terminal at a height of 1.1m.

In **Figure 52**, the color-coded temperature profile is plotted and shows the temperature stratification occurring at approximately 4-6^{o}C (7.2-10.8^{o}F) from floor to ceiling. The cool air dissipates rapidly after the impinging jet reaches the floor. The same distribution is confirmed by the temperature profile recorded using the infrared thermography technique in **Figure 52** (right).

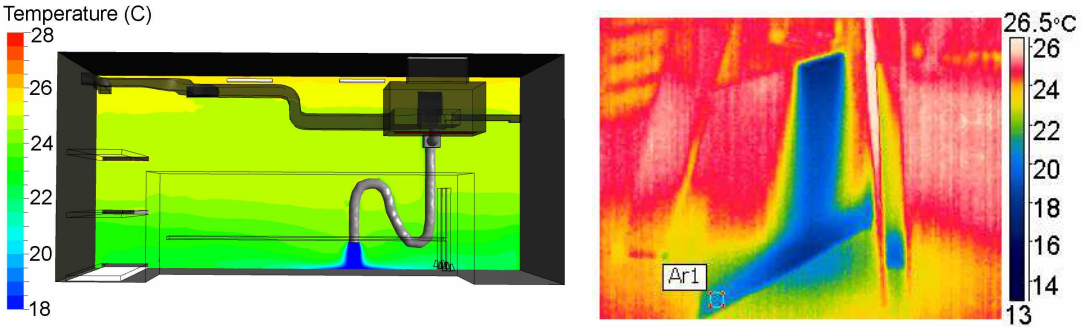

Figure 52 CFD temperature profiles (left) and infrared image of impinging jet in cooling mode (right).

The velocity profile of the isothermal and buoyant impinging jet is compared in **Figure 53**. The examples of the velocity profile at x/d=3 and x/d=7 indicate the similarity between the CFD and experiment results. Since the velocity profile of the isothermal and the buoyant IJV are identical, the velocity distribution of the impinging jet is independent of its supply temperature (in cooling mode).

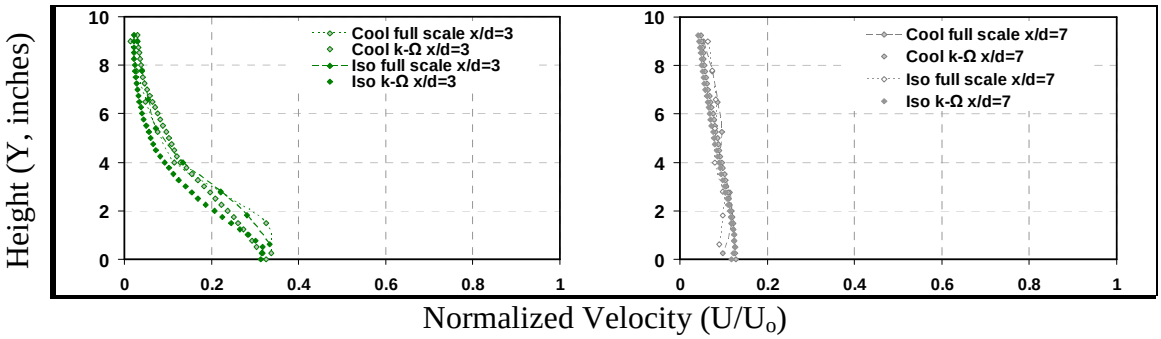

Figure 53 Normalized velocity profiles of CFD and full-scale experiment of isothermal and buoyant impinging jet.

Previously, the k-Ω model accurately predicted the velocity distribution of the IJV system. In this section, this model is used to study the temperature distribution of the impinging jet. The test is made only in the cooling scenario where the cool supply air is gradually mixed with the heat generated by the heat sources. After warming, the cool jet stream completely dissipates and reaches the control temperature. A quick or slow mixing process is determined by the normalized temperature (θ/θ_o). The variables for

calculating the normalized temperature are the reference temperature (T_r), temperature at any given point (T), and the supply temperature (T_s). See the calculation in

Equation 32. In this study, the T_r of 25°C (78°F) is applied. At any given point, if the air temperature almost equals the supply temperature, the normalized temperature is close to one. On the contrary, if the temperature reaches the reference temperature, θ/θ_o approaches zero.

$$\frac{\theta}{\theta_o} = \frac{T_r - T}{T_r - T_s} \qquad \text{Equation 32}$$

In **Figure 54**, the normalized temperature and velocity from the CFD and the full-scale experiment are compared by using the data from x/d=1, x/d=3, x/d=5, and x/d=7. Overall, since the normalized temperature dissipates slower than the normalized velocity does, the maximum normalized temperature (θ_m) is always higher than the maximum normalized temperature (U_m) of 0.2 at all nozzle distances. As with the normalized velocity profile, θ_m occurs close to the surface boundary (floor) and gradually decreases along the room height. For the CFD validation, the error bars due to sensor error are also overlaid in these charts. Like the velocity prediction, CFD fails to predict the temperature profile of the transitional region, x/d=1. Beyond the x/d=3 range, the CFD temperature prediction is within the acceptable error ranges. Based on these results, not only is the velocity, but also the temperature prediction is reasonably acceptable using the k-Ω model.

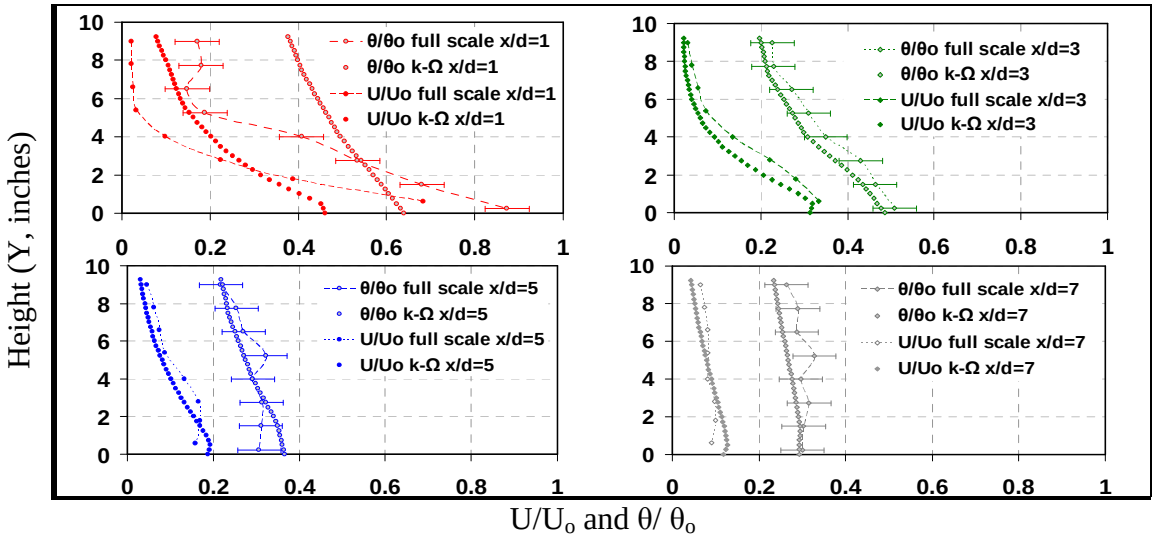

Figure 54 Normalized temperature and velocity profiles of CFD and full-scale experiment

To substantiate the validity of CFD, both the temperature and velocity near the surface boundary, as well as the temperature and velocity from CFD, are compared with the experimental measurements obtained along the room height. See **Figure 55** and **Figure 56**. The data from different selected nozzle distances-x/d=3, x/d=5, and x/d=7- are measured at 0-2.1m (0-7ft). The CFD and experimental data are nearly identical for both temperature and velocity. Accordingly, the CFD sucessfully simulate the temperature and velocity dissipation, not only near the floor, but also accurately along the room height. Based on the recommendations of ASHRAE RP 1133, these results offer critical evidence for the claim that CFD parameters are appropriate for such modeling.

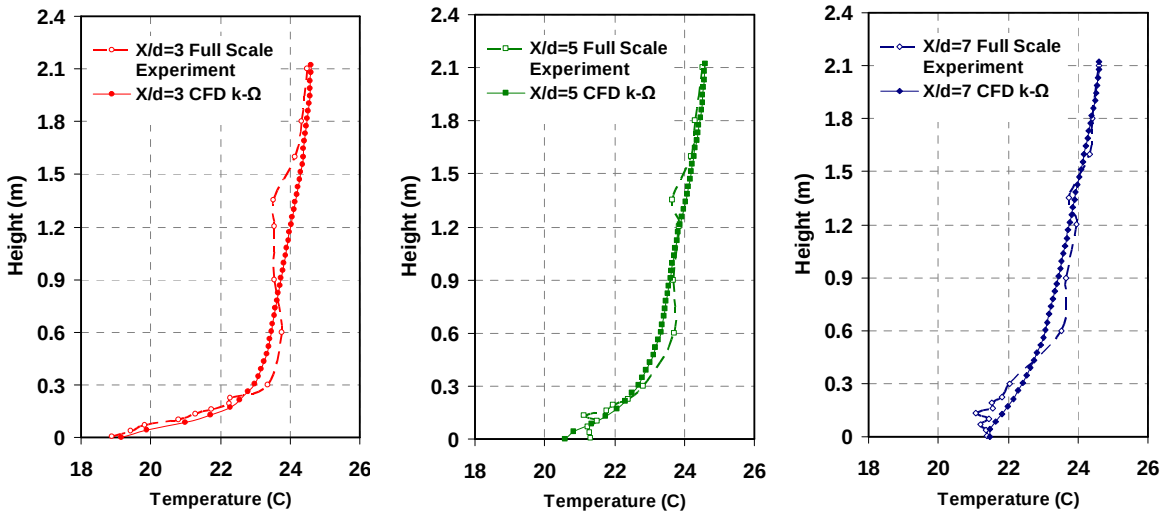

Figure 55 Room temperature profiles of CFD and full-scale experiment of radial IJV in cooling mode

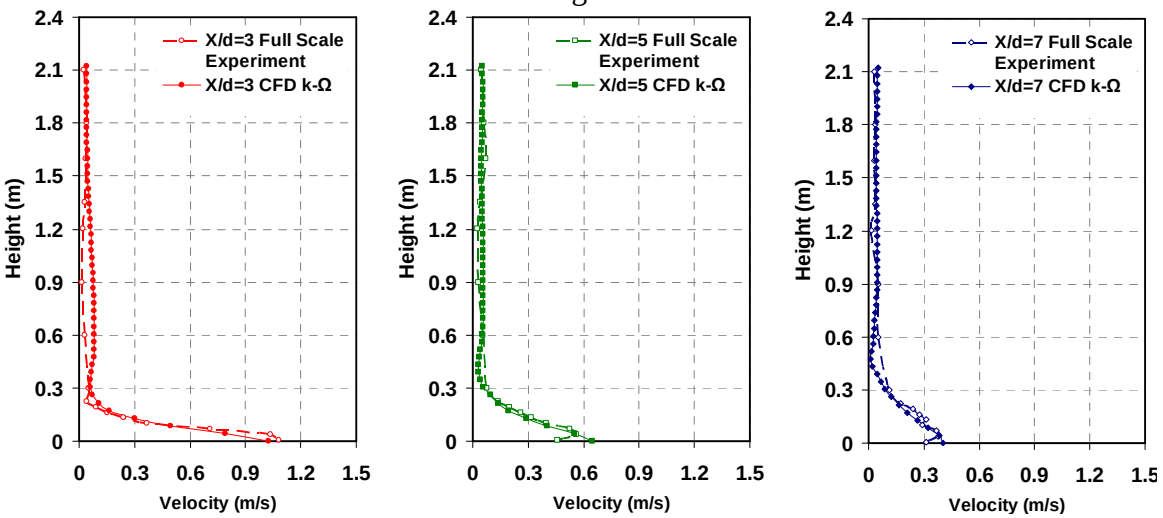

Figure 56 Room velocity profiles of CFD and full-scale experiment of radial IJV in cooling mode

WALL IMPINGING JET IN ARCHITECTURAL SETTING

Unlike a radial impinging jet where is no impact from any side-wall, once a side-wall is mounted to an impinging jet tube, it is categorized as a wall impinging jet. Previously studied by Karimipanah and Awbi, a wall impinging jet is tested in a full-scale experiment [21]. In their study, the measurements are made at three angles-30, 60, and 90 degrees- using a nozzle as the mid-point as shown in **Figure 57**. Then measurement points are placed at the normalized distances ($x/\sqrt{A}$) of 3.5-9.25. A supply velocity (U_o) of 1.6m/s (5.3f/s) at 18^{o}C (64^{o}F) is provided from a rectangular nozzle. This nozzle has a free area of 0.1sq.m. (1sq. ft) and is located above the floor at ranges from 0.3-1.0m (1-3.3 ft). The peak (U_m), half ($U_{1/2}$) jet velocity and jet spread angle ($Y_{1/2}/\sqrt{A}$) are recorded. The same experimental setup as Karimipanah, et al. is adopted in this study. In a variation from Karimipanah, et al., a rectangular nozzle is replaced by a round nozzle 1ft (0.3m) diameter. In order to study the wall effect, this study also adds an extra measurement angle of 0 degrees (parallel to the side-wall). The supply temperature is lowered to 13^{o}C (55^{o}F) and the velocity is increased to 3.4m/s. Both CFD and experimental data are compared in the following section.

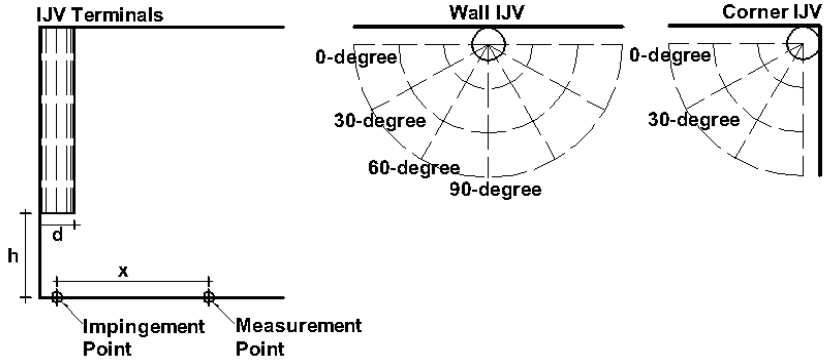

Figure 57 Experimental setup and sensor layout

Comparison of CFD and full-scale data of buoyant wall impinging jet

The results in **Figure 58** compare the velocity profiles of CFD and the full-scale experiment conducted in this study with the velocity profiles measured by Karimipanah, et al. (indicated by the bright green and orange dots). The normalized distances of x/d=3 and x/d=7 are shown in the left and right column, respectively. The results indicate that the strongest velocity measured is near and parallel to the wall (at 0 degrees). The U/U_o at 0 degrees reaches 0.2 at x/d=7, while the U/U_o at the other points (30, 60, 90 degrees) are less. Additional momentum may be the reason for the high velocity measured at 0

degrees. Blocked by the side-wall, the remaining momentum forces the redirection of its course and increases the jet momentum along the side-wall.

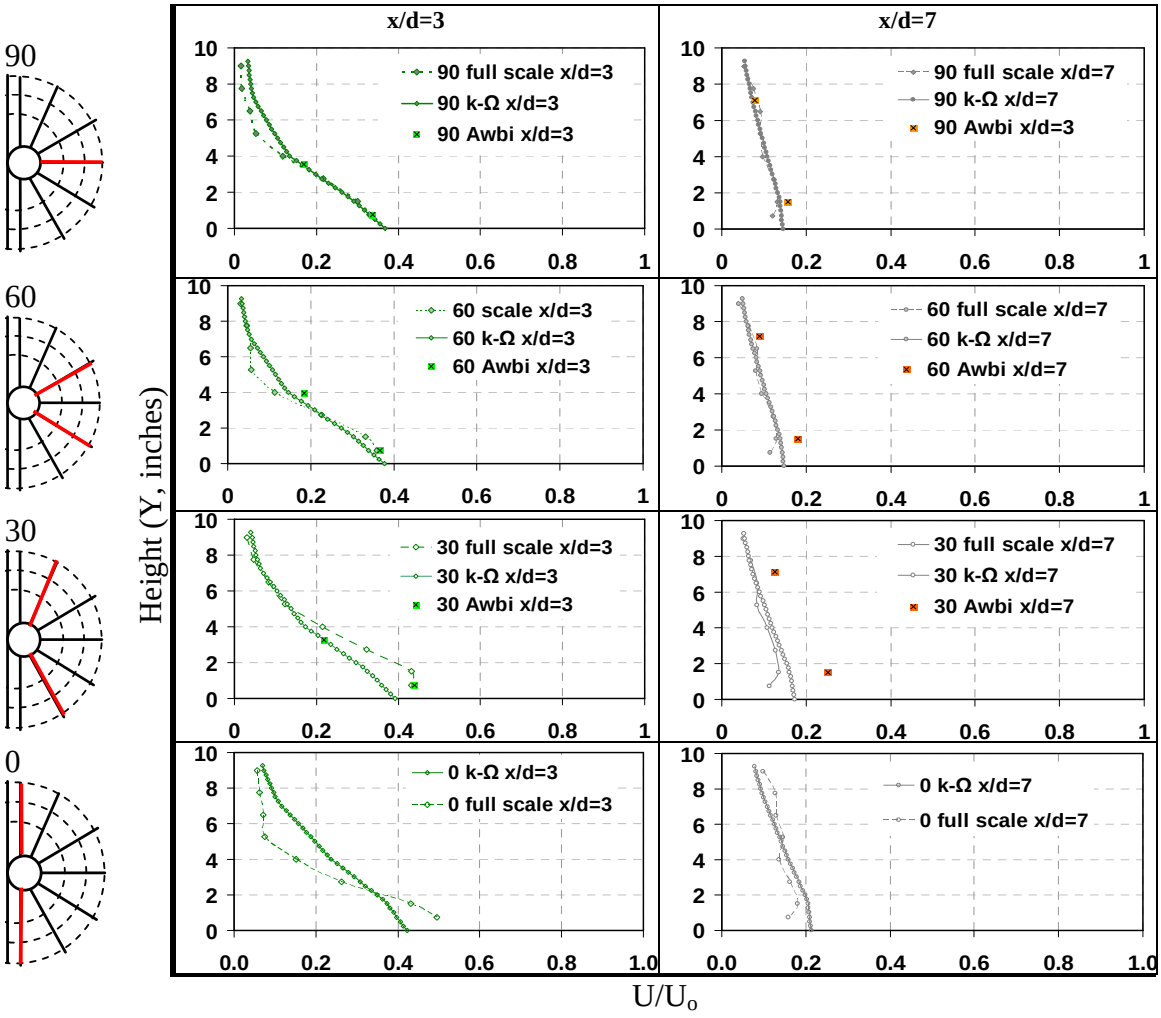

Figure 58 Normalized velocity profiles of wall impinging jet

Since the CFD and full-scale data show agreement, CFD parameters such as grids resolution, turbulent models and others are appropriate for further studies. The turbulent model, k-Ω, is suitable not only for a radial impinging jet, but also for a wall impinging jet. Given that only peak and half jet velocity data is available from Karimipanah, et al., the same concurrence is found in two out of the three measurement angles-90 degree and 60 degree. With the 30 degree, the velocity data presented by Karimipanah, et al. exceeds that found in this study. The velocity difference may stem from the use of different nozzle shapes or from experimental error.

In Awbi's experiment, the rectangular nozzle is used, whereas in this study the round nozzle is used. The effect of nozzle shape has been studied by Rajaratnam and Pani who have conducted experiments with circular, square, rectangular, and elliptical nozzles using a 3D wall jet. The setting of the nozzles of a wall impinging jet and of a 3D wall jet are similarly attached to a side-wall, and thus the initial jet structure of both jets is alike. An additional element of the wall impinging jet differing from that of the 3D wall jet is the opposite floor facing the impinging jet nozzle. Based on the 3D wall jet diagram in **Figure 59**, Rajaratnam and Pani conclude that the normalized centerline velocity (U_{mo}/U_o) and spreading rate (b_y/h) of a 3D wall jet are similar for all nozzle shapes [76]. **Figure 60** shows the normalized centerline velocity decays of different nozzle shapes which are almost identical and **Figure 61** demonstrates that the jet spreading rate of different nozzle shapes along the y axis is also similar. Because of these similarities in 3D wall jet study, the jet structure of a wall impinging jet supplied with different nozzle shapes makes no significant difference.

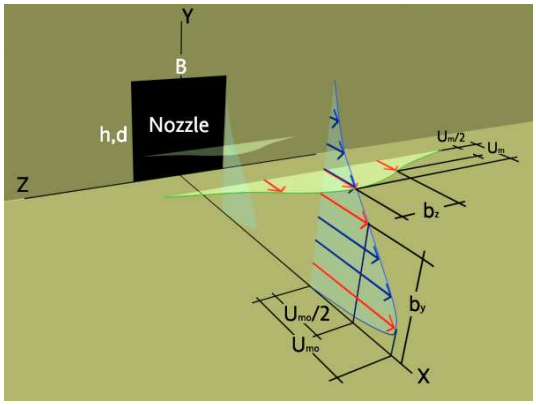

Figure 59 3D wall jet variables (top left)

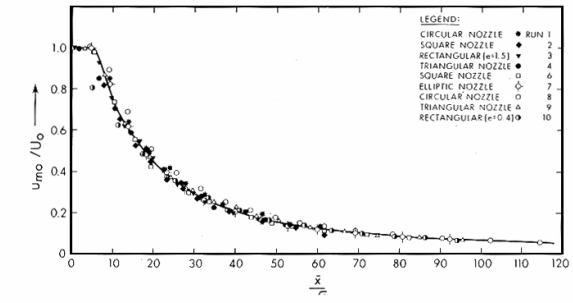

Figure 60 3D wall jet centerline velocity decay (top right) [76]

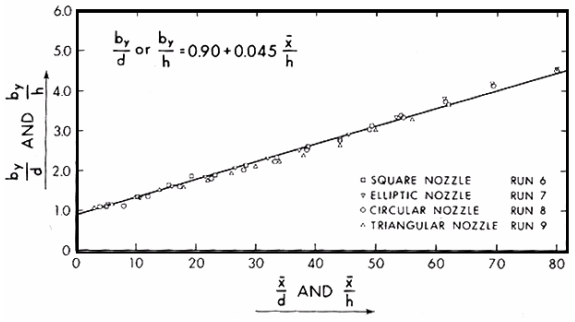

Figure 61 3D wall jet spread angle of Y axis (bottom right) [76]

Studies by Zhao, et al. also using a radial impinging jet with different nozzle shapes, likewise concluded that the nozzle shapes, whether square, circle, or ellipse, have no significant impact on the impinging jet structure [77]. Because of this finding, the differing velocity profiles at the 60 degree angle of the present study and of the

Karimipanah, et al. studies may, in fact, arise from measurement error stemming from sensor accuracy, calibration process, measurement repeatability, etc.

Besides the velocity profile, the temperature profile is also important for the impinging jet analysis. Because the study conducted by Karimipanah, et al. does not discuss the temperature distribution of a wall IJV, this present study will therefore undertake to address this gap in the research. See **Figure 62**. Like the velocity profile, the results indicate a close agreement between CFD and full-scale data. Unlike the velocity profile where a wall has a strong impact, temperature distribution dissipates similarly in all measured angles. Overall, the peak normalized temperature at x/d=3 starts at 0.7 and declines to 0.4 at x/d=7.

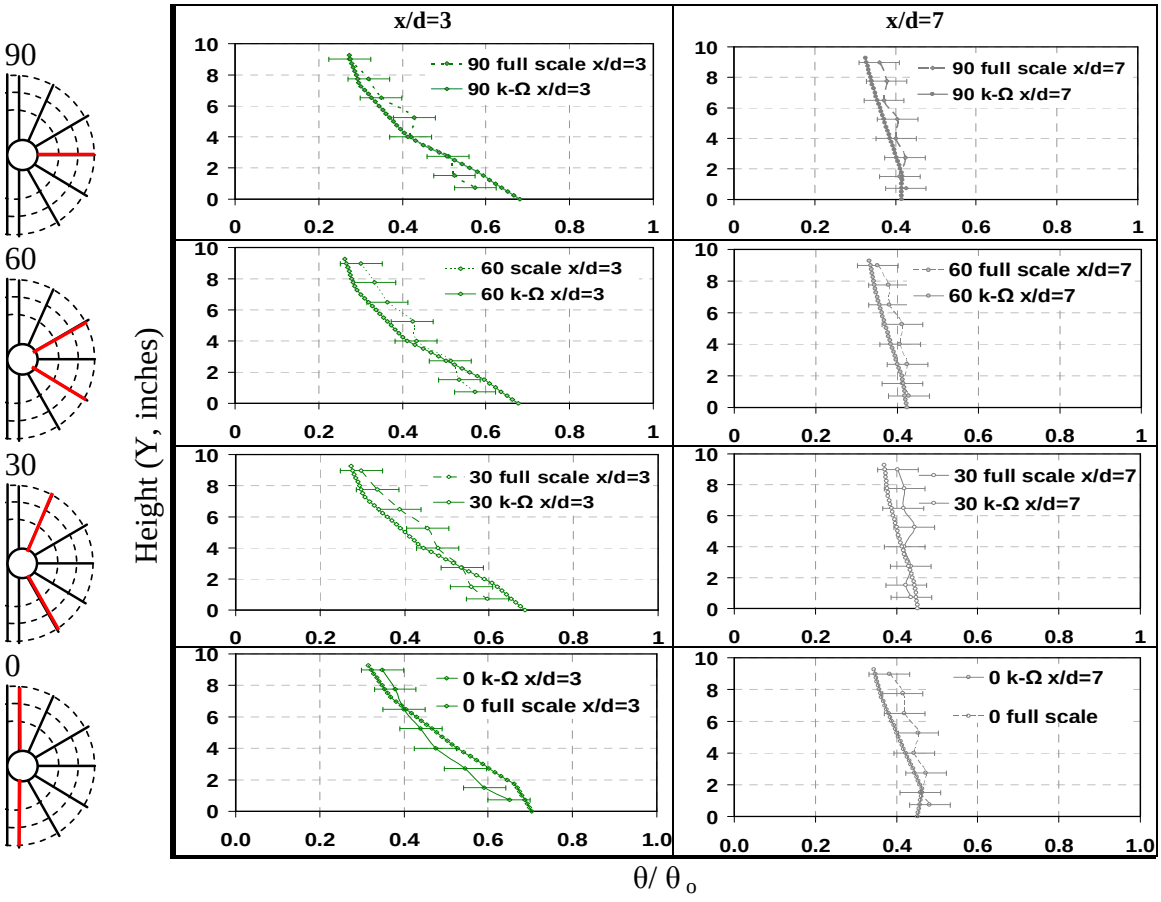

Figure 62 Normalized temperature profiles of wall impinging jet

CORNER IMPINGING JET IN ARCHITECTURAL SETTING

A corner impinging jet may be suited for many architectural spaces. Unlike the radial and wall impinging jets, a corner impinging jet is affected in a greater way by walls. The side

walls keep the jet velocity dissipating from the corner towards the central room space. Instead of having a 360 degree distribution like a radial IJV, a corner IJV only has room for a 90 degree distribution in a typical room corner. As a result, the jet momentum is more intense and the velocity is stronger.

Comparison of CFD and full-scale data of buoyant corner impinging jet

The normalized velocity of a corner impinging jet using both full-scale and CFD simulation is plotted in **Figure 63**. At a 0 degree angle the jet profile is parallel to the wall, while at a 30 degree angle the jet is measured towards the center. Like the wall IJV, the side walls increase the velocity of the 0 degree more than that of the 30-degree. CFD and full-scale data are generally similar, except when x/d is less than or equal to 3.

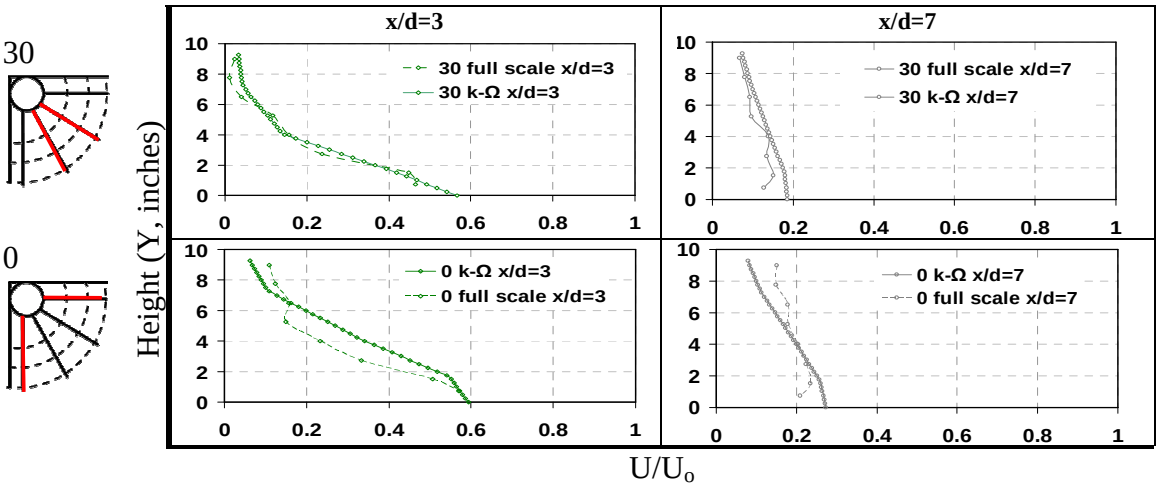

Figure 63 Normalized velocity profiles of corner impinging jet

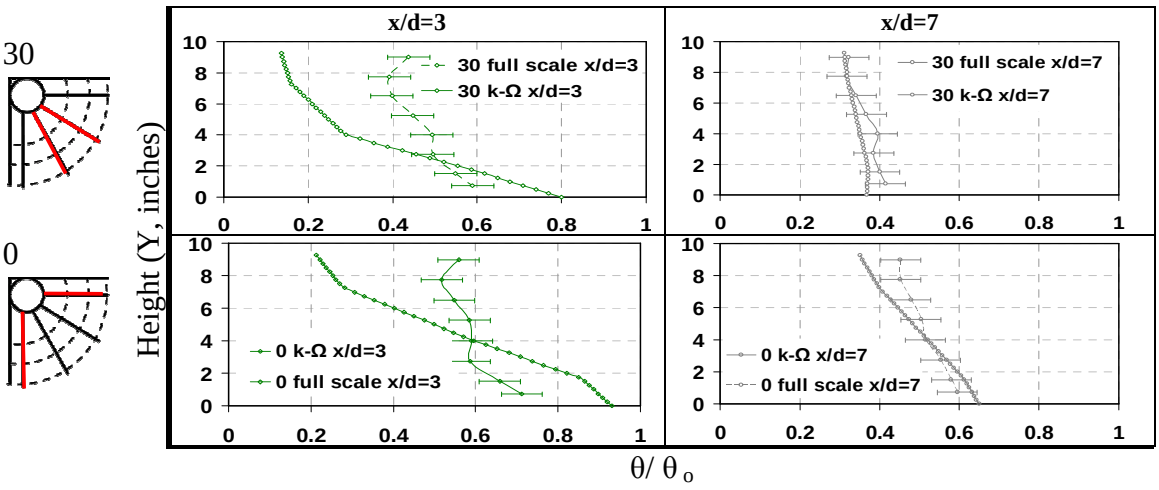

Figure 64 Normalized temperature profiles of corner impinging jet

Figure 64 shows the normalized temperature profiles of a corner impinging jet with data from both CFD and a full-scale experiment. Analogous to the normalized velocity profile,

the temperature also dissipates slower than the radial and wall impinging jets do. Large error is found in the near field (x/d=3), but then it gradually decreases and shows close correlation in far field (x/d=7). The cause of CFD error may lie in the effects of the measured distances and in the effects of both a floor and side-wall. Similar to the velocity profile, a larger error gap of the normalized temperature profile is found when measuring parallel to the wall at 0 degrees.

IJV WITH DIFFERENT TERMINAL HEIGHTS

Aside from the nozzle locations, the terminal height may affect impinging jet characteristics. In the previously-mentioned study by Karimipanah, et al., only the terminal height at 0.75m (2.5 ft) is studied. Two additional terminal heights, 0.30m (1.0 ft) and 1.05m (3.5 ft) are added in this section.

Supply height has a small impact on both velocity and temperature distribution. The normalized velocity and temperature of IJV with varying terminal heights are plotted in **Figure 65**. When supplying at an elevated height, velocity decays somewhat slower, while the temperature decays faster. When moving the nozzle towards the floor, the friction increases; thus, the velocity is reduced. Unlike velocity, temperature distributes with less friction. Cool supply air penetrates more deeply if the nozzle is moved closer to the floor. These findings are numerically confirmed by comparing both full-scale and CFD simulations as shown in **Figure 66**.

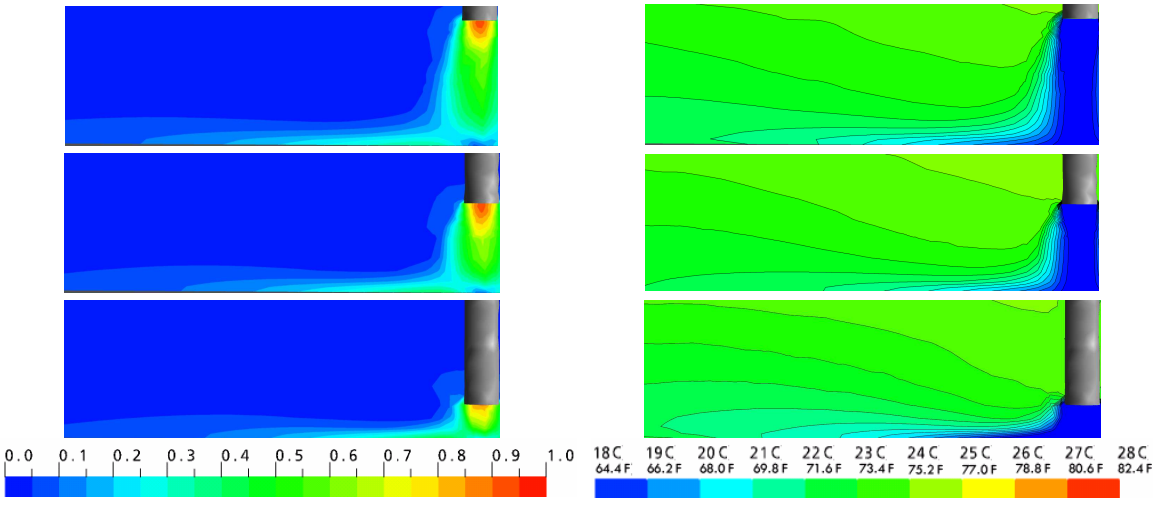

Figure 65 Normalized velocity and temperature of IJV with different heights

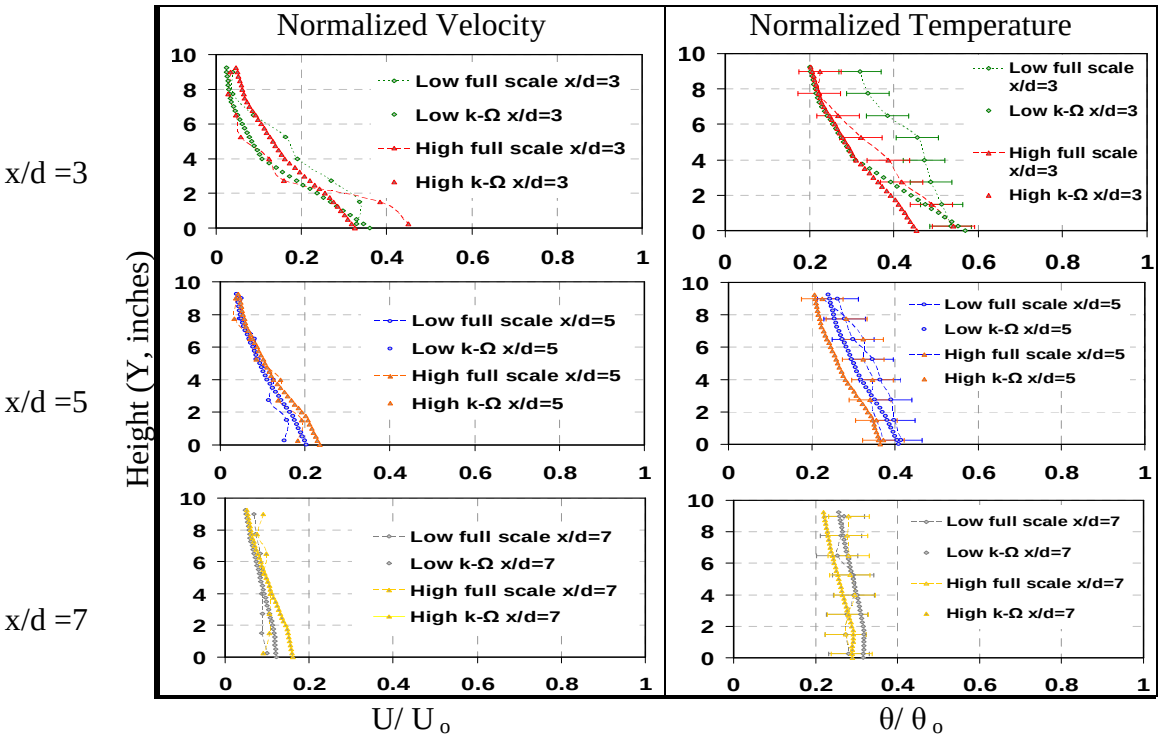

Figure 66 Normalized velocity profiles and temperature of IJV at different heights

After completing the parametric simulations, models are proposed predicting the peak normalized velocity (U_m/U_o) and the normalized jet spread ($y_{1/2}/d$) depending on the normalized distance (x/d). These variables are described in the impinging jet diagram as shown in **Figure 35**. **Table 13** and **Table 14** conclude the predictive models of the radial, wall, and corner IJV with different measured angles and terminal heights, respectively.

$$\frac{U_m}{U_o} = A\left(\frac{x}{d}\right)^B$$

Angle	90-degree		60-degree		30-degree		0-degree	
	Radial Impinging Jet							
Constant	*A*	*B*	*A*	*B*	*A*	*B*	*A*	*B*
H = 0.30m	1.066	-1.767	N.A.	N.A.	N.A.	N.A.	N.A.	N.A.
H = 0.75m	0.888	-1.027	N.A.	N.A.	N.A.	N.A.	N.A.	N.A.
H =1.05m	0.708	-0.824	N.A.	N.A.	N.A.	N.A.	N.A.	N.A.
Constant	**Wall Impinging Jet**							
H = 0.30m	1.265	-1.252	1.463	-1.384	1.397	-1.161	1.255	-0.892
H = 0.75m	1.111	-1.068	1.176	-1.089	1.091	-0.973	0.987	-0.794
H =1.05m	0.844	-0.837	0.882	-0.870	0.839	-0.767	0.808	-0.699
Constant	**Corner Impinging Jet**							
H = 0.30m	N.A.	N.A.	N.A.	N.A.	2.241	-1.294	1.526	-0.905
H = 0.75m	N.A.	N.A.	N.A.	N.A.	1.854	-1.115	1.45	-0.896
H =1.05m	N.A.	N.A.	N.A.	N.A.	0.936	-0.657	0.696	-0.379

Table 13 Predictive model for normalized peak velocity of IJV

$\frac{y_{1/2}}{d} = C\left(\frac{x}{d}\right) + D$								
Angle	90-degree		60-degree		30-degree		0-degree	
	Radial Impinging Jet							
Constant	*C*	*D*	*C*	*D*	*C*	*D*	*C*	*D*
H = 0.30m	0.115	-0.170	N.A.	N.A.	N.A.	N.A.	N.A.	N.A.
H = 0.75m	0.113	-0.150	N.A.	N.A.	N.A.	N.A.	N.A.	N.A.
H =1.05m	0.057	-0.158	N.A.	N.A.	N.A.	N.A.	N.A.	N.A.
Constant	**Wall Impinging Jet**							
H = 0.30m	0.115	-0.101	0.099	-0.062	0.078	0.033	0.065	0.129
H = 0.75m	0.083	0.035	0.079	0.030	0.057	0.137	0.052	0.247
H =1.05m	0.052	0.177	0.034	0.286	0.031	0.299	0.026	0.38
Constant	**Corner Impinging Jet**							
H = 0.30m	N.A.	N.A.	N.A.	N.A.	0.078	0.026	0.057	0.165
H = 0.75m	N.A.	N.A.	N.A.	N.A.	0.057	0.137	0.052	0.246
H =1.05m	N.A.	N.A.	N.A.	N.A.	0.026	0.287	0.026	0.293

Table 14 Predictive model for normalized jet spread of IJV

Table 13 is used for maximum jet velocity prediction, while **Table 14** is used for jet spread prediction. For example, in order to predict the corner IJV at a 0.3m (1ft) height at a 30 degree angle, a constant A of 1.397 and a B of -1.161 can predict U_m/U_o. A constant C of 0.078 and a D of 0.033 can then predict $y_{1/2}/d$. See the highlighted cells in **Table 13** and **Table 14**.

SUMMARY

In this chapter, predictive models for radial, wall and corner impinging jets are not the only outcomes. Parameters for accurate CFD simulation of an IJV system are also described. The turbulent model and nozzle velocity profile are the key parameters for an impinging jet simulation. The turbulent model, k-Ω, and a nozzle with a boundary velocity profile provide the most satisfactory accuracy. By using these CFD parameters, placements and heights of an impinging tube are simulated. The resulting predictive models are validated by the experimental data. Based on these models, the velocity and the jet spread of an impinging jet are strongly impacted by the measured distances and by the side walls. These findings and acquired CFD parameters are used in the next chapter which discusses the effect of a terminal configuration of an IJV system in detail.

CHAPTER 4

NOZZLE TREATMENTS AND TERMINAL CONFIGURATIONS OF IMPINGING JET SYSTEM

Results in the previous chapter show that the placement of supply terminals may affect airflow parameters such as temperature and velocity profiles. Placement of supply terminals is only one aspect among many terminal configurations. Understanding the IJV terminal configurations and their impacts are the second objective of this dissertation and will be discussed in this chapter. CFD simulation which relies on validated CFD parameters obtained from the previous chapter is the main research tool for this chapter.

SETUP OF CFD SIMULATION

A medium-size space is chosen as a case study. The layout and CFD model are shown in **Figure 67**. This case study is located in the northern hemisphere (U.S.) with south facing glass. The cooling load generated by external sources (glass, wall, and roof) and internal sources (humans and appliances) reaches 116 W/m^2. The direct solar radiation measured before hitting the south window glass is at 600 W/m^2, and then, using the Solar Heat Gain Coefficient (SHGC) of 0.43, it is reduced to 250 W/m^2 (290 W/m^2 after accounting for conduction) after passing through the glass. The pollutant, CO_2, is assumed to be produced by human exhalation. The CFD input parameters are summarized in **Table 15**.

Sources	Load/unit	Amount	Load
Thermal Load (q)			
Glass	290 W/M^2	20 M^2	5,800 W
Light	60 W/unit	8 units	480 W
Human heat	75 W/people	2 people	150 W
Total Cooling Load			**6,430 W**
Humidity (W_p)			
Human vapor	2.7x10^{-5}kg/s	2 people	**5.4x10^{-5}kg/s**
Pollution (M_p)			
Human CO_2	0.77 x10^{-5}kg/s	2 people	**1.5x10^{-5}kg/s**

Table 15 Load calculation summary for the study of IJV terminal configurations

This chapter divides the IJV terminals' study into two aspects. First, the nozzle treatments with different velocity profiles are investigated once again since, as suggested

in the previous chapter, they are a critical parameter for accurate CFD simulation. This time, the investigation is not concerned with the impinging jet profile but rather shifted toward the thermal comfort and IAQ. Unlike the nozzle velocity profile, the second aspect examines the impact of terminal configurations like nozzle size, height, tilted angle, location and grills. These terminal configurations and the nozzle velocity profiles are then tested against relevant indices like ventilation effectiveness, CFD ventilation performances and PMV-PPD.

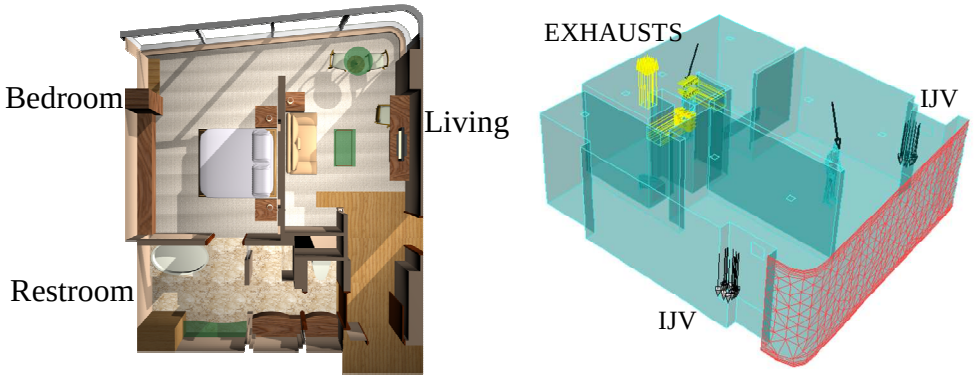

Figure 67 Case study space plan (left) and CFD model (right)

Nozzle treatments with different velocity profiles

An IJV nozzle is treated as an "inlet" in CFD-inputted parameters. When the supply velocity is specified, the default usually assumes that the velocity is uniform throughout the area of a given inlet. As proved in the previous chapter, a uniform velocity profile is not appropriate for jet velocity profile studies. For greater accuracy, a boundary layer profile is the solution. On the negative side, the setting of a boundary layer profile is complicated because it requires additional mathematical functions. When a boundary layer is applied, the velocity at any given point within the supply area is no longer uniform. Velocity gradually increases from zero near a nozzle edge and reaches a peak at the center. See the difference between both nozzle velocity profiles in **Figure 68**. Through the different nozzle velocity profiles, the jet profiles along the floor are impacted. Whether this impact will similarly occur to room thermal comfort and IAQ is the question.

Figure 68 IJV nozzle uniform (left) and boundary layer velocity profiles (right)

Mathematical functions are required for specifying the nozzle boundary layer profile. Unlike in the previous chapter, the nozzle shape changes from a circle to a rectangle. The function for a circular nozzle as shown in **Equation 30** must be modified for a rectangular nozzle. For any rectangular nozzle, **Equation 33 is used** with x and y being the distances along the x and y axis measured from the center. If x_{max} and y_{max} are the maximum distances measured from the nozzle center, the width and length of the nozzle are $2x_{max}$ and $2y_{max}$, respectively. The constant to adjust the velocity boundary curve, α., of 0.167[17] is specified. U_o is the maximum velocity at the nozzle center and U which is the velocity at any point in the nozzle cross section is the product of **Equation 33**.

$$U = U_o (1 - \frac{x}{x_{max}})^{\alpha} (1 - \frac{y}{y_{max}})^{\alpha} \qquad \text{Equation 33}$$

In the CFD specification process, flow rate is easily determined by using the ventilation requirement in **Equation 2**-**Equation 4** as presented in Chapter 2. As a required CFD input, the supply velocity of a nozzle with a uniform velocity profile is easily obtained by dividing the flow rate by the nozzle area. On the other hand, to specify the supply velocity of a nozzle with a boundary layer profile is not a simple activity. In this case, U_o is the required unknown variable in the CFD simulation. The process of solving U_o is presented in **Equation 34** and **Equation 35**. If assuming the flow rate of both nozzles with different profiles is equal, then, the flow rate of a nozzle with a uniform velocity of $4Ux_{max}y_{max}$ equals the integration of **Equation 33,** which is plugged into **Equation 34**. After solving **Equation 34**, **Equation 35** is the function that solves the U_o of a nozzle with a boundary velocity profile. In this study, the $2x_{max}$ and $2y_{max}$ are 1 ft and α equates to 0.167. If the U of the uniform velocity profile is 1.8 m/s, the U_o of the boundary layer profile is 2.5 m/s which is then used as an input in the CFD simulation.

$$4Ux_{max}y_{max} = 4\iint U dxdy = 4U_o \int_{X_{max}}^{0} \int_{Y_{max}}^{0} (1 - \frac{x}{x_{max}})^{\alpha} (1 - \frac{y}{y_{max}})^{\alpha} dxdy \qquad \text{Equation 34}$$

$$4Ux_{max}y_{max} = 4\iint U dxdy = 4U_o (\frac{x_{max}y_{max}}{(\alpha+1)^2}) \qquad \text{Equation 35}$$

Parametric study of IJV terminal configurations

As previously discussed, the nozzle velocity profile changes the supply condition by mathematical manipulation. The physical setting of the IJV terminals is another variable

[17] More detailed explanations are found in Chapter 3 (**Figure 45**)

that significantly changes the initial supply conditions. Once a supply condition is changed, room comfort and the IAQ may be affected. To understand the impact of the physical setting of the IJV terminals, six IJV configurations as shown in **Figure 69** are tested by using Variable Air Volume (VAV) with a supply temperature of 13^{o}C (55^{o}F) from two IJV terminals. Six terminal configurations are tested under the same cooling, humidity, and pollutant loads in the the same case study room used in the investigation in the previous section. Detailed explanations of each configuration to be tested are described as follows:

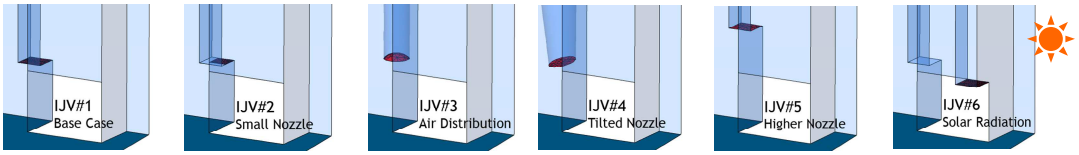

Figure 69 Six physical settings of IJV terminal configurations

Base Case (IJV#1)-For this study, the setup was similar to the nozzle with a uniform velocity profile as discussed previously. A rectangular supply terminal with an area of 1 ft^2 (1ftx1ft) is located above the floor at 0.75 m (2.5 ft).

A Small Nozzle (IJV#2) increases the supply velocity by rushing the air through the small supply area. Once the supply velocity increases, room thermal comfort and the IAQ might be directly impacted. In this scenario, the same configurations as the base case are used except that the area of the nozzle is reduced by half which then doubles the supply velocity.

Air Distribution (IJV#3) here refers to the flow pattern or air directionality which usually changes when employing the supply diffusers or grills. A supply diffuser is an important component for preventing draft caused by a typical mixing system. Once activated, a diffuser alternates air distribution whichever ways the designers wish. For this study, the diffuser shown in **Figure 70** is used. This diffuser is designed to lessen the spread of cool air along the floor so that stratification discomfort should be hindered.

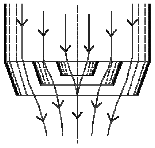

Figure 70 IJV with supply grill to alternate air distribution

Tilted Nozzle (IJV#4) refers to the angle between a nozzle and a floor. The IJV with a nozzle perpendicular to a floor is typical, but a non-perpendicular or tilted nozzle is

however rarely discussed. A tilted nozzle changes the supply air direction as a whole toward the tilted direction. A tilted angle of 15 degrees toward the wall aims the nozzle simultaneously at both wall and floor. As with the IJV#3, this setting should lessen stratification discomfort and draft.

Height of a nozzle (IJV#5) was studied in the previous chapter for the impinging jet characteristics. The findings show that a higher elevation slightly increases the jet peak velocity along the floor. This characteristic affects room thermal comfort and the IAQ more than anticipated. To study this impact, the nozzle height is moved from 0.75 (2.5ft) to a height of 1.2m (4ft).

Location of a nozzle (IJV#6) may strongly affect the performances of the IJV system, especially where radiation through glass is concerned. When the room is radiated, the floor close to the glass is usually heated first by the high sun. By placing a nozzle close to or away from the glass, the cool supply air encounters different floor temperatures rising from shaded or unshaded areas. After the supply and room air is mixed, the room thermal comfort and the IAQ may vary extremely. In order to examine the effects of glass radiation, the same nozzle as in the base case is relocated closer to the south-facing window glass.

SIMULATION RESULTS

The simulation results are reported in two parts. First, the temperature, normalized CO_2, and velocity along the room height of the nozzles, each with different velocity profiles, are presented in **Figure 71**. This data is obtained from measurements at the center of the room as shown in **Figure 72**.

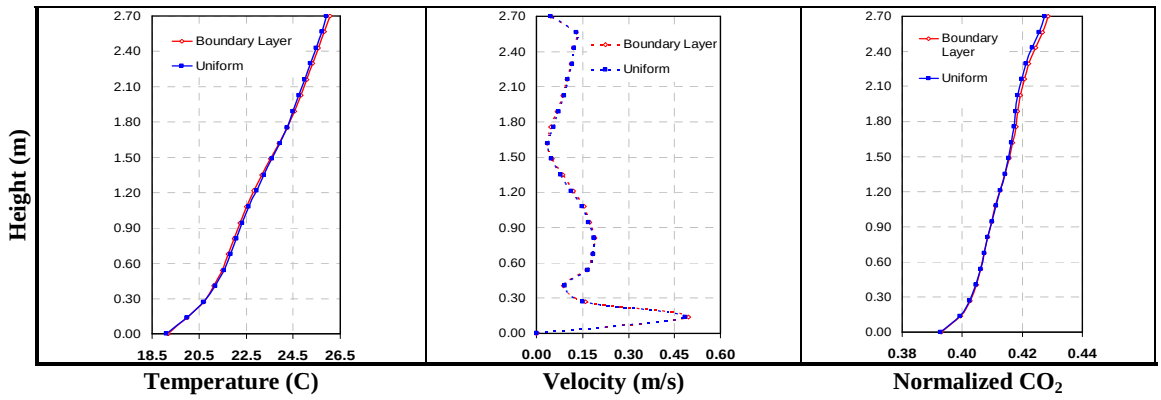

Figure 71 Temperature (left), velocity (mid), and normalized CO_2 (right) along the room height of different supply velocity profiles

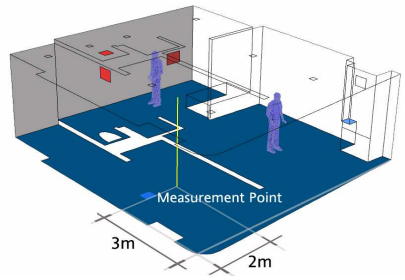

Figure 72 Measurement location for comparing the results from IJV with different velocity profiles

Second, results of IJV with different terminal configurations are plotted on a cross section of a case study room. Such results as shown in **Figure 73** include profiles of temperature and normalized CO_2.

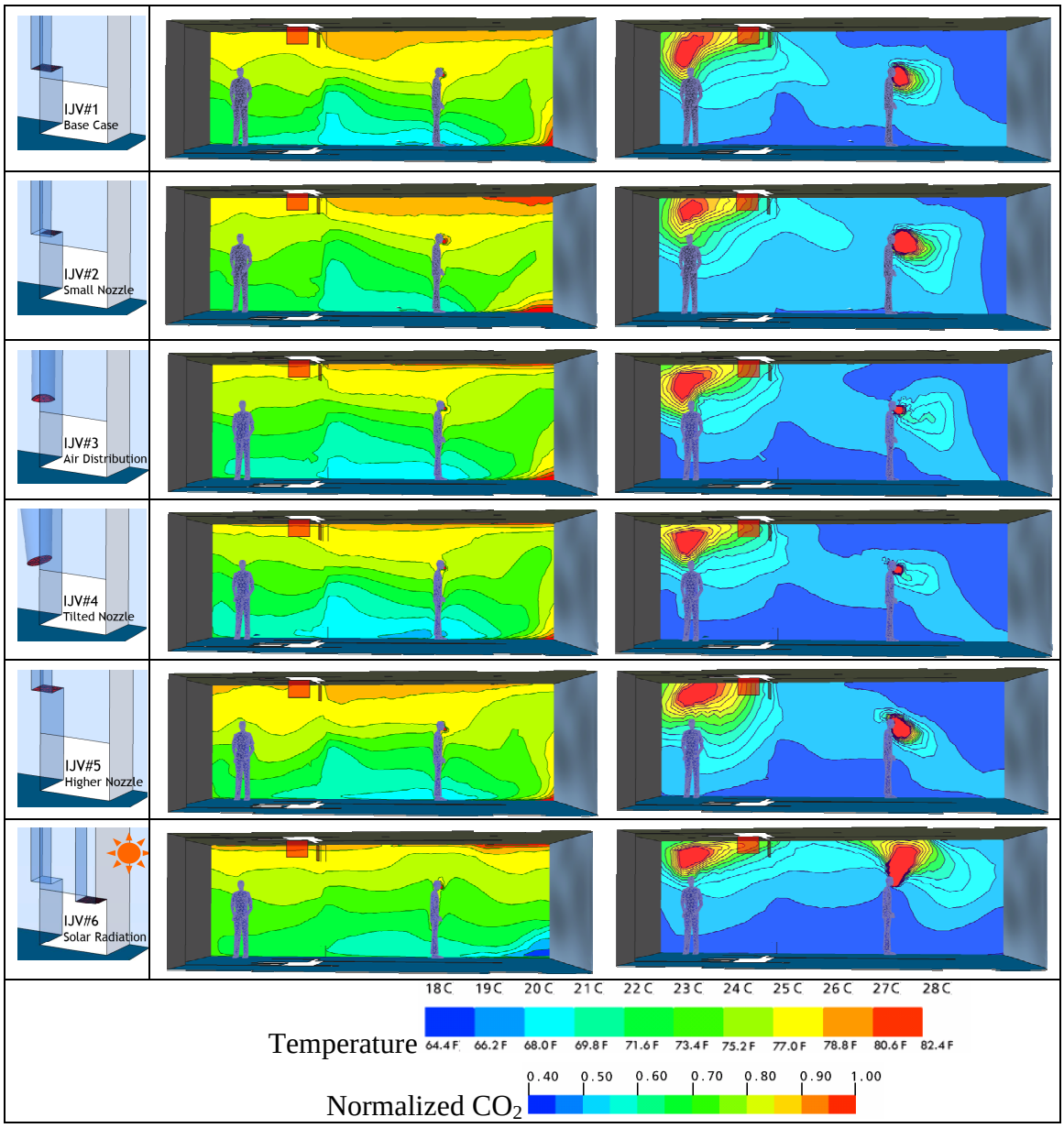

Figure 73 Temperature contour of IJV with different terminal configurations

DISCUSSION

As with the simulation results, the discussion also consists of two parts: the results using the nozzle with the different velocity profiles and the IJV with the different terminal configurations. Both are analyzed with three ventilation indices; ventilation effectiveness, CFD ventilation performances, and PMV-PPD. These indices are discussed and introduced in Chapter 2.

Nozzle with different velocity profiles

In **Figure 71**, temperature, velocity, and normalized CO_2 measured at the room center show close agreement between the nozzles with the uniform and boundary layer profiles. The difference is small compared to the sensor error of the IFS-200 system which has a temperature error of $\pm 0.5^{o}C$ and a velocity error of ±0.03 m/s. The error of CO_2 measurement is also relatively large compared to the CFD data. The best CO_2 sensor from HOBO has a CO_2 error of 50 ppmv which is equal to the normalized CO_2 of 0.05.

Calculated by **Equation 7** and **Equation 8**, ventilation effectiveness (ε) of both nozzle velocity profiles is quite similar. ε_t for both cases shows closer agreement than ε_c. ε_t of both cases are identical at 1.09. ε_c of a nozzle with a uniform velocity profile and a boundary velocity profile are 1.37 and 1.28 respectively.

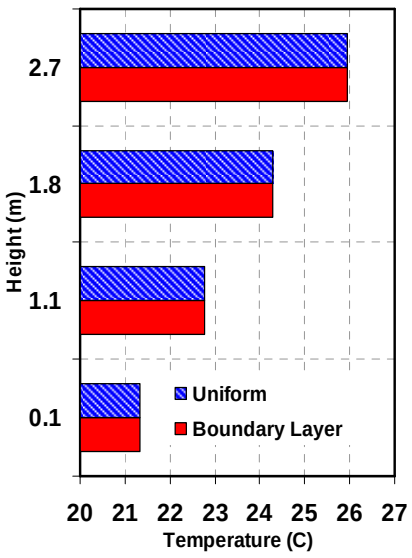

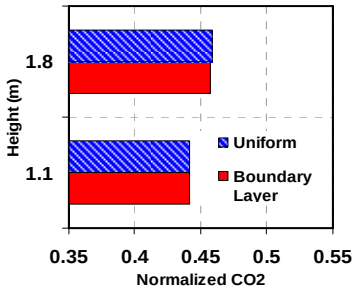

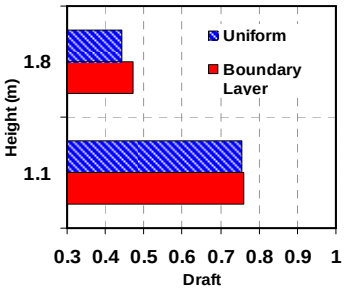

Figure 74 Average temperature of different nozzle velocity profiles (top left)

Figure 75 Normalized CO_2 of different nozzle velocity profiles (top right)

Figure 76 Normalized draft of different nozzle velocity profiles (bottom left)

Calculated by **Equation 15**, **Equation 16**, and **Equation 17, the** CFD ventilation performances of both nozzle velocity profiles are quite the same. Results of CFD nodes shown in **Table 11** are plotted and summarized in **Figure 74**, **Figure 75**, and **Figure 76**

where the average air temperature and normalized CO_2 and draft are compared. The close agreement of both velocity profiles is found not only from these variables, but also from stratification discomfort which both reach at 0.21. Draft at the 1.8m height of both nozzle velocity profiles is the most dissimilar, but is still very small because the error of the normalized draft (room normalized area caused by draft) differs by only 0.4%.

Analogous to the CFD ventilation performances, both nozzle velocity profiles have almost identical PMV-PPD. The PPD of a uniform velocity profile and a boundary velocity profile are 29.3% and 27.9%, respectively. The 1.4% difference comes from the air velocity sensitivity in the PPD calculation in **Equation 24**-**Equation 26**. The PPD is extremely high when air velocity exceeds 0.11 m/s. If the velocity then rises by only 0.01 m/s above that, the PPD increases from 28.3% to 30.3% or by 2%.

IJV with different terminal configurations

After discussing the results of the IJV with different nozzle velocity profiles, the same ventilation indices are used for comparing the IJV with different terminal configurations. First, the discussion begins with ventilation effectiveness (ε). Using ε_t and the ventilation control technique presented in **Figure 32** (Chapter 2), the flow rate is determined for each IJV terminal configuration which brings room temperature up to 23.5°C (74°F). As **Figure 77** shows, the ε_t of all terminal configurations is quite alike. The lowest ε_t is at 1.09, while the highest ε_t is at 1.12. Like the ε_t, the ε_c of all configurations range closely from 1.08 to 1.32 as shown in **Figure 77**. Because both the ε_t and the ε_c of the six terminal configurations chosen for this study exceed one, the selected terminal configurations may not impact so negatively on energy conservation, thermal comfort, and the IAQ when using the IJV system.

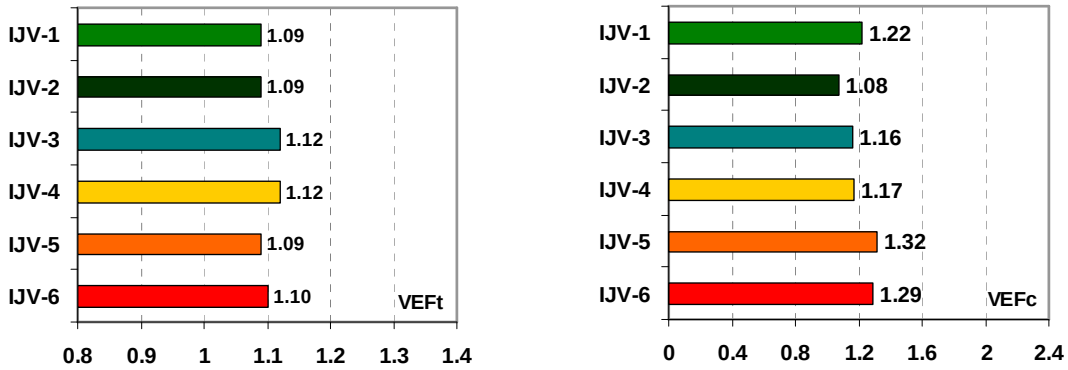

Figure 77 $\boldsymbol{\varepsilon_t}$(Left) and $\boldsymbol{\varepsilon_c}$(Right) of IJV terminal configurations

The next indices to be discussed are the CFD ventilation performances. By using **Equation 15-Equation 17**, the CFD ventilation performances of all terminal configurations are shown in **Figure 78**. The indicator that makes almost no difference in any terminal configurations is normalized CO_2. Overall, normalized CO_2 increases when the measured height increases with about a 1.5% difference (or 15 ppmv). On the other hand, draft and stratification discomfort show the differences when different terminal configurations are adopted. The base case, IJV#1, causes the highest stratification discomfort in around 21% of the room area. When switching to the other configurations, stratification discomfort tends to similarly decrease. Among these configurations, the most effective method is to increase the supply velocity as seen in IJV#2, which reduces stratification discomfort to 9%. However, when the supply velocity is too strong, draft is the consequence. IJV#2 exponentially increases normalized draft from 1 to16%, while others maintain the same low level of draft. Supplying with half the velocity of IJV#2, IJV#1 causes normalized draft from 1 to 1.5% for both the 1.1m and 1.8m heights. After moving the IJV tubes higher as in IJV#5, the draft increases slightly from the base case to 2-2.5%. This finding corresponds to the findings in Chapter 3 which conclude that increasing the nozzle height increases the jet velocity along the floor. Using the supply grill (IJV#3) and relocating the tubes (IJV#6) also increases draft at 1.8m to 3-5% when compared to the base case. The most effective technique to reduce draft to nearly nil is achieved by tilting the tubes toward the wall (IJV#4).

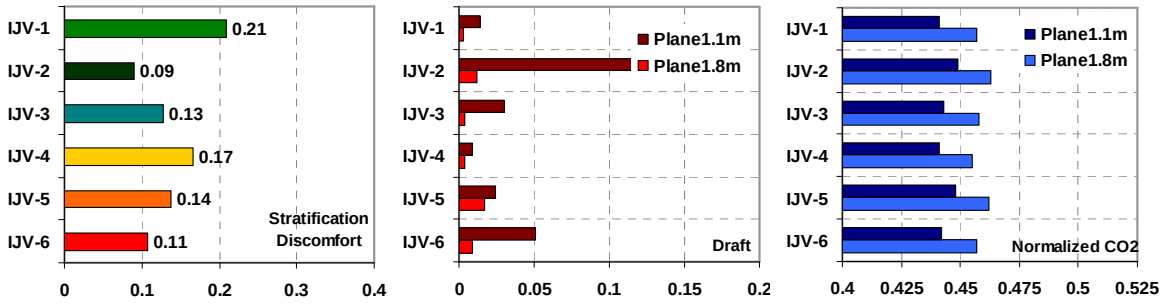

Figure 78 CFD ventilation performances of all IJV terminal configurations

PMV-PPD of IJV with different terminal configurations

The PPD of all terminal configurations lies around 27-29% which exceeds the thermal comfort threshold by 17-19%. As shown in **Figure 79**, only slight differences in the PPD are found because high PPD is caused by high PMV near the radiating glass assigned in

all cases. This effect is seen in **Figure 80** where the isosurface of PMV +0.75 is plotted. This isosurface is created by connecting the data points of equal value, which in this case is a PMV of +0.75. To reduce the PPD caused by high PMV, glazing irradiance in a room with any IJV terminal configurations must be reduced by selecting glass with lower SHGC or by using shading devices.

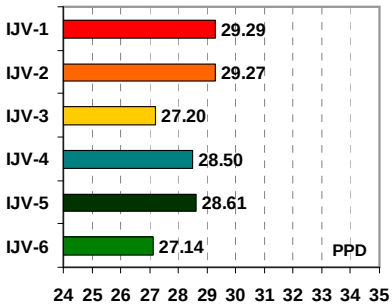

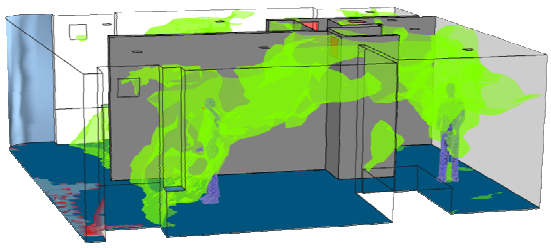

Figure 79 PPD of all IJV terminal configurations (left)
Figure 80 Isosurface of PMV +0.75 of IJV#1 (right)

SUMMARY

In this chapter, the nozzles with different velocity profiles and IJV with different terminal configurations are studied. Unlike the impinging jet characteristics in the previous chapter, this chapter shows that using a nozzle with a uniform velocity profile gives the same results when using the nozzle with a boundary layer profile. Outcomes like ventilation effectiveness, CFD ventilation performances, and PMV-PPD, are similarly obtained with the simpler CFD set-up which in turn makes further simulations easier. When these indices are applied to the comparison of IJV with different terminal configurations, commonalities are found among all six configurations, with the exception of CFD ventilation performances. Different terminal configurations distinctly impact draft and stratification discomfort. The most effective way to reduce stratification discomfort is to increase supply velocity, but at the same time excessive draft must be a concern. Supply velocity not only has strong impacts, but it is also the most common variable in HVAC design. Thus, it deserves further examination which will be presented in the next and following chapters. Studies about the other terminal configurations are not continued in this dissertation, but this does not mean that these topics are exhausted. Since each configuration shows unique advantages and disadvantages for specific HVAC applications, the demand for future studies of these new IJV terminal configurations is great.

CHAPTER 5

PERFORMANCES OF DIFFERENT VENTILATION STRATEGIES UNDER VARIABLE AIR VOLUME SYSTEM

The principle of Variable Air Volume (VAV) is to control the room temperature by varying the flow rate or the supply air volume [78]. This mechanism is possible because of equipment called a VAV box. The VAV box contains an actuator which can be rotated to adjust the amount of supply air. The amount of supply air is determined by a thermostat that detects the room air temperature, and then the VAV box reacts by increasing or decreasing the supply flow rate. Supplied flow rate and room temperature are balanced by following the relationship in **Equation 2**. When using flow rate as a control parameter, advantages are the temperature control precision and small, smooth temperature swing [41]. An additional benefit is energy conservation which can be obtained if the fan size or speed of the Air Handling Unit (AHU) is reduced. When cooling demand decreases, the flow rate can be reduced without the use of additional heating energy. Because of these advantages, VAV becomes a common system for medium and large buildings. However, VAV also has some negative consequences. VAV still relies on the duct and actuator which drop the efficiency due to system friction [78]. The supply temperature is usually fixed at the dew point (usually 13^{o}C or 55^{o}F) which is not flexible for the control of humidity. Another drawback of VAV is the dropping of IAQ when flow rate is inadequate. Low flow rate determined by low cooling load is not sufficient to remove the pollutants generated by humans or other soures, and the concentration level might exceed the threshold set by ASHRAE-62. To minimize this problem, the minimum flow rate of the VAV system is usually set up and strictly maintained by using the number of occupants and space sizes as the criteria [7, 13]. This minimum flow rate forces the VAV system to use heating energy in maintaining thermal comfort by activating the reheat coil to slightly increase the supply temperature. Only

within this condition, must VAV be operated for heating and cooling simultaneously, which thereby causes a drop in energy efficiency.

The objective of this chapter is to study how each ventilation strategy performs under a VAV system. The three ventilation strategies to be tested include MJV, DV, and IJV which have been already introduced in Chapter 1 (see **Figure 81**). As discovered in the previous chapter, supply velocity is important. IJV, which has two supply velocity ranges, includes IJV#2 which has twice the supply velocity of the IJV#1. Combining these two with DV and MJV, four ventilation strategies were tested against four different cooling load scenarios operated with the VAV system. Results will be discussed by using ventilation effectiveness, CFD ventilation performances, and PMV-PPD. Similar results were published by the author of this dissertation, and can be found in the peer-reviewed journal [32] shown in the list of references.

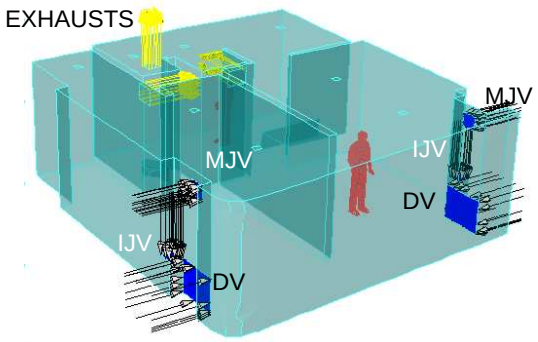

Figure 81 The CFD model of the case study space with different ventilation strategies

COOLING LOAD SCENARIOS AND eQUEST SIMULATION

A wide range of cooling load scenarios was set up to study the performances of different ventilation strategies. By using the direct calculation method from **Equation 2**, four cooling loads ranging from low to high of 9, 47, 116, and 160 W/m^2 were studied. Each represented the thermal environment for a particular time and/or season. Solar irradiance is a major contributor to these cooling loads. Solar irradiance is mainly determined by sun positions as shown in **Figure 82**. The figure shows the sun chart for latitude 40 of northern hemisphere. The 9 W/m^2 case represents the morning and evening scenarios, when the oblique angle from the sun is almost parallel to the glass. The 47 W/m^2 and 116 W/m^2 cases represent the before noon and after noon conditions, when the oblique angle from the sun is less parallel to the glass. The former represents the partly cloudy

condition, while the latter represents clear sky conditions. The case with the peak cooling load, 160 W/m^2, occurs in winter noon, when the sun is almost perpendicular to the glass.

At latitude 40, the solar incident angle to the glass can be as low as 26.5 degrees. Referring to the riverlo's function, which is the relationship of transmitted/reflected radiation energy and the incident angle, the sun with an incident angle of 26.5 degrees can have as much penetration into the space as does the sun with an angle of 0 degrees [79]. After adding to the other cooling load components, peak cooling load reaches 160 W/m^2. eQUEST, a DOE-2 energy simulation software, confirmed that this peak cooling load will occur on February 7th at 1 pm [80, 81]. Modeled by this software, **Figure 83** shows an energy model of the studied space and the whole building in both plan and perspective views.

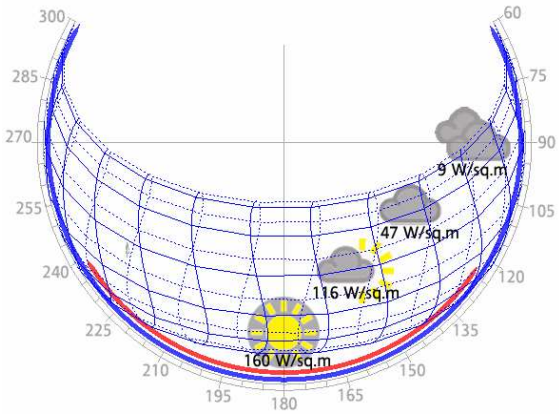

Figure 82 the load scenarios setup in relation to the sun positions

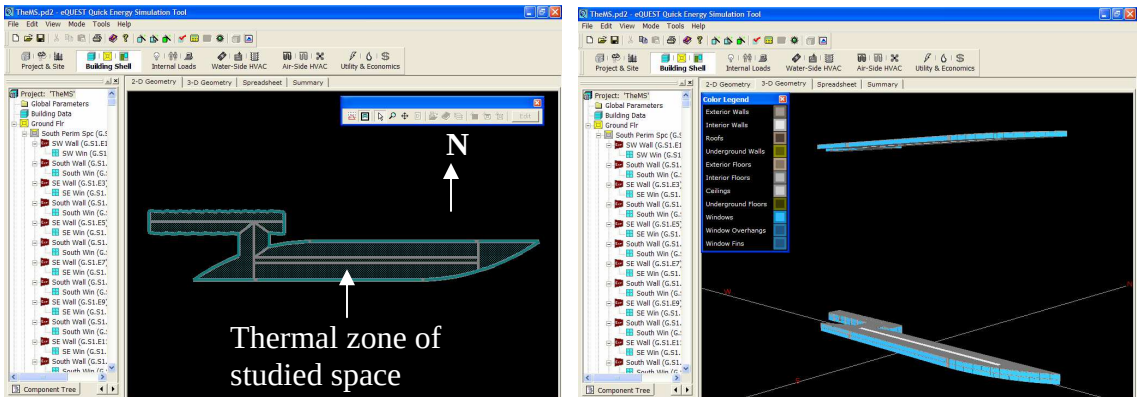

Figure 83 the case studied space modeled with eQUEST

CFD SCENARIOS SETUP

Detailed data of cooling, humidity, and pollutant loads are necessary for CFD simulation. In addition to humidity and pollutant loads, cooling loads mentioned previously were

broken down by contributing components, and presented in **Table 16**. Based on these cooling loads, flow rates for each scenario as shown **Table 17** can be obtained by using **Equation 2,** where the supply temperature of the VAV system was fixed at 13°C (55°F) and the control temperature of 23.5°C (74°F). Shown in both actual and Air Change per Hour (ACH) formats, these flow rates were used to determine the supply velocity of each ventilation strategy. This supply velocity impacts both Re and Ri[18]. If the supply temperature is fixed, faster supply velocity can increase Re, while reduce Ri. With the lowest supply velocity, DV has the lowest Re range, while has the highest Ri range. With the highest supply velocity, Re of IJV#2 becomes the highest, and Ri becomes the lowest.

	Cooling Load Scenario			
	Case 9W/m^2	**Case 47W/m^2**	**Case 116W/m^2**	**Case 160W/m^2**
Glass SC/ U-value/ Area	0.7/ 0.29 Btu/h ft F/ 20 m^2			
Conduction	169 W	432 W	839 W	-726 W[19]
Vertical radiation	207 W	1,576 W	4,987 W	8,982 W
Humans (2 people)	146 W			
Light	0 W	464 W		
Total cooling load	**523 W**	**2,618 W**	**6,436 W**	**8,866 W**
Vapor (2 people)	**5.4x10^{-5}kg/s**			
CO2 (2 people)	**1.5x10^{-5}kg/s**			

Table 16 The cooling, humidity, pollutant load summary for VAV simulation

	Ventilation Strategies			
	MJV	DV	IJV#1	IJV#2
	CFD#1	CFD#1	CFD#1	CFD#1
Load (160 W/m^2)				
Flow rate (m^3/s)	0.68	0.68	0.68	0.68
ACH	15.23	15.23	15.23	15.23
Velocity (m/s)	3.14	0.44	3.66	7.32
Re/Ri	83,595/ 0.0182	31,292/ 2.482	90,251/ 0.012	127,635/ 0.002
Load (116 W/m^2)				
Flow rate (m^3/s)	0.50	0.50	0.50	0.50
ACH	11.2	11.2	11.2	11.2
Velocity (m/s)	2.5	0.32	2.69	5.38
Re/Ri	63,961/ 0.028	22,883/ 0.047	66,347/ 0.023	93,828/ 0.004
Load (47 W/m^2)				
Flow rate (m^3/s)	0.20	0.20	0.20	0.20
ACH	4.48	4.48	4.48	4.48
Velocity (m/s)	0.95	0.129	1.08	2.15
Re/Ri	24,936/ 0.197	9,189/ 28.921	26,588/ 0.142	37,514/ 0.026
Load (9 W/m^2)				
Flow rate (m^3/s)	0.04	0.04	0.04	0.04
ACH	0.9	0.9	0.9	0.9
Velocity (m/s)	0.185	0.026	0.215	0.430
Re/Ri	4,921/ 5.251	1,845/ 709.210	5,305/ 3.607	7,503/ 0.638

Table 17 The CFD flow rate setup for the VAV simulations

[18] Discussed in Chapter 2 in the section of dimensionless flow parameters
[19] Conduction heat loss

SIMULATION RESULTS

The CFD results are rendered in temperature and pollutant distribution formats.

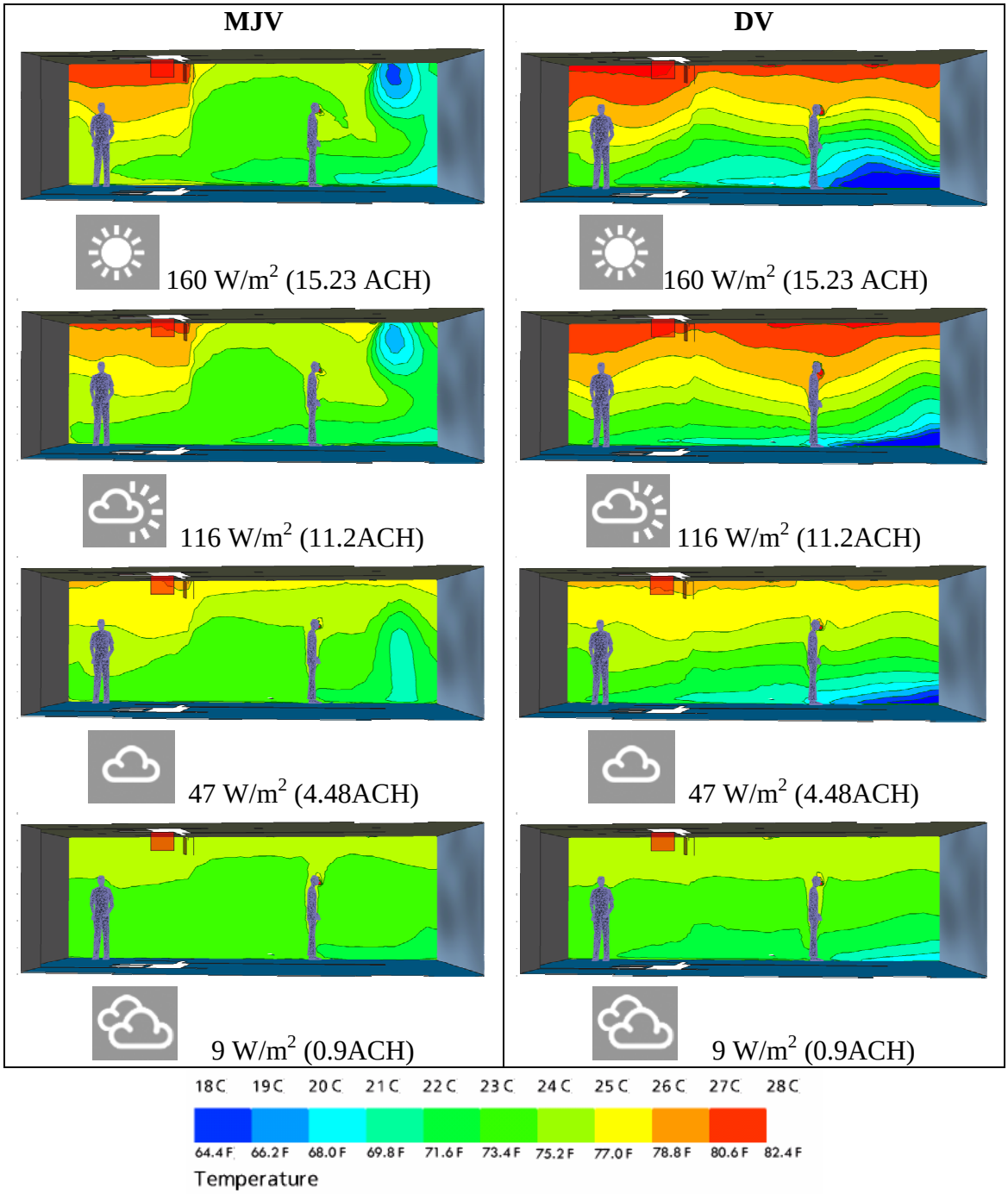

Figure 84 The temperature profiles of MJV and DV under the VAV system

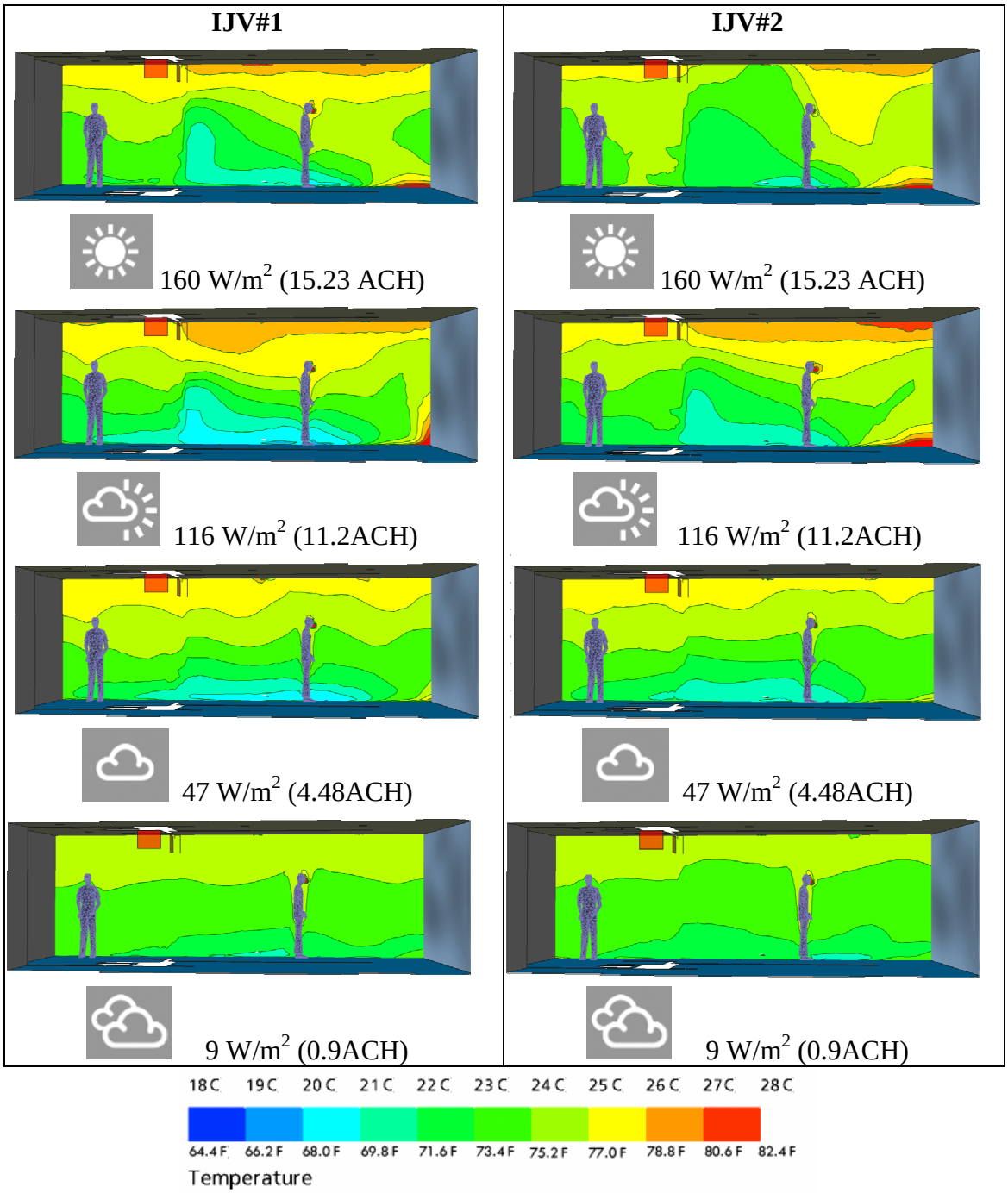

Figure 85 The temperature profiles of IJV#1 and IJV#2 under the VAV system

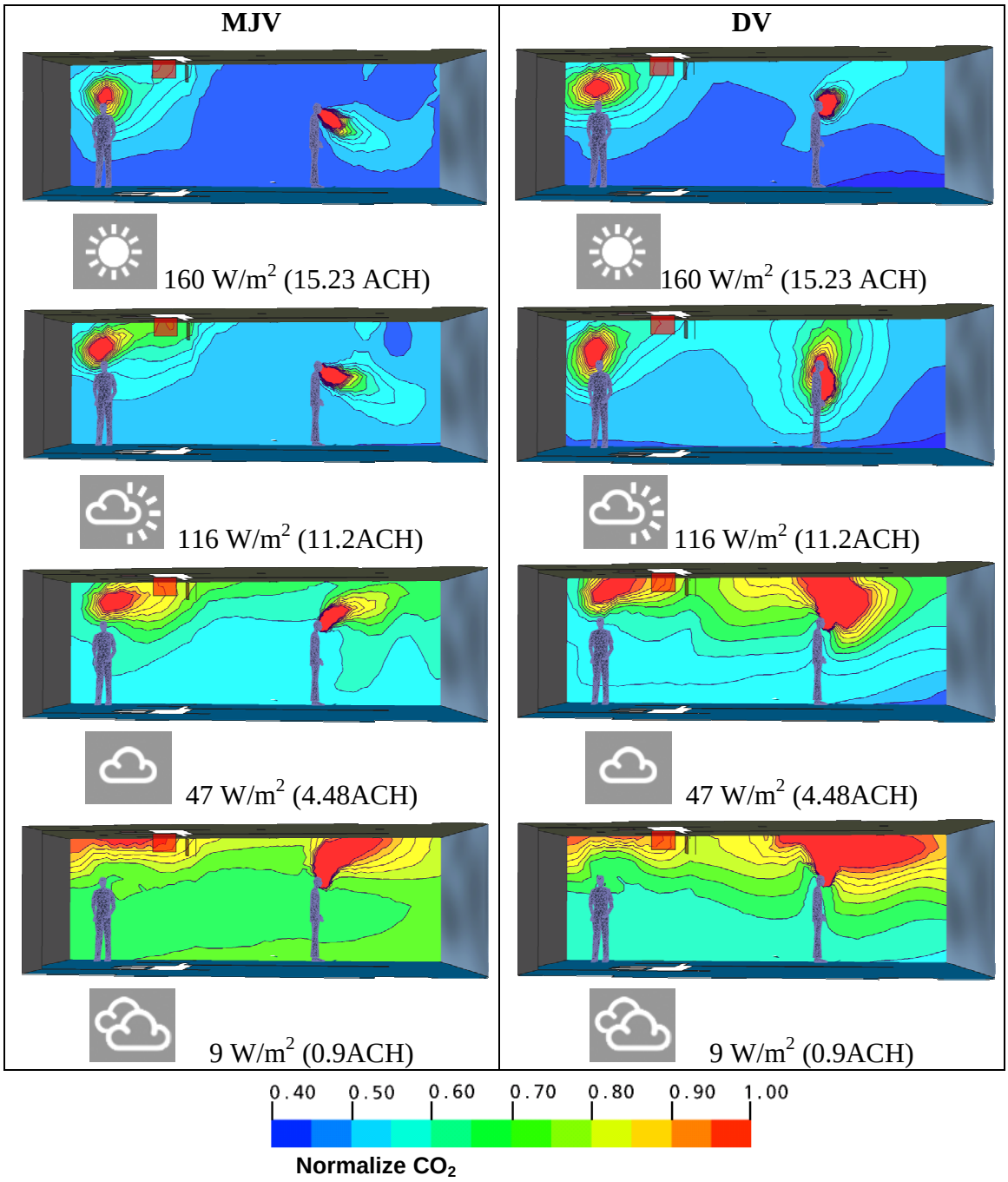

Figure 86 The CO_2 concentration profiles of MJV and DV under the VAV system

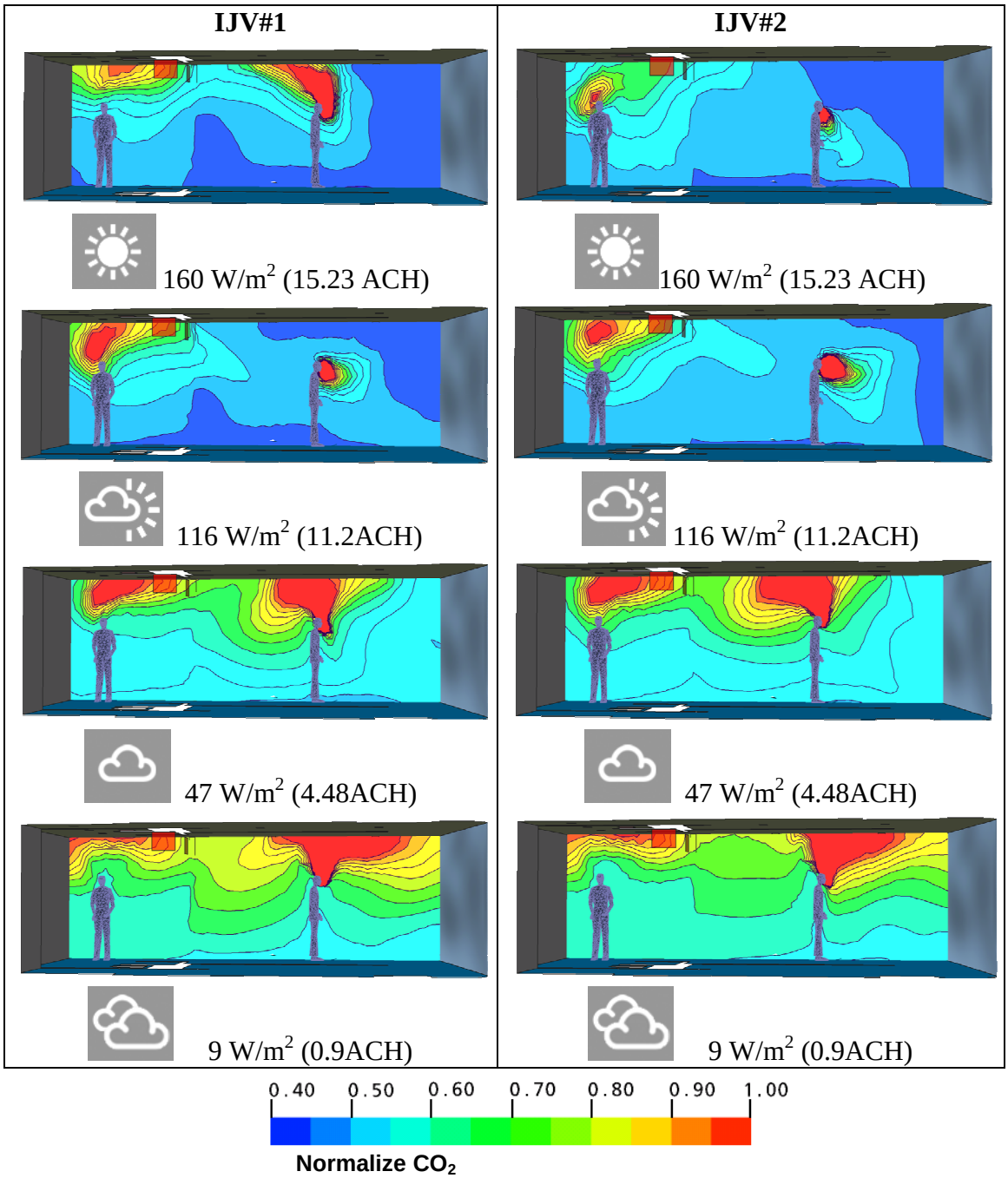

Figure 87 The CO_2 concentration profiles of IJV#1 and IJV#2 under the VAV system

DISCUSSION

The discussion is divided into three parts which include ventilation effectiveness, CFD ventilation performances, and PMV-PPD.

Ventilation Effectiveness of ventilation strategies under the VAV system

Ventilation effectiveness (ε) of MJV, DV, IJV#1, and IJV#2 was plotted from **Figure 88** to **Figure 91**, where only the selected scenarios of low (9 W/m^2) and high (116 W/m^2) cooling loads are shown. **Figure 88** and **Figure 89** represent ε_t using **Equation 7**, while **Figure 90** and **Figure 91** represent concentration ε_c using **Equation 8**.

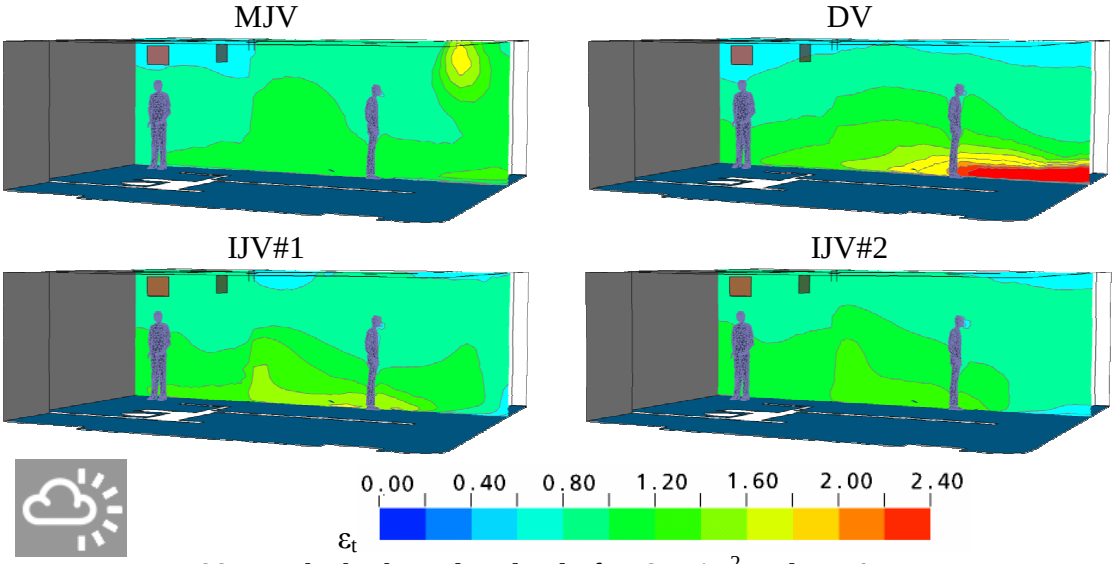

Figure 88 ε_t at the high cooling load of 116 W/m^2 under VAV system

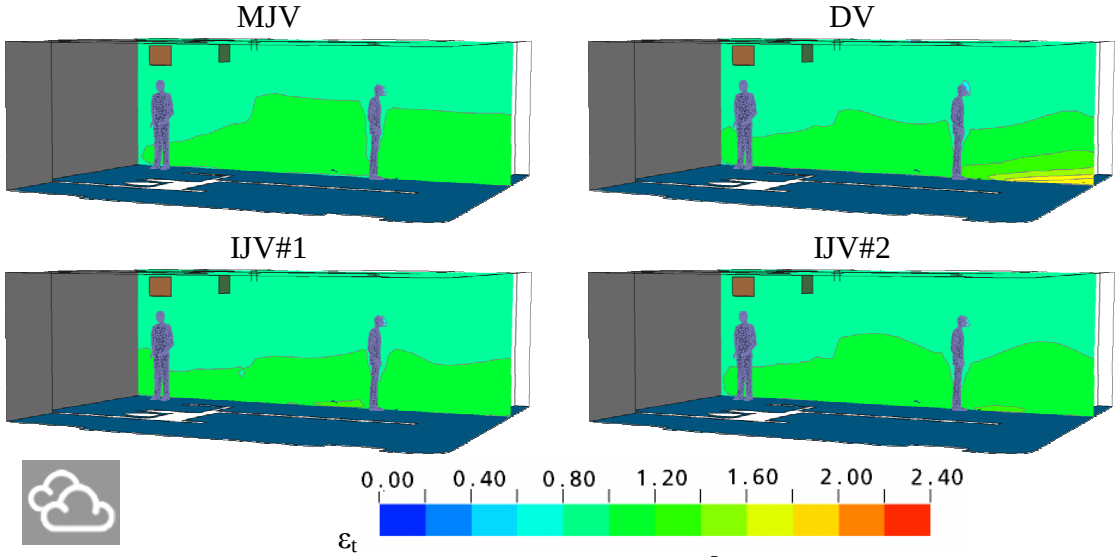

Figure 89 ε_t at the low cooling load of 9 W/m^2 under VAV system

From the results plotted in **Figure 88** and **Figure 89**, it can be seen that increasing the cooling load makes ε_t near the floor highly differentiated from the ceiling, but decreasing cooling load makes ε_t at all heights uniform. If one is concerned only with ε_t within breathing zone, ε_t of both DV and IJV#1 tends to be highest as shown in **Figure 88** (high cooling load). IJV#2 has a lower ε_t, but still higher than ε_t of MJV. These results confirm that MJV homogenously mixes the air in the space, and equally distributes ε_t. On the contrary, since IJV and DV utilize stratification, the higher ε_t in the breathing zone can be expected. IJV#2, which utilizes a faster supply velocity than IJV#1, mixes the air faster, and thus stratification decreases. Low cooling load reduces stratification and makes the ε_t of all strategies similar, as shown in **Figure 89**.

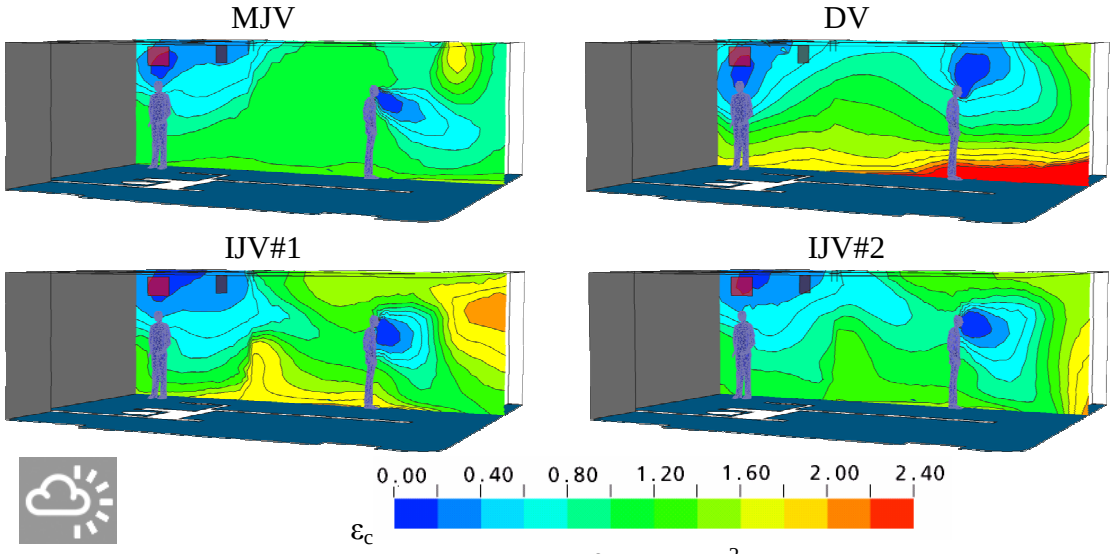

Figure 90 ε_c at the high cooling load of 116 W/m^2 under VAV system

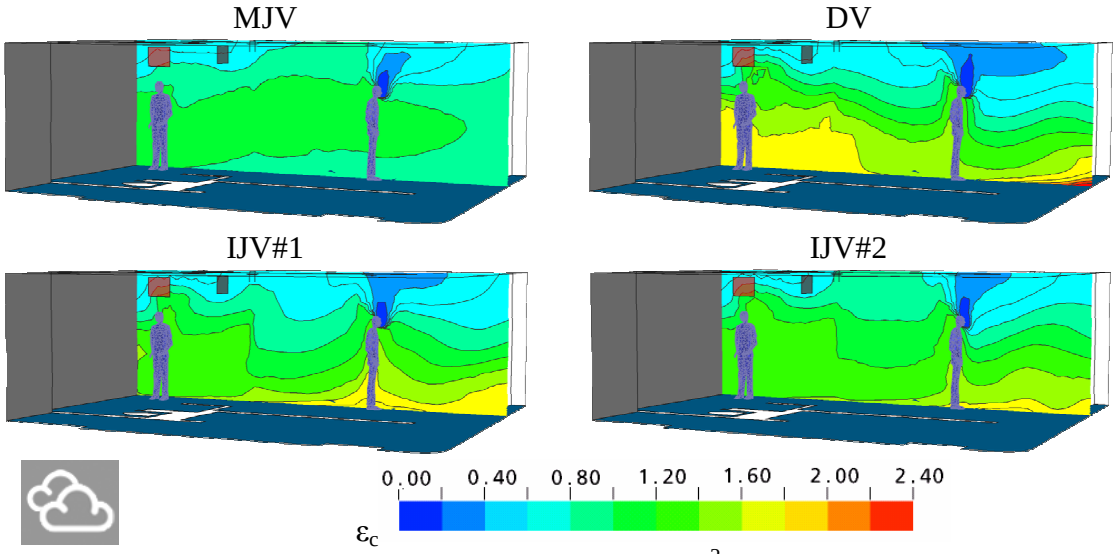

Figure 91 ε_c at the low cooling load of 9 W/m^2 under VAV system

The ε_c of four strategies are plotted in **Figure 90** and **Figure 91** to represent high and low cooling load scenarios, respectively. High ε_c, with color values greater than 1.0 and indicated by the yellow to red color, represents clean air. The ε_c near the human nose is low (less than 1), because of the high CO_2 level produced by exhaling. Similar to ε_t, high cooling load increases the ε_c differential from floor to ceiling. For high cooling load (**Figure 90**), MJV and IJV#2 have the most homogeneous ε_c. IJV#1 and DV perform better because they can sustain high ε_c within the breathing zone. When supply velocity increases, the CO_2 plume might not form successfully and rise toward the ceiling. As a result, the concentrated CO_2 is mixed with breathing zone air, and reduces ε_c. This negative characteristic affects both MJV and IJV. Conversely, DV is capable of maintaining high ε_c for both cooling loads, because low supply velocity does not disturb the plume, which rises vertically toward the ceiling. In **Figure 91** (low cooling load), as opposed to the ε_t plots, IJV#1 and IJV#2 clearly perform better than MJV because ε_c of both ventilation strategies is distinctly noticeable. The cleaner air (high ε_c) of IJV is preserved within the breathing zone, and exhaled CO_2 successfully rises upward.

ε_t and ε_c were plotted against cooling load variation in **Figure 92,** where both ε values were calculated by averaging the grid data in the breathing zone at heights of 1.1 and 1.8 meters. MJV consistently maintains ε_t just above 1.0 in all cooling load ranges but still low compared to DV. DV starts to exceed MJV at a cooling of 85 W/m^2, and has the highest ε_t at the peak cooling load range. Both IJV surpass MJV at a cooling of 50 W/m^2. Beyond this point, ε_t of both IJV sharply increases. Both IJV have ε_t reaching 1.1 at a cooling load of 116 W/m^2, but when cooling load increases to 160 W/m^2, both ε_t drop to be the same as with MJV. As mentioned in Chapter 2, high ε_t may reduce overall air flow rate in HVAC system. Thus, the overall flow rate reduction of IJV is considered possible when the cooling load range is within 50-160 W/m^2.

Compared with ε_t, different results were found if ε_c was applied to IJV. All strategies have a ε_c higher than 0.9, which is recommended by LEED for IAQ scoring [8]. As expected, MJV maintains ε_c slightly above 1.0 in all cooling load scenarios, and DV has higher ε_c than MJV in all scenarios. The ε_c of DV increases when cooling load increases, and it reaches 1.34 at cooling load of 160 W/m^2. Unlike ε_t, IJV#1 clearly performs above IJV#2. IJV#1 has the highest average ε_c, reaching 116 W/m^2 when cooling load is lower

than 130 W/m^2. If cooling load continues to rise, the ε_c drops to meet MJV at the peak cooling load. IJV#2, with double the supply velocity of IJV#1, is able to maintain ε_c above MJV, but less than both IJV#1 and DV. If cooling load surpasses 140 W/m^2, the ε_c of IJV#2 drops below MJV. Since overall IJV has higher ε_c than the MJV system, the fresh air intake rate can be proportionally reduced, and this reduction leads to energy conservation for HVAC system. This finding can be added to ASHRAE 62 standard in the ventilation effectiveness section [7], where if MJV is suggested to have ε_c (or E_z) of 1.0, IJV should achieve the higher rating. To expect high IJV performances, one should be aware that supply velocity strongly affects ε_c, and low supply velocity is more effective than high velocity. In addition, high cooling load (more than 160 W/m^2) should be avoided because it can significantly reduce the ε_c of an IJV system.

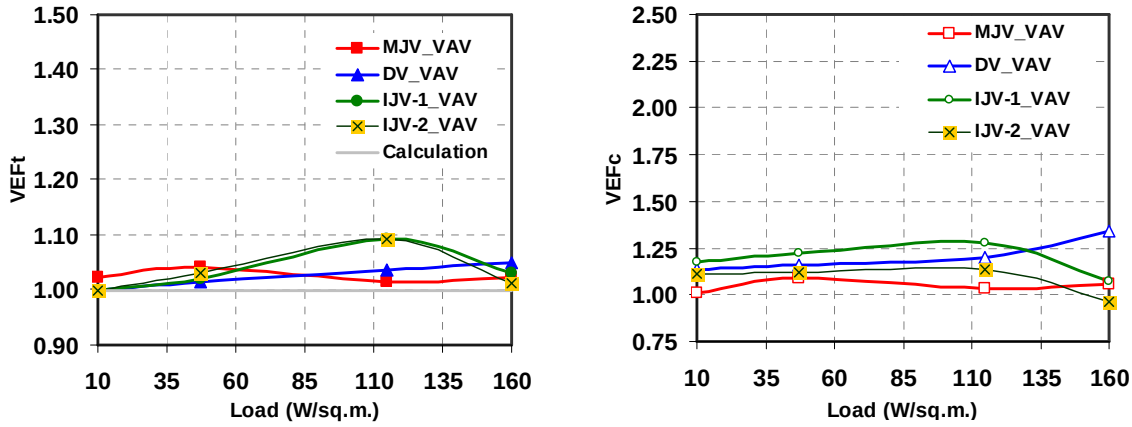

Figure 92 average ε_t (left) and ε_c (right) of the VAV system

In order the reduce peak cooling load, a standard such as ASHRAE 90.1 and 90.2 should be strictly implemented [82]. Based on these standards, the cooling load can be reduced by glass and wall selection, and maintain appropriate window to wall ratio (WWR). The results from eQUEST demonstrate that when the glass with SHGC of 0.7 is replaced by 0.21, the peak cooling load is reduced by 93 W/m^2. The same reduction can be expected if the glass area is minimized. With this cooling load reduction, the IJV systems become suitable options for this case study space.

CFD ventilation Performances of ventilation strategies under VAV system

In this section, the CFD ventilation performances of MJV, DV, and IJV are compared. Using **Equation 15 - Equation 17**, the normalized stratification discomfort, draft, and normalized CO_2 are the indicators. A good ventilation strategy should bring these

variables as close to zero as possible, because it means the room has no stratification discomfort, draft and free of CO_2. When these indicators are not zero, some problems can be detected. For instance, for stratification discomfort, $A_{t>3C}/A_{room}$ of 0.5 means half of the room exceeds the threshold of temperature difference (3^oC from 1.1m-0.1m). For draft, $A_{PD>10\%}/A_{room}$ of 0.5 means half of the room at a given height exceeds PD caused by draft of 10%. For nominated CO_2, $C_{cfd}/C_{1000ppmv}$ of 0.5 means that the CO_2 concentration reaches half of the standard (1000 ppmv).

From **Figure 93** to **Figure 95**, the CFD ventilation performances of each strategy were plotted against cooling load variation. Both draft and normalized CO_2 were plotted for both 1.1m and 1.8m height to represent the head position of different activities. Both advantages and disadvantages of each ventilation strategy will be discussed below.

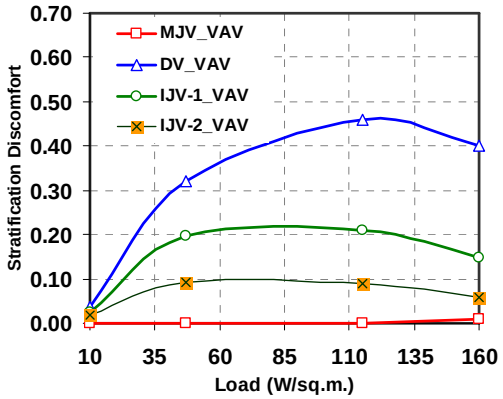

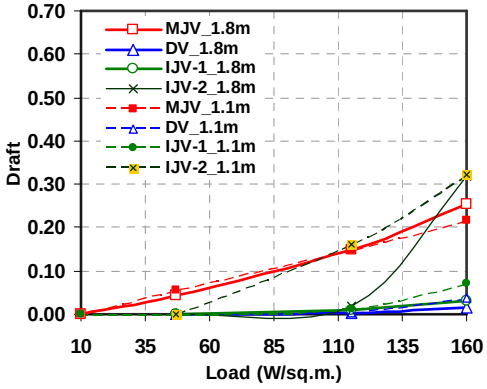

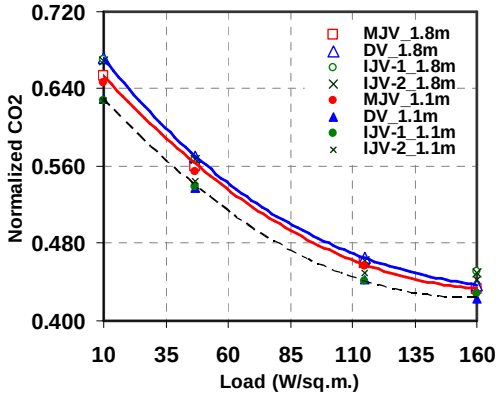

Figure 93 Stratification discomfort of different ventilation strategies under theVAV system (top left)

Figure 94 Draft of different ventilation strategies under the VAV system (top right)

Figure 95 Normalized CO_2 of different ventilation strategies under the VAV system (bottom left)

MJV has a major advantage in stratification discomfort prevention because stratification discomfort does not occur in all cooling scenarios. A disadvantage of MJV is excessive draft which linearly increases as the cooling load goes up. The peak of draft for both 1.1m and 1.8m reaches 0.22 and 0.25 at peak cooling load, respectively. See the red line in **Figure 94**. In **Figure 96**, where the magenta color area is PD exceeding 10%, the draft

of the MJV system generally occurs near the glass and the wall. With this high velocity, the CO_2 level is almost identical for both the 1.8m and 1.1m planes (see the red line in **Figure 95**). In contradiction to a previous study [12], MJV does not always have the worst IAQ. At 1.8m height, MJV almost always performs slightly better than the others, but in the lower height (1.1m), MJV loses the opportunity to improve IAQ because no stratification has been utilized.

DV has the highest stratification discomfort (see blue line in **Figure 93**). The supply velocity of DV is low, and not strong enough to sufficiently dilute the cool supply air to the desired room temperature. The consequence of this is to cause stratification discomfort reaching 0.44 at cooling load of 116 W/m^2. This problem can be solved by using a reheat system or power induction box [41, 80]. As discussed in the Chapter 1, both modifications lead to additional energy demand and more HVAC cost. Because of the low supply velocity of DV, a major advantage of DV is draft which is almost zero. The highest draft is below 0.04 for the peak cooling load condition at 1.1m height (see blue line in **Figure 94**). **Figure 96** confirms that PD caused by draft of the DV system is the lowest, and it only occurs near the wall which is opposite to the supply terminal. Utilizing stratification, DV maintains low CO_2 concentration at 1.1m height, but CO_2 concentration increases by 3% at 1.8m height. This relationship is sustained for all cooling scenarios. In contrast to a previous study [12], the normalized CO_2 of DV is not always better than MJV, particularly at the standing height (1.8m). The blue line in **Figure 95** shows that normalized CO_2 of DV can exceed MJV at around 0.01 in all cooling load scenarios.

Results show that IJV can solve stratification discomfort of DV without any HVAC modification by using stronger supply velocity. IJV#1 has stratification discomfort at 0.21 for both 47 and 116 W/m^2, but it can be reduced to 0.09 if using higher supply velocity, as it is in IJV#2. See both green lines in **Figure 93**. With the same supply velocity, IJV has lower draft than the MJV system. The peak draft reaches 0.07 for the peak cooling load scenario. This draft skyrockets when supply velocity is doubled in IJV#2. Still, IJV#2 can maintain lower draft than MJV, if the cooling load is low and should be less than 110 W/m^2. At this cooling load, draft exceeds the MJV (see dark green line in **Figure 94**). **Figure 96** confirms that IJV#1 causes less draft than IJV#2. PD

of over 10% (magenta area) of IJV#1 only occurs near the wall, while PD of the IJV#2 occurs intensely throughout the conditioned space. In order to reduce the draft problem of IJV#2, the cooling load must be decreased. Similar to the findings in **Figure 94**, **Figure 97** shows that the PD of over 10% for the IJV#2 significantly declines when compared with MJV at a cooling load of 116 W/m^2. Like DV, IJV successfully utilizes stratification by having normalized CO_2 at the 1.1m height lower than MJV. This normalized CO_2 at the 1.1m height is also consistently lower than that of the 1.8m height of around 0.03. However, in peak cooling load scenarios, the 160 W/m^2, the IJV might not perform as well as expected if the supply velocity is too strong. **Figure 95** shows that its normalized CO_2 surpasses both DV and MJV.

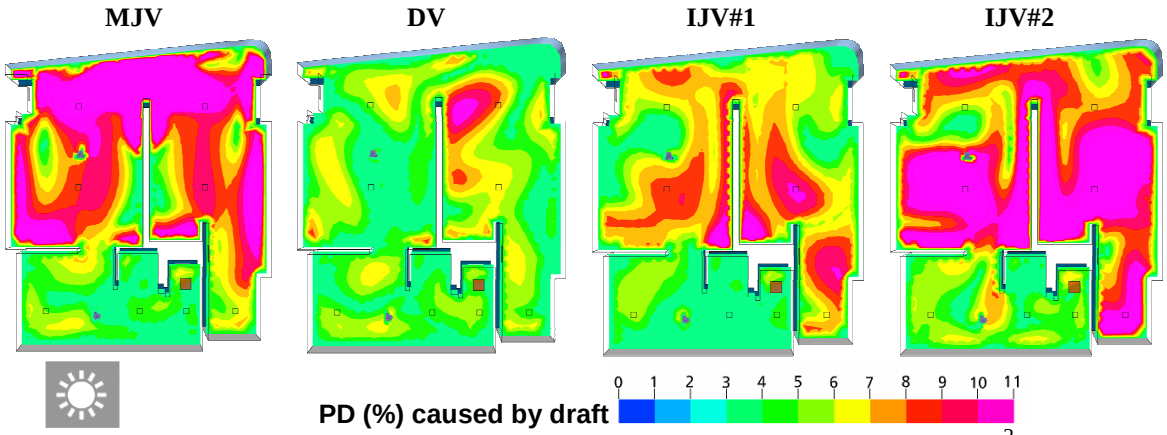

Figure 96 Draft at the 1.8m height for the cooling load of 160 W/m^2

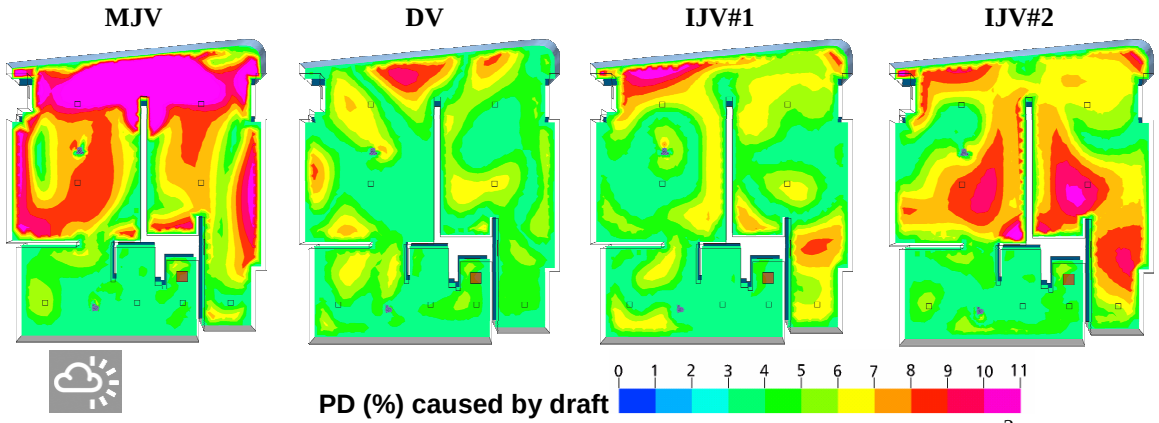

Figure 97 Draft at the 1.8m height for the cooling load of 116 W/m^2

PMV-PPD of different ventilation strategies under the VAV system

In **Figure 98**, the PMV's for four ventilation strategies were plotted. PMV increases as cooling load increases, particularly PMV monitored near glass where intense radiation occurs. These results mean that the occupant near glass can suffer from thermal

discomfort regardless of which ventilation strategy is applied. None of the strategies can solve this problem unless glass with a lower U-value and lower SHGC is installed. When the space is properly designed by minimizing the cooling load, the PMV can be reduced to zero. These results point to the fact that energy efficient design not only reduces the direct cost of energy, but also promotes thermal comfort as an additional benefit.

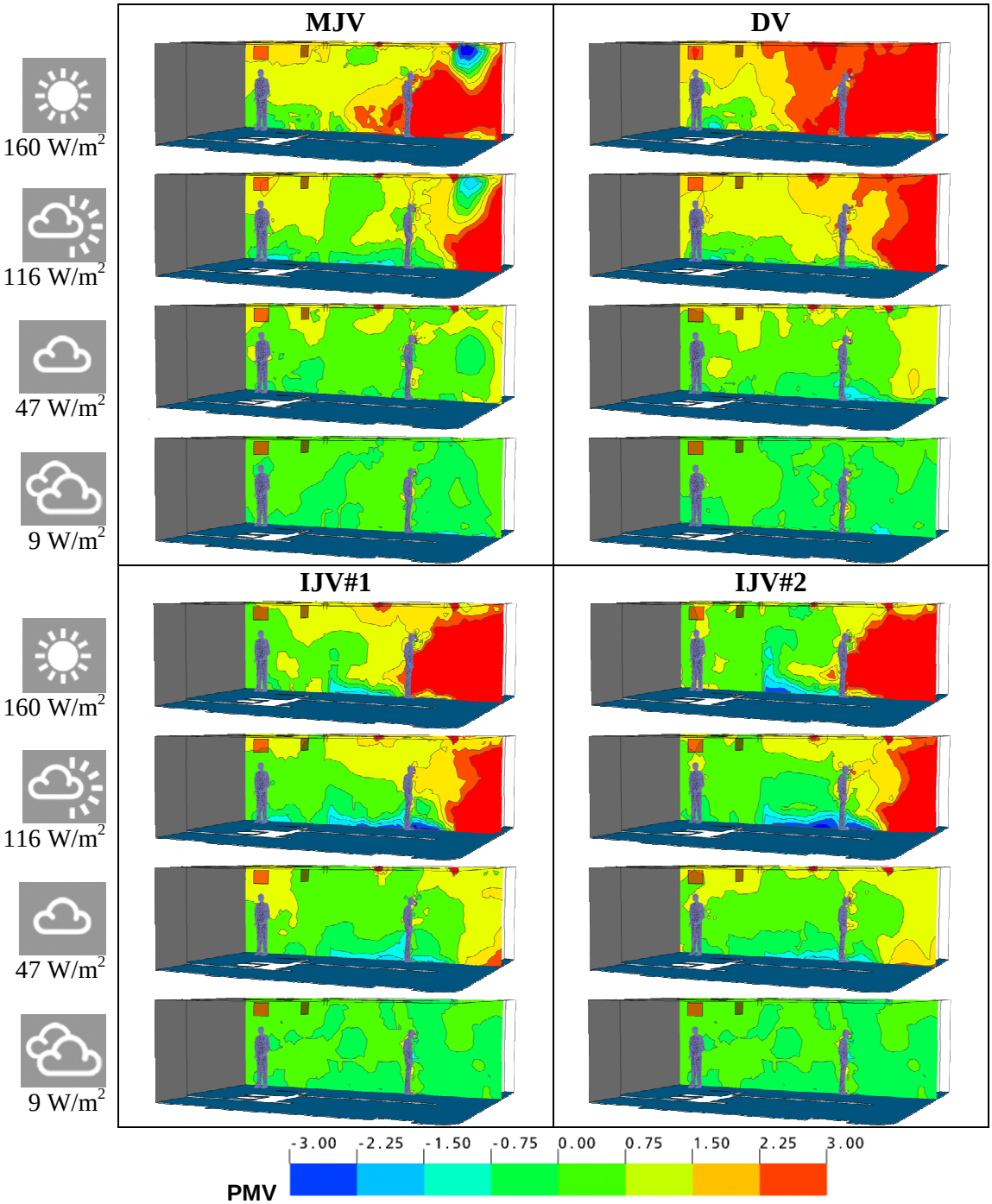

Figure 98 The PMV of different ventilation strategies under the VAV system

One interesting finding is found when the IJV has a high PMV near glass. With this extremely warm condition, IJV might surprisingly suffer from a low PMV near the floor because of a strong jet velocity being supplied from the IJV terminals. To prevent this low PMV problem, supply velocity must be appropriately maintained. At a cooling of 47 W/m^2, IJV#2 supplies with a velocity of 2.15 m/s, but still does not produce the low PMV near the floor. Then, this supply velocity range (around 2 m/s) should be set as the highest limit for the IJV system.

Calculated by using **Equation 26**, the PPD of each strategy is plotted in **Figure 99**. Based on ISO 7730, where the PPD in conditioned space (category C) should not exceed 10% [13], all strategies similarly maintain a PPD within this threshold for the low cooling load range. If cooling load goes beyond 35 W/m^2, the PPD will exceed 10% for all strategies. Within this upper range, each ventilation strategy starts to perform differently. The PPD of DV skyrockets reaching 71% at a cooling load of 116 W/m^2. At the same time, IJV#2 maintains the lowest PPD at 41%, because it has the highest average air velocity. This high velocity accelerates the body's heat loss and, in turn, can reduce PMV and PPD. It should be a concern that this PPD reduction comes with excessive draft, which was discussed previously.

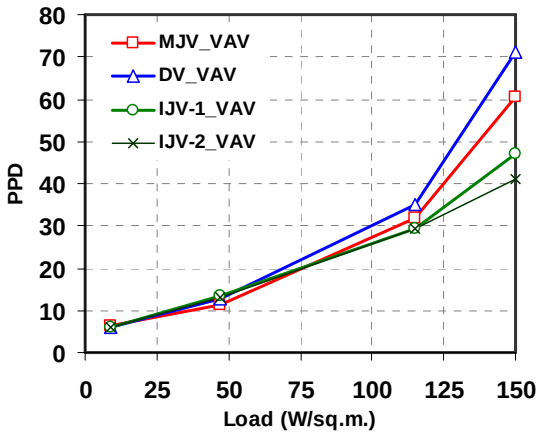

Figure 99 The PPD of each strategy under the VAV system

SUMMARY

In the VAV system, major ventilation indices show that IJV has superior performance over the mixing and displacement systems. To maintain this performance, IJV must be strictly operated within specific boundaries. Both ε and CFD ventilation performances of IJV point to the same outcome. When the cooling load exceeds 116 W/m^2, ε potentially drops, and draft increases dramatically. Within this range, the ε_t and ε_c of IJV exceed

those of MJV. Since the ε_c of a DV and an MJV system in cooling mode recommended by ASHRAE 62-2004 is 1.2-1.0, respectively, this study found that the ε_c of an IJV reaches at least 1.1. Additional advantages of the IJV system are found when using CFD ventilation performances. Allowing faster supply velocity to be used, IJV can substantially reduce stratification discomfort to less than that of DV. This strong supply velocity must be maintained to avoid excessive draft. Without disturbance from high velocity, stratification allows lower pollutant concentration to occur at the lower head height (1.1m). In addition to CFD ventilation performances, PMV-PPD is a major concern especially when cooling load skyrockets because of intense radiation. To solve this high PMV problem, ventilation strategy is not the key variable. Rather, the building fenestration system must be energy efficient in order to maintain a PPD lower than 10%. Glass and opaque walls should be well insulated, or have low U-value and SHGC. Besides the PMV, a high cooling load can bring another negative impact to IJV. If cooling load is too high, the IJV might suffer from extremely high (radiation near glass) and a low (cold jet stream near floor) PMV. To solve a low PMV problem, the peak supply velocity of the IJV should not exceed 2m/s. If this supply velocity is applied at the peak cooling load of 47 W/m^2, the stratification discomfort less than 0.09 can be expected. On the contrary, if a velocity of 2 m/s is applied for a cooling load of 94 W/m^2, the stratification discomfort will double to 0.21.

These findings are valid for a VAV system when supply temperature is fixed. When the supply temperature is varied, as it is in a CAV system, the impact of IJV and other strategies are yet mentioned here, but they will be discussed in the next chapter.

CHAPTER 6

PERFORMANCES OF DIFFERENT VENTILATION STRATEGIES UNDER CONSTANT AIR VOLUME SYSTEM

Unlike a VAV system, a Constant Air Volume (CAV) fixes the flow rate, but alternates the supply temperature. Basically, the supply air temperature is determined by the cooling load as shown in **Equation 2**. When the cooling load increases, the supply temperature decreases within the typical range of 23.5^{o}C (74^{o}F control temperature) to 13^{o}C (55^{o}F). When it is possible to supply with warm temperature, it helps the system, as in the cases of DV and IJV, to reduce the stratification discomfort problem. See more detail in Chapter 5. In addition, constant supply air of CAV is a feature that solves the IAQ problems found in a poorly designed VAV where the flow rate might be inadequate. Because of the ability to alternate the supply temperature, CAV is commonly used when the space has heating demands [41]. A VAV system can also duplicate this ability by using reheat coils, which are recommended for use in perimeter zones with occasional heating demands. Once the reheat coil is activated, a VAV system acts like a CAV system by maintaining the minimum flow rate, and relying on the reheat coil to adjust the supply temperature.

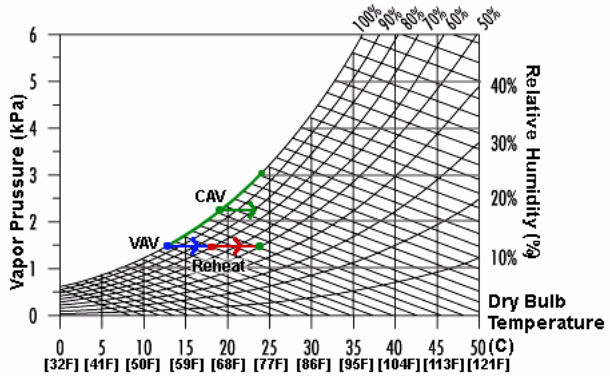

Figure 100 The overlay of CAV and VAV on the psychrometric chart.

Even tough a CAV system provides excellent IAQ, there are some circumstances that make CAV not perform as well as VAV. When a dehumidification process is needed, the condensation at the cooling coil is necessary. Condensation will happen if the coil

temperature is cool enough, and should be at least lower than the dew point of room air temperature. In any case, it should be lower than 13^{o}C if room temperature is controlled at 23.5^{o}C. This process can be explained by using the psychrometric chart as drawn with the blue line in **Figure 100**. Because of this required dehumidification, when altering the supply temperature, but not maintaining the cool coil lower than 13^{o}C, the air is not properly dehumidified (green line). As a result, the room air might have the proper temperature, but the humidity level can be very high. To overcome this problem, CAV requires extra energy to control the humidity level, and this becomes a major drawback. This extra energy is commonly used by adding dry heat to the supply air (red line) after it has been already cooled down and the moisture has been removed. The process of adding dry heat can be done in two ways. First, a reheat coil can adjust the quantity of dry heat adding to the cool supply air until reaching the appropriate supply temperature. This technique provides excellent IAQ, but it wastes a lot of energy from operating cooling and heating at the same time [41]. Second, a Power Induction Unit (PIU) can warm the supply air up by using the heat generated directly from the room. A small fan draws in the room air and mixes it with the cool air before it is supplied to the room. This technique can warm the supply air up without reheat coil; thus, there is no simultaneous heating and cooling taking place. This system might use the energy efficiently, but it also has some limitations. By recirculating the (polluted) room air, supply air might not be as clean as when using a reheat coil, and this can impact room IAQ negatively.

Because of these unique characteristics of a CAV system, it is necessary to understand how each ventilation strategy will perform when it is operated under this system. Using the CFD parameters from Chapter 3, this chapter will first show the cooling and heating scenarios to be set for CFD simulation. Next, the results will be discussed using ventilation effectiveness, CFD ventilation performances, and PMV-PPD.

COOLING AND HEATING SCENARIOS FOR CFD SIMULATION

Similar to the VAV studies in Chapter 5, the same cooling scenarios except for the peak cooling condition were set up for CFD simulation in this chapter. Peak cooling load is not necessary because the supply temperate and flow rate of CAV become identical to VAV. Given the supply temperature of 13^{o}C at peak cooling condition, the maximum flow rate

was fixed and then used for setting up the CAV scenarios. These cooling load scenarios include high cooling load (116 W/m^2), moderate cooling load (47 W/m^2), and low cooling load (9 W/m^2). These scenarios, which were simulated in the last chapter, are all for cooling because the VAV system is not intended for the heating mode. Since CAV is applicable for heating; a single heating scenario was added. This heating scenario is based on morning or evening of winter season as shown in the psychrometric chart (See **Figure 101**).

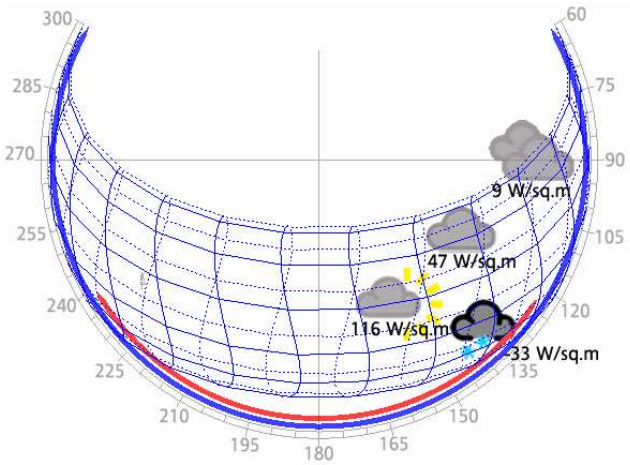

Figure 101 The load scenarios setup in relation to the psychrometric chart

For CFD set up, **Table 18** shows not only the cooling loads coming from each component, but also the pollutant and vapor loads generated by two occupants. Components of three cooling load cases similar to the previous chapter, and a heating scenario, were reported. In this heating scenario, the extreme outdoor temperature of -15^{o}C (5^{o}F) makes heat loss from the glass to be -2017 W. After adding the internal heat from humans, the heat loss reduces to -1871 W, or a heating load density of -33 W/m^2.

	Cooling Load Scenario			
	Case 9W/m^2	**Case 47W/m^2**	**Case 116W/m^2**	**Case -33W/m^2**
Glass SC/ U-value	0.7/ 0.29 Btu/h ft F			
Glass Area	20 m^2			
Conduction	169 W	432 W	839 W	-2017 W[20]
Normal irradiance	207 W	1,576 W	4,987 W	0W
Humans (2 people)	146 W			
Light	0 W	464 W		0 W
Total cooling load	**523 W**	**2,618 W**	**6,436 W**	**-1871 W**
Vapor (2 people)	**5.4x10^{-5}kg/s**			
CO2 (2 people)	**1.5x10^{-5}kg/s**			

Table 18 The cooling/heating, humidity, pollutant load summary for the CAV simulation

[20] Conduction heat loss

The constant flow of 0.68 m^3/sec, or 1,428 cfm, makes the supply velocity in all scenarios constant. Using **Equation 2,** and this fixed flow rate, the supply temperature for each load scenario can be determined and listed in **Table 19**. In the cooling mode, the supply temperature ranges from 22.65°C-14.05°C (72.8°F-57.3°F). This supply temperature range provides a good opportunity to study the humidity control of the CAV system as mentioned earlier. The warm supply temperature was assumed not to provide dehumidification. Ideally, the vapor concentration should be lower than 0.01 kg/m^3 (if the control room temperature is 23.5°C at RH 50%), but vapor concentration was set from 0.017 kg/m^3 to 0.011 kg/m^3 in this study. With this high humidity, inappropriate humidity control can be expected, and its consequences will be discussed in the PMV-PPD section. In reality, CAV does not necessary to have this problem but, as discussed earlier, it requires energy to mitigate this problem. In the heating mode, it is assumed that the dry cold air from outdoor is used as a cooling source; thus, the dehumidification is automatically adequate. This allows the suitable vapor concentration of 0.01 kg/m^3 to be assigned.

	Ventilation Strategies			
	MJV	DV	IJV#1	IJV#2
	CFD#1	CFD#1	CFD#1	CFD#1
Supply Velocity (m/s)	3.14	0.44	3.66	7.32
Flow rate (m^3/s)	0.68	0.68	0.68	0.68
ACH	15.23	15.23	15.23	15.23
Load (116 W/m^2)				
Supply Temp (C)	14.05	14.05	14.05	14.05
Re/Ri	97,586/ 0.015	36,530/ 2.013	105,357/ 0.010	148,998/ 0.002
Vapor Conc (kg/m^3)	0.011	0.011	0.011	0.011
Load (47 W/m^2)				
Supply Temp (C)	19.18	19.18	19.18	19.18
Re/Ri	94,662/ 0.007	35,435/ 0.920	102,200/ 0.005	144,533/0.001
Vapor Conc (kg/m^3)	0.0147	0.0147	0.0147	0.0147
Load (9 W/m^2)				
Supply Temp (C)	22.653	22.653	22.653	22.653
Re/Ri	92,765/ 0.001	34,725/ 0.176	100,152/ 0.001	141,636/ 0.0002
Ri	0.0013	0.1762	0.0009	0.0002
Vapor Conc (kg/m^3)	0.018	0.018	0.018	0.018
Load (-33 W/m^2)				
Supply Temp (C)	26.589	26.589	26.589	26.589
Re	80,347/ 0.005	30,077/ 0.658	86,745/ 0.003	122,676/ 0.0006
Vapor Conc (kg/m^3)	0.0101	0.0101	0.0101	0.0101

Table 19 The CFD supply temperature setup for CAV simulations

Besides pollutant and vapor loads, Re and Ri of each ventilation strategy were also reported in **Table 19**. The supply temperature which is not equal for each scenario makes Ri and Re varied. When supply temperature varies, kinematic viscosity of supply air is affected. Re, which depends on kinematic viscosity, is slightly changed. After calculating DV, which is supplied with the slowest velocity, has the lowest Re, while IJV#2 with the strongest supply velocity has the highest Re. Unlike Re, Ri depends not only the supply velocity, but also the difference between supply and room temperature. In this case, DV has the highest Ri, while IJV#2 has the lowest Ri.

SIMULATION RESULTS

Based on the results simulated by using CFD, the temperature and normalized CO_2 profiles of each ventilation strategy were plotted from **Figure 102** to **Figure 105**.

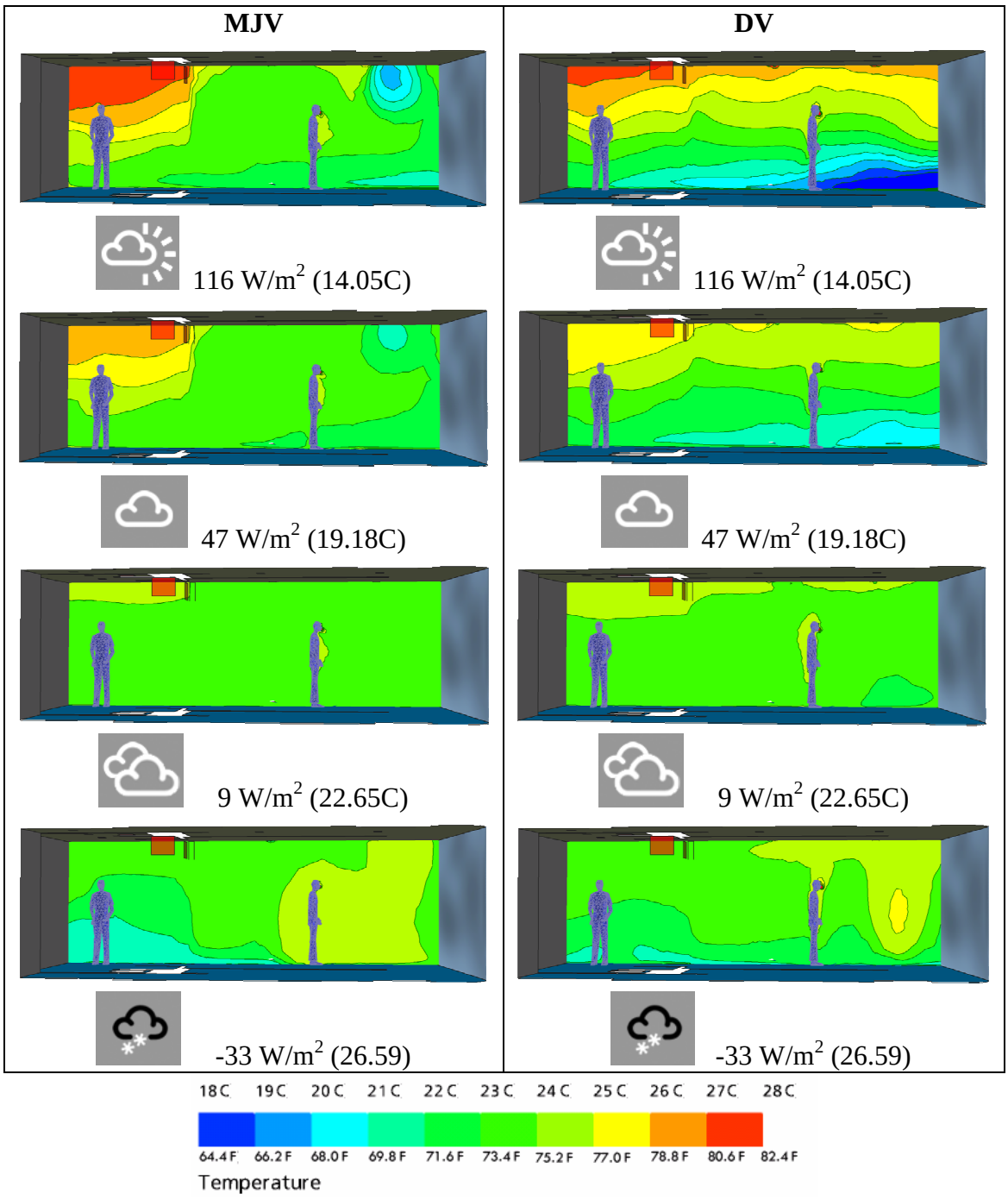

Figure 102 The temperature profiles of MJV and DV under the CAV system

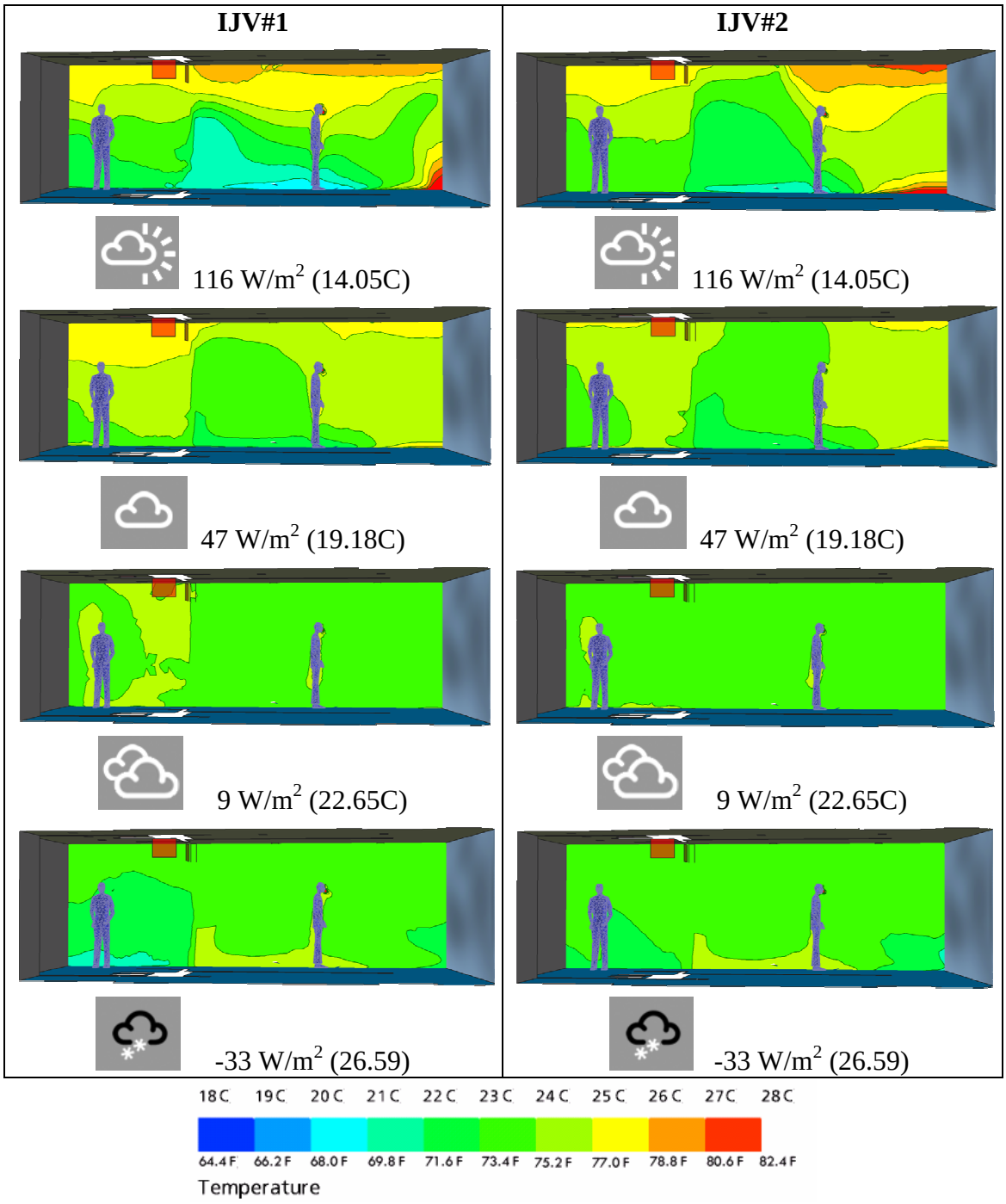

Figure 103 The temperature profiles of IJV#1 and IJV#2 under the CAV system

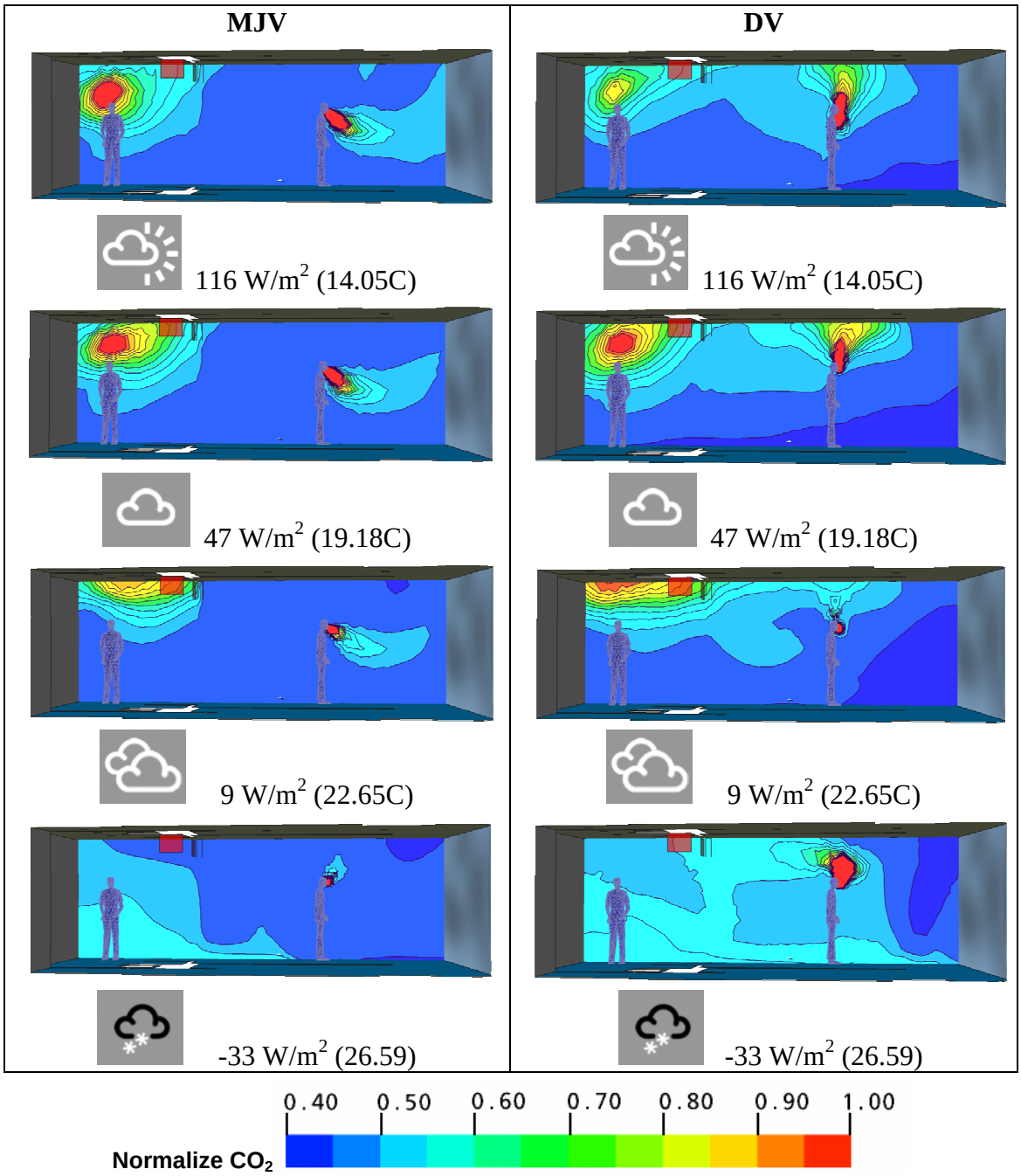

Figure 104 The CO_2 concentration profiles of MJV and DV under the CAV system

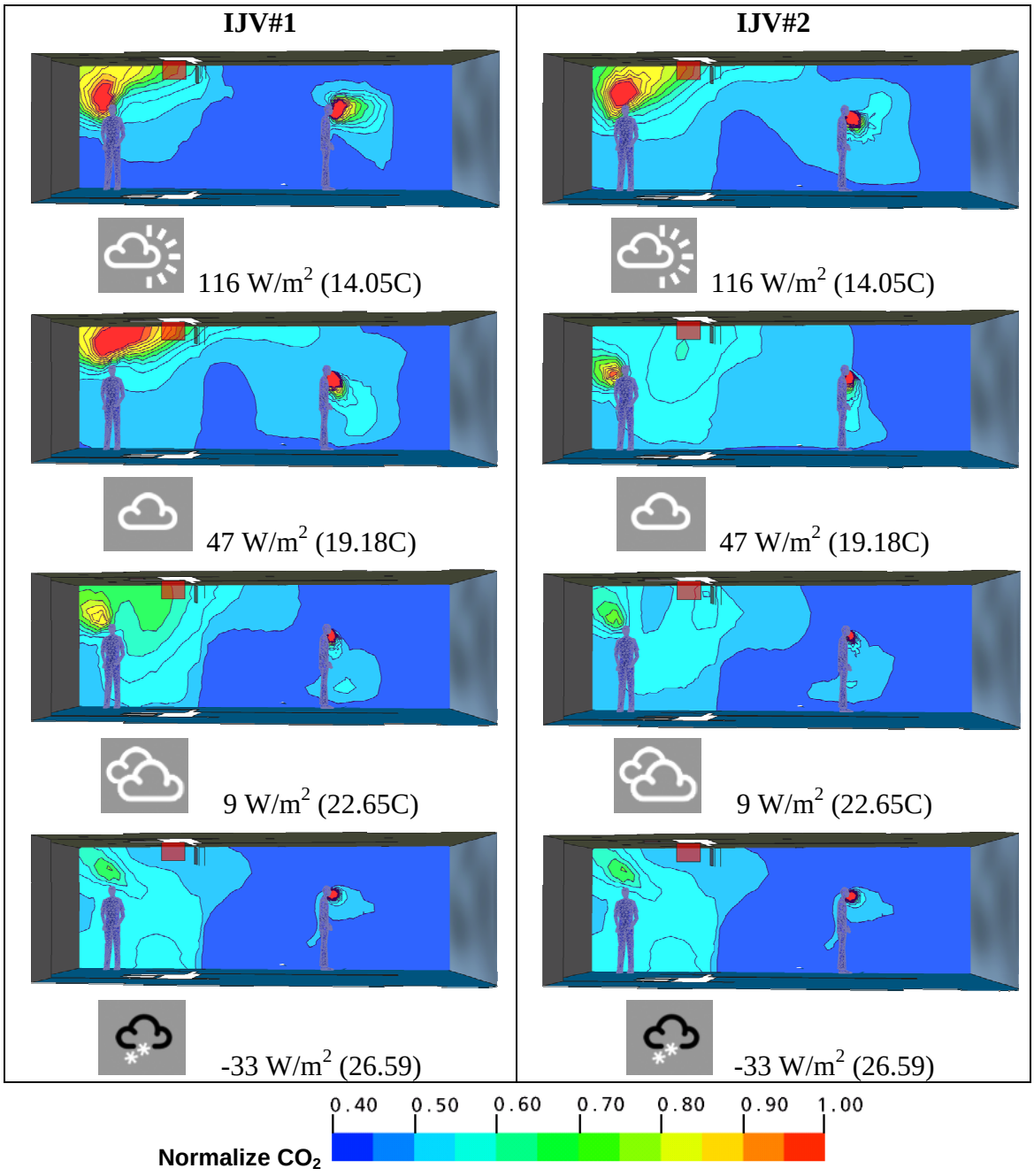

Figure 105 The CO_2 concentration profiles of IJV#1 and IJV#2 under the CAV system

DISCUSSION

Similar to the previous chapter, ventilation effectiveness, CFD ventilation performances, and PMV-PPD, were used as indicators to analyze the CFD results from the CAV system.

Ventilation Effectiveness of ventilation strategies under the CAV system

Under the CAV system, constant flow rate makes ε of each strategy solely affected by the supply temperature. In this analysis, only ε_t and ε_c of a high cooling load (116 W/m^2) and heating were selected to be shown in **Figure 106** to **Figure 109**. In the cooling mode, ε_c tends to be higher than ε_t and high ε near floor decreases toward the ceiling. Having this characteristic the least, MJV has ε_t and ε_c uniformly close to 1.0. On the other hand, DV successfully maintains high ε_t and ε_c within the breathing zone, which is indicated by red highlighted color. High ε_c means that the air is clean as compared to the low ε_c near ceiling where the polluted air is. See **Figure 107**. IJV#2, for which the supply velocity is the fastest, behaves similarly to MJV, but IJV#1, which has lower supply velocity, tends to be the same as DV. Higher ε can be expected from IJV#1, because it successfully utilizes stratification, while strong supply velocity of IJV#2 mixes heat and pollutants too well. Given this result, it confirms the findings from the previous chapter, that the supply velocity strongly affects performances of IJV system.

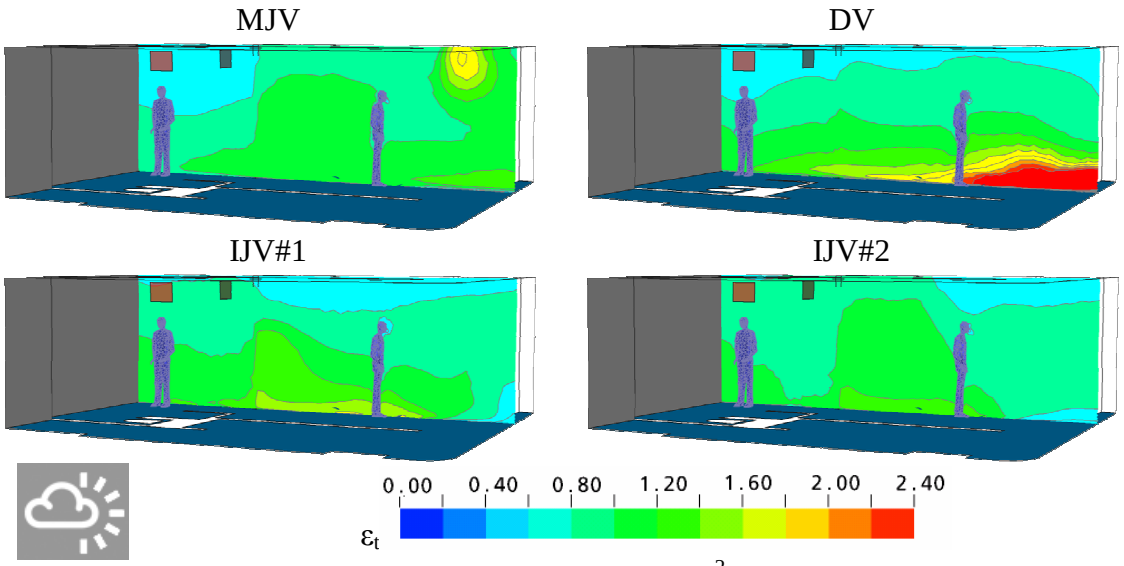

Figure 106 ε_t of the high cooling load of 116 W/m^2 under the CAV system.

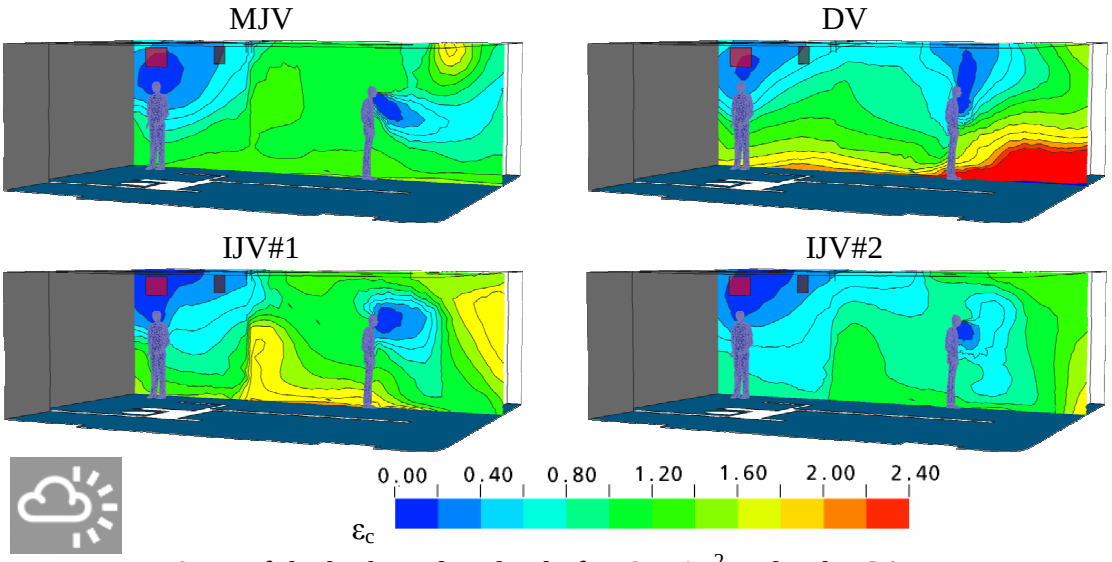

Figure 107 ε_c of the high cooling load of 116 W/m^2 under the CAV system

In the heating mode (**Figure 108** and **Figure 109**), warm supply temperature works against MJV and DV. The warm supply air of MJV and DV floats toward the ceiling, and the results are the dropping of both ε_t and ε_c. Compared to MJV, this warm supply temperature tends to negatively impact DV the most. Unlike both DV and MJV, IJV has sufficient velocity to maintain the supply air within the breathing zone, and this keeps ε_t and ε_c high. Similar to the cooling mode, low supply velocity is more effective in providing high ε_t and ε_c than the high velocity. In some areas, it is still possible to see poor ε_t and ε_c. This area is the restroom, where the side-wall blocks the supply air from flowing into the room properly.

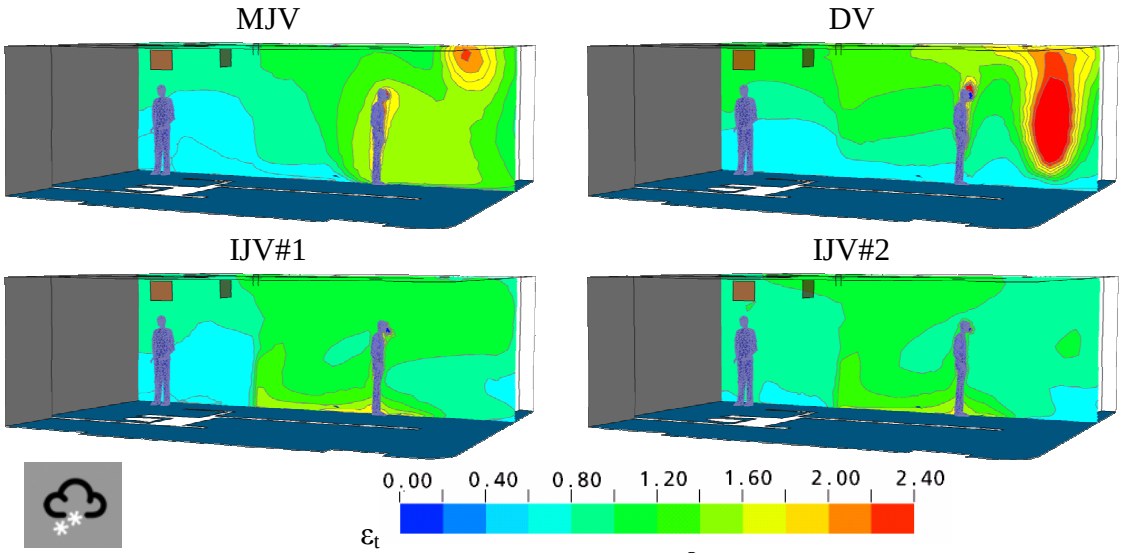

Figure 108 ε_t of the heating load of -33 W/m^2 under the CAV system

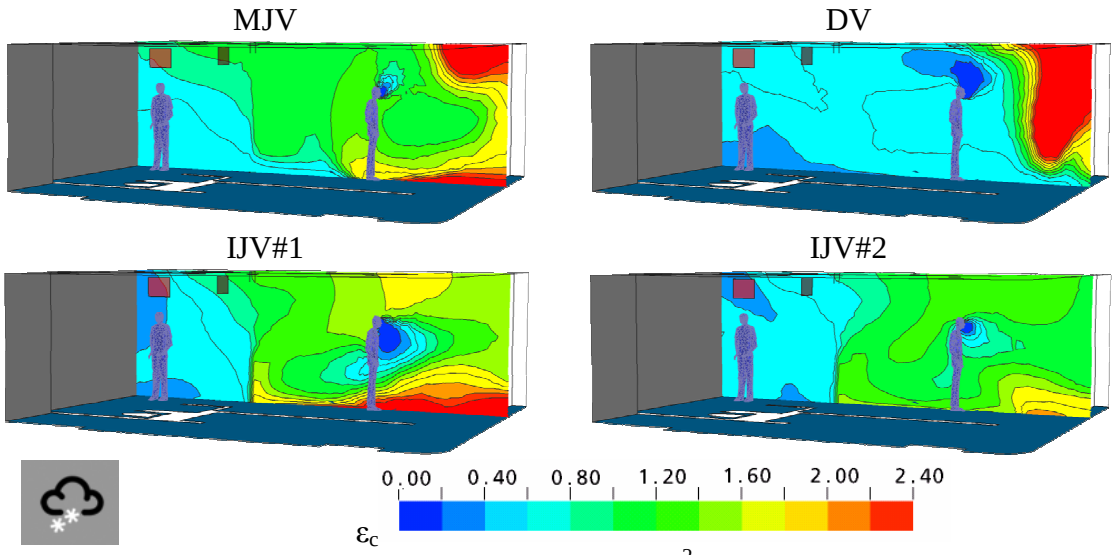

Figure 109 ε_c of the heating load of -33 W/m^2 under the CAV system

ε_t and ε_c of the CAV system were quantitatively plotted in **Figure 110**. Both the ε_t and ε_c of all strategies exceed 1.0 in all scenarios, except heating. Similar to the discussion earlier, IJV#1 performs better than IJV#2. When supply temperature increases to 16^{o}C or 61^{o}F (a cooling load of 90 W/m^2), ε_t and ε_c of IJV#1 are high, or the same as the DV system. When cooling load goes lower than this point, the supply temperature is forced to be warmer. This supply temperature becomes equal to the room temperature when the cooling is almost nothing. At his point, the jet characteristics of both DV and MJV become isothermal and fully exposed without any tilted angle caused by buoyancy. This clean jet air directly exposes the CFD nodes used for ε_t and ε_c calculation, and thus increases both indicators sharply. In this case, ε_c of MJV and DV reaches 1.7 and 2.0, respectively. This characteristic does not happen to IJV because the shape of impinging jet is almost consistent regardless of any supply temperature as discussed in Chapter 3. Based on this finding, practitioners should be aware that IJV can still maintain high ε_t and ε_c with supply temperature warmer than 16^{o}C, but both MJV and DV do better. This result is reversed when heating is applied. DV performs poorly by having ε_c of 0.82, which is even lower than ε_t. It corresponds to the recommended ε_c for DV made by ASHRAE 62-2004, which is at 0.7 [7]. See **Table 5**. ASHRAE 62-2004 also recommends ε_c for MJV in heating mode at 0.8, while ε_c of 0.9 is found in this study. In this study, it was also found that ε_c of IJV#1 can be highest with heating, and it can reach

1.2. This ε_c drops in IJV#2 to 0.9, which is equal to MJV. Again, the strong supply velocity can reduce ε_c. Therefore, the appropriate supply velocity should be used. It is true that the supply velocity of 3.66 m/s is adequate to achieve high ε_c (reaching 1.2), but when supply velocity goes lower, the impact on ε_c is unknown. This indicates the necessity of future studies of IJV performances in the heating mode.

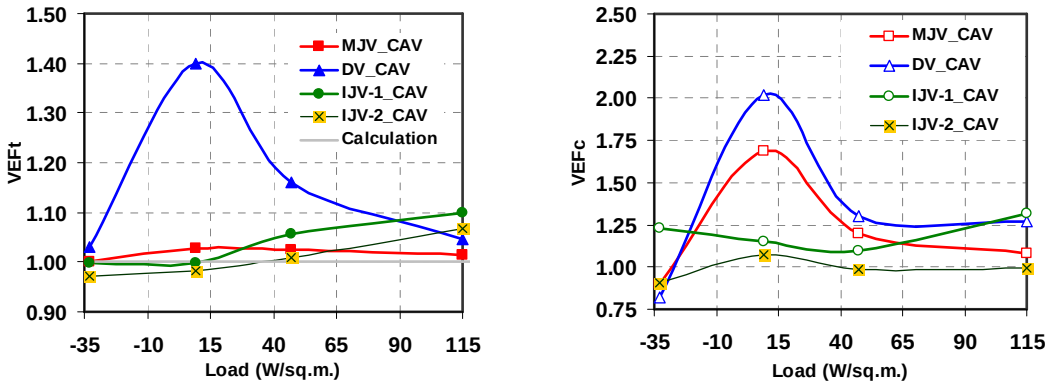

Figure 110 average ε_t (left) and ε_c (right) for the CAV system.

CFD Ventilation Performances of ventilation strategies under CAV system

CFD ventilation performances including stratification discomfort, draft, and normalized CO_2 were calculated using **Equation 15, Equation 16,** and **Equation 17** and then analyzed below. From **Figure 111** to **Figure 113**, CFD ventilation performances were plotted against different cooling and heating loads and the results will be discussed as follows.

Similar to VAV system, MJV has no stratification discomfort problems, but the draft can be severe. A draft at 1.8m height is at 0.22-0.28, consistently, while a draft at 1.1m height drops to 0.17-0.22. When supply temperature increases, the draft reduces slightly, like the normalized CO_2 as shown in **Figure 113**. The CO_2 level at a 1.8m height is slightly higher than that of a 1.1m height. Corresponding to the ε_c, normalized CO_2 in the heating mode sharply increases. The streamline analysis in **Figure 114** confirms this result by revealing that the warm jet supplying for MJV terminals attaches to the ceiling, and poorly circulates throughout the breathing zone. Only when the supply temperature comes close to the room temperature, can better normalized CO_2 be expected from the MJV system.

Unlike MJV, DV faces the stratification discomfort problem if supply temperature is too cool. Stratification discomfort still reaches 0.44 when supply temperature is at 14.05^{o}C

(57°F). It takes a supply temperature up to 19.18°C (66.5°F) to reduced stratification discomfort to zero. This finding correlates with previous research that recommends supply temperature of DV to be only 2-3°C less than control temperature [12, 13]. In compensation of stratification discomfort, less draft is an advantage of the DV system. Draft is minimized for both 1.8m and 1.1m heights for all cooling and heating loads, but still the draft in heating mode can reach 0.08, which is far less than the draft from MJV. In cooling mode, normalized CO_2 at 1.8m is significantly higher than 1.1m, and this CO_2 level decreases significantly when supply temperature is close to the room temperature (9 W/m^2). Like ε_c, the normalized CO_2 at the sitting level (1.1m) increases when supplied with heated air. See **Figure 114**. Similar to MJV, DV is suitable when supply temperature comes close to the control temperature (not too warm and cold). It will not only minimize stratification discomfort, but also provide lower normalized CO_2.

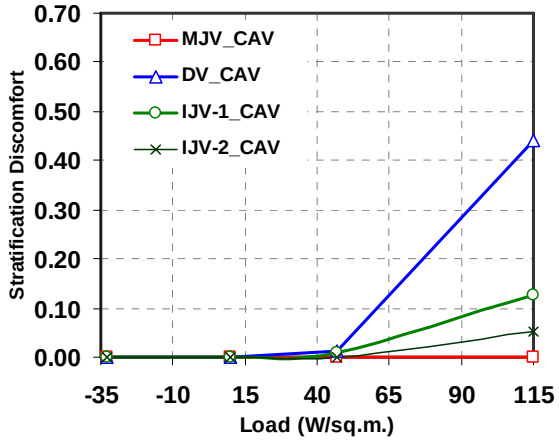

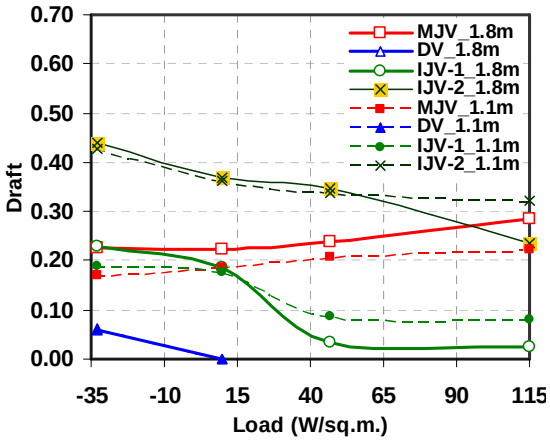

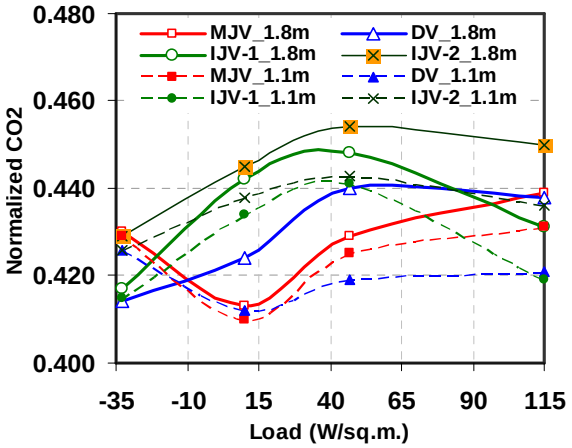

Figure 111 Stratification discomfort of different ventilation strategies under the CAV system (top left)

Figure 112 Draft of different ventilation strategies under the CAV system (top right)

Figure 113 Normalized CO_2 of different ventilation strategies under the CAV system (bottom left)

Referring to the VAV analysis, if the velocity is too strong, IJV might not perform as well as expected. Since IJV#1 supplies air in a more suitable range (not more than 2 m/s), the results confirm that IJV#1 performs better than IJV#2. Stratification discomfort of

IJV#1, which is usually a major drawback, is significantly resolved if supplied with air in a warmer temperature range 14-19^{o}C (57^{o}F-66.5^{o}F). Compared with the VAV system, stratification discomfort is reduced by half if the supply temperature is raised only 1^{o}C. This provides an alternative for reducing stratification discomfort besides accelerating supply velocity as is done in IJV#2. The strong supply velocity of IJV#2 produces the highest draft for both 1.8m and 1.1m heights, and it can reach 0.45 in the heating scenario. When supply velocity is reduced by half, draft also drastically decreases as demonstrated by IJV#1. Still, the draft of IJV#1 reaches the peak at 0.20 in the heating mode. For IAQ, IJV#1 has not only lower draft, but also lower normalized CO_2 at both 1.8m and 1.1m heights. Unlike DV and MJV, IJV does not perform well when supply temperature is close to control temperature where the normalized CO_2 can slightly increase in this supply temperature range. The reason comes for the jet characteristics of IJV, which is previously discussed in the ventilation effectiveness section. This poor performance can be reversed when heating is applied. The normalized CO_2 level drops for both of the IJV cases, but only IJV#1 can have CO_2 level lower than the rest. The reason can be seen from IJV streamline plot in **Figure 114**, which shows that IJV#1 has adequate supply velocity to keep the heated supply attached to the floor.

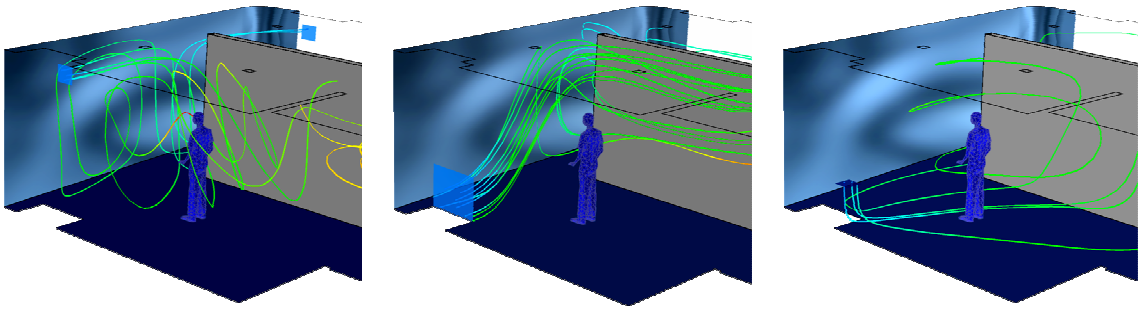

MJV **DV** **IJV**

Figure 114 The streamline plot of the heating system

Overall, IJV should be used in the CAV system when the supply temperature is either lower than 16^{o}C or high than the room temperature [35] with suitable supply velocity (not more than 2m/s). With the supply temperature close to room temperature, the stratification discomfort problem is solved, but the CO_2 level surpasses other strategies.

PMV-PPD of different ventilation strategies under the CAV system

The PMV of all strategies were plotted in **Figure 115**. Similar to the VAV system, the PMV improves when the cooling load is low. PMV can be poor near glass due to glass radiation and temperature, which can be either too hot or too cold. This high or low PMV near glass in extremely high and low loads is the cause of a high PPD that can exceed 10%.

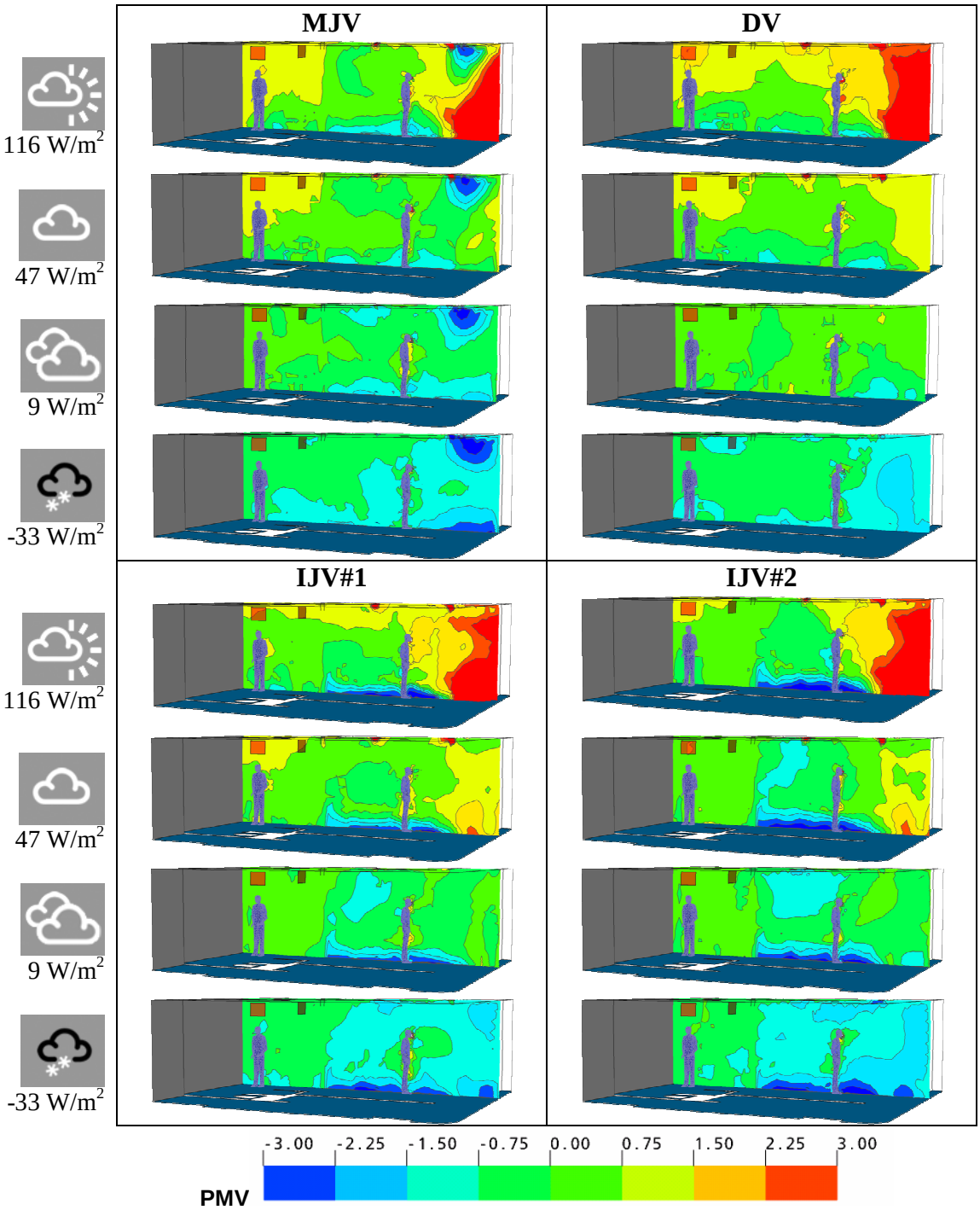

Figure 115 The PMV of MJV and IJV under the CAV system

The blue highlighted color in **Figure 115** is low PMV occurring near the floor for both IJV#1 and IJV#2. This indicates that the supply velocity of both IJV might be too strong. IJV#1 with the supply velocity of 3.66 m/s might have a high ε, but undesirable PMV-PPD near the floor is still problematic. To solve this problem, lower supply velocity should be utilized. The appropriate supply velocity range can be referred to the VAV studies in the last chapter. **Figure 98** shows that the supply velocity of around 2 m/s of IJV#2 at 47 W/m^2 does not create the low PMV-PPD near the floor. Accordingly, this supply velocity of 2m/s should again be used as a threshold for IJV supply velocity.

PMV at the body core height (1.1m) can be converted to PPD as shown in **Figure 116**. PPD of all strategies is minimized when cooling load is almost nothing. Compared to VAV, PPD is still high, and the reason might be because of the humidity. Humid air was supplied to study the impact of poor dehumidification, which might happen in CAV. This high RH did occur in CAV, and caused PPD to be higher than expected. Among these ventilation strategies, DV, which has the lowest supply velocity and draft, tends to minimize PPD most if cooling load is below 40 W/m^2. With an almost similar supply velocity, IJV#1 performs almost identically to MJV. The high supply velocity of IJV#2 increases draft and causes the highest PPD in the heating scenario. Low supply velocity can lower the PPD to be less than 10%, and allows the appropriate cooling and heating loads to be broader as it did in DV. DV has the widest load of -8 to 20 W/m^2 which allows PPD to be less than 10%. When cooling load is high (more than 50 W/m^2), this low velocity is no longer desirable because it can not create a cooling effect for bringing down the PMV. The supply velocity of MJV and IJV is strong enough to create this cooling effect, but still not enough to reduce PPD to be less than 10%. The more effective solution is to use or design the proper building envelopes. Similar to the VAV system, the use of low U-value and less SHGC can reduce envelops' heat transfer, and cause less PPD from glass. This finding confirms that the energy efficient design is the most effective strategy to enhance thermal comfort given the choices of any operation system and ventilation strategy.

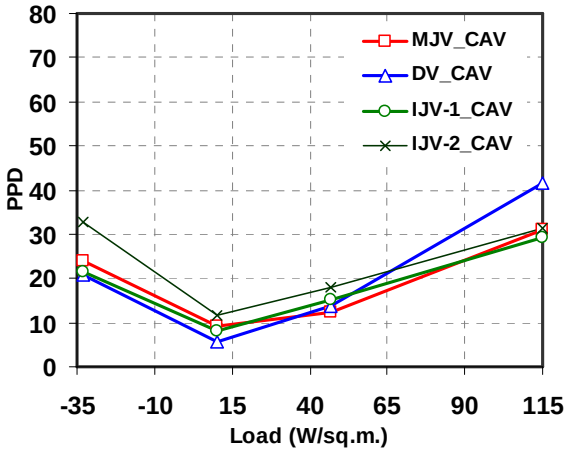

Figure 116 The PPD of all strategies under the CAV system

SUMMARY

In the CAV system, the supply velocity and temperature of the IJV system alternates its ventilation effectiveness, CFD ventilation performances, and PMV-PPD. Among these indictors, low PMV near floor is the most critical parameter for IJV, and can be avoided if the supply velocity is less than 2 m/s. With supply temperature of 14-16^{o}C in cooling mode, this supply velocity makes the performances of IJV superior to other strategies. Within this range, ventilation effectiveness is higher than 1.0 with almost no stratification discomfort and draft problem. When supply velocity is stronger than this threshold, draft and PMV-PPD can exceed the appropriate level. If supply temperature is warmer than 16^{o}C, the IAQ can become worse than MJV and DV. On the other hand, if IJV is operated in the heating mode, the ventilation effectiveness and CFD ventilation performances are recovered and become better than both MJV and DV.

Different ventilation strategies were extensively studied in this and the previous chapter. Still, the results which are the appropriate IJV parameters came from a single case study. When geometries and volumes of the studied space are changed, the impacts are not yet known. The next chapter is dedicated to the studies of these impacts.

CHAPTER 7

PERFORMANCES OF DIFFERENT VENTILATION STRATEGIES UNDER DIFFERENT SPACE VOLUMES

In previous chapters, many advantages of IJV have been indicated, but the results are based only on a single space, which is categorized as a medium size space (55.25 m^2, 595 ft^2). Two additional spaces were added in order to compare the performances of the IJV system under the different space volumes. The additional spaces include a small space (13.81 m^2, 149 ft^2.) and a large space (334 m^2, 3594 ft^2.). This makes the medium space larger than the small space by four times and the large space larger than the small space by 24 times. See **Figure 117**. Similar to the volume sizes, the floor to ceiling heights ranging from small to large are 3m (10ft), 3.3m (11ft), and 4.5m (15ft), respectively.

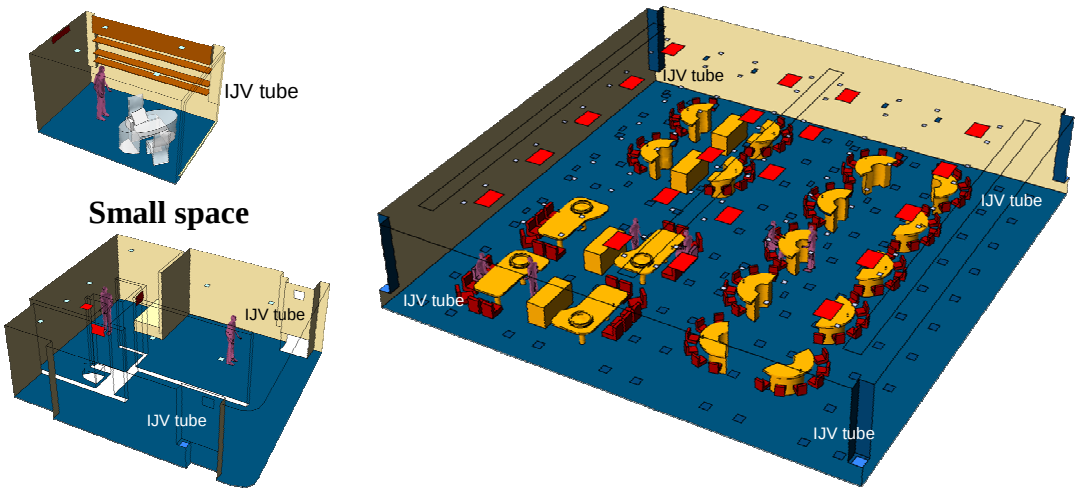

Figure 117 The small, medium, and large space for the IJV studies

Results show that IJV#2 with a wide range of supply velocities generates drastic results regarding drafts. Part of the study was already done in the medium space discussed in the previous chapters. In this chapter, IJV#2 was applied to the small space, which is a personal office, and the large space which is a casino hall. Using normalized flow rate discussed in the following section, the supply velocity is set to be equal in all spaces. Next, these spaces were tested under four cooling load scenarios ranging from low to

peak using a VAV system. Based on these results, indicators to be discussed include ventilation effectiveness, CFD ventilation performances, and PMV-PPD.

NORMALIZED VENTILATION RATE

In order to study the impacts of space size, the parameters such as cooling and pollutant loads must be normalized by keeping load and pollutant density equal for all spaces. Dividing load (q) by an area (A), a load density can be used to compute flow rate per area or normalized flow rate (Q/A) as demonstrated in **Equation 36**. To be able to compare different space volumes against ventilation indices, all spaces must have equal supply velocity. The equal velocity can be obtained by using **Equation 37** where the ratio (η) between supply area (a) and room area (A) must be identical in all spaces. Combining **Equation 37** and **Equation 36**, the result is **Equation 38**. Similar values for η and the cooling load density (q/A) make the supply velocity (v or Q/a) for all spaces identical. In this study, η is constant at 0.0016 or supply area is 0.16% of the room area.

$$\frac{Q}{A} = \frac{q/A}{k(T_a - T_s)} \qquad \text{Equation 36}$$

$$\eta = \frac{a}{A} \qquad \text{Equation 37}$$

$$\eta\frac{Q}{a} = \eta v = \frac{q/A}{k(T_a - T_s)} \qquad \text{Equation 38}$$

Where
- Q = flow rate (CFM, m^3/sec)
- q = total cooling load (Btu/h, W)
- T_a = room temperature (F, C)
- T_s = supplied temperature (F, C)
- k = 1.08 in IP system, 1.227 in SI system
- A = room area (ft^2, m^2)
- a = supply free area (ft^2, m^2)
- v = supply velocity (fpm, m/sec)

In order to compare space sizes, not only load density, but also pollutant load density must be controlled. **Equation 39** shows how the CO_2 load (M_p) is normalized by the room area (A). In all space volumes, the normalized CO_2 load (M_p/A) must be kept the same, and this will make normalized flow rate (Q/A) identical as well. Here, as expected, this normalized flow rate based on CO_2 load is less than for the cooling load (as discussed in chapter 2), so the latter was used as overall flow rate to be specified in CFD simulation.

$$\frac{Q}{A} = \frac{M_p / A}{(C_a - C_s)}$$ Equation 39

Where Q = supplied flow rate (m^3/s)
M_p = total CO_2 emission rate (kg/s)
C_a = room air CO_2 level (kg/m^3)
C_s = supplied air CO_2 level (kg/m^3)
A = room area (ft^2, m^2)

COOLING LOAD SCENARIOS AND eQUEST SIMULATION

The cooling load set up for this chapter is the same as in Chapter 5, which ranges from low (9 W/m^2), moderate (47 W/m^2), high (116 W/m^2), and peak (160 W/m^2). **Table 20** concludes the cooling load components by relying on the solar positions from the sunchart for 42°N as shown in **Figure 82**. Based on this sunchart, the peak cooling load occurs during winter season (February) from the low sun angle radiating on south glass. In addition to cooling load components, normalized CO_2 and vapor load from occupants were added in this table.

Cooling Load Scenario				
Small Space (13.81 m^2.)				
	Case 9W/m^2	**Case 47W/m^2**	**Case 116W/m^2**	**Case 160W/m^2**
Conduction	0 W	65.48 W	279.67 W	-362.89 W
Vertical radiation	0 W	184.56 W	924.75 W	2,407.55 W
Humans (1 people)	73 W			
Light (appliances)	73.27 W (51.2W)	232.34 W (93 W)	232.34 (93W)	0 (93 W)
Total cooling load	**124.48 W**	**650 W**	**1,603 W**	**2,210.3 W**
Vapor	**$1.35x10^{-5}$kg/s**			
CO2	**$0.375 x10^{-5}$kg/s**			
Medium Space (55.25 m^2.)				
	Case 9W/m^2	**Case 47W/m^2**	**Case 116W/m^2**	**Case 160W/m^2**
Conduction	169 W	432 W	839 W	-726 W
Vertical radiation	207 W	1,576 W	4,987 W	8,982 W
Humans (2 people)	146 W			
Light (appliances)	0 W	464 W		
Total cooling load	**523 W**	**2,618 W**	**6,436 W**	**8,866 W**
Vapor	**$5.4x10^{-5}$kg/s**			
CO2	**$1.5x10^{-5}$kg/s**			
Large Space (334 m^2.)				
	Case 9W/m^2	**Case 47W/m^2**	**Case 116W/m^2**	**Case 160W/m^2**
Conduction	0 W	986.78 W	3,322.17 W	3,322.17 W
Vertical radiation	0 W	7,228.4 W	27,707.85 W	42,647.73 W
Humans (6 people)	439.62 W			
Light (appliances)	2089.22 W (486.9 W)	6,691.45 W(486.9 W)		
Total cooling load	**3,015 W**	**15,832 W**	**38,647 W**	**53,587 W**
Vapor	**$32.4x10^{-5}$kg/s**			
CO2	**$9x10^{-5}$kg/s**			

Table 20 Cooling load components summary for IJV with different space volumes

CFD modeling and parameters setup

In addition to the cooling load scenarios, the space volumes relate directly to CFD meshing resolution. This meshing resolution should be reported and discussed as one of the requirements for ASHRAE RP-1133. **Figure 118** shows the meshing results of three space volumes using the ANSYS ICEM 10 software [52]. Meshing types and resolution are critical for obtaining a good CFD model. In this study, the global meshing is meshed by an unstructured element, such as tetra-type, which was assigned for assembly or control volume (body) and surfaces (elements). The size of these tetra meshes was set to be large for minimizing the file size, but this resolution might not be fine enough to predict the flow near objects. The finer meshes near objects or boundaries (such as walls) are needed because the flow properties near these areas sometimes change rapidly. This limitation was solved by assigning finer resolution at the objects and using the prism-type meshes as multiple layers. The prism layers allow meshes to grow from thin layers to thicker layers, which then blend with the typical tetra meshes in the space.

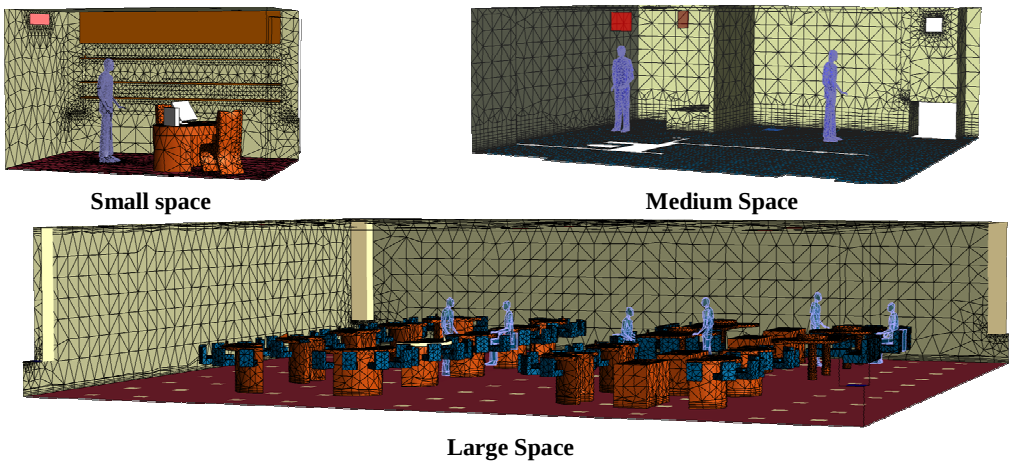

Figure 118 The meshing results of the three space volumes

The resolution of meshed surfaces depends on surface size and details. The smaller surfaces require the finer meshing resolution. **Table 21** shows all meshing sizes used in previous chapters and this chapter. Nodes are meshes in the fluid body, while elements are meshes on the object surfaces. The small and medium spaces have a similar combined number of nodes and elements at around 185,000, while the large space has the highest number of nodes and elements at almost 1,200,000. The meshing size of 1,200,000 requires a lot of computational power which, in this study, came from a computer with 64-bits quad core (4x1.7 GHz) processors. Larger numbers of nodes and elements

increases computational time rapidly, but the denser nodes and elements generally reduce error from the CFD simulation. The optimum meshing resolution can be reached when the flow properties become independent of grid resolutions, or so-called grids independency [10, 57]. To have both accurate results and less computational time, the meshes of all three space volumes are complied with this criterion.

	Small space		**Medium Space**		**Large Space**	
Components	Component Name	Meshing size (inches)	Component Name	Meshing size (inches)	Component Name	Meshing size (inches)
Inlet	IJV, NOSE	3, 0.2	IJV, NOSE	3, 0.5	IJV, NOSE	3, 0.6
Outlet	OUTLET	6	OUTLET	6	OUTLET	12
Wall	LIGHT, HUMAN	3, 4	LIGHT, HUMAN	3, 4	LIGHT, HUMAN	3, 4
Assembly (body)	ROOM	24, 1x3 (1.2 rate)	ROOM	18, 1x6 (1.2 rate)	ROOM	30, 1x5 (1.2 rate)
Elements	**147,123**		**144,673**		**949,387**	
Nodes	**38,002**		**34,519**		**216,384**	

Table 21 The meshing details summary

	Ventilation Strategies		
	Small	Mid	Large
	CFD#1	CFD#1	CFD#1
Load (160 W/m^2)			
Normalized Flow rate (m^3/h m^2)	44.3		
Normalized Flow rate (cfm/ft^2)	2.4		
Velocity (m/s)	7.32		
Re	63,817	127,635	312,640
Ri	0.001099	0.00220	0.005386
Load (116 W/m^2)			
Normalized Flow rate (m^3/h m^2)	32.57		
Normalized Flow rate (cfm/ft^2)	1.77		
Velocity (m/s)	5.38		
Re	46,914	93,828	229,832
Ri	0.002036	0.00407	0.009972
Load (47 W/m^2)			
Normalized Flow rate (m^3/h m^2)	13.03		
Normalized Flow rate (cfm/ft^2)	0.71		
Velocity (m/s)	2.15		
Re	18,757	37,514	91,890
Ri	0.01275	0.02550	0.06247
Load (9 W/m^2)			
Normalized Flow rate (m^3/h m^2)	2.61		
Normalized Flow rate (cfm/ft^2)	0.14		
Velocity (m/s)	0.430		
Re	3,751	7,503	18,378
Ri	0.318792	0.63758	1.561755

Table 22 The normalized flow rate and supply velocity of the IJV summary

Identical to the previous chapters, the supply velocity and flow rate are reported in **Table 22**. For matching the flow rate from different space volumes, flow rate was normalized by the room area. By using **Equation 38**, the results are the equal supply velocity for

each cooling scenario. Then, the supply velocity and temperature were used to compute Re and Ri, which are also reported in this table.

SIMULATION RESULTS

The CFD simulation results are shown in **Figure 119** to **Figure 126** which include the results from the four cooling loads scenarios.

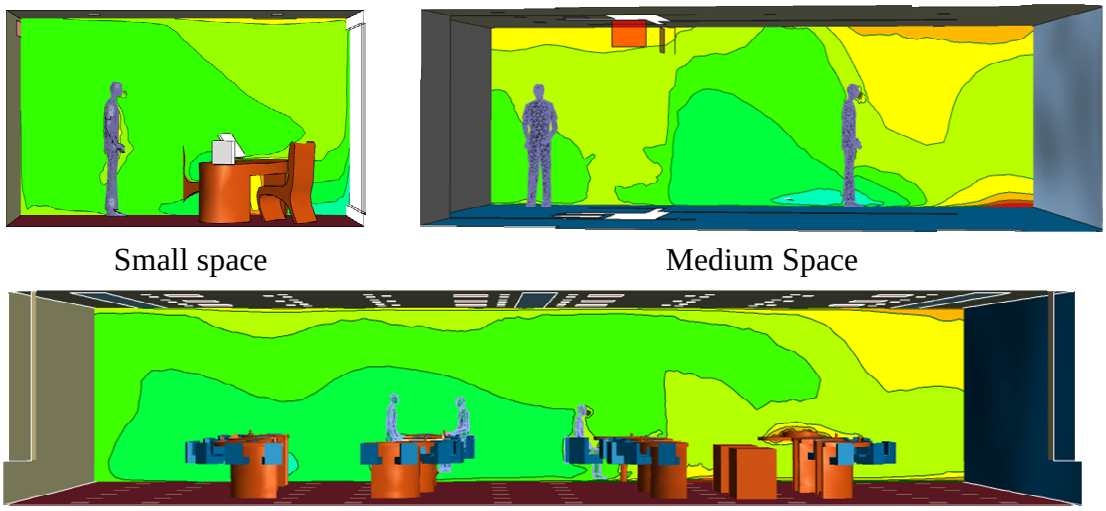

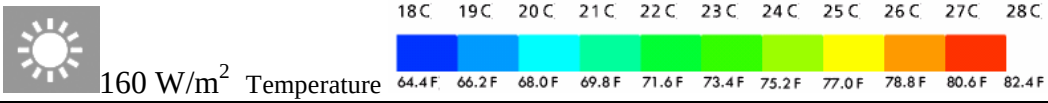

Figure 119 Temperature of different space volumes at the cooling load of 160 W/m^2

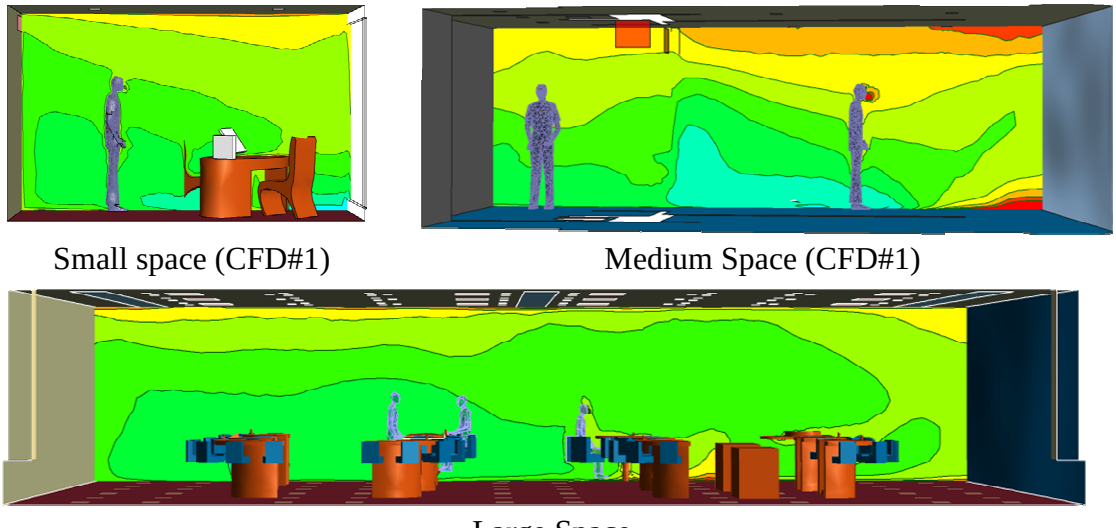

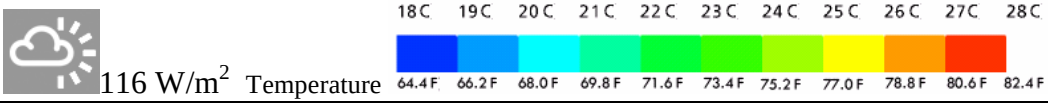

Figure 120 Temperature of different space volumes at the cooling load of 116 W/m^2

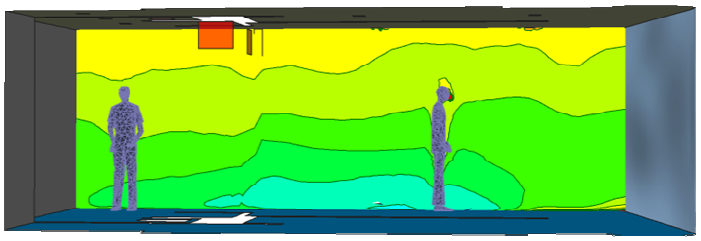

Small space

Medium Space

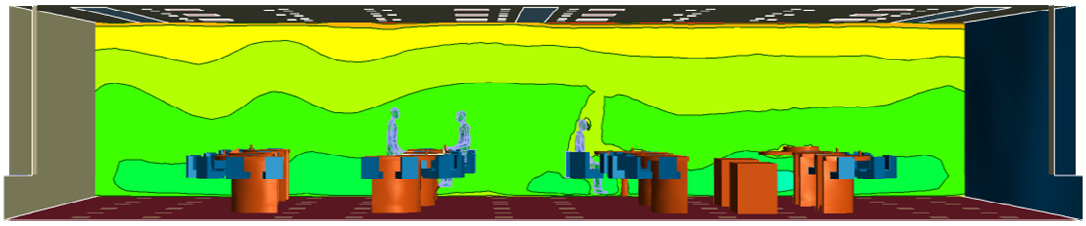

Large Space

47 W/m^2 Temperature

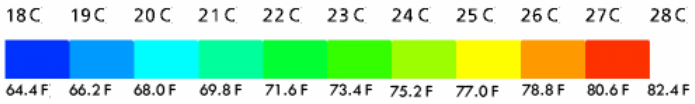

Figure 121 Temperature of different space volumes at the cooling load of 47 W/m^2

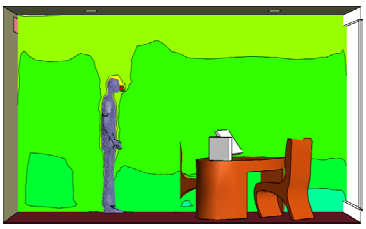

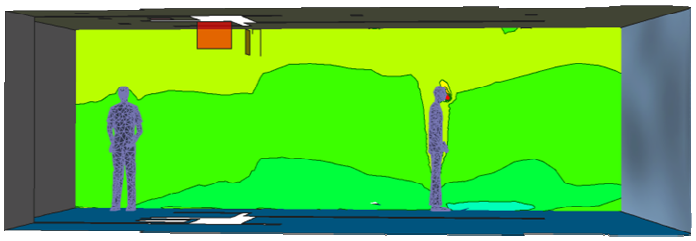

Small space (CFD#1)

Medium Space (CFD#1)

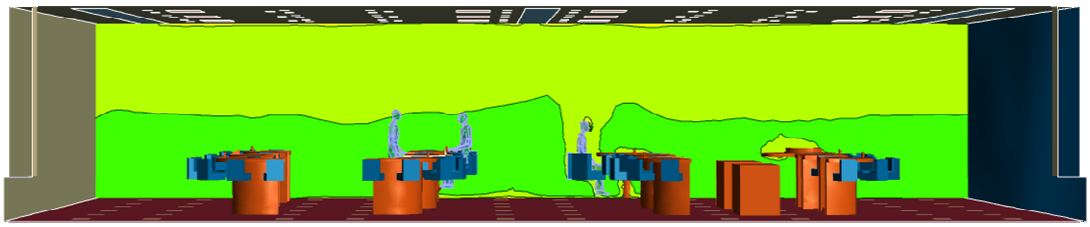

Large Space

9 W/m^2 Temperature

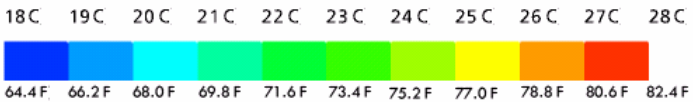

Figure 122 Temperature of different space volumes at the cooling load of 9 W/m^2

Temperature profiles are shown in **Figure 119** to **Figure 122** and the normalized CO_2 profiles are shown in **Figure 123** to **Figure 126**.

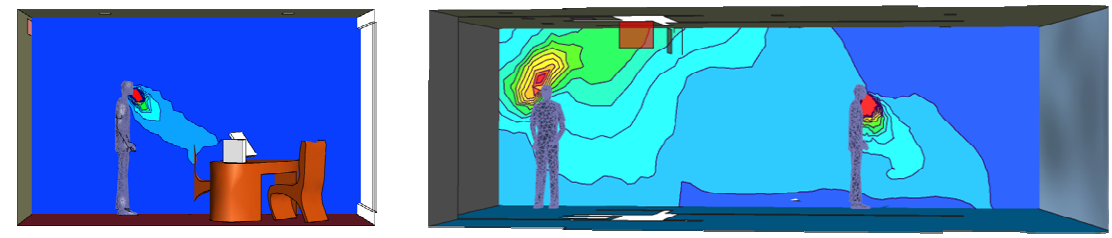

Small space Medium Space

Large Space

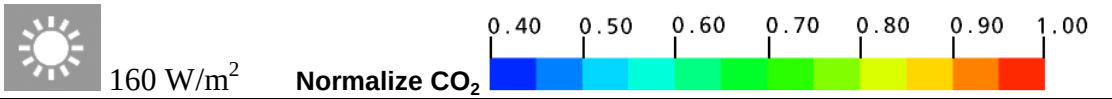

Figure 123 Normalized CO_2 of different space volumes at the cooling load of 160 W/m^2

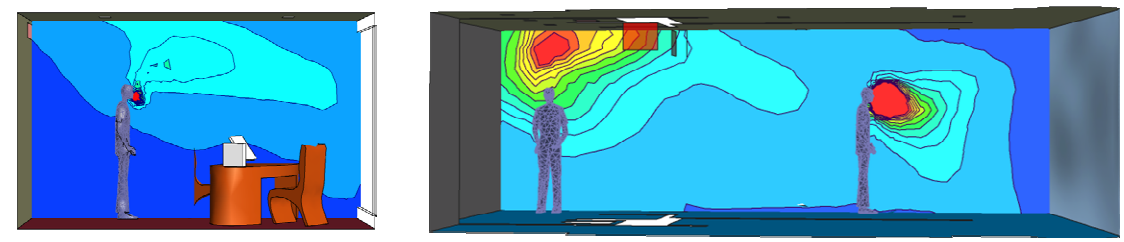

Small space Medium Space

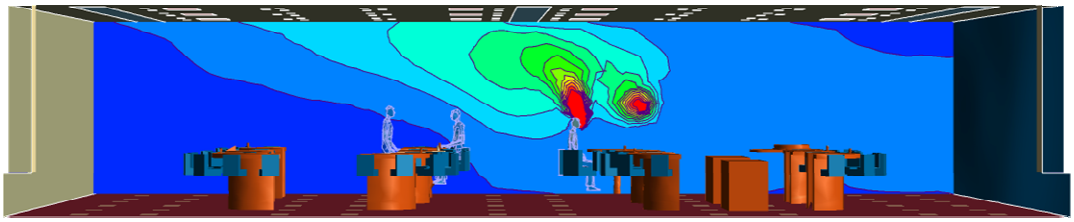

Large Space

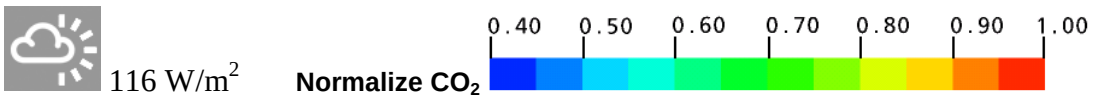

Figure 124 Normalized CO_2 of different space volumes at the cooling load of 116 W/m^2

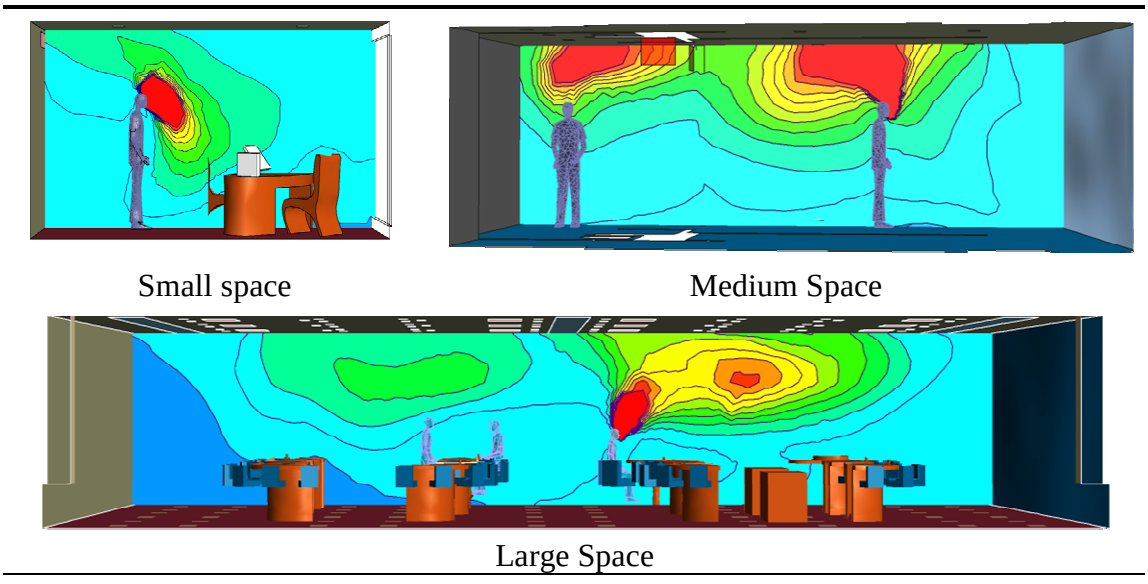

Figure 125 Normalized CO_2 of different space volumes at the cooling load of 47 W/m^2

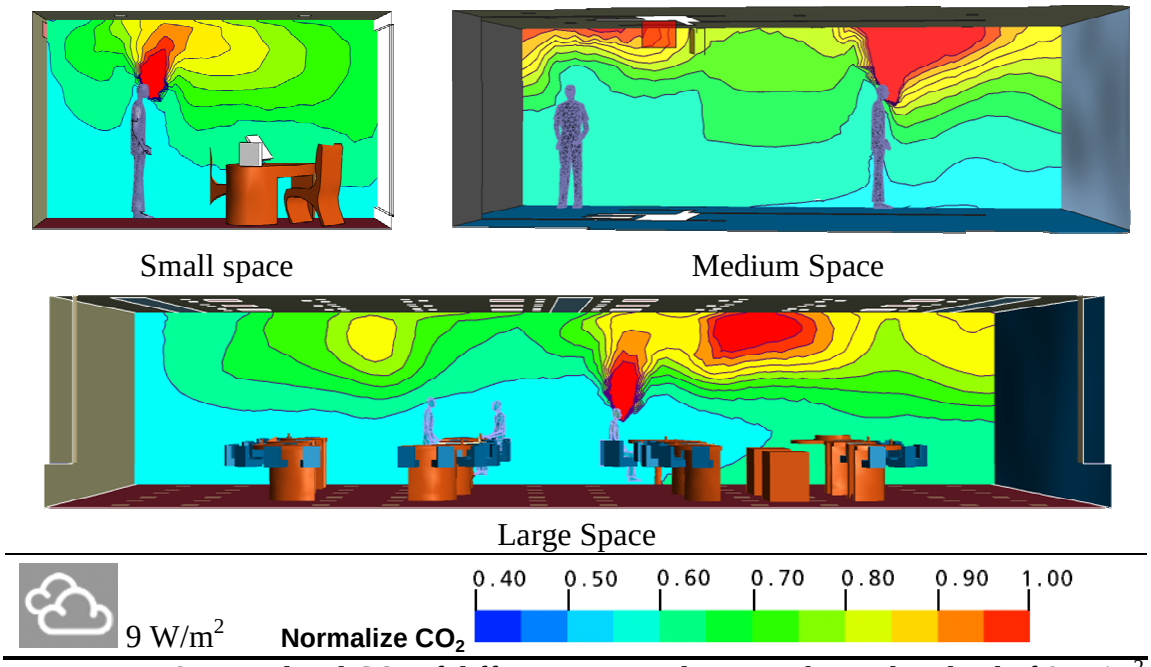

Figure 126 Normalized CO_2 of different space volumes at the cooling load of 9 W/m^2

DISCUSSION

Like most of the previous chapters in this dissertation, the discussion can be divided into three parts. These include ventilation effectiveness, CFD ventilation performances, and PMV-PPD.

Ventilation Effectiveness of IJV in different space volumes under VAV system

ε_t of the IJV system in different space volumes was plotted in **Figure 127** and **Figure 128**. IJV successfully maintains high ε_t in the breathing zone and ε_t tends to be improved if the cooling load increases. ε_t higher than 1.0 occurs in all spaces but the large space tends to have an upper hand. At cooling load of 116 W/m^2, radiation and high surface temperature reduces ε_t monitored near the glass.

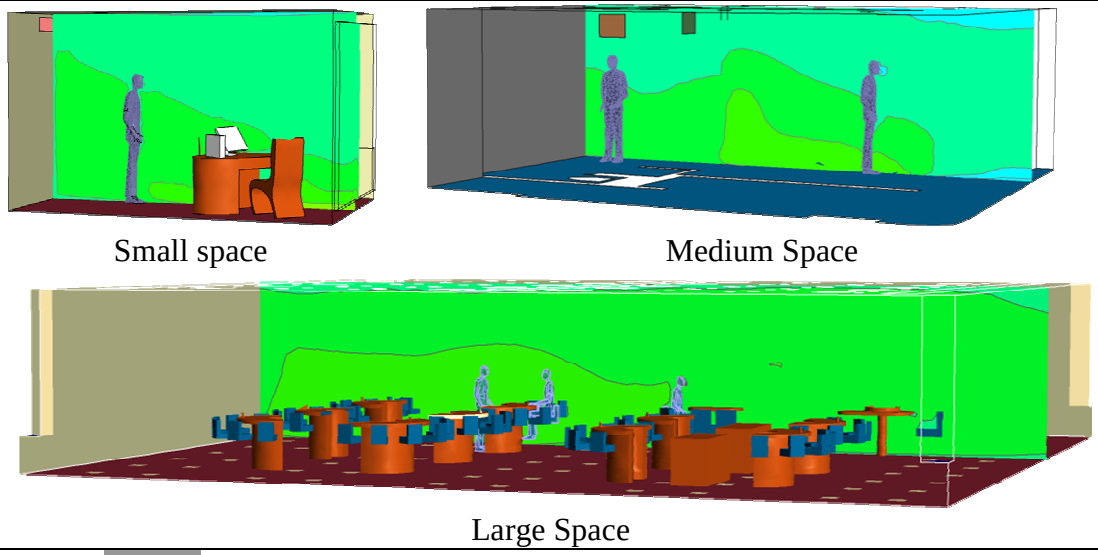

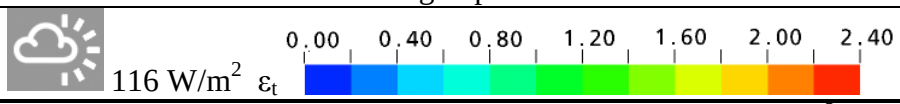

116 W/m^2 ε_t

Figure 127 ε_t of IJV in different space sizes at 116 W/m^2

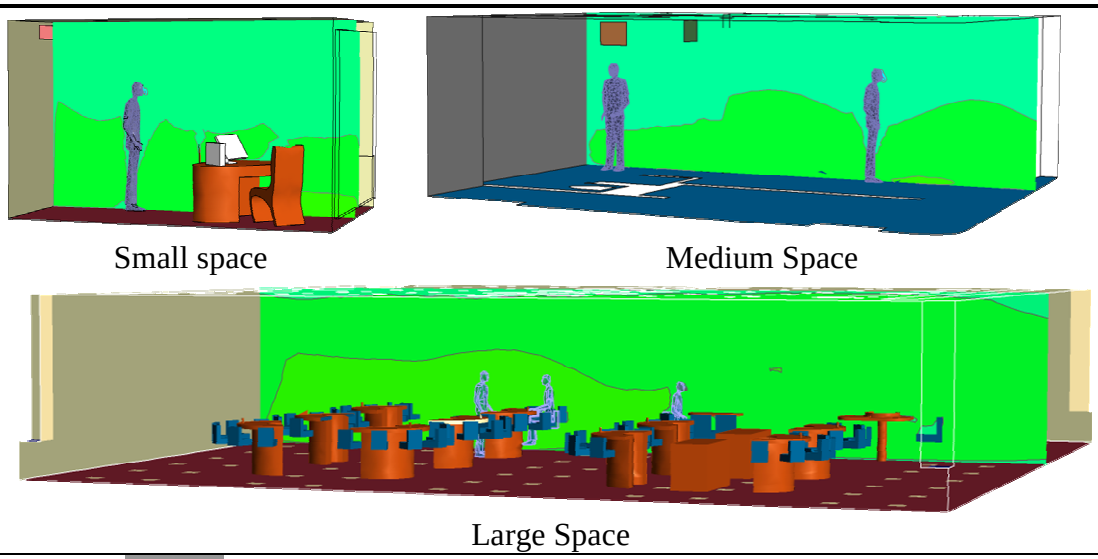

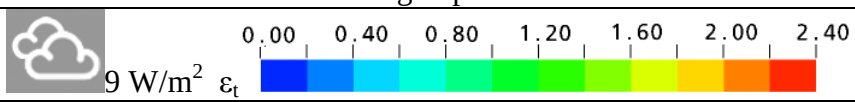

9 W/m^2 ε_t

Figure 128 ε_t of IJV in different space sizes at 9 W/m^2

At a cooling load of 9 W/m^2, ε_t reduces and become close to 1.0, uniformly. Stratification still maintains high ε_t near the floor which decreases toward the ceiling. Similar to high cooling load, ε_t of the large space tends to be the highest.

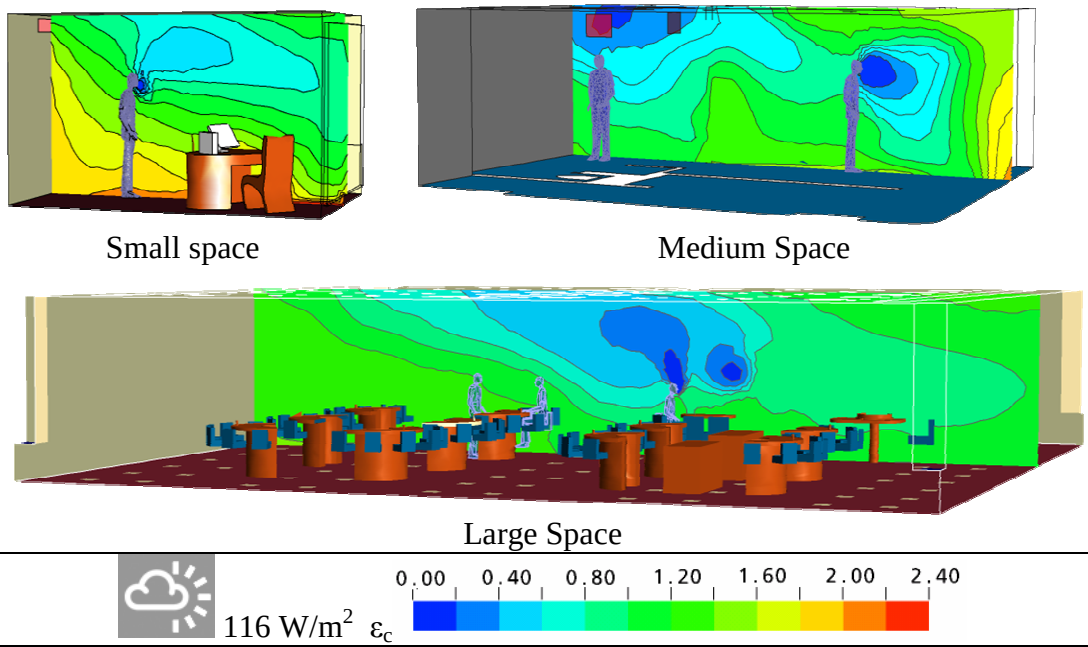

Figure 129 ε_c of IJV in different space sizes at 116 W/m^2

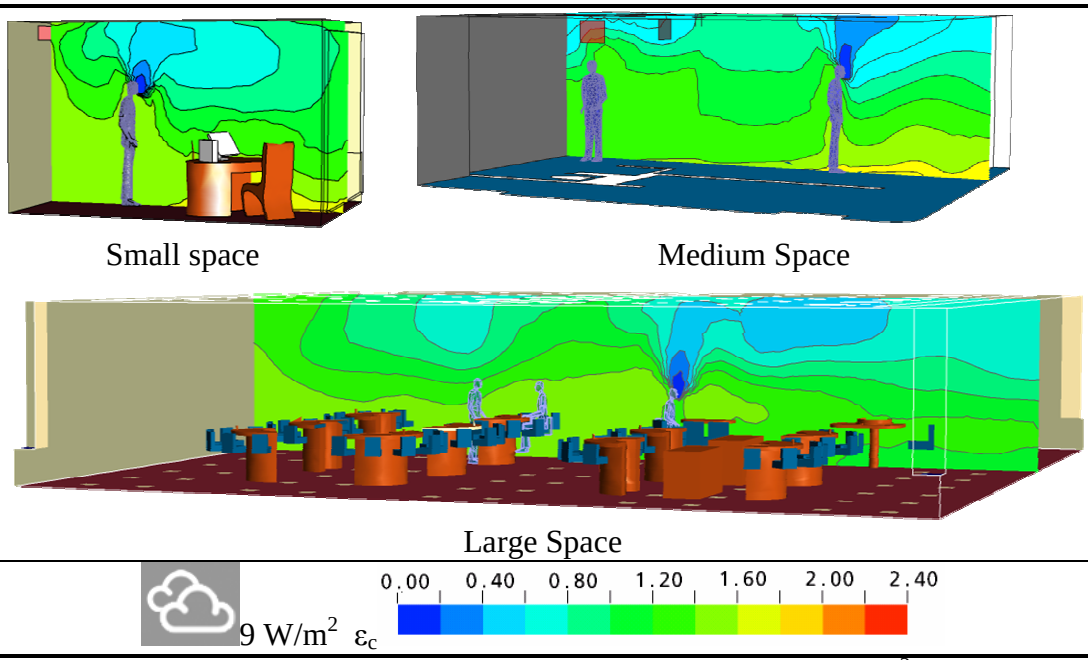

Figure 130 ε_c of IJV in different space sizes at 9 W/m^2

In **Figure 129** and **Figure 130**, ε_c of the IJV system in different space sizes is plotted. Low ε_c occurs near pollutant sources such as human noses and high ε_c occurs near the floor. At a cooling load of 116 W/m^2, ε_c tends to decrease in all spaces, except the small

space, which is able to maintain high ε_c layer near the floor (yellow and red color). When the cooling load is reduced to 9 W/m^2, ε_c increases in all spaces. A high ε_c layer is equally preserved within the breathing zone, while low ε_c is vertically formed toward the ceiling without mixing with the clear air down below.

The average ε_t and ε_c were plotted in **Figure 131**, respectively. All spaces indicate that both ε reduce when the cooling load exceeds 116 W/m^2. For ε_t, small and medium spaces perform better than the large one by having ε_t reaching 1.05-1.09 at cooling of 116 W/m^2. The large space might have the lowest ε_t, but still overall is above 1.0. In contrast, ε_c for the large space can be the highest, particularly when cooling load is below 85 W/m^2. Peak ε_c can reach 1.41 in the low cooling load condition, and the ε_c drops to 1.2 when cooling load reaches 160 W/m^2. The small space tends to perform close to the large space, while the medium space performs worst. ε_c of all spaces drops when the cooling load become too high. This results confirms the conclusion from Chapter 5 and 6. High ε_c of an IJV system can be expected if cooling load does not exceed 116 W.m^2 (at supply velocity of 5.38 m/s). If using other indicators such as PMV-PPD and draft, the maximum cooling load and supply velocity range becomes even lower. The discussion of this limitation can be found in the following section.

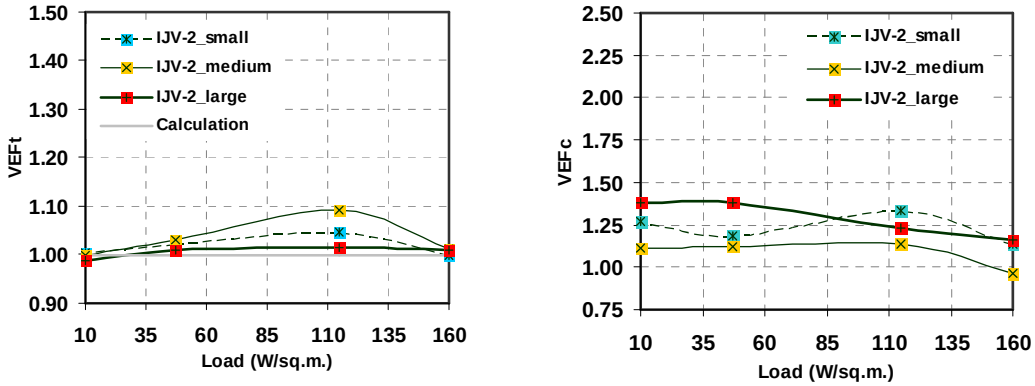

Figure 131 ε_t and ε_t of IJV in different space volumes

CFD Ventilation Performance of IJV in different space volumes under the VAV system

Based on **Equation 15-Equation 17**, stratification discomfort, draft and normalized CO_2 can be quantified. Again, the major obstacle of the IJV system is stratification discomfort which can be different when the space volumes are changed. Results are shown in **Figure 132**, where IJV#1 (low supply velocity) from the previous chapter are added and plotted

as a reference. Compared with IJV#2, IJV#1 has peak stratification discomfort at 0.21, and when supply velocity increases, stratification goes lower than 0.09 (IJV#2 mid space). When different space volumes were applied, the reduction of space volumes led to the higher stratification discomfort, in which the peak reaches 0.16 at cooling load of 47 W/m^2. In contrast, the large volume can bring the peak stratification discomfort down to 0.11. Similarly the peak stratification discomfort occurs at mid the cooling load, and then decrease if the cooling is either less or higher than this point.

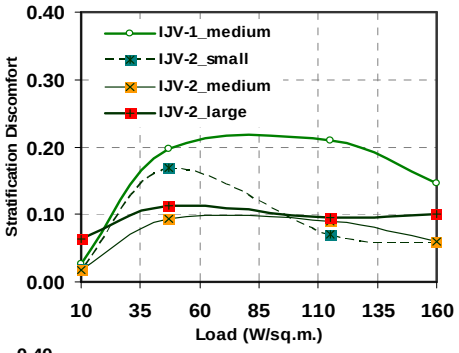

Figure 132 The stratification discomfort of IJV in different spaces (top left)

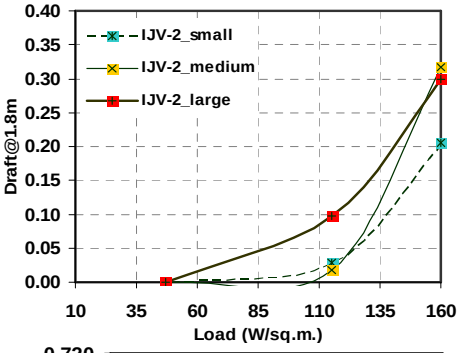

Figure 133 Draft of IJV system in different spaces at 1.8m (mid left) and 1.1m (mid right)

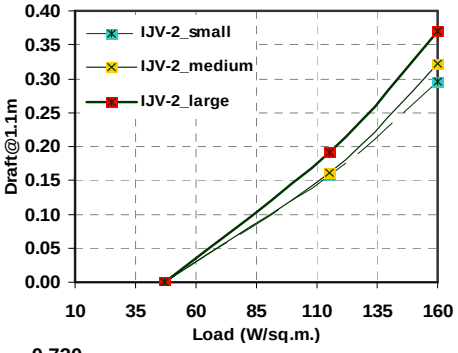

Figure 134 The normalized CO_2 of IJV in different spaces at 1.8m (bottom left) and 1.1m (bottom right)

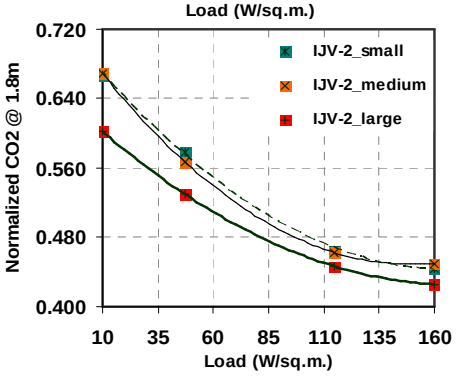

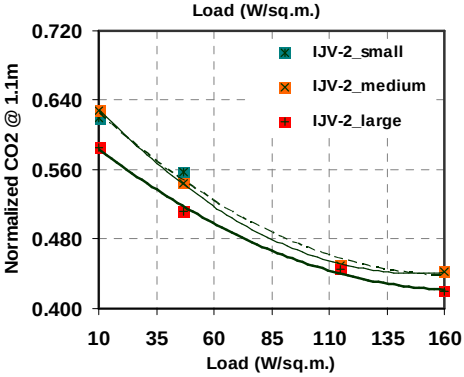

In general, stratification comfort occurs quite constant at 0.10 or 10% of the room area when high supply velocity is strong enough. This indicates that when the room area increases, the actual area affected by stratification also increases. The 10% of the medium space is 5.5 m^2 (out of room area of 55 m^2), while 10% of large space is 33 m^2. (out of room area of 330 m^2). This shows that, at the same stratification discomfort, the smaller

space has a smaller area impacted. Stratification discomfort of 16% for the small space might actually have less actual impacted area, which is only 2.2 m^2 (out of room area of 13.81 m^2). In other words, it indicates that the shape of the impinging cool air already became constant, and will not be smaller than this area. For instance, in the room with the IJV system with area of 6 m^2, if the estimation of stratification discomfort is 10%, the actual area over which the temperature is stratified more than 3^oC should be 0.6 m^2. However, the actual area impacted by stratification discomfort might actually reach higher than 2.2 m^2. Based on this result, practitioners should keep in mind that when the conditioned space is small, the CFD simulation should be performed if an accurate prediction of stratification discomfort is required.

Figure 133 indicates that a draft at 1.1m height is stronger than at 1.8m height. The large space suffers from draft more than the rest by having a draft of 0.40 at 1.1m height and at a cooling load of 160 W/m^2. Compared with this large space, the small space has a small advantage because the draft is slightly less. At the 1.8m height, the draft of small space only reaches 0.20, while draft of the large space reaches 0.30. When the cooling load reduces, the draft drastically decreases for all space volumes. At a cooling load of 47 W/m^2, the draft is nil. If using 10% of the room as a threshold for draft, the supply velocity of IJV can be up to 3.66 m/s at a cooling load of 80 W/m^2 for all space volumes.

In **Figure 134**, when cooling increases (flow rate increases), normalized CO_2 reduces. Due to stratification, normalized CO_2 at a 1.8m height is higher than at a 1.1m height, about 0.01-0.03. This gap is widest when the cooling load is low. The large space performs better in all cooling load scenarios. This finding corresponds to the ventilation effectiveness discussed in the previous section.

PMV and PPD of IJV in different space volumes under the VAV system

In **Figure 135** and **Figure 136**, the PMV of both the high and low cooling loads are shown, and typical characteristics of IJV are found. PMV can be higher than three near glass due to high radiation intensity. PMV is also high near the ceiling, and becomes close to zero in breathing zone. Since the supply velocity at a cooling load of 116 W/m^2 is too strong, a low PMV layer occurs near the floor. This problem can be solved by the supply velocity being less than 2 m/s as discussed in Chapter 5. Once the supply velocity

is reduced, the low PMV layer is eliminated as shown in the low cooling case (**Figure 136**). At this low cooling load, overall PMV is also close to zero uniformly.

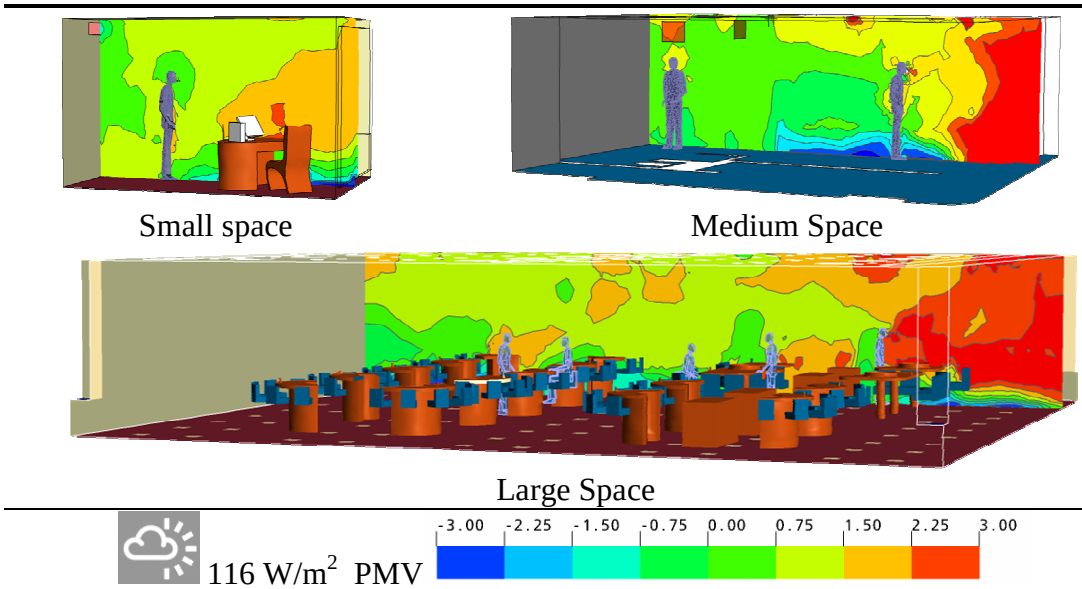

Figure 135 PMV in different space sizes at the cooling of 116 W/m^2

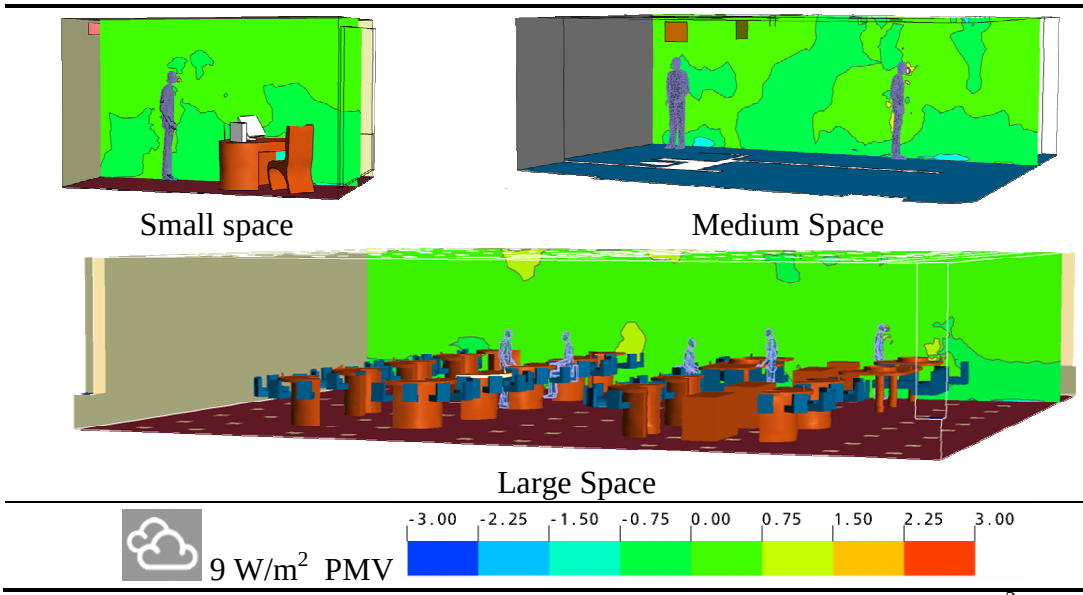

Figure 136 PMV in different space sizes at the cooling of 9 W/m^2

In **Figure 137**, the PMV is converted to PPD by **Equation 26**. The large space tends to have worse thermal comfort condition by producing the highest PPD, while the medium and small spaces successfully maintain a lower PMV. This outcome can be explained by referring to glass radiation. In the large space, intense radiation is required to increase the cooling load since the area is large. To match the same cooling load density, peak radiation falling on the glass was forced to reach 500 W/m^2. This intense radiation

directly affects PPD, and the relationship is quite liner as shown in **Figure 138**. Peak radiation of the large space ranges almost the highest (red cursors) and thus causes the highest PPD. This relationship also shows that PPD increases every 10% of every 100 W/m^2 of peak radiation. If using PPD of 10% as a threshold, it only allows peak radiation to be up to 50 W/m^2. This threshold can be referred to if the practitioners really want to maintain low PPD regardless of space volumes. To increase this peak radiation limit, the only alternative is to adjust other comfort factors such as air temperature. By setting the room thermostat to be much lower than 23.5^{o}C (74^{o}F), high PPD caused intense radiation might decreases, but with the cost of extra HVAC energy.

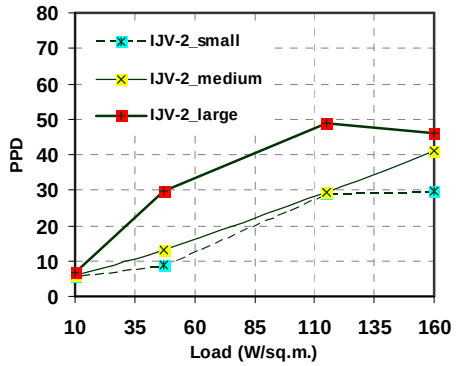

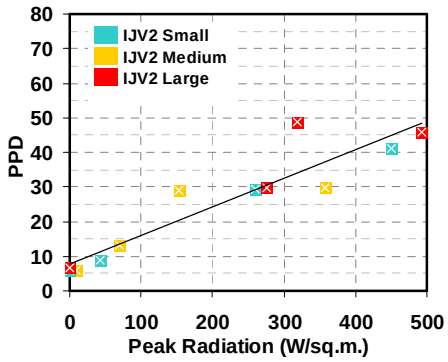

Figure 137 The PPD of IJV in different space sizes (left)
Figure 138 The relationship of the peak glass radiation and PPD (right)

SUMMARY

When applying IJV to different space volumes, ventilation indices including ventilation effectiveness (ε), CFD ventilation performances, and PMV-PPD vary. There is some correlation between space volumes and these indicators. Such correlation indicates that a large space tends to be most suitable for applying IJV system. To maintain peak performances of an IJV system, results similar to Chapters 5 and 6 were found. The low peak cooling load is preferred when using IJV. To avoid dropping ε, increasing draft, and low PMV near the floor, supply velocity should not exceed 2 m/s. To maintain low PPD, the peak radiation must be minimized as close to zero as possible. Once again, the relationship between ventilation strategies and building envelope was found. In term of local discomfort, the indicator that is strongly impacted by space volumes is stratification discomfort, which will not go smaller than 0.16 (or actual area of 2.2 m^2) for any small space volume.

CHAPTER 8
IJV GUILDELINE FOR ARCHITECTURAL APPLICATIONS

In this chapter, the results from the previous chapters are summarized, and the outcomes to the objectives of this dissertation are used to draw conclusions regarding parameters that maximize performances of an IJV. To prove the success of IJV parameters, they have been applied to the existing classroom, and were subsequently both monitored and simulated by using CFD.

The four objectives established in the first chapter were accomplished. The first objective in Chapter 3 was to study the impinging jet structure. This resulted in the predictive models which practitioners can use to predict the jet velocity and spread. In Chapter 4, nozzle variables such as supply velocity, height, size, tilting angle, and location, were investigated using ventilation effectiveness, CFD ventilation performances and PMV-PPD. Among these variables, supply velocity is the most important variable which can impact both stratification discomfort and draft. In Chapters 5 and 6, the IJV system was tested using MJV and DV systems, operated under both VAV and CAV systems. Due to excessive draft and low PMV near the floor, peak supply velocity of IJV should be maintained closely to 2 m/s. IJV performances are maximized when supply temperature in the cooling mode does not exceed 16^{o}C which improves most ventilation indices. Draft is minimized and ε_c remains high (reaching 1.1 in the cooling mode and 1.0 in the heating mode). Cooling load controls both stratification discomfort and PMV-PPD. If cooling load does not exceed 40-50 W/m^2, stratification discomfort is only 0.09 (at supply velocity of 2 m/s), and PMV-PPD is close to 10%. In Chapter 6, IJV was tested with the last variable, the volumes of the spaces. Results show that IJV in any volume of space performs well when the cooling load is below 50 W/m^2. Within this range, IJV is most suitable for large spaces because ε_c is high, while draft and stratification discomfort are the lowest. If the cooling load goes above 50 W/m^2, the large space and others are no longer suitable for the IJV system because of increasing draft and poor IAQ. In contrast

to other indicators, PPD is not directly impacted by the volumes of spaces, but rather relates to peak radiation from glass. In order to maintain PPD less than 10%, peak radiation should not exceed 50 W/m^2 for every space volume.

Based on these discoveries, **Table 23** summarizes the IJV parameters that the practitioner should follow if intending to use IJV in any space. This data should be used for designing IJV at peak load scenarios, where supply velocity is the critical factor. It is recommended for any case, that the peak supply velocity should not exceeding 2 m/s. It is preferred to maintain an appropriate supply velocity, as well as a cooling load less than 50 W/m^2. In reality, there are many architectural spaces that might have higher cooling loads. The parameters of the IJV system for a cooling load of 100 W/m^2 are then added, along with their consequences, which are high stratification discomfort and PPD. This table is applicable for applying IJV in both cooling and heating scenarios. Using the results from a single heating simulation in Chapter 6, only single heating parameters can be recommended. Accordingly, future studies are required for other heating parameters under different scenarios.

Thermal load (W/m^2)	Supply temp (C,F)	Supply velocity (m/s, fpm)	VEF_t/VEF_c $(\varepsilon_t/\varepsilon_c)$	Draft	Stratification Discomfort	PMV-PPD
<100	13,55	2.0, 400	1.0/1.1	0	0.2-0.4	<25%
<50	13,55	2.0, 400	1.0/1.1	0	0.09-0.16	<10%
<50	16,61	2.0, 400	1.0/1.1	0	<0.09	<10%
>-10	26.5,80	2.0, 400	1.0/1.0	<0.2	0	<10%

Table 23 The recommended IJV parameters for HVAC design

THE EXAMPLE OF THE CLASSROOM SPACE USING IJV PARAMETERS

The implementation of proposed predictive models and IJV performances were demonstrated through a case study. In **Figure 139**, a case study of a classroom in the Art and Architecture Building at The University of Michigan was selected as a candidate for upgrading to IJV system. Using occupant density specified by ASHRAE 62, the room maximum capacity with area of 100 m^2 (1,080 ft^2) has 35 seats [7]. The sensible load from these 35 occupants is 2,450 W (35x70W). The total heat gain generated by electric lights is 3,120W. For ensuring the good IAQ, the fresh outdoor air must be induced into the AHU. The peak design temperature of Ann Arbor of 30.6^{o}C (87^{o}F) was used to compute the system cooling capacity [1]. Using table 6-1 from ASHRAE standard 62-

2004 [7], the fresh air intake for 35 people is 0.22 m^3/s or 470 cfm (10 cfm per person and 0.12 cfm/ft^2). ASHRAE 62-2004 also categorizes the efficiency of different ventilation strategies by using a parameter called ventilation effectiveness (VEF_c or ε_c). Since the VEF_c of an IJV system was estimated at 1.1 [83], the actual fresh air for this room is 427 cfm or 43 cfm (9%) reduction (see calculation in **Equation 12**). As a result, the peak sensible load is 7,340 W or 73.4 W/m^2. This calculation is summarized in **Table 24**, which shows the cooling load components and airflow rate of a typical MJV and the proposed IJV systems. The only difference is the cooling load coming from the fresh air intake.

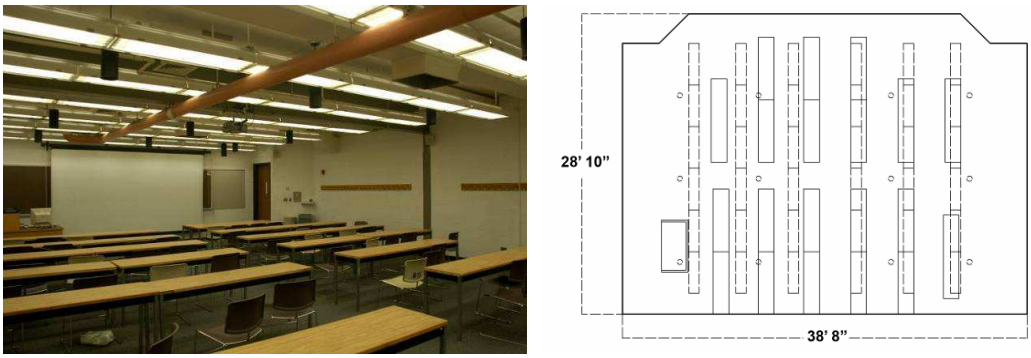

Figure 139 The case study classroom at A&A building, The University of Michigan

Ventilation Strategies	**MJV**		**IJV**	
Cooling load components	Sensible	Latent	Sensible	Latent
Lights	3,120 W		3,120 W	
Occupants	2,450 W	1,580 W	2,450 W	1,580 W
Fresh Air	1,947 W	2,392 W	1,770 W	2,177 W
Total	7,517 W	3,972 W	7,340 W	3,757 W
Sensible Heat Ratio (SHR)	0.65		0.66	
Outdoor Air Fraction (OA)	0.38		0.35	
Overall flowrate	1,249 cfm		1,220 cfm	

Table 24 The cooling load components of both the MJV and the IJV systems

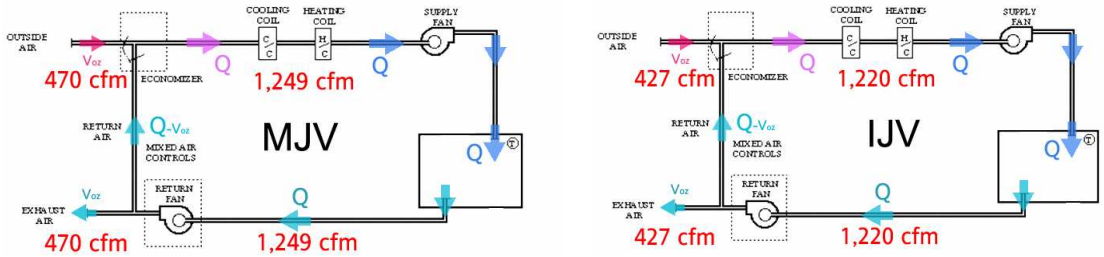

Figure 140 Assigned flow rate of both the MJV and the IJV systems

Using **Equation 2**, the flow rate for thermal ventilation requirement is 1,220 cfm, if the control temperature is 23.5°C (74°F) and the supply temperature is 13°C (55°F). After

obtaining the overall flow rate of both systems, they were overlaid in HVAC air-side loops shown in **Figure 140**. Operating with a supply velocity of 2 m/s (**Table 23**), the free supply area of 0.286 m^2 (3.08 ft^2) is specified. After considering the space function, the four round nozzles of 0.30 m (12") diameter were placed. (Another possibility could be square terminals with dimension of 0.27x0.27m (9.7"x9.7").) These nozzles were placed at the corners of the room and the center of the wall as shown in **Figure 141**.

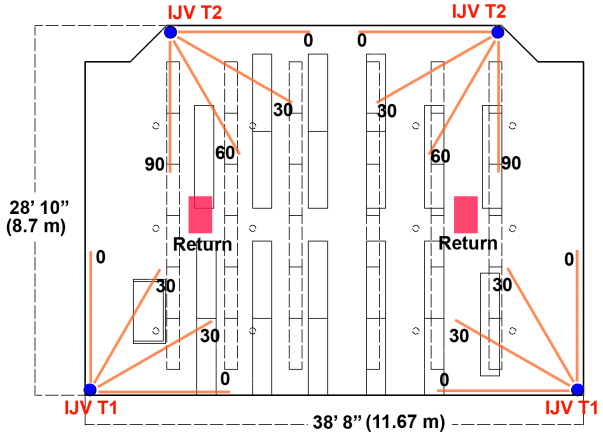

Figure 141 IJV terminal locations in the case study space

To estimate the impact of jet velocity along the floor surface, predictive models are now available. In Chapter 2, the predictive normalized velocity profile is presented in **Table 13** and **Table 14**. Since two types of IJV, wall and corner, were specified, the predictive model was selected, and is presented in **Table 25**.

IJV T2			
90 degree	60 degree	30 degree	0 degree
$\frac{U_m}{U_o} = 1.111\left(\frac{x}{d}\right)^{-1.068}$	$\frac{U_m}{U_o} = 1.176\left(\frac{x}{d}\right)^{-1.089}$	$\frac{U_m}{U_o} = 1.091\left(\frac{x}{d}\right)^{-0.973}$	$\frac{U_m}{U_o} = 0.987\left(\frac{x}{d}\right)^{-0.794}$

IJV T1	
30 degree	0 degree
$\frac{U_m}{U_o} = 1.854\left(\frac{x}{d}\right)^{-1.114}$	$\frac{U_m}{U_o} = 1.45\left(\frac{x}{d}\right)^{-0.896}$

Table 25 The predictive models of the IJV velocity profile used in this case study

In HVAC terminal designs, the jet throw or the maximum axial jet velocity of 0.25 m/s is usually used as a reference [13]. Since the supply velocity is 2 m/s, the velocity of 0.25 m/s equals normalized velocity (U_m/ U_o) of 0.125. Using the mathematical relationship, the nozzle distance can be determined. In **Figure 142**, the highlight indicates intense

velocity near the floor. Thus, the utilization of the space within this area should be a circulation pathway, rather than areas that are sensitive to draft, such as student seats.

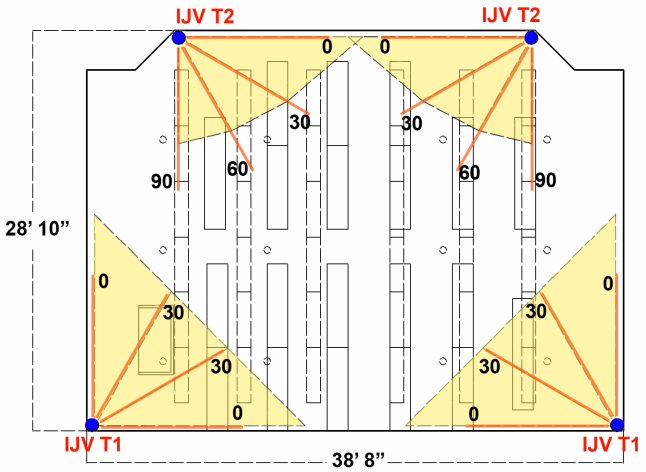

Figure 142 The jet throw area of IJV system in the case study class room

When using four IJV terminals, one of the terminals can also impact the instructor's seat (lower left corner). Removing this nozzle is the best solution to this problem, and that means the nozzles must be reduced to three. If only three terminals are installed, each terminal area must be enlarged for maintaining the same flow rate. Supply velocity must also be reduced to maintain equal or less area impacted by the jet throw. After recalculating, if a supply velocity of 1.5m/s is applied, each terminal should have a diameter of 0.37m (1' 2"). See the new area impacted by the jet throw in **Figure 143**. The results of this new design show the same area of jet throw at each supply terminal, and the elimination of the high velocity impact near the instructor's seat.

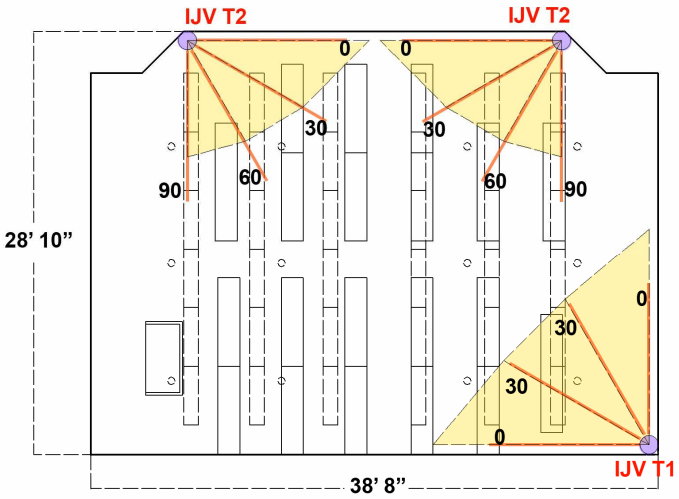

Figure 143 The improved jet throw area of the IJV system in the case study class room

Since the IJV system of the case study classroom follows the criteria in **Table 23**, the ε_c and CFD ventilation performances should be as good as expected. The ε_c is 1.1, while stratification discomfort should be less than 20% of the room area. To prove that this statement is true, a full scale experiment as well as a CFD simulation of this classroom must be performed as shown in the following section. The study is divided into two parts, **full scale experiment and CFD simulation of the existing case study classroom** and **CFD simulations of MJV and IJV systems**

Full scale experiment and CFD simulation of existing case study classroom

To obtain comprehensive ventilation indices from a ventilated space, the CFD simulation is necessary. Before using CFD simulation, the issue of accuracy must be resolved. To assure the validity of the CFD based on ASHRAE RP 1133 [10], the classroom with the existing mixing system was monitored, and then simulated. Using monitoring a system called IFS-200 (See **Figure 144**), the temperature and velocity were compared against the CFD data. Measurements were taken at each diffuser and along the room height. To visualize the surface temperature, infrared thermography techniques were implemented. The images from the infrared camera confirm what the supply temperature should be used in the CFD simulation (**Figure 145** (top right) and **Figure 146** (bottom right)). The main cooling load comes from the light fixtures with surface temperatures of approximately 36°C (97°F).

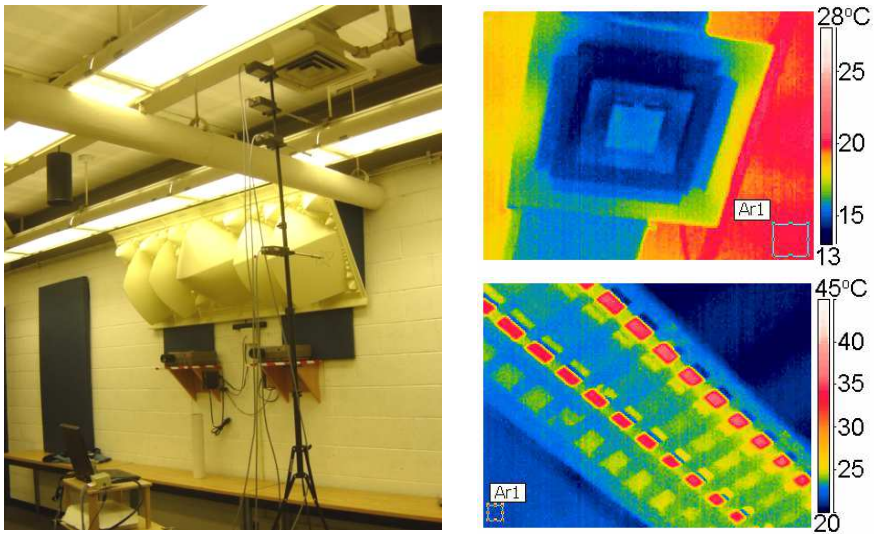

Figure 144 The full scale measurement of the existing classroom (left)
Figure 145 The infrared thermography of the MJV diffusers (top right)
Figure 146 The infrared thermography of the MJV diffusers (bottom right)

Using the data obtained from the full scale measurement, a similar virtual model of the space using CFD was created as shown in **Figure 155**. The light fixtures and desks were laid out by replicating the actual setting. Also, the MJV diffusers were realistically modeled to simulate the actual air distribution (see **Figure 148** (right)). Line A and B represent the measurement locations from floor level to the height of 1.8 m (6 ft). The measured results and CFD data are presented in **Figure 149**. The velocity and temperature profiles of the CFD model and the actual measurements matched. Therefore, these CFD parameters are adequately accurate, and can be utilized for further studies.

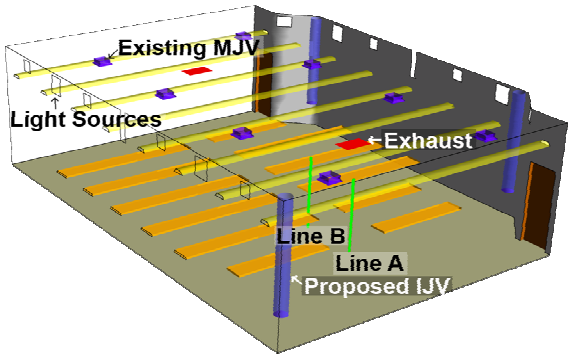

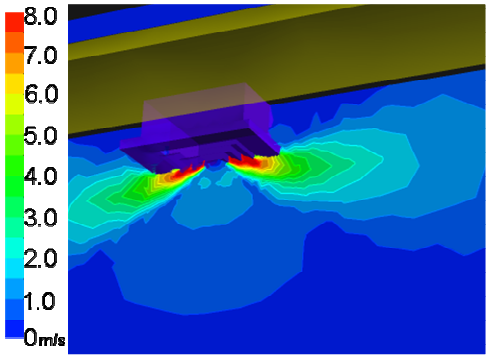

Figure 147 The CFD model of the case study classroom

Figure 148 The velocity profile of the MJV diffuser

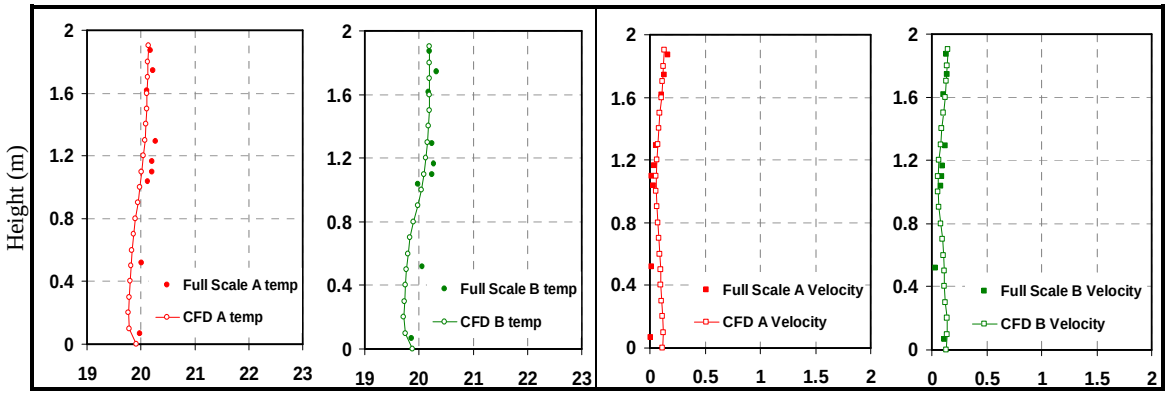

Figure 149 The temperature and velocity profiles of the CFD model and the full scale experiment

The CFD simulations of the MJV and the IJV systems

Once the CFD parameters were validated, CFD can be used to investigate the performances of IJV system. Due to the irregular shape of the human body, a CFD model of the occupants would require large clusters of CFD nodes. To minimize time and increase the accuracy of the CFD, the occupants were excluded, and only light fixtures

were simulated as a heat source in this scenario. In the previous section, the estimate of the room's peak cooling load for both the lights and occupants was 73.4 W/m^2. This was reduced to 25.7 W/m^2 for the cooling load concerning only lights. Both MJV and IJV were assigned with the same supply flow rate of 427 cfm and a supply temperature of 13^{o}C (55^{o}F). In addition, the room was initially filled with CO_2 at 3000 ppmv, with both systems supply air at 377 ppmv. **Figure 150** shows the examples of the results from CFD simulations of both MJV and DV. After simulations were completed, results of the existing MJV and the new IJV systems were compared against important ventilation indices including ventilation effectiveness (ε), CFD ventilation performances, and PMV-PPD.

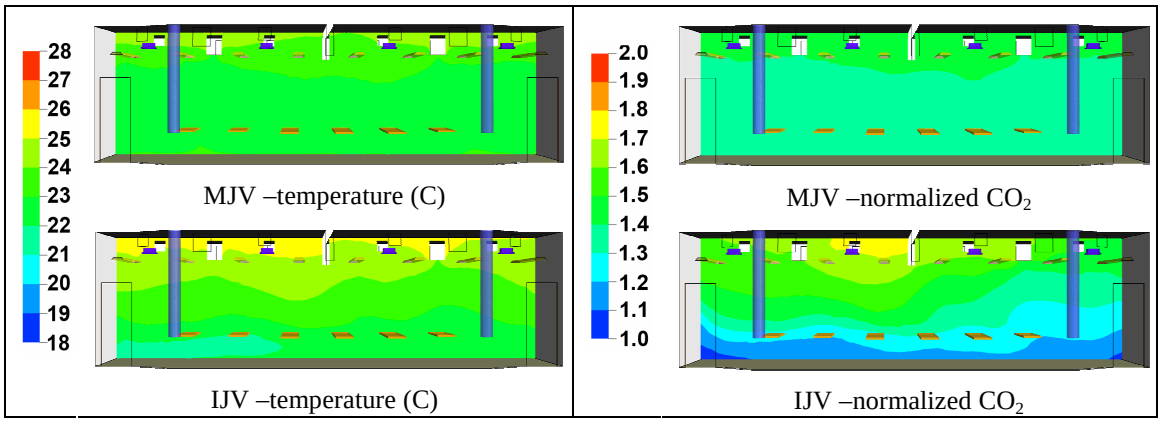

Figure 150 The temperature and normalized CO_2 of the MJV and IJV systems

Table 26 concludes the performances of the MJV and IJV systems. ε_c of the IJV system reaches 1.1 as used in the ventilation rate calculation process. Due to a higher ε_c, the energy saving of the IJV system can be obtained by fresh air intake reduction. IJV causes 12.5% of room area to be too stratified, while draft can not be found. Usually, high velocity and strong stratification occurs near the IJV terminals. By locating the IJV terminals within the circulation area, both problems can be mitigated. Since the PMV-PPD of both strategies is less than 10%, both meet the thermal comfort standard proposed by ASHRAE 55 [6]. **Figure 151** shows the velocity profile at floor level of the MJV and IJV systems. The overall velocity profile of the IJV system is similar to the profile predicted by the proposed mathematical models. Thus, practitioners can use the predictive models as an alternative, if CFD software is not available.

System	ε_t	ε_c	Draft (1.8m/1.1m)	Stratification discomfort	PMV-PPD
MJV	1.01	1.01	3.8%/3.8%	0	6.09 %
IJV	1.02	1.10	0%/0%	12.5%	5.88 %

Table 26 The performances summary of MJV and IJV for the case study classroom

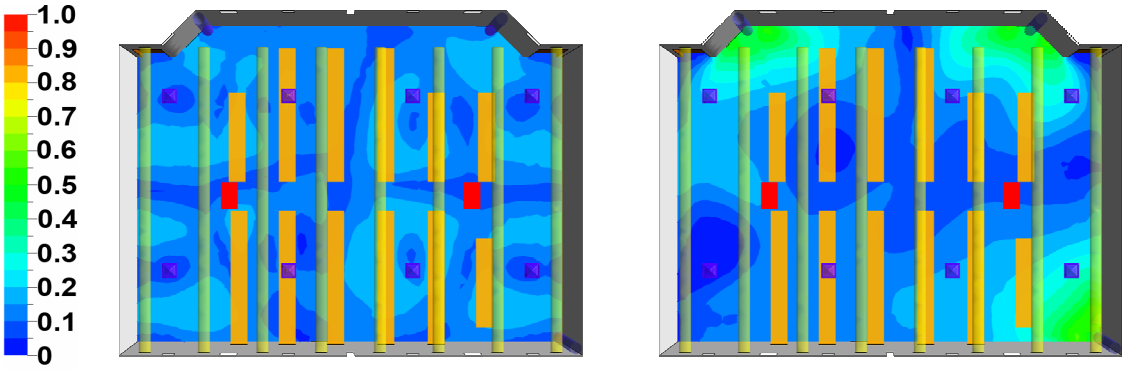

MJV-normalized velocity profile IJV-normalized velocity profile

Figure 151 The normalized velocity profiles at floor level of MJV and IJV

SUMMARY

This dissertation proposes original parameters for use with IJV that give the expected performance of major ventilation indices. Validated by a full scale experiment at the actual site, results from a case study classroom confirm that with some cautions, such as stratification discomfort, the other variables, such as ventilation effectiveness and draft, are improved by using an IJV system. With these promising results, the applications for IJV systems are numerous. The conclusion of this dissertation and future directions of IJV will be discussed in the next chapter.

CHAPTER 9
CONCLUSION AND FUTURE DIRECTIONS OF IJV SYSTEM

In this dissertation, a new ventilation strategy called Impinging Jet Ventilation (IJV) has been proposed and then investigated as a possible solution to thermal comfort, IAQ and energy problems. Utilizing this system to its maximum capability, four objectives have been proposed and then examined. These objectives include four variables: impinging jet characteristics (Chapter 3), terminal configurations (Chapter 4), HVAC operation schemes like VAV and CAV (Chapter 5 and 6), and space volumes (Chapter 7). Upon completion of the study, the results show that velocity, supply temperature and peak cooling load are important parameters to bring IJV to its peak operation. The summary of these results can be found in the previous chapter. At its peak, IJV has ventilation effectiveness of at least 1.1 and little draft, but stratification discomfort and strong velocity current near a nozzle may occur. Throughout this study, CFD is the main simulation tool since it has been validated by the full-scale data from HVAC-IEQ laboratory. Obtaining accurate CFD results is not so easy, because the CFD parameters must be appropriate and comply with standards such as the ASHRAE RP 1133. As first described in this study, the turbulent model and the nozzle velocity profile are both critical parameters for IJV simulation using CFD. Along with the process of using CFD, the new potential for ventilation studies is being recognized. The many data points available in CFD models can be mapped and then quantified in terms of either average value of an area or of a given value. This capability solves the spatial problems of some ventilation indices proposed by ASHRARE 55, 62, and ISO 7730 such as stratification discomfort, draft, and CO_2 level. Therefore, these new indicators were grouped and called "CFD ventilation performances" as exclusively proposed by this dissertation. See more details in Chapter 2.

With the capability of CFD simulation, graphics used in this dissertation made complicated data easily understood. Nevertheless, these graphics must be presented in

book format in which animation is not possible. Animation gives the sense of time and allows users to visualize the movement of air or how the pollutant is distributed and circulated. An example of animated streamline particles from an IJV simulation is shown **Figure 152**. One limitation of animation is a fixed viewing angle which does not allow turning or rotation during animated scenes. This issue is solved by using technology called Virtual Reality (VR). In a virtual environment, users freely interact with the CFD model. Many visualization techniques such as the section plane, streamline, isosurface, etc., are available. The scope of virtual reality can range from interaction with a typical computer screen to immersion in virtual environments such as Cave Automatic Virtual Environment (CAVE).

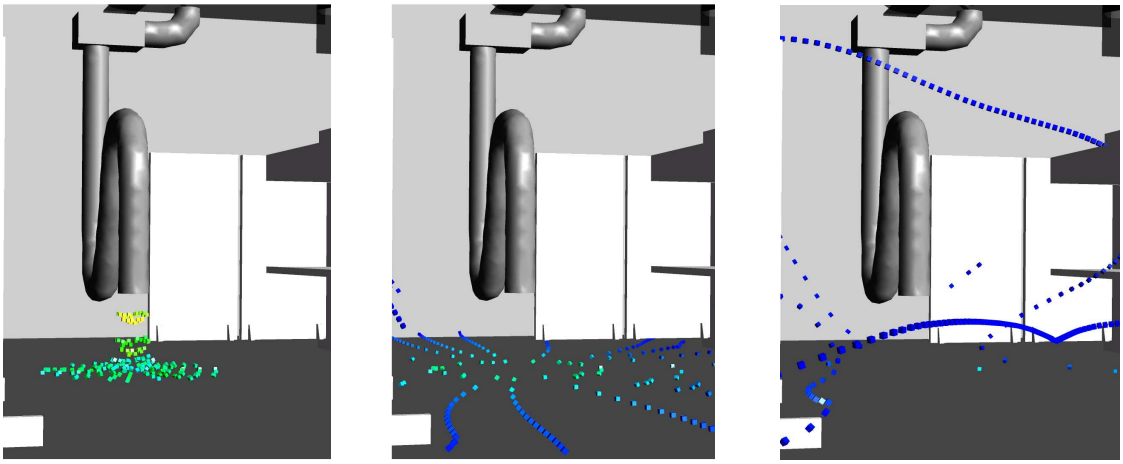

Figure 152 Streamline animation of IJV system

Figure 153 shows the integrated CFD data and 3D model of the Michigan Solar House. In this virtual house, users can not only navigate around the house, but also experience the effect of natural ventilation. Also, users can accelerate wind speed and visualize air temperature variation. If this data is integrated with actual VR devices, users can experience the flow vividly. The application of VR devices is shown in **Figure 154** where the temperature and velocity of the room cross section can be seen by the user through a head-mounted device. When wearing a virtual glove, users can move the cross section plan along a predefined axis. While the plane moves, it displays the current temperature and velocity of that current location. Compared with this technology, the limitations of using a book format as a media are clear. In the near future, it will be interesting to see how this issue is resolved.

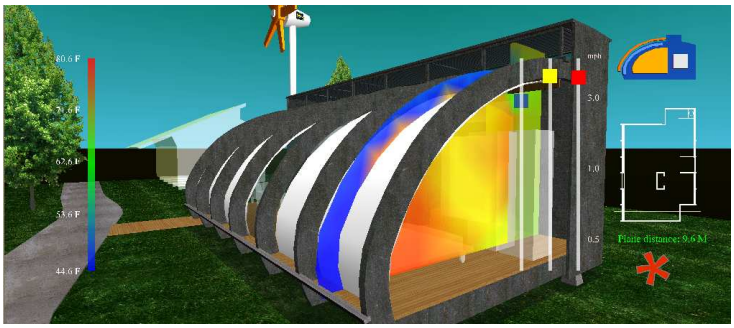

Figure 153 Snapshot from virtual model of MiSO house [48]

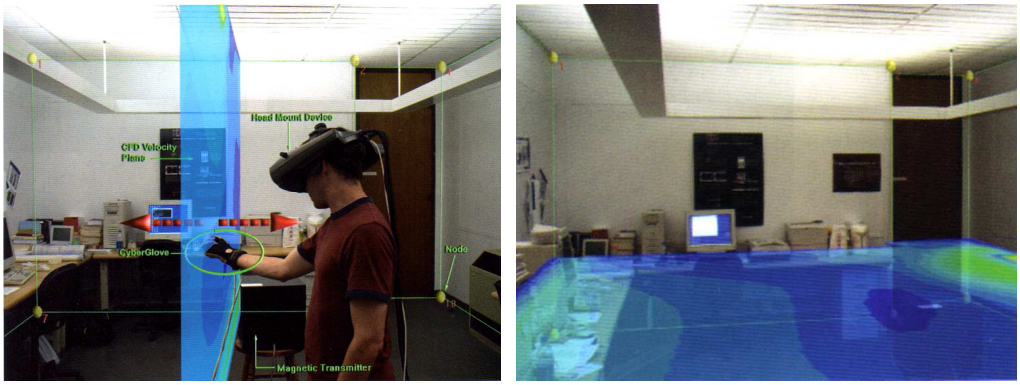

Figure 154 The integration of CFD data and the actual space [84]

Both the full-scale and CFD results presented in this dissertation answer the basic question of how to implement the IJV system in general. Research objectives correspond to the variables which have take precedence in the investigation. Yet, there are many more questions related to unknown variables that need to be investigated. Transient state behavior, furniture lay-out, floor surface characteristics, etc., are all variables which may impact IJV performances in unexpected ways. Also, the long term measurement of the IJV system in an actual building has yet to be carried out because buildings equipped with IJV systems are rare in the US. Nevertheless, at this point, given the impressive performances of IJV, it should be tested in real architecture applications. There are a variety of such applications many of which will be discussed in the following section.

ARCHITECTURAL APPLICATIONS OF IJV SYSTEM

Based on results from this dissertation, the terminal configurations of IJV are important and it is possible for them to be integrated with the architectural elements. The implementation of IJV terminals depends on the creativity of the designers and the function of the space. For actual building elements, such as walls and columns, solutions might be integrated IJV terminals on one side of structural columns or on both sides of

the column. See **Figure 155** (left and middle).When a large area of supply terminals is required, the whole wall can consist of IJV supply terminals by using liner slot terminals as shown in **Figure 155** (right). Two examples of actual and possible implementations based on this concept are presented as follows.

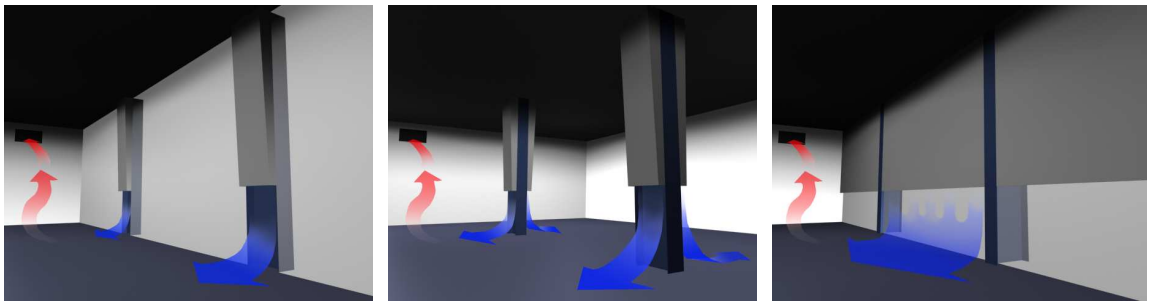

Figure 155 The IJV integrated with different architectural purposes

First, **Figure 156** is a good example of how IJV terminals are integrated into the walls of the gallery area of the Getty Center in Los Angeles. Instead of using IJV as a tube, a slot-type IJV was chosen since it was a better fit for the function of this space. The IJV slots are located 1 ft above the floor and aimed at it. They are distributed at equal intervals along the side wall of the room. Exhausts are located at the ceiling to vent out the polluted air induced by stratification.

Figure 156 The IJV system in gallery room at Getty Center, Los Angeles

Secondly, another example of an IJV system is the Michigan Solar House (MiSO). This house uses a solar chimney for passive heating which is then altered to become an IJV system. Upon entering the slot, air is warmed and rises to the height of the solar chimney and then it is supplied from slots at the ceiling. This is the typical operation of a solar chimney for passive heating. When cooling is needed, the process is reversed. The cool air is supplied from the slots located above the window along the south façade and the

warm air is vented out at the slots in the ceiling. See **Figure 157**. This operation replicates the air distribution of an IJV system which will improve IAQ or reduce the cooling energy of this house.

Figure 157 The IJV system in Michigan Solar house (MISO)

These examples illustrate the flexibility of IJV. Among the many architectural applications, space volumes are the major concern in differentiating the IJV performances based on the results of this dissertation. Large spaces such as airport terminals, atriums, train stations, manufacturing plants, underground tunnels, etc., are most compatible with IJV system. See **Figure 158**. If the IJV is to be used in a smaller space, the design parameters mentioned in this dissertation must be implemented. Once the appropriate parameters are implemented, common spaces such as residences and offices are also excellent candidates for the IJV system. Other spaces with special requirements such as operating rooms, passenger cabins, laboratories, and smoking spaces may also.

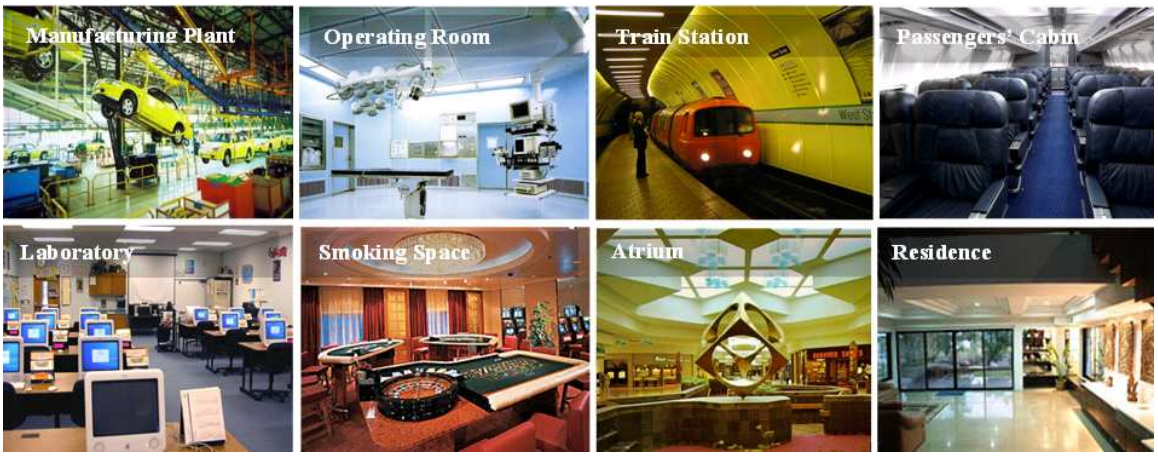

Figure 158 Potential spaces for IJV system

All previous examples and applications have in common that the preliminary design process should included the discussion about the use of an IJV system. The IJV terminals

and exhausts are to be placed where they fit the architectural purposes, and yet do not violate the IJV parameters proposed by this dissertation. The IJV terminal possibly has a variety of shapes and should be well integrated with the architectural elements. Given this design freedom, the performances of IJV in various designs may differ from the findings of this dissertation. Under these circumstances, designers or practitioners may at least use this dissertation as a protocol for analysis using the proposed techniques of full-scale and CFD simulation, so that optimal results for thermal comfort, IAQ, and energy consumption are assured.

APPENDICES

APPENDIX A

IFS-200 HARDWARE COMPONENTS

Referred to in Chapter 2, the hardware components of an IFS-200 system include omni-transducers and a CTA module, connector box, data acquisition card, and IFS-200 software. The diagram of an IFS-200 component assembly is shown in **Figure 159**.

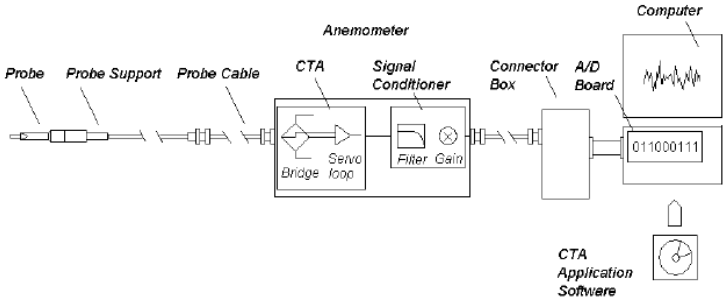

Figure 159 Diagram of a typical Dantecdynamics flow measurement system (right) [37]

Omni-Transducers and CTA module

Omni-transducers measure velocity (unknown direction) and air temperature simultaneously. See **Figure 160**. These transducers work like a hot-wire anemometer. The manufacturer recommends that the velocity should range from 0-1m/s for the 54T21 module. Since the velocity at the ventilation supply terminals sometimes exceeds this range, a special customization was requested. After adding a special coating, the velocity range was increased to 0-6 m/s. Air temperature can be measured for a 0-50^{o}C range. The accuracy depends on flow direction exposure and the dynamic responses of the CTA module. Overall, the standard error of velocity is around ± 0.03m/s[21] for 0-6m/s, while the temperature error is $\pm 0.5^{o}$C. The CTA module converts the electrical range of 0-5V for velocity and 0-2V for air temperature at the given response time (dynamic response). This is the sensor sensitivity for capturing the air flow dynamic caused by a small scale eddy. The manufacturer claims that the response time is as quick as 0.1s. This is fast enough for indoor comfort measurement according to current standards which recommend a response time from 0.2-1s [85].

[21] Converted from the electrical error of 0.025 V

	Dantec 54T21	ISO 7726	ASHRAE	ISO 7726 draft	EU project recommendations (MAT1-CT93-0039
Velocity range (comfort zone)	0.05-1 m/s	0.05-1 m/s	0.05-0.5 m/s	0.05-1 m/s	0.05-1 m/s
Accuracy in velocity	±0.01m/s ±0.025·Va *	±0.05 m/s ±0.05·Va **	±0.05 m/s **	±0.02 m/s ±0.07·Va **	±0.03 m/s *
Influence from directional sensitivity	<±5% error in Vmean <±10% error in Vrms within 3.9π	Accuracy independent of dir. within 3π	Omnidirectional or carefully orientated	Accuracy independent of dir. within 3π	<±5% in Umean <±10% in Urms within 3.9π
Dynamic response (Response time, τ)	<±10% error in Vrms at 2 Hz (τ<0.1s)	 τ ≈1s	 τ ≈1-10s	 τ ≈0.2-0.5s	<±10% error in Urms at 1 Hz (desirable 2 Hz)
Influence from temp.variations	<±0.25% error in V per 1°C temp. change	not specified	not specified	not specified	<0.25% per °C
Temperature range	0-45°C				
Accuracy in temperature	±0.5°C				
Velocity output	0-5 V				
Temperature output	0-2 V				
Termination	Screw terminals or cable (optional)				
Power requirements	7-12 V DC				

*) Calibration accuracy does not include directional sensitivity.
**) Accuracy includes directional sensitivity.

Figure 160 The omni-transducer with CTA module (left)
Table 27 The transducer performances compared with various standard (right) [85]

Various standards, ASHRAE, ISO 7726, ISO 7726 draft and EU, are compared against the specifications of this transducer shown in **Table 27**. It indicates that these transducers can measure the indoor air flow in compliance of these standards. To maintain this performance, the manufacturer suggests that the sensors be re-calibrated annually [69].

Connector Box

The connector box links the electrical power, the CTA module, and the DAQ card. See **Figure 161**. The connector box converts standard electrical current (220 V/110 V AC) to the CTA modules which support up to four units per one connector box (four omni-transducers). Additional sensors are added up to 16 CTA modules if an additional connector with 12 channels is provided. Four 10 m transducer cables are used to connect CTA modules to deliver the data to a connector box. Then, the data from the connector box is sent by a SH100100 I/O noise rejecting shield cable to the DAQ card.

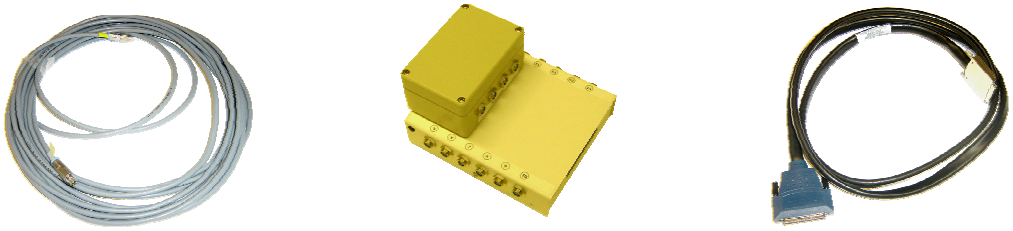

Figure 161 Transducer cables (left), connector boxes (mid), and noise rejecting cable (right)

Data Acquisition Card (DAQ card)

To communicate the data from connector box to computer, the DAQ card is required and its specification must match the CTA module specification. The number of analog input channels must be adequately provided to receive the data from the CTA modules and the data transfer rate must be fast enough to capture the real time behavior [86]. Three DAQ cards from National Instruments which are used in this dissertation are shown in **Figure 162**. Proposed for use in laptop computers with a PCMCIA slot, NI DAQCard-6024E (for PCMCIA) handle data from four omni-transducers with 16 analog input, 12 bits, and sampling rate of 200 KS/s [87]. Similar to NI DAQCard-6024E, NI PCI-6220 takes data from four omni-transducers with 16 analog input, 16 bits, and larger sampling rate of 250 KS/s [88] but this card is only for desktop computers. Since this research aims at extending the set-up to 16 omni-transducers, The choice for computer desktop is NI PCI-6033E which has 64 analog inputs, 16 bits, and sampling rate of 250 KS/s [89] . All DAQ cards are operated with the drivers from National Instruments which has to provide the DAQ management software to check whether the cards are properly functioning.

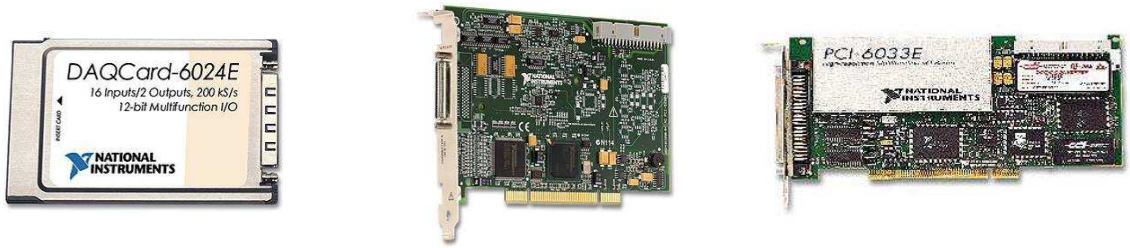

Figure 162 NI DAQCard-6024E (left), NI PCI-6220 (mid), and NI PCI-6033E (right)

APPENDIX B
PHYSICS OF JETS AND PLUMES

To understand an impinging jet better, it is necessary to explain the jet and the plume, since they are the fundamental basis of it. A jet is usually utilized for a HVAC supply system where the room temperature and velocity depend on the condition of the jet supply. Proper jet design seeks to avoid the thermal discomfort and draft which a strong velocity current. Unlike the jet, a plume typically occurs from heat sources such as occupants and appliances. The thermal force causes not only the hot air, but also the pollutants to rise upward. Ventilation strategies, such as Displacement Ventilation (DV) and Impinging Jet Ventilation (IJV), utilize the characteristics of the plume to improve Indoor Air Quality (IAQ). In the following section, turbulent jet structure, 2D and 3D jets, vertical buoyant jets, and plumes are discussed.

TURBULENT JET STRUCTURE

Jet is a momentum driven flow from a nozzle to a given space. The momentum force creates the shear layer between the potential core and the environment. As a result of this process, eddies are produced by shear force between the jet and the environment. Studying the behavior of these eddies is beneficial for characterizing the turbulent mixing phenomenon. To understand the process of turbulent mixing, it is important to understand the structure of the jet with its four main regions: potential core, characteristic decay, axisymmetric decay, and terminal region [1, 13]. See **Figure 163**.

- **Potential Core Region** is the initial range near the nozzle. The fluid in this range is still pure and similar to the fluid at the nozzle because mixing of the fluid does not occur. Since there is no mixing, pressure and velocity of the jet is constant and the center axis velocity along potential core (U_m) is equal to the initial nozzle velocity (U_o). Typically, the length of potential core varies from 5-10 nozzle diameter lengths.

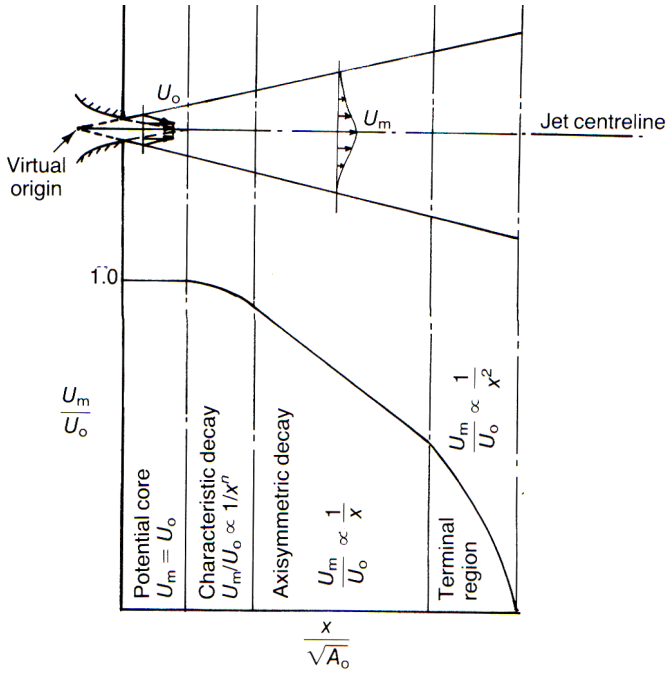

Figure 163 The turbulent jet structure [13]

- **Characteristic Decay Region** is the range in which the mixing initially begins. The jet velocity decreases following the relationship of **Equation 40** where n ranges from 0.33-1. Since n is less than one, the velocity slowly decreases and so likewise the mixing. The length of the region is short when in a 3D jet, but it is extended in 2D jet (Details about 2D and 3D jet will be described in following section).

$$\frac{U_m}{U_0} \sim \frac{1}{X^n} \qquad \text{Equation 40}$$

- **Axisymmetric Decay Region** is called the Inertia Subrange in which the eddies range from the largest scale to smallest scale. Large eddies contain the bulk of kinetic energy; while in small scale eddies the energy transforms into heat by viscous dissipation. Based on the Komogorov theory, the smallest scale eddies have a local Re equal to 1 [90]. The energy flux per unit mass (E) is constant in any eddy size. **Equation 41** shows the calculation of rate of energy per unit mass (E) by using eddy velocity (U_γ) and eddy size (γ). Using the Komogorov theory, the ratio of the largest eddies' size (δ) to the smallest eddies' (γ_o) size depends on the Re to the power of ¾ as shown in **Equation 42.** The calculation of Re is based on the largest scale eddies [90]. However, this theory dose not take the stratification effect, density difference effect, compressible flow, and super sonic flow, into account.

$$E = \frac{U_\gamma^3}{\gamma} \qquad \text{Equation 41}$$

$$\frac{\delta}{\gamma_o} \sim \mathrm{Re}^{\frac{3}{4}} \qquad \text{Equation 42}$$

Since the mixing occurs from the largest or smallest scale eddies, this mixing occurs rapidly in comparison to the previous region. Because of faster mixing, it makes the velocity decrease faster by the following relationship as shown in **Equation 43**. The length of this region is longer when the jet is 3D as compared to when the jet is a 2D jet. In the circular jet, the axisymmetric region typically occurs within 9-100 nozzle distances measured from the nozzle.

$$\frac{U_m}{U_0} \sim \frac{1}{X} \qquad \text{Equation 43}$$

- **Terminal region** is the range that the jet is fully mixed with the surrounding fluid/gas. The velocity decays rapidly and follows the relationship in **Equation 44**.

$$\frac{U_m}{U_0} \sim \frac{1}{X^2} \qquad \text{Equation 44}$$

2D AND 3D JET

Jet flow is divided into two types: a 2D jet and a 3D jet. Both jets are differentiated by the shape of their nozzle as shown in **Figure 164**. If the ratio of the width and height nozzle (b/h) is less than 40, it is considered to be a 3D jet. If the ratio of the nozzle is equal to or greater than 40, the jet is considered to be a 2D. Square, circle or rectangular nozzles are considered to be 3D jets, while a long, linear nozzle is obviously a 2D jet. In the 2D jet, the width of the nozzle (b) is neglected. Only the height of the nozzle is considered. On the contrary, a 3D jet requires both width (b) and height (h) of the nozzle to be considered. For circular and square nozzles where width and height are equal, the diameter of a circular nozzle or the length of a single dimension of a square nozzle is considered.

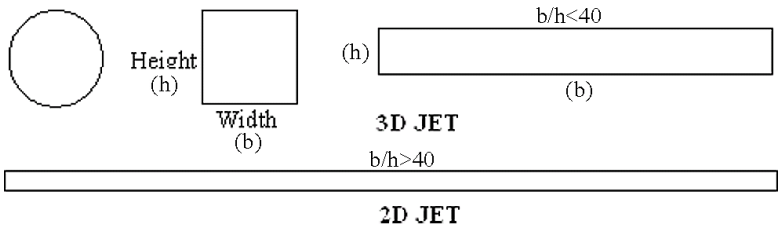

Figure 164 The 2D and 3D jet categorized by nozzle shapes

Both 2D and 3D jets have four, similar, turbulent flow regions: potential core, characteristic decay, axisymmetric decay, and terminal region, but the length of each region is proportionally different. The 2D jet tends to extend the characteristic decay region longer than the 3D one where the characteristic decay region is longer. The characteristic decay length also increases as a function of the ratio between width and height of the nozzle [73]. In **Figure 165**, a study is done by using b/h up to 1000 which has the longest characteristic decay range, but almost no axisymmetric decay region. At the other end of the spectrum, a square jet (b/h=1) has almost no characteristic decay region but has the longest axisymmetric decay region.

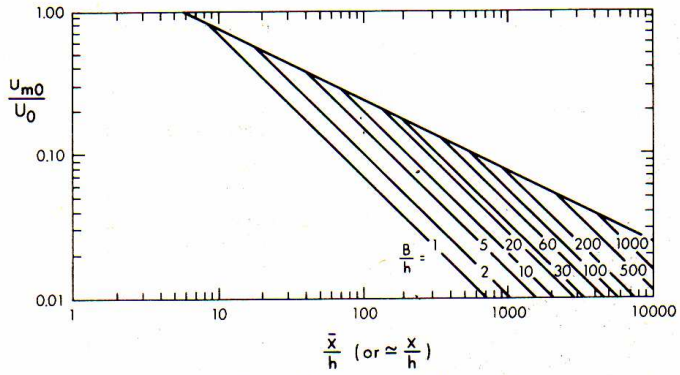

Figure 165 The velocity decay patterns of 2D and 3D jet [73]

To understand the flow characteristics of a 2D and 3D jet, the law of the conservation of momentum is applied. The momentum across the section of the jet is determined by using **Equation 45** for a 2D jet and **Equation 46** for a 3D jet. T_o is the initial momentum at the nozzle, while T is the total momentum at any given point downstream. ρ is fluid density and U_o is the initial speed. How to apply the nozzle in both equations is what differentiates 2D and 3D jets. A_o is the area of the nozzle used in a 3D jet, while h is the nozzle height used for a 2D jet. For both jets, it is assumed that all momentum of the jet is conserved; thus, T is equal to T_o. Using this assumption, the eddy size (δ_m) and velocity (U_m) at a given point can be determined.

$$T_o = \rho U_o^2 h = T = \rho U_m^2 \delta_m \qquad \text{Equation 45}$$

$$T_o = \rho U_o^2 A_o = T = \rho U_m^2 \delta_m^2 \qquad \text{Equation 46}$$

Based on **Equation 43**, a jet in an axisymmetric region has $U_m \sim x^{-1}$. The size of the large scale eddy always grows with x which is the distance from the nozzle ($x \sim \delta_m$). Thus, the velocity (U_m) is determined by using either x_m or δ_m over time (t) as shown in **Equation**

47. Assuming that the T_o and ρ are constant, the relationship between the four variables time (t), U_m, x and δ_m is estimated by using a technique called dimension analysis as shown in **Equation 48** and **Equation 49**. **Equation 48** is for a 2D jet and **Equation 49** is for a 3D jet.

$$U_m = \frac{X_m}{t} = \frac{\delta_m}{t} \quad \text{Equation 47}$$

$$\delta_m \sim t^{\frac{1}{3}} \sim x_m \sim U_m^{-2} \quad \text{Equation 48}$$

$$\delta_m \sim t^{\frac{1}{2}} \sim x_m \sim U_m^{-1} \quad \text{Equation 49}$$

The empirical model was developed for predicting the velocity of the axisymmetric region of a 3D jet. In the case of a square or a rectangle (b/h <40), **Equation 50** shows how to use U_o, x_m and A_o to predict the U_m, while K is the constant that can be obtained by experiment. If the nozzle is circular, **Equation 51** is used. The most common K for a circular jet is 6.5, as suggested by Rajaratnam [73]. Another value is proposed by Tollmien and Goertler who suggest that K is 7.32 and 5.75 respectively [13].

$$\frac{U_m}{Uo} = K\frac{\sqrt{Ao}}{X_m} \quad \text{Equation 50}$$

$$\frac{U_m}{Uo} = K\frac{d_o}{X_m} \quad \text{Equation 51}$$

VERTICAL BOUYANT JET

The setup for a vertical buoyant jet is the same as for a jet. As shown in **Figure 166**, the nozzle supplies the jet fluid or gas to the environment, but the distinctive characteristic of the vertical buoyant jet is that the jet is supplied upward and the effect of fluid density difference is included. The gravitational force and the fluid density difference between supplied and surrounding fluid/gas differentiates this jet from the previous 2D and 3D jets. In order to understand the physics of this flow, the mathematical relationship of volumetric force (F) and the Richardson Number (Ri) are applied. In **Equation 52**, Ri is calculated from the normalized density difference (δ_m), z-axis velocity (w), and length scale which in this case is the largest size of eddies (δ_m). Normalized gravitational acceleration ($g^{'}$) is the relationship between gravitational acceleration (g), density difference (ρ-ρ_o) and supplied density (ρ_o). At the nozzle, F can be calculated using a

nozzle area (¶d^2/4), nozzle velocity (w_o), and g$'$. See **Equation 53**. Along the jet convective current, F can be calculated by the largest eddy area (δ_m^2), w, and g$'$.

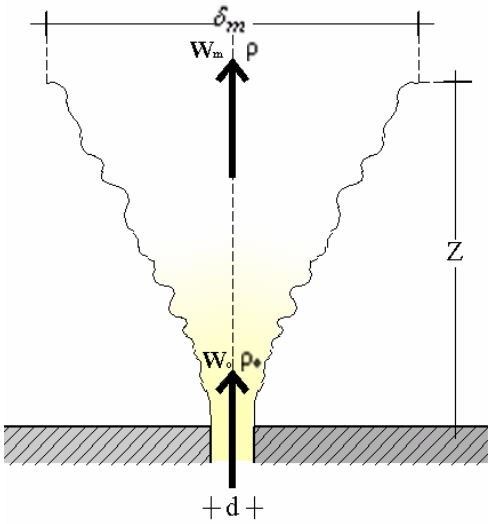

Figure 166 The diagram of vertical buoyant jet

$$Ri = \frac{g'\delta_m}{w^2} = \frac{(\rho - \rho_o)g\delta_m}{\rho w^2} \qquad \text{Equation 52}$$

$$F = \pi \frac{d^2}{4} \times w_o \times g' = \delta_m^2 w g' \qquad \text{Equation 53}$$

If the entraining fluid is well mixed with the surrounding fluid, the turbulent force overcomes the buoyancy force. This means that Ri is at least equal to one. Using this principle, the relationship between z (distance from the nozzle along the z axis), δ_m, w, and g$'$ can be formulated as shown in Equation 54.

$$z \sim \delta_m \sim w^{-3} \sim g'^{-\frac{3}{5}} \qquad \text{Equation 54}$$

PLUME

Unlike momentum, the driven plume and the thermal driven plume rise by purely heat energy. As with the vertical buoyant jet, the convective current is also formed vertically. To understand the thermal driven plume, Ri and F must be applied. F of a thermal driven plume is calculated by δ_m and g$'$ (see **Equation 55**). If Ri is equal to 1, z (distance from nozzle along z axis), δ_m, w, and g$'$ can be derived and their relationship is shown in **Equation 56**.

$$F = \delta_m^3 g' \qquad \text{Equation 55}$$

$$z \sim \delta_m \sim w^{-1} \sim g'^{-\frac{1}{3}} \qquad \text{Equation 56}$$

REFERENCES

1. ASHRAE, **ASHRAE Handbook. Fundamentals**. 2005, Atlanta, Ga: American Society of Heating, Refrigerating and Air-Conditioning Engineers, Inc.

2. ASHRAE, **Indoor Air Quality: Position Document Approved by ASHRAE Board of Directors**. 2005, ASHRAE: Atlanta, Ga. p. 5.

3. Baechler, M.C., **Sick Building Syndrome : Sources, Health Effects, Mitigation**. Pollution technology review, 0090-516X ; no. 205. 1991, Park Ridge, NJ.: Noyes Data Corp.

4. Stein, B., J. Reynolds, and W.J. McGuinness, **Mechanical and Electrical Equipment for Buildings**. 1992, New York: J. Wiley & Sons.

5. DOE. **Energy Information Administration / Annual Energy Review 2005**. 2006; Available from: http://www.eia.doe.gov/emeu/aer/pdf/pages/sec2.pdf.

6. ASHRAE, **ANSI/ASHRAE 55-2004: Thermal Environmental Conditions for Human Occupancy**. 2004, Atlanta, GA: ASHRAE.

7. ASHRAE, **ANSI/ASHRAE 62-2004: Ventilation for Acceptable Indoor Air Quality**. 2004, Atlanta, GA: ASHRAE.

8. USGBC, **LEED Reference Guide for New Construction & Major Renovations (LEED-NC), Version 2.1**. LEED Reference Guide for New Construction & Major Renovations (LEED-NC), Version 2.1. 2003, Washington, DC U.S. Green Building Council.

9. ISO, **ISO 7730-2005 Ergonomics of The Thermal Environment — Analytical Determination and Interpretation of Thermal Comfort using Calculation of the PMV and PPD Indices and Local Thermal Comfort Criteria**. 2005, International Standard: Switzerland.

10. Chen, Q. and J. Srebric, **ASHRAE RP-1133: How to Verify, Validate, and Report Indoor Environment Modeling CFD Analyses**. 2001, ARSHRAE: Atlanta, GA. p. 53.

11. Zhang, Y., **Indoor Air Quality Engineering**. 2005, Boca Raton, FL: CRC Press.

12. Skistad, H., **Displacement Ventilation**. Control of the built environment series ; 1. 1994, Taunton, Somerset, England ; New York :: Research Studies Press : Wiley.

13. Awbi, H.B., **Ventilation of Buildings**. 2003, London ; New York: Spon Press.

14. Rouaud, O. and M. Havet, **Numerical Investigation on The Efficiency of Transient Contaminant Removal from A Food Processing Clean Room using Ventilation Effectiveness Concepts**. *Journal of Food Engineering*, 2005. 68(2): p. 163-174.

15. ASHRAE, **ASHRAE 62-1999 Ventilation for Acceptable Indoor Air Quality**. 1999, Atlanta, GA: ASHRAE.

16. ASHRAE, **Environmental Tobacco Smoke: Position Document Approved by ASHRAE Board of Directors**. 2005, ASHRAE: Atlanta, Ga. p. 10.

17. Repace, J.L. and K.C. John, **Can Displacement Ventilation Control Secondhand ETS?** *ASHRAE IAQ Applications*, 2006. 7(4): p. 2-6.

18. Bjorn, E. and P.V. Nielsen. **Passive Smoking in a Displacement Ventilated Room**. in *Proceedings of Indoor Air'96, The 7th International Conference on Indoor Air Quality and Climate*. 1996. Nagoya, Japan,.

19. Awbi, H.B., **Air Distribution in Rooms : Ventilation for Health and Sustainable Environment : Proceedings of the 7th International Conference on Air Distribution in Rooms, 9-12 July 2000, Reading, UK**. 2000, Amsterdam ; New York: Elsevier Science Ltd.

20. FreshAB. 1996; Available from: http://www.airinnovation.se/engelsk/AQ.htm.

21. Karimipanah, T. and H.B. Awbi, **Theoretical and Experimental Investigation of Impinging Jet Ventilation and Comparison with Wall Displacement Ventilation**. *Building and Environment*, 2002. 37(12): p. 1329-1342.

22. Karimipanah, T., M. Sandberg, and H.B. Awbi. **A Comparative Study of Different Air Distribution Systems in A Classroom**. in *ROOMVENT2000*. 2000. Oxford: Elsevier.

23. Varodompun, J., **Airflow Simulation Techniques for Architectural Applications**, in *TCAUP college of architecture*. 2005, The University of Michigan: Ann Arbor. p. 71.

24. Cotel, A.J., et al., **Laboratory Experiments of A Jet Impinging on A Stratified Interface**. *Experiments in Fluids*, 1997. 23(2): p. 155-60.

25. Van Brecht, A., et al., **Image Processing to quantify the Trajectory of a Visualized Air Jet**. *Journal of Agricultural Engineering Research*, 2000. 76(1): p. 91-100.

26. Gharib, M., **Perspective: The Experimentalist and The Problem of Turbulence in The Age of Supercomputers**. *Transactions of the ASME. Journal of Fluids Engineering*, 1996. 118(2): p. 233-42.

27. Sugiyama, T.e.a. **Field Measurement on Indoor Climate of Passenger Terminal Building of Kansai International Airport under two Different Operation Models of its Air Conditioning System**. in *ROOMVENT96*. 1996.

28. Settles, G.S., **Schlieren and Shadowgraph Techniques : Visualizing Phenomena in Transparent Media**. c2001, Berlin ; New York: Springer. 376.

29. Settles, G.S., **Visualizing Full-Scale Ventilation Airflows**. *ASHRAE Journal*, 1997. 39(7): p. 19-26.

30. Settles, G.S. **The Penn State Full-Scale Schlieren System**. in *The 11th International Symposium on Flow Visualization*. 2004. Notre Dame University.

31. Varodompun, J., **HVAC Ventilation Strategies: The Contribution for Thermal Comfort, Energy Efficiency, and Indoor Air Quality**. *Journal of Greenbuilding*, 2007. 2(2): p. 131-150.

32. Varodompun, J., A.J. Cotel, and M. Navvab. **Ventilation Performances of Mixing, Displacement, and Impinging Jet system in different HVAC scenarios: Part I & II**. in *EPIC 2006 AIVC Technologies & Sustainable Policies for a Radical Decrease of the Energy Consumption in Buildings*. 2006. Lyon, France.

33. Varodompun, J. and M. Navvab. **The Full Scale and CFD simulation of Impinging Jet Ventilation**. in *The 6th International Conference of Indoor Air Quality, Ventilation, and Energy Conservation in Buildings (IAQVEC)*. 2007. Sendai, Japan.

34. Varodompun, J. and M. Navvab. **The Impact of Terminal Configurations in Impinging Jet Ventilated Room**. in *The 6th International Conference of Indoor Air Quality, Ventilation, and Energy Conservation in Buildings (IAQVEC)*. 2007. Sendai, Japan.

35. Christianson, L.L., R.a.A.-C.E. American Society of Heating, and F. National Science, **Building Systems : Room Air and Air Contaminant Distribution**. 1989, Atlanta, Ga: American Society of Heating, Refrigerating and Air-Conditioning Engineers, Inc.

36. ANSYS, **ANSYS CFX 10.0 User's Manual**. 2005, ANSYS.

37. Jørgensen, F.E., **How to Measure Turbulence with Hot-Wire Anemometers - A Practical Guide**. 2002, Dantecdynamics: Skovlunde, Denmark. p. 52.

38. Dantecdynamics, **IFS-200 Data Acquisition Software, User's Manual**. 2002, Dantecdynamics: Skovlunde, Denmark.

39. TOSHIBA, **TOSVERT™ VF-S11, Instruction Manual**. 2004, TOSHIBA.

40. Bushby, S.T., N.S. Castro, and J. Schein, **Project 2.3 – Air Handling Unit and VAV Box Diagnostics/ Task 2.3.3 – Testing AHU rule-based diagnostic tool & VAV diagnostic tool using the VCBT**, in *Task Report for the Energy Efficient and Affordable Small Commercial and Residential Buildings Research Program*, J.M. House, Editor. 2001, NIST: Gaithersburg, Maryland.

41. Bobenhausen, W., **Simplified Design of HVAC Systems**. Parker-Ambrose series of simplified design guides. 1994, New York: Wiley.

42. SIEMENS, **Insight 3.6 User's Guide**. Insight Online Documentation ed. 2004: SIEMENS.

43. Cowen, E.A., K.A. Chang, and Q. Liao, **A Single-Camera Coupled PTV-LIF Technique**. *Experiments in Fluids*, 2001. 31(1): p. 63-73.

44. Arcoumanis, C., J.J. McGuirk, and J.M.L.M. Palma, **On The Use of Fluorescent Dyes for Concentration Measurements in Water Flows**. *Experiments in Fluids (Historical Archive)*, 1990. 10(2 - 3): p. 177-180.

45. Ozcan, S.E., E. Vranken, and D. Berckmans, **A Temperature-Based Method for Determination of The Two-Dimensional Trajectory of An Air Jet**. *Building and Environment*, 2005. 40(10).

46. FLIR, **ThermaCAM E45 User's Manual**, FLIR.

47. FLIR, **ThermaCAM QuickView User's Manual**. 2005, FLIR.

48. Navvab, M. and J. Varodompun. **Qualitative and Quantitative Evaluation of Michigan Solar Decathlon Home**. in *ISES/ASES solar world congress 2005*. 2005. Orlando, Florida: ISES/ASES.

49. Navvab, M. and J. Varodompun. **Pedestrians' Comfort Index in Urban Settlements Using CFD Analysis**. in *EPIC 2006 AIVC Technologies & Sustainable Policies for a Radical Decrease of the Energy Consumption in Buildings*. 2006. Lyon, France.

50. AutoDesk, **AutoCAD2006**. 2005, AutoDesk.

51. AutoDesk, **3DsMAX 8.0 User's References Guide**. 2005, AutoDesk.

52. ANSYS, **ANSYS ICEM 10.0 User's Manual**. 2005, ANSYS.

53. IEA, **Annex20:Airflow Patterns within Buildings-Subtask 1: Room Air and Contaminant Flow, Evaluation of Computational Method** in *Energy Conservation within Buildings and Communities Systems Programme*, A.D. Lemaire, Editor. 1993, International Energy Agency (IEA): Delft, Netherlands. p. 82.

54. Luo, S., J. Heikkinen, and B. Roux, **Simulation of Air Flow in the IEA Annex 20 Test Room--Validation of A Simplified Model for The Nozzle Diffuser in Isothermal Test Cases**. *Building and Environment*, 2004. 39(12): p. 1403-1415.

55. Yoshie, R., et al. **Cooperative Project for CFD Prediction of Pedestrian Wind Environment in the Architectural Institute of Japan**. in *EACWE4 - The Fourth European & African Conference on Wind Engineering*. 2005. Prague.

56. Sorensen, D.N. and P.V. Nielsen, **Quality Control of Computational Fluid Dynamics in Indoor Environments**. *Indoor Air*, 2003. 13(1): p. 2-17.

57. Nielsen, P.V., **Computational Fluid Dynamics and Room Air Movement**. *Indoor Air*, 2004. 14(s7): p. 134-143.

58. Etheridge, D.W. and M. Sandberg, **Building Ventilation : Theory and Measurement**. 1996, Chichester, New York: John Wiley & Sons.

59. Kavanaugh, S., **Psychrometric Spreadsheet**. *ASHRAE Journal*, 2006. 48(1): p. 28-32.

60. Awbi, H.B., **Energy Efficient Room Air Distribution**. *Renewable Energy*, 1998. 15(1-4): p. 293-299.

61. BSR/ASHRAE, **BSR/ASHRAE Standard 129-1997 (RA): Measuring Air-Change Effectiveness**. 2002, Atlanta, GA: ASHRAE.

62. Persily, A.K., S.W. Dols, and S.J. Nabinger, **Air Change Effectiveness Measurement in Two Modern Office Buildings**. *Indoor Air*, 1994. 4: p. 40-55.

63. Sandberg, M., **What is Ventilation Efficiency?** *Building and Environment*, 1981. 16(2): p. 123-135.

64. Taylor, S.T., **LEED and Standard 62.1**. *ASHRAE Journal*, 2005. 47: p. s4-s8.

65. Stanke, D., **Standard 62-2001 Addendum 62n: Single-Path Multi-Zone System Design** *ASHRAE Journal*, 2005. 47(1): p. 28-35.

66. Herrmann, D.C., **Understanding CO_2 and ASHRAE 62 A Technical Note**. *Energy Engineering 99, no. 1*, 2001.

67. Fisk, W.J., **Measuring OA Intake Rates**. *ASHRAE Journal* 2006. 48: p. 50-57.

68. Olgyay, V. and A. Olgyay, **Design with Climate: Bioclimatic Approach to Architectural Regionalism. Some Chapters based on Cooperative Research with Aladar Olgyay**. 1963, Princeton, NJ.: Princeton University Press.

69. ISO, **ISO 7726, Thermal Environments- Instrument and Methods for Measuring Physical Quantities**. 1985: Geneva.

70. Fanger, P.O., **Thermal Comfort: Analysis and Applications in Environmental Engineering**. 1972, New York :: McGraw-Hill.

71. SQUAREONE, **PSYCHTOOL**. 2000, SQUAREONE.

72. Poreh, M., Y.G. Tsuei, and J.E. Cermak, **Investigation of a Turbulent Radial Wall Jet** *Transaction of ASME, Journal of Applied Mechanics*, 1967: p. 457-463.

73. Rajaratnam, N., **Turbulent Jets**. Developments in water science. 5. 1976, Amsterdam ; New York :: Elsevier Scientific Pub. Co.

74. Abramovich, G.N., **The Theory of Turbulent Jets**. 1963, Cambridge, Mass: M.I.T. Press.

75. Knowles, K., **Computational Studies of Impinging Jets using k-e Turbulence Models**. *International Journal for Numerical Methods in Fluids*, 1996. 22(8): p. 799-810.

76. Rajaratnam, N. and B.S. Pani, **Three-Dimensional Turbulent Wall Jets**. *Journal of The Hydraulic Division*, 1974. 100: p. 69-83.

77. Zhao, W.N., K. Kumar, and A.S. Mujumdar, **Flow and Heat Transfer Characteristics of Confined Noncircular Turbulent Impinging Jets**. *Drying Technology*, 2004. 22(9): p. 2027-2049.

78. Turner, W.C., **Energy Management Handbook**. 2005, Lilburn, Ga: Fairmont Press ; Distributed by Marcel Dekker.

79. Cabeza, J.M. and J.M. Almodovar. **The Architect Roberto Rivero and Daylighting Research**. in *PLEA 2003 - The 20th Conference on Passive and Low Energy Architecture*. 2003. Santiago, Chile.

80. DOE, **eQUEST**. 2004.

81. Hirsch, J.J., **Energy Simulation Training for Design & Construction Professionals**, in *eQUEST Quick energy Simulaton Tool*. 2004.

82. ASHRAE, **ASHRAE Standard 90.1 2001: Energy Standard for Building Except Low-rise Residential Building**. 2001, ASHRAE: Atlanta, GA.

83. Varodompun, J., **Architectural and HVAC Application of Impinging Jet Ventilation using Full Scale and CFD Simulation**, in *TCAUP college of architecture*. 2007, The University of Michigan: Ann Arbor.

84. Malkawi, A. and G. Augenbroe, **Advanced Building Simulation**. 2004, London ; New York: Spon.

85. Dantecdynamics, **Product Information, Omnidirectional Transducer 54T21 for Indoor Air Flows**: Skovlunde, Denmark. p. 4.

86. NI, **DAQ Getting Started Guide**, National Instruments Corporation.

87. NI, **Portable E Series Multifunction DAQ 12 or 16-Bit, up to 1.25 MS/s, 16 Analog Inputs**, National Instruments Corporation.

88. NI, **Low-Cost M Series Multifunction DAQ –16-Bit, 250 kS/s, up to 80 Analog Inputs**, National Instruments Corporation.

89. NI, **Full-Featured E Series Multifunction DAQ 12 or 16-Bit, up to 1.25 MS/s, up to 64 Analog Inputs**, National Instruments Corporation.

90. Komogorov, A.N., **Local Structure of Turbulence in An Incompressible Viscous Fluid at Very High Reynolds Numbers**. *Sov. Phys. Usp*, 1968. 10(No. 6): p. 734-736.